



저작자표시-비영리-변경금지 2.0 대한민국

이용자는 아래의 조건을 따르는 경우에 한하여 자유롭게

- 이 저작물을 복제, 배포, 전송, 전시, 공연 및 방송할 수 있습니다.

다음과 같은 조건을 따라야 합니다:



저작자표시. 귀하는 원저작자를 표시하여야 합니다.



비영리. 귀하는 이 저작물을 영리 목적으로 이용할 수 없습니다.



변경금지. 귀하는 이 저작물을 개작, 변형 또는 가공할 수 없습니다.

- 귀하는, 이 저작물의 재이용이나 배포의 경우, 이 저작물에 적용된 이용허락조건을 명확하게 나타내어야 합니다.
- 저작권자로부터 별도의 허가를 받으면 이러한 조건들은 적용되지 않습니다.

저작권법에 따른 이용자의 권리는 위의 내용에 의하여 영향을 받지 않습니다.

이것은 [이용허락규약\(Legal Code\)](#)을 이해하기 쉽게 요약한 것입니다.

[Disclaimer](#)

공학박사 학위논문

고성능 리튬이차전지용 올리빈계
양극소재에 관한 연구

Tailoring olivine cathode electrode materials
for high performance lithium secondary battery

2016 년 02 월

서울대학교 대학원

재료공학부

박 규 영

Abstract

Tailoring olivine cathode electrode materials for high performance lithium secondary battery

Kyu-Young Park

Department of Materials Science and Engineering

College of Engineering

Seoul National University

Lithium iron phosphate (LFP) has attracted much attention as a cathode electrode material for next-generation lithium rechargeable battery system because of its superior chemical/thermal stability, long term cycle life from rigid crystal structure, suitable energy density for using large scale energy storage system and use of low-cost element, iron. In the ideal case, the lithium iron phosphate could release and insert lithium ions on their crystal structure with a theoretical gravimetric energy density specific capacity of 580 Wh kg⁻¹(theoretical capacity of ~ 169 mAh g⁻¹, Fe^{2+/3+} redox voltage of

3.42 V (vs. Li/Li⁺)) through the one dimensional lithium diffusion channels being along the [010] direction of crystal structure (*Pnma*). However, the presence of immobile defects in the diffusion paths, which may originate from impurities or Li-Fe cation site exchange defect (anti-site defect), can significantly retard the mobility of ions of lithium iron phosphate. In particular, crystals with only one-dimensional diffusion pathways, such as olivine-type materials lithium iron phosphate, are detrimental with the presence of defects. Depending on synthesis process, approximately 0.5–7 % of the Li-Fe anti-site defect is present in crystal structure, which results in immobile Fe ions in the [010] lithium ion diffusion channel. According to report, the presence of 0.1 % anti-site defects in a micron-sized particle reduces its energy density to almost half of theoretical capacity and decreases the lithium ionic conductivity by two or three orders of magnitude.

Chapter 2 introduce a new method to remove anti-site defects in olivine crystals using electrochemical charge carrier injection process at a room temperature. The Fe anti-site defects in LiFePO₄ are effectively reduced by the electrochemical recombination of Li/Fe anti-sites. The healed crystal structure of lithium iron phosphate recovers its specific capacity and high-power capabilities. In this chapter, various configuration of anti-site defects and its recombination mechanisms are discussed.

Chapter 3 and 4 deals with a new type lithium-excess composition lithium iron phosphate having zero Fe anti-site in their crystal structure. It is confirmed that the Fe anti-site defects are completely removed in lithium-excess composition lithium iron phosphate due to its unique Fe oxidation state, showing superior rate capability and long term cycle ability. In this chapter, not only the structural characterization of lithium-excess lithium iron phosphate with zero Fe anti-site but also electrochemical behavior arising from thermodynamic and kinetic properties, especially Spinodal decomposition behavior and memory effect, will be discussed.

Keywords: Energy storage, Lithium rechargeable battery, cathode, olivine

Table of Contents

Chapter 1. General Introduction	1
1.1 Preface.....	1
1.1.1 General background	1
1.1.2 Spinodal decomposition behavior on electrode.....	4
1.1.3 References.....	8
Chapter 2. Anti-site reordering in LiFePO₄ using charge carrier injection	11
2.1 Introduction.....	11
2.2 Experimental	15
2.3 Results and Discussion.....	18
2.3.1 Anti-site configuration & possible recombination process...	18
2.3.2 Charge carrier injection method to reduce anti-site concentration	25
2.4 Conclusion.....	43
2.5 References	44
Chapter 3. Lithium-excess olivine for zero Fe_{Li} defect	51

3.1 Introduction	51
3.2 Experimental	55
3.3 Results and Discussion	57
3.3.1 Structural characterization of lithium-excess olivine	57
3.3.2 Local atomic configuration and origin of zero Fe anti-site of lithium-excess olivine	75
3.3.3 New [101] diffusion path of lithium-excess olivine	91
3.3.4 Electrochemical properties	101
3.4 Conclusion	103
3.5 References	104
Chapter 4. Thermodynamic and kinetic issues	121
4.1 Hysteresis gap and Memory effect of LiFePO_4	121
4.1.1 Experimental section	121
4.1.2 Lowed Spinodal decomposition barrier	122
4.1.3 Less memory effect at new LFP system	125
4.2 Conclusion	145
4.3 References	146
Chapter 5. Summary	157

Chapter 6. Abstract in Korean	159
Curriculum Vitae.....	163

List of Figures

Figure 2-1. Calculated formation energy of anti-site defect in LiFePO ₄ and its configuration corresponding to the distance between Li ⁺ on Fe ²⁺ site and Fe ²⁺ on Li ⁺ site.	22
Figure 2-2 Formation energies for 45 different vacancy-Fe defect configurations of the single-phase Li _{1-x} FePO ₄ from first principles calculations.	23
Figure 2-3. Energy curve and schematics of the Fe-Li cation site re-ordering process during discharge.	24
Figure 2-4 The 15 ~ 55° high resolution powder diffraction patterns of prepared by hydrothermal synthesis.....	32
Figure 2-5 (a) Magnified (200) peak of high resolution powder diffraction patterns of the prepared samples. (b) Rietveld refinement results of solid-solution Li _{0.9} FePO ₄ . The inset figure is an SEM image of micro-size Li _{0.9} FePO ₄	33
Figure 2-6. Rietveld refinement results of hydrothermally prepared LiFePO ₄	34

Figure 2-7. Rietveld refinement results of solid-solution $\text{Li}_{0.9}\text{FePO}_4$	35
Figure 2-8. Rietveld refinement result of electrochemically treated LiFePO_4	36
Figure 2-9. Defect characterization.....	37
Figure 2-10. Lattice parameter with change modification with anti-site ratio at room temperature	38
Figure 2-11. The electrochemical profile of solid-solution $\text{Li}_{0.9}\text{FePO}_4$ at C/100.....	39
Figure 2-12. $15 \sim 55^\circ$ XRD patterns of prepared by solid-state method samples	40
Figure 2-13. SEM image of prepared LiFePO_4	41
Figure 2-14. (a) First charge/discharge profile at C/200 of electrochemically treated micro- LiFePO_4 and hydrothermally grown micro- LiFePO_4 . (b) C-rate capability of electrochemically treated nano- LiFePO_4 (red) and conventional nano- LiFePO_4 (black).	42
Figure 3-1. Various synthetic condition and the impurity	61

Figure 3-2 Structure characterization results of lithium-excess LFP	62
Figure 3-3 Neutron diffraction (ND) Rietveld refinement results	65
Figure 3-4. XRD Rietveld refinement results	68
Figure 3-5. High resolution XRD experiment and simulation results	69
Figure 3-6. SEM image of normal and 5 % lithium-excess LFPs	70
Figure 3-7. Fe XANES measurements	71
Figure 3-8. TEM image of lithium-excess LFP surface	72
Figure 3-9. Surface analysis on 5 % lithium-excess LFP (red line) and normal LFP. (black line) 10 nm etched surface of lithium-excess LFP	73
Figure 3-10. Fourier transform infrared spectroscopy (FT-IR) results	74
Figure 3-11. ^6Li NMR resonance	81
Figure 3-12. Local atomic configurations	82
Figure 3-13. Local Fe ion oxidation state	83
Figure 3-14. In-situ temperature controlled XRD patterns	84

Figure 3-15. Possible cation exchange sites (LiFe-FeLi anti-site) at lithium-excess phase 87

Figure 3-16. Anti-site configuration and its formation energy 88

Figure 3-17. Anti-site defect formation energies at lithium-excess LFP as a function of distance from Li_{Fe} 89

Figure 3-18. The most stable anti-site configuration..... 90

Figure 3-19. Activation barriers for lithium ion hopping for normal and lithium-excess LFPs. 94

Figure 3-20. Conductivity change of Li-excess and normal LFPs..... 95

Figure 3-21. The schematics of Li ion diffusion along [010] direction in lithium-excess LFP. 96

Figure 3-22 The schematics of Li ion diffusion along [101] direction in lithium-excess LFP 97

Figure 3-23. The schematics of Li ion diffusion along [101] direction in normal LFP 98

Figure 3-24. [101] activation barrier of lithium-excess LFP. 99

Figure 3-25. [101] activation barrier of normal LFP.	100
Figure 3-26 Electrochemical properties of lithium-excess and normal LFPS	114
Figure 3-27. Hysteresis gap of electrodes	115
Figure 3-28. Rate capability of lithium-excess LFP (red) and normal LFP (black).	116
Figure 3-29. Galvanostatic discharge profiles	117
Figure 3-30. Ragone plot of various surface or chemical modified LFPS ·	118
Figure 3-31. Cycle life test of lithium-excess LFP with a current density ·	119
Figure4-1 . Mixing free energy and atomic configuration of lithium-excess LFP (orange) and normal LFP	130
Figure4-2 . Detailed DFT calculation results	131
Figure4-3. The single particle chemical potential	132
Figure4-4 Thermal phase diagram of lithium-excess LFP	133
Figure4-5 . Thermal XRD patterns of lithium-excess LFP	135

Figure4-6 . Memory effect of normal LFP.....	136
Figure4-7 Memory effect of lithium-excess LFP.	137
Figure4-8. OCV change of both electrodes.....	138
Figure4-9 . The effective diffusivity.....	139
Figure4-10 . Conductivity measurement.....	141
Figure4-11 . Confirmation on memory effect depending on rest time	144

Chapter 1. General Introduction

1.1 Preface

1.1.1 General background

Now a days, the global community faces an energy and environmental issues arising from exhaustion of fossil fuel resources, CO₂ emissions and global warming problem.[1] Thus, the energy generation paradigm is moved from fossil fuel based phase to renewable energy generation using sustainable resources, such as wind power, solar and geothermal energy.[1, 2] However, because those sustainable energy generation systems are tied to geometrical and temporal limitations, the energy demands and generation are not always coincident. Therefore, the development of large scale energy storage systems is required to overcome the intermittent energy generation problems. Among the various energy storage systems, the lithium rechargeable battery system is attracted great attentions as a solution of intermittent energy generation problems due to its high energy density, power density and round-trip efficiency.[1, 2]

Most electrode materials for lithium rechargeable batteries store energy based on intercalation mechanism.[1] The guest ions move from thermodynamically stable interstitial sites to out of crystalline host materials with electrons extraction, and the reverse reaction occurs with the injection

of electrons. Therefore, the ability of ion diffusion in the crystal structure strongly affects on the electrochemical properties in terms of energy density, power density and round-trip efficiency.[3-5] The ionic diffusion ability sensitively undergo changes with several factors such as temperature, diffusional activation energy and local atomic configuration. Among them, the defect in crystal structure is one of inevitable factors that determine ionic diffusion ability, therefore, careful choices of synthesis route or post treatment are required to control defect concentration.[6, 7] Especially, the electrode materials having a limited one- (1-D) or two-dimensional (2-D) guest ion diffusion pathway, such as olivine type LiFePO_4 for Li rechargeable electrode, are susceptible to presence of defects that could impede Li ion diffusion.[8-10]

The lithium iron phosphates (LFP) has been intensely investigated for last two decades as a cathode electrode material and model of thermodynamic Li ion intercalation for phase separating electrode materials.[11-14] The LFP shows promising electrochemical properties for applying a large scale energy storage system such as superior thermal stability, low cost, long term cycle stability and suitable theoretical energy density. Theoretically, the LFP could release and insert Li ion on their crystal structure with a theoretical gravimetric energy density of 580 Wh kg^{-1} (theoretical capacity of $\sim 169 \text{ mAh g}^{-1}$, $\text{Fe}^{2+/3+}$ redox voltage of 3.42 V (vs. Li/Li^+)) through the 1-D channels

being along the [010] direction of crystal structure (*Pnma*).[15] However, in practice, the Li-Fe cation site exchange defect (anti-site) in Li diffusion channel always forms with 1 ~ 5 % ratio depending on synthesise route, resulting in denying LFP to reach at a desired energy and power density.[4] For example, the presence of 0.1 % anti-site ratio in micro size LFP makes statically its energy density to almost half of original value and reduces ionic conductivity with two or three orders.[8] Since the nano-sizing[8] or post crystal structural treatment[9] on LFP has been widely applied to avoid immobile Fe anti-site effect, these approaches cannot completely get rid of the anti-site effects from LFP because anti-site still remains under 1% in their structure. In addition, the nano-synthesis leads to other problems, such as lowering tap density of electrode, generating other surface defects, surface side reaction during cycling and additional cost problem at synthesizing.[16, 17] Therefore, it is difficult for these approaches to be an ultimate solutions as satisfying high gravimetric/volumetric energy density and low cost active materials.

1.1.2 Spinodal decomposition behavior on electrode

Since the pioneering work on olivine type electrode materials, the phase behavior during electrochemical cycling of LiFePO_4 compounds is well investigated as the typical phase separation behavior at room temperature. *i. e.* two-phase reaction. [1] At the bulk scale LiFePO_4 , the lithium-rich and lithium-poor phases are coexisted in their crystal structure, forming phase boundary between those phases during cycling. [1-5] However, the recently experimental works on LiFePO_4 revealed that some thermodynamic factors could change the solubility limits of LiFePO_4 , resulting in distinguishable phase behavior with pure bulk one.[11-15] These new insight on the phase behavior open the chance to understanding the intrinsic properties of electrode materials. [12-13] Especially, the Spinodal decomposition behavior, which is one of well-known phase separation mechanism, at nano-sizing olivine materials provides a key clues on solving the unexpected fast charge/discharge behavior of LiFePO_4 . [19] According to the previous research that investigated on how the interfacial energy, coherency strain energy induced by lattice parameter difference between lithium-rich and lithium-poor olivine phases or surface energy modified as decreasing particle size.[ref] This increasing internal coherency energy bring the result of thermodynamic positive energy penalty, resulting in curvature like shape lithium-chemical potential during charge/discharge. The LiFePO_4 operating

with Spinodal decomposition mechanism could exhibit higher rate-capability due to lack of phase boundary movement in a single particle. [12, 19]

Moreover, the Spinodal decomposition with electrode materials exhibits some unique properties. First, it is an origin of ‘hysteresis gap’ between charge/discharge at an ultra-low current density. Theoretically, operation voltage of the lithium ion battery system is based on the thermodynamic phase equilibrium state with counter electrode. Therefore, in ideal case *i.e.* state without polarization came from cell system, such as concentration or resistance polarization, the voltages is only determined by state of charge regardless charge or discharge process. However, the nano-sizing LiFePO₄ exhibit the un-narrow-able polarization gap between charge and discharge even in an ultra-low current density. Previous research revealed that this ‘hysteresis gap’ is came from Spinodal decomposition barrier, providing new insight on lithium-ion battery system which could have ‘thermodynamic polarization. [12]

Second, the Spinodal decomposition chemical potential shape cause the memory effect on lithium-ion battery. As discussed at previous section, because the lithium ion battery is operated based on reversible reactions, the battery system could not ‘memorize’ how much electrode is charged or discharged. However, recently, Sasaki and *et. al*, firstly discovered that the

electrode casted with LiFePO_4 exhibit unexpected voltage bumped phenomena when the cell is re-charged after partially charge/discharge process.[13] They concluded that this strange observation is came from the particle-by-particle phase separating caused by Spinodal decomposition behavior.

Chapter 2 deals with a new defect control method using an electrochemical procedure at room temperature.[18] By tailoring the local environment around defects according to a strategy suggested by first principles calculations, it was found that the energy level of defects and the activation barrier for recombination could be lowered significantly. Experimental verification with a case study of LiFePO_4 revealed that significant defect annihilation occurred from a structural analysis, which substantially boosted the power capability of the material. In this work, an effective way to reduce Li-Fe defects is proposed using a simple electrochemical treatment at room temperature.

Chapter 3 introduces the lithium-excess concept could be expanded from layered type electrode to polyanion-based electrode, especially at olivine type that is one of the most promising cathode electrode materials.[19] The Li-excess LFP shows superior rate performance that it release almost half of

theoretical capacity at a high current density as well as stable electrochemical cycling.

The Chapter 4 introduces that lithium-excess configuration plays role as a “*phase mixing seed*” that reduces thermodynamic phase transition activation energy. The intrinsic thermodynamic and kinetic changes of Li-excess LFP induce lowering thermal solid-solution temperature and less memory effect than stoichiometric LFP.

1.1.3 References

1. Armand, M. and J.M. Tarascon, Building better batteries. *Nature*, 2008. **451**(7179): p. 652-657.
2. Kang, K., et al., Electrodes with High Power and High Capacity for Rechargeable Lithium Batteries. *Science*, 2006. **311**(5763): p. 977-980.
3. Kang, K. and G. Ceder, Factors that affect Li mobility in layered lithium transition metal oxides. *Physical Review B*, 2006. **74**(9): p. 094105.
4. Chen, J. and J. Graetz, Study of Antisite Defects in Hydrothermally Prepared LiFePO₄ by in Situ X-ray Diffraction. *ACS Applied Materials & Interfaces*, 2011. **3**(5): p. 1380-1384.
5. Dathar, G.K.P., et al., Calculations of Li-Ion Diffusion in Olivine Phosphates. *Chemistry of Materials*, 2011. **23**(17): p. 4032-4037.
6. Hoang, K. and M. Johannes, Tailoring Native Defects in LiFePO₄: Insights from First-Principles Calculations. *Chemistry of Materials*, 2011. **23**(11): p. 3003-3013.
7. Van der Ven, A. and G. Ceder, Lithium Diffusion in Layered Li_xCoO₂. *Electrochemical and Solid-State Letters*, 2000. **3**(7): p. 301-304.
8. Malik, R., et al., Particle Size Dependence of the Ionic Diffusivity. *Nano Letters*, 2010. **10**(10): p. 4123-4127.
9. Chen, J. and M.S. Whittingham, Hydrothermal synthesis of lithium

- iron phosphate. *Electrochemistry Communications*, 2006. **8**(5): p. 855-858.
10. Tealdi, C., C. Spreatico, and P. Mustarelli, Lithium diffusion in $\text{Li}_{1-x}\text{FePO}_4$: the effect of cationic disorder. *Journal of Materials Chemistry*, 2012. **22**(47): p. 24870-24876.
 11. Gibot, P., et al., Room-temperature single-phase Li insertion/extraction in nanoscale Li_xFePO_4 . *Nat Mater*, 2008. **7**(9): p. 741-747.
 12. Dreyer, W., et al., The thermodynamic origin of hysteresis in insertion batteries. *Nat Mater*, 2010. **9**(5): p. 448-453.
 13. Sasaki, T., Y. Ukyo, and P. Novák, Memory effect in a lithium-ion battery. *Nat Mater*, 2013. **12**(6): p. 569-575.
 14. Delacourt, C., et al., The existence of a temperature-driven solid solution in Li_xFePO_4 for $0 < x < 1$. *Nat Mater*, 2005. **4**(3): p. 254-260.
 15. Padhi, A.K., K.S. Nanjundaswamy, and J.B. Goodenough, Phospho-olivines as Positive-Electrode Materials for Rechargeable Lithium Batteries. *Journal of The Electrochemical Society*, 1997. **144**(4): p. 1188-1194.
 16. Julien, C.M., A. Mauger, and K. Zaghbi, Surface effects on electrochemical properties of nano-sized LiFePO_4 . *Journal of Materials Chemistry*, 2011. **21**(27): p. 9955-9968.
 17. Wang, J., et al., Size-dependent surface phase change of lithium iron phosphate during carbon coating. *Nat. Commun.*, 2014. **5**.
 18. Park, K.-Y., et al., Anti-Site Reordering in LiFePO_4 : Defect

Annihilation on Charge Carrier Injection. *Chemistry of Materials*, 2014.
26(18): p. 5345-5351.

[19] Delmas. C., et al., Lithium deintercalation in LiFePO₄ nanoparticle via a domino-cascade model. *Nat. Mater.*, 2008. 7, p. 665-671

Chapter 2. Anti-site reordering in LiFePO₄ using charge carrier injection

(The content of this chapter has been published in *Chemistry of Materials*. Reprinted with permission from K.-Y Park *et al.* Anti-Site Reordering in LiFePO₄: Defect Annihilation on Charge Carrier Injection. *Chem. Mater.*, **2014**, 26 (18) pp. 3545-5351 (DOI: 10.1021/cm502432q). Copyright 2014 American Chemical Society.

2.1 Introduction

Defects in crystals are an important factor governing the intrinsic properties of materials, such as mechanical strength, electronic conductivity, and mass diffusion rates.[1-3] While the concentration of defects in a crystal at a certain temperature and pressure is determined by thermodynamics,[4-6] materials synthesized via non-equilibrium routes generally contain higher concentrations of defects. Careful choices of synthesis conditions or post-treatment methods are needed to control the level of defects and to tune the properties of materials.[7-10] In conventional semiconductor systems, it is known that the type and concentration of defects determine the electronic properties of materials.[11-13] Similarly, in ion mass-transfer systems, they critically affect kinetic properties.[14-16]

Defects in a crystal can impede ion transport by blocking diffusion pathways in one- (1-D) or two-dimensional (2-D) ionic conductors [17-19] LiFePO_4 , an important material in batteries, is a good example of this. While it has been considered a promising electrode material [20-22] due to its stability [23, 24] and relatively high energy density [25, 26], kinetic issues arising from the restrictive diffusion pathways for lithium ions and the low electronic conductivity have been problematic. [27] In particular, lithium ions can diffuse only through a 1-D tunnel in the crystal. Thus, this diffusion is susceptible to the presence of defects that may block the tunnel. [3] Since nano-sizing has been conducted widely for this material, the reduction in diffusion length can partly resolve the low-power problem. However, more importantly, nano-sizing is capable of reducing the detrimental effects of the defects blocking the channel. Malik *et al.* recently revealed that with 0.1% of Li-Fe site exchange in LiFePO_4 , ~45% of Li ions are trapped, statistically, between the defects in a 1- μm LiFePO_4 particle. However, this drops significantly, to ~5% in a 100-nm LiFePO_4 particle. [3] For these trapped lithium ions to participate in the battery reaction, they must diffuse through other unfavorable diffusion pathways that require higher activation barriers ($> 1 \text{ eV}$). [27-29]

Important practical issue with nano-sized LiFePO_4 that needs to be urgently

addressed, nevertheless, is the low electrode tap density, which results in a significant reduction in the volumetric energy density. It is simply because the interactions between nanoparticles make it difficult for them to be packed densely. This issue is more serious for LiFePO_4 , the crystal density of which is only 3.6 g/cm^3 , which is substantially lower than those of commercial electrodes, such as LiCoO_2 (5.1 g/cm^3) and LiMn_2O_4 (4.2 g/cm^3). [30, 31] Using nano- LiFePO_4 , in this regard, can hardly satisfy the requirements for batteries with high volumetric energy density. In this regards, it is increasingly important to develop a micro- LiFePO_4 electrode material that is capable of delivering satisfactory performance with reasonably high gravimetric/volumetric energy density. However, previous studies on large-size LiFePO_4 particles have shown that the material delivers undesirably low specific capacity or power capabilities. [3, 32, 33]

The minimization of defects in micro- LiFePO_4 can contribute to enhancing the transport properties because it reduces the possibility of blocking lithium diffusion tunnels. Since the blocking effect becomes more serious in larger particles, as noted, the control of anti-site defects becomes more critical in developing larger LiFePO_4 particles having fast transport properties. Previous approaches to reducing defects in crystals have mainly used high temperatures, with post heat treatment to recombine defects. [18] Here, we

report a novel way to reduce anti-site (Li-Fe) defects in LiFePO_4 electrochemically at room temperature. In this approach, we intentionally introduced a vacancy in the lithium channel by partial charging, and carried out a deep discharge below the conventional voltage cut-off. As a result, we observed significant Fe_{Li} -defect annihilation, resulting in defect-less LiFePO_4 from a structural analysis. Furthermore, the electrochemical performance could be enhanced markedly in the ‘healed’ sample. Density functional theory calculations suggest that Fe_{Li} -defect migration and annihilation could be facilitated by the introduction of vacancies near defects and the injection of excess electrons during over-discharge, which lowers the migration barrier for Fe defects.

2.2 Experimental

LiFePO₄ with a high concentration of defects was synthesized by a hydrothermal method. LiOH (Sigma Aldrich, 99.9%), FeSO₄·7H₂O (Sigma Aldrich, 99.8%), and H₃PO₄ (Sigma Aldrich, 85 wt% in water base) were used as precursors at a molar ratio of 3:1:1 in deionized water. The mixture was heated to 180°C in an autoclave and maintained for 2 h in an air atmosphere. The synthesized powder was filtered and then moved to a drying oven at 120°C for 24 h to remove water.

The solid-state synthesis of LiFePO₄ used precursors such as Li₂CO₃ (Sigma Aldrich, 99.9%), FeC₂O₄·H₂O (Sigma Aldrich, 99%), NH₃HPO₄ (Aldrich, 98%), and pyromellitic acid hydrate (Fluka, 6 wt%, PA, 99%) as the organic additive. The powders were ball-milled in acetone for 14 h and dried at 70°C. The mixture was first calcined at 500°C in an Ar atmosphere for 10 h. For additional carbon coating, 6 wt% of pyromellitic acid hydrate and 1 wt% of ferrocene (Aldrich, 98%) were mixed with the calcined powder using a ball-mill in acetone for 2 h. The acetone was then evaporated at 70°C in a drying oven. The dried mixture was pelletized under 200 kg cm⁻² pressure in a disk-shaped mold, and then sintered again at 600°C under Ar for 10 h.

The prepared LiFePO₄ powders and NO₂BF₄ powder were mixed in

acetonitrile for 4 h at a molar ratio of 1:0.1 for chemical delithiation. After the drying process, partially de-lithiated powder was heated again to 380°C for 4 h and quenched with liquid N₂. An electrode was fabricated by mixing the synthesized powders, pre-mixed with super P (22 wt%) in a ball mill for 24 h, and polyvinylidene fluoride (PVDF, 10 wt%) in N-methyl-2-pyrrolidone (NMP). The mixture was cast on Al foil and dried at 120°C for 2 h. Electrochemical cells were assembled using a CR2016-type coin cell with lithium metal as the counter electrode, a separator (Celgard 2400), and 1 M LiPF₆ in ethyl carbonate/dimethyl carbonate (Panax, EC/DMC, 1:1 v/v) as the electrolyte in an Ar-filled glove box.

First principle calculations were performed using the Perdew–Burke–Ernzerhof exchange-correlation parameterization to density functional theory (DFT) with the spin-polarized generalized gradient approximation (GGA).[34] A plane-wave basis set and the projector-augmented wave (PAW) method, as implemented in the Vienna *ab initio* simulation package (VASP), were used. Hubbard parameters (GGA+U) were added to correct the incomplete cancellation of the self-interaction of GGA.[35, 36] A U value of 4.3 eV (the on-site Coulomb term) and a J value of 1.0 eV (the exchange term) were used for the Fe atoms.[37] To study the defect configuration in Li_xFePO₄ ($x = 1/16$), we considered all possible orderings within the 1 × 2 × 2 supercell

of LiFePO_4 (112 atoms) generated with the CASM program, which contains defects of one Li in the M2 site, one Fe in the M1 site, and one vacancy in the M1 site.[38] All plausible configurations of Li-Fe cation site-exchange and a Li-vacancy within the 16-formula unit were considered. Activation energies for the ionic diffusion were calculated using the nudged-elastic-band (NEB) method.[39] Appropriate replicate systems were used as starting points for the NEB method, with linear interpolation between the initial and final states of the diffusion pathways.

High-resolution powder diffraction patterns were recorded using synchrotron X-ray radiation (the 8C2-HRPD beam-line at the Pohang Accelerator Laboratory, Korea). The incident X-rays were collimated using a mirror and monochromatized to a wavelength of $\sim 1.5495 \text{ \AA}$ using a Si (111) monochromator. The diffraction data were collected in the 10 to 130° range with a step size of 0.01° . Rietveld refinement of the HRPD results was conducted using the “Fullprof” program.[40] The size and morphology of the powders were observed using field emission scanning electron microscopy (FE-SEM, Philips, XL 30 FEG).

2.3 Results and Discussion

2.3.1 Anti-site configuration & possible recombination process

In perfect olivine LiFePO_4 , all Li and Fe ions occupy M1 and M2 octahedral sites, respectively. However, Li/Fe cation site exchange may lead to Li ions in M2 sites and Fe ions in M1 sites.[20, 41] This type of cation disorder can be an edge-shared Li/Fe defect or a corner-shared Li/Fe defect, as shown in Figure 2-1.[17, 41] Calculation of the defect formation energies indicates that both defects are comparable in energy, but the edge-shared Li/Fe defect (~ 390 meV) is slightly more probable than the corner-shared one (~ 490 meV), consistent with previous observations.[17] It has also been noted that the defect formation energy tends to decrease as the $\text{Fe}_{\text{Li}} - \text{Li}_{\text{Fe}}$ distance decreases among the types of anti-site. This indicates that an effectively attractive interaction does exist between Fe_{Li} and Li_{Fe} defects (see the formation energies for various defect types in Figure 2-1). Generally, it is known that these types of Li/Fe site exchange do not recombine during charging/discharging process or at room temperature due to the relatively high activation energy for recombination.[41]

The types of stable anti-site configurations differ with the introduction of a lithium vacancy, *i.e.*, $\text{Li}_{1-x}\text{FePO}_4$. DFT calculations on various anti-site

configurations showed that the corner-shared Li/Fe defect becomes more probable in Li-deficient olivine, even though both corner-shared (Figure 2-2 (a)) and edge-shared Figure 2-2 (b)) Li/Fe defects are comparably stable. However, it has been noted that all the stable anti-site configurations contain the vacancy as the first nearest neighbor to the Fe defect at the M1 octahedral site along the *b*-direction. It is believed that the relatively high valent Fe³⁺ exhibits stronger electrostatic repulsion, and thus prefers a vacancy to Li⁺ as its neighbor. As a consequence of the reduction in the electrostatic repulsion, the defect formation energy becomes lower in Li_{1-x}FePO₄ (~100 to 200 meV) than in LiFePO₄ (~400 to 500 meV; Figure 2-2). Furthermore, defect formation is energetically more stable than the defect-free Li_{15/16}FePO₄ phase (dotted line in Figure 2-2). This suggests that a meta-stable Li_{15/16}FePO₄ phase, if any, is likely to contain appreciable amounts of Li/Fe site exchange, although the most stable state is the two-phase coexistence of LiFePO₄ and FePO₄.

Close examination of the stable anti-site configurations revealed that the major defect type (corner-shared defect, Fig. 1(a)) has a plausible re-ordering route. In the possible route, shown in Figure 2-3, Li migrates to the vacant M1 site (inset 1, 2), then Fe moves sequentially to the M2 site (inset 3, 4), annihilating the defect. To assess this possible defect recombination, we

calculated the activation energy following the hypothetical migration path using NEB calculations. Figure 2-3 illustrates the energy profile along the recombination path. The recombination involved a relatively high activation energy of ~ 1.4 eV. When the lithium ion diffuses from M2 to the vacant M1 site, the system becomes destabilized gradually by ~ 1 eV (inset 2 of Figure 2-3) and iron migration carries an additional ~ 400 meV barrier (inset 3 of Figure 2-3). The high activation barrier of ~ 1.4 eV is attributable to the strong electrostatic repulsion among cations during the migration, and implies that the recombination of the defect in such conditions is unlikely to occur at room temperature.[28, 29] However, we found that a slight reduction of the system can significantly lower the activation barrier. When we intentionally injected excess electrons into the system, Fe^{3+} in the M2 site becomes reduced locally to Fe^{2+} , leading to a decrease in the activation barrier of iron migration from ~ 1.4 eV to ~ 0.8 eV. Considering that the activation barriers in many operable electrodes at room temperature range within several hundreds meV,[12, 28, 41] this indicates that recombination of the defect at room temperature is quite plausible in this case. While the injection of excess charge into the system is purely artificial in the calculations, we suggest that it can occur in the dynamic circumstances of charging or discharging of the electrode in electrochemical systems. A local charge imbalance due to the differing mobilities of the cation (Li ion) and electron during discharge can also induce such a situation.

However, the second major defect type, the edge-shared defect (Figure 2-2(b)), does not have an apparent re-ordering route, indicating that an edge-shared defect would not recombine and would remain, even with this healing process, which we will discuss further below.

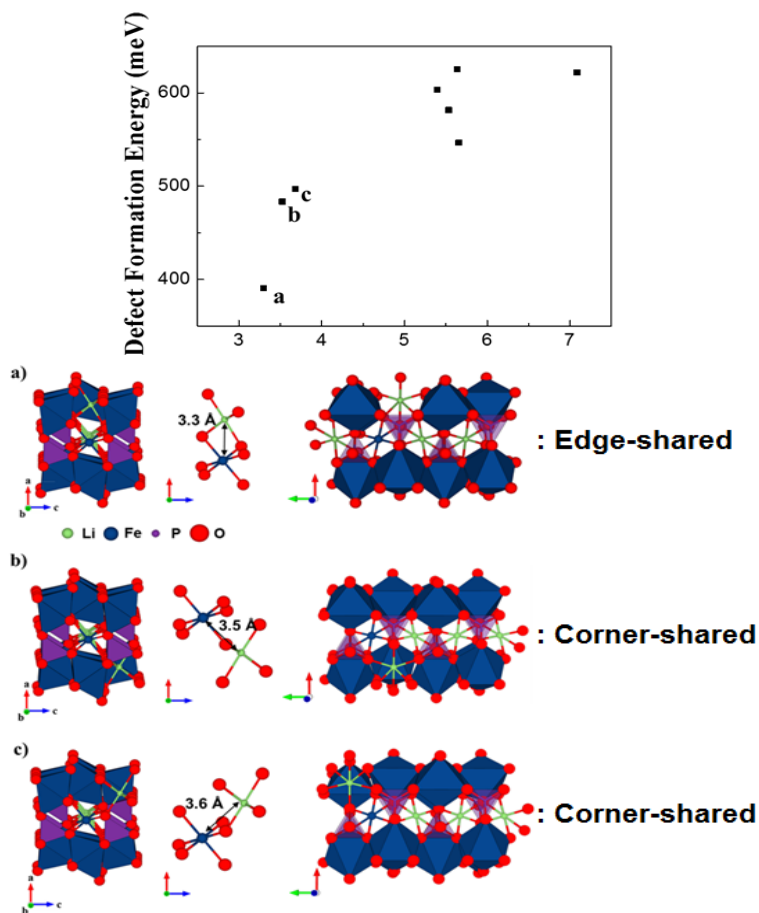


Figure 2-1. Calculated formation energy of anti-site defect in LiFePO₄ and its configuration corresponding to the distance between Li⁺ on Fe²⁺ site and Fe²⁺ on Li⁺ site. Near anti-site defect has lower formation energy. (a) Edge-shared anti-site defect with the lowest formation energy (about 390 meV) (b), (c) Corner-shared anti-site defect with the formation energy of about 490 meV.

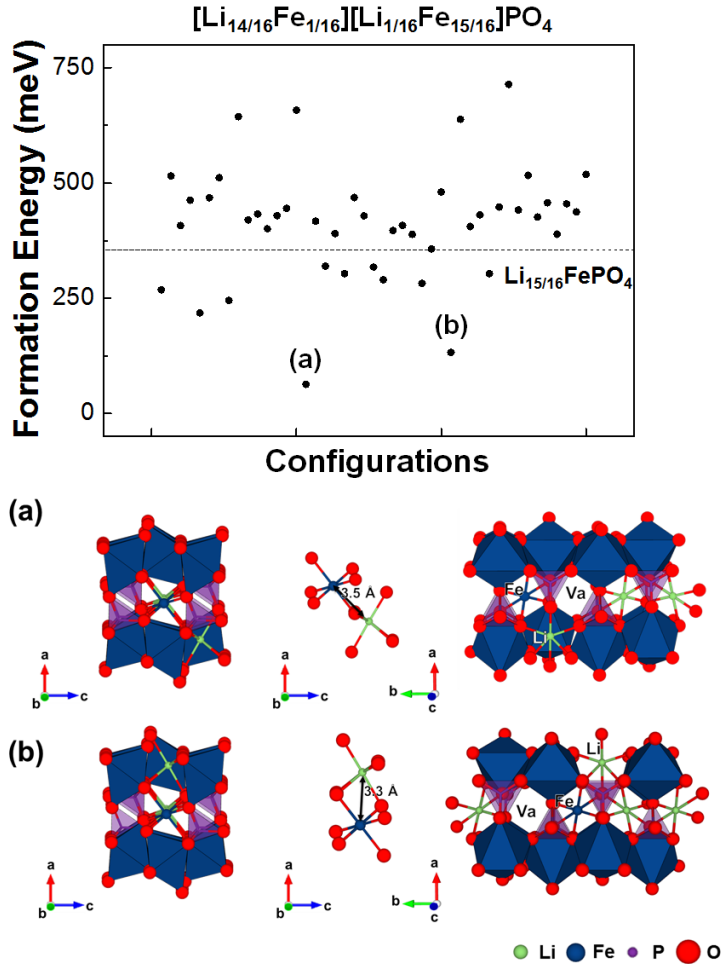


Figure 2-2 Formation energies for 45 different vacancy-Fe defect configurations of the single-phase $\text{Li}_{1-x}\text{FePO}_4$ from first principles calculations. The most stable energy is observed in (a) the corner-shared configuration and the second most stable configurations is shown as (b) the edge-shared configuration.

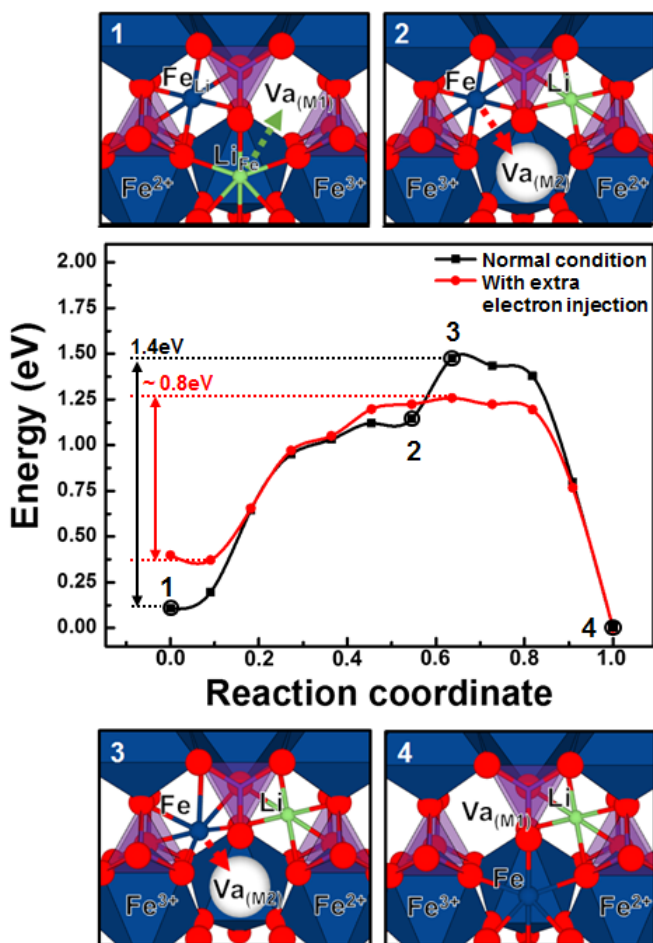


Figure 2-3. Energy curve and schematics of the Fe-Li cation site re-ordering process during discharge. The black line is the Fe/Li recombination route with no charge carrier injection. The red line is the hypothetical Fe/Li recombination route with a charge carrier (electron) injection. Schematics 1 – 4 schematics are Fe-Li cation site re-ordering processes at each point.

2.3.2 Charge carrier injection method to reduce anti-site concentration

Inspired by these theoretical results, we prepared a vacancy-introduced LiFePO_4 , *i.e.*, $\text{Li}_{0.9}\text{FePO}_4$, in the form of solid solution from a defective LiFePO_4 . First, the LiFePO_4 was synthesized hydrothermally and delithiated chemically to obtain a mixture of LiFePO_4 and FePO_4 with a molar ratio of 9:1 (high-resolution powder X-ray diffraction (HRPD) patterns are provided in Figure 2-4). The two-phase mixture was heated and quenched to retain a $\text{Li}_{0.9}\text{FePO}_4$ solid-solution phase. Figure 2-5 shows that the (200) peak of FePO_4 can be detected at $\sim 18^\circ$ in the mixture, which disappears after heating and quenching. The shift of the (200) peak confirms the formation of solid-solution $\text{Li}_{0.9}\text{FePO}_4$. Rietveld refinements of the $\text{Li}_{0.9}\text{FePO}_4$ in Figure 2-5 (b) show that the solid-solution phase was obtained successfully with $a = 10.328 \text{ \AA}$, $b = 6.007 \text{ \AA}$, and $c = 4.706 \text{ \AA}$. Comparison with pristine LiFePO_4 indicated that the lattice parameters decreased after the delithiation, in good agreement with previous reports.[42] The LiFePO_4 and $\text{Li}_{0.9}\text{FePO}_4$ contain $\sim 4.2\%$ and $\sim 4.0\%$ Li-Fe site exchange, respectively (detailed refinement results are provided in Figure 2-6 and 2-7). Those values match well with previous reports that hydrothermally prepared LiFePO_4 generally contains approximately ~ 3 to 4% defects, which are maintained even at the low post-heat-treatment temperature[42, 43] The particle size of the sample

was $\sim 2 \mu\text{m}$, as shown in the inset of Figure 3(b).

By constructing an electrochemical cell using the defective $\text{Li}_{0.9}\text{FePO}_4$, we then attempted to mimic the theoretical results of Li/Fe anti-site recombination. Figure 2-9 (a) shows the galvanostatic intermittent titrations (GITT) discharge profile of $\text{Li}_{0.9}\text{FePO}_4$. While the $\text{Li}_{0.9}\text{FePO}_4$ was capable of lithiating 0.1 Li up to $\sim 1.6 \text{ V}$ discharge, notably high polarization was observed in the profile. However, the open-circuit voltage (OCV) after the relaxation matched that of conventional $\text{Li}_{0.9}\text{FePO}_4$, indicating that the lithium insertion into $\text{Li}_{0.9}\text{FePO}_4$ solid solution occurred with a large kinetic barrier. The high polarization of $\text{Li}_{0.9}\text{FePO}_4$ at this stage will be discussed later.

After imposing the dynamic situation where lithium ions and electrons were injected into the defective $\text{Li}_{0.9}\text{FePO}_4$, we detected an unusual change in structural parameters. The tables in Figure 2-9 (b) and 2-10 compare the structural parameters obtained from the careful refinements of HRPDs for pristine LiFePO_4 and $\text{Li}_{0.9}\text{FePO}_4$ before and after electrochemical treatment. The first remarkable observation is that the lithiation of the defective $\text{Li}_{0.9}\text{FePO}_4$, following the protocol above (recombined LiFePO_4 in the Table) resulted in a significant *reduction* in the c lattice, along with the a lattice and

the volume. This is in contrast to the general trend with lithiation into olivine where the a and b lattice parameters and volumes *increase*, and the c lattice parameter decreases.[42] Also, the concentration of anti-site defects decreased from 4.0% to 1.86%. This unusual behavior indicated that not only the lithium content but also other structural rearrangement(s) affected the lattice parameters in the new LiFePO_4 .[44] At this point, it should be mentioned that the complete annihilation of the defects was not possible even after multiple electrochemical annealing, which we believe is due to the presence of edge-shared Li/Fe defect. As noted above, the edge-shared defect is also comparably probable with the corner-shared defect in the sample, but cannot be recombined due to the absence of the reordering routes.

From comparisons with previous reports on lattice parameters, we found that lattice parameters of olivines are sensitive to the concentration of defects and that the observed change was likely due to a decrease in Fe_{Li} defects, consistent with our theoretical predictions. In Figure 2-9 (c), we plot the previously reported lattice parameters of LiFePO_4 as a function of the refined value of Li/Fe site exchange.[20, 32, 42, 44] This revealed that as the Fe_{Li} defect concentration increased, the a lattice and volume of the olivine increased, following an almost linear relationship. To our surprise, the refined lattice parameters before and after the electrochemical healing of our

defective LiFePO_4 (denoted with stars) also showed a similar trend, suggesting that the Li/Fe site exchange had decreased after the healing. Figure 2-10 shows that the b and c lattice parameters followed the same trend, further confirming the decrease in anti-site defects.

Fourier transform infrared spectroscopy (FT-IR) spectra analyses also supported the decrease in the Fe_{Li} defect concentration in the new LiFePO_4 . Previous theoretical and experimental works have indicated that the IR absorption of PO_4^{3-} is sensitive to the presence of defects in the olivine crystal.[32, 45] Defect-free LiFePO_4 shows the PO_4^{3-} absorption typically at ~ 956 to 963 cm^{-1} , whereas LiFePO_4 with a high defect concentration has a PO_4^{3-} signal at ~ 983 to 1003 cm^{-1} . [32, 45, 46] In our FT-IR measurements, we found that the PO_4^{3-} absorption varied considerably, depending on the sample. Figure 2-9 (d) shows that the absorption bands of the P-O symmetric stretching vibration of the LiFePO_4 (anti-sites $\sim 4.2\%$) and $\text{Li}_{0.9}\text{FePO}_4$ (anti-sites $\sim 4.0\%$) were observed at $\sim 985 \text{ cm}^{-1}$. In contrast, electrochemically treated LiFePO_4 (anti-sites $\sim 1.8\%$) and the reference LiFePO_4 (anti-sites $\sim 1.0\%$) showed absorption at $\sim 960 \text{ cm}^{-1}$, suggesting that the new LiFePO_4 contained fewer Fe-Li cation site exchanges after our experiment, mimicking the charge carrier injection process. Our result is in contrast to previous reports that the recombination of Fe_{Li} defects in LiFePO_4 is only possible

above $\sim 500^\circ\text{C}$ with heat treatment⁴⁰ and not during a charging/discharging process.[47]

An unusually high polarization was observed during the initial lithiation of the defective $\text{Li}_{0.9}\text{FePO}_4$ during the electrochemical treatment. Nevertheless, the OCV after relaxation, which was close to ~ 3.42 V, agreed well with the average redox potential of $\text{Fe}^{2+}/\text{Fe}^{3+}$. This indicates that the lithiation process of the defective $\text{Li}_{0.9}\text{FePO}_4$ was a significantly sluggish process that required a high over-potential. We believe that this kinetic barrier was related to the recombination process of the Li/Fe site exchange. As shown before, the recombination required an activation barrier of ~ 0.8 eV, which is higher than that of typical lithium diffusion in conventional LiFePO_4 (~ 0.3 eV).[48] Thus, it would require a high over-potential once it occurs at room temperature in an electrochemical cell. The large polarization was only observed during the initial discharge process, and disappeared subsequently in this region (Figure 2-11). This supports the idea that the polarization stems from a structural rearrangement involving the defect recombination.

Using this electrochemical recombination process, we prepared two kinds of defect-less LiFePO_4 : one starting from hydrothermally synthesized micro- LiFePO_4 , and the other from nano- LiFePO_4 obtained with a conventional

solid-state synthesis. The synthesis and characterization of samples are illustrated in the supporting materials (Figure 2-12 and 2-13). Although highly defective LiFePO_4 with micron-size particles usually shows very small capacity at room temperature, the reduction in Li/Fe site exchange could enhance electrochemical performance markedly. Figure 2-14 (a) shows that the reversible capacity of micro- LiFePO_4 could be increased considerably after the recombination process. About ~ 0.2 Li ion capacity could be additionally achievable even with micron-sized LiFePO_4 . It is believed that the reduction of anti-site defect from 4.0% to 1.86% could liberate those amounts of trapped lithium ions. The full utilization of Li in micro- LiFePO_4 was not possible due to the presence of edge-shared Li/Fe defects. The effect of defect reduction was also observable in the nano- LiFePO_4 electrodes. Figure 2-14 (b) shows that the electrochemical recombination could enhance the power capability of the conventional nano- LiFePO_4 synthesized from a solid-solution reaction (~ 100 to 200 nm; SEM images in Figure 2-13 (c) and (d)). The electrochemically treated nano- LiFePO_4 delivered ~ 9.3 to 12.3% higher capacity at higher current rates than its counterpart. At a 30-C rate, the electrochemically annealed sample could achieve ~ 115 mAh/g, ~ 20 mAh/g higher than that of conventional nano- LiFePO_4 . This confirms that the simple electrochemical treatment described can result in the enhancement of the power capability of defective crystalline electrode materials regardless of the

particle sizes. We believe that the suggested defect recombination mechanism may be broadly applicable to electrode materials that typically suffer from restrained diffusion paths in crystals due to the presence of defects[3, 42]

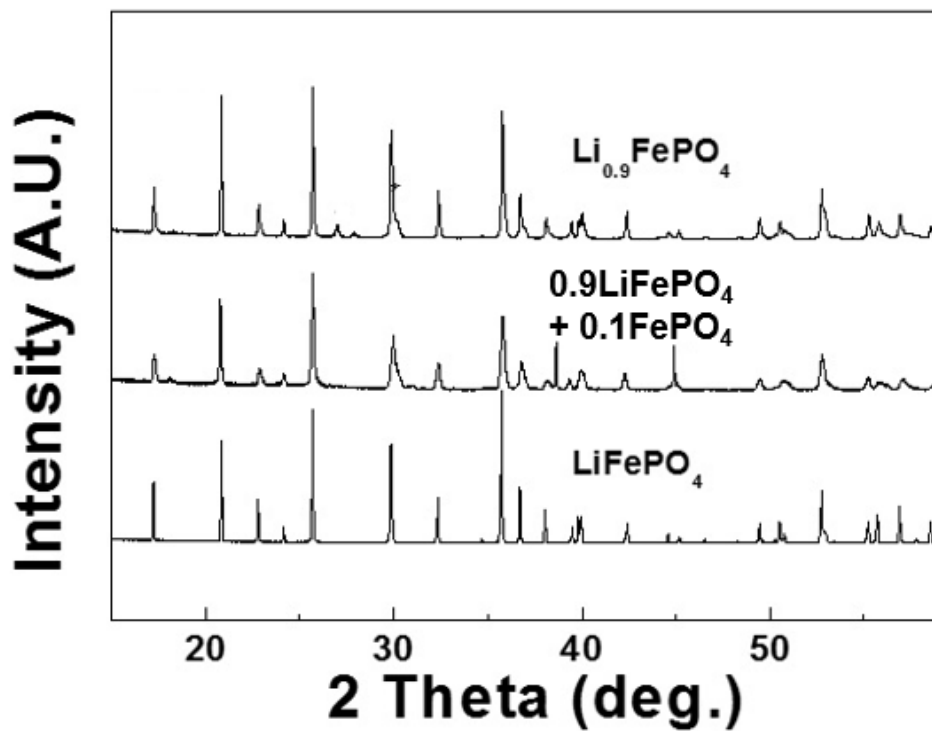


Figure 2-4 The 15 ~ 55° high resolution powder diffraction patterns of prepared by hydrothermal synthesis

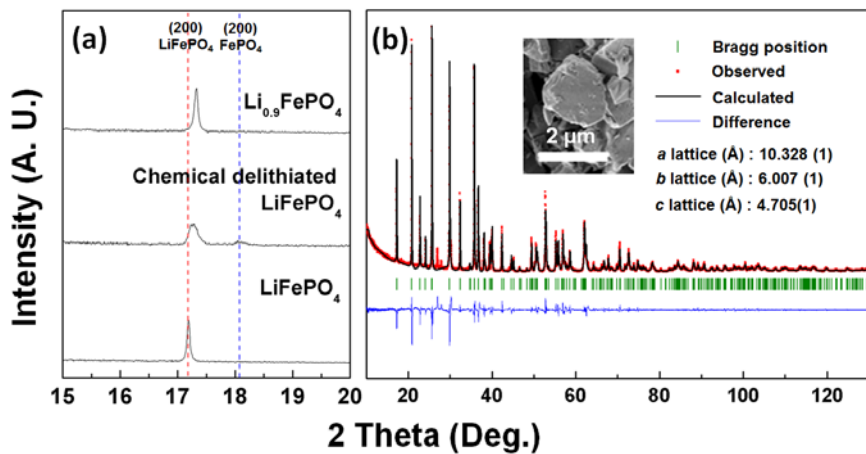
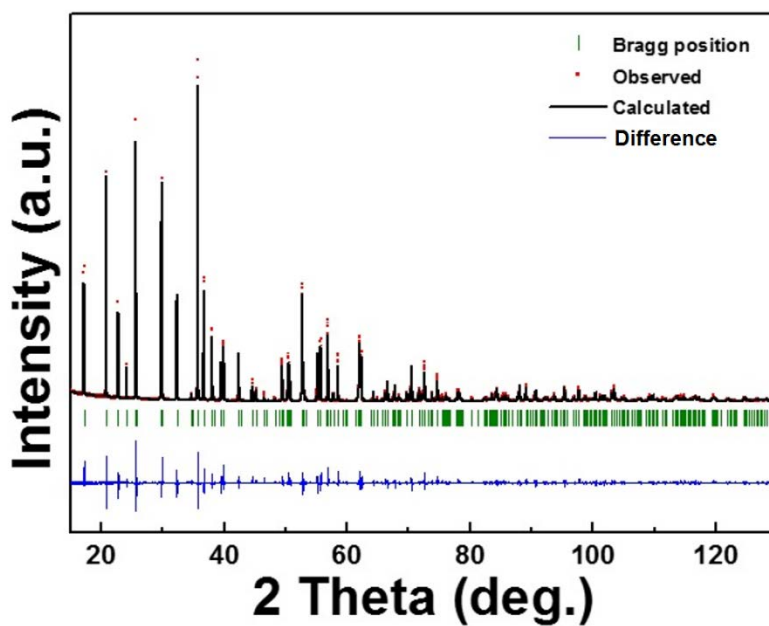


Figure 2-5 (a) Magnified (200) peak of high resolution powder diffraction patterns of the prepared samples. (b) Rietveld refinement results of solid-solution $\text{Li}_{0.9}\text{FePO}_4$. The inset figure is an SEM image of micro-size $\text{Li}_{0.9}\text{FePO}_4$

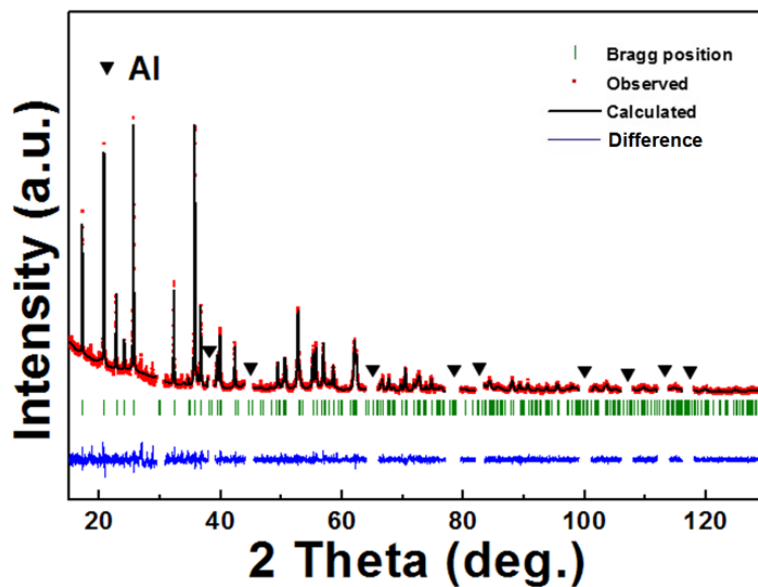


Atom	X	Y	Z	Biso	Mult.	Occ.		
Li	0.00000(0)	0.00000(0)	0.00000(0)	1.49	4	0.479	Chi ²	5.49
Fe	0.28189(7)	0.25000(0)	0.97522(17)	0.395	4	0.479	R _p	11
Li _{Fe}	0.28189(7)	0.25000(0)	0.97522(17)	1.49	4	0.021	R _I	5.02
Fe _{Li}	0.00000(0)	0.00000(0)	0.00000(0)	0.395	4	0.021	R _f	3.44
P	0.09524(13)	0.25000(0)	0.41750(26)	0.282	4	0.500	Unit cell V.	292.640(1)
O1	0.09721(34)	0.25000(0)	0.74437(64)	0.495	4	0.500	Lattice a(Å)	10.35027(3)
O2	0.45596(36)	0.25000(0)	0.20695(65)	0.482	4	0.500	Lattice b(Å)	6.01304(2)
O3	0.16747(28)	0.04299(38)	0.28245(42)	0.518	8	1.000	Lattice b(Å)	4.70205(1)

Figure 2-6. Rietveld refinement results of hydrothermally prepared LiFePO₄.

Atom	X	Y	Z	Biso	Mult.	Occ.		
Li	0.00000(0)	0.00000(0)	0.00000(0)	1.49	4	0.430	Chi ²	9.65
Fe	0.28139(13)	0.25000(0)	0.97462(35)	0.395	4	0.480	R _p	14.2
Li _{Fe}	0.28139(13)	0.25000(0)	0.97462(35)	1.49	4	0.020	R _I	7.71
Fe _{Li}	0.00000(0)	0.00000(0)	0.00000(0)	0.395	4	0.020	R _f	4.71
P	0.09592(23)	0.25000(0)	0.41781(48)	0.282	4	0.500	Unit cell V.	291.998(5)
O1	0.10082(60)	0.25000(0)	0.74909(113)	0.495	4	0.500	Lattice a(Å)	10.32877(8)
O2	0.45482(66)	0.25000(0)	0.20070(109)	0.482	4	0.500	Lattice b(Å)	6.00752(6)
O3	0.16566(49)	0.03936(72)	0.27621(71)	0.518	8	1.000	Lattice b(Å)	4.70582(4)

Figure 2-7. Rietveld refinement results of solid-solution Li_{0.9}FePO₄.



Atom	X	Y	Z	Biso	Mult.	Occ.		
Li	0.00000(0)	0.00000(0)	0.00000(0)	1.375(90)	4	0.4907(8)	Chi ²	1.50
Fe	0.28166(15)	0.25000(0)	0.97498(43)	0.369(20)	4	0.4907(8)	R _p	6.67
Li _{Fe}	0.28166(15)	0.25000(0)	0.97498(43)	0.280(90)	4	0.0093(8)	R _i	3.94
Fe _{Ti}	0.00000(0)	0.00000(0)	0.00000(0)	1.464(20)	4	0.0093(8)	R _f	2.74
P	0.09816(29)	0.25000(0)	0.41935(49)	0.356(41)	4	0.500	Unit cell V.	290.637(4)
O1	0.09531(71)	0.25000(0)	0.74595(118)	0.590(142)	4	0.500	Lattice a(Å)	10.32416(8)
O2	0.44798(82)	0.25000(0)	0.21221(109)	0.192(126)	4	0.500	Lattice b(Å)	5.99040(6)
O3	0.16480(53)	0.04815(79)	0.28282(81)	0.676(90)	8	1.000	Lattice b(Å)	4.66938(4)

Figure 2-8. Rietveld refinement result of electrochemically treated LiFePO₄

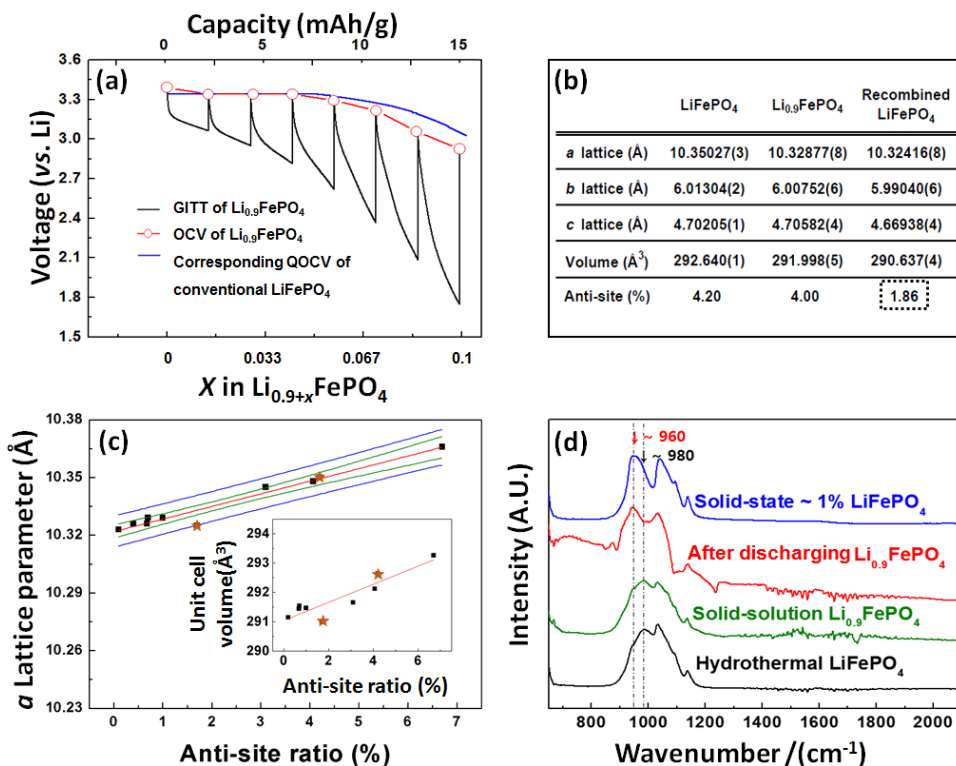


Figure 2-9. Defect characterization (a) Black: GITT result of $\text{Li}_{0.9}\text{FePO}_4$, red: quasi-OCV result of $\text{Li}_{0.9}\text{FePO}_4$, blue: quasi-OCV of conventional LiFePO_4 . (b) Lattice parameters, volume and anti-site ratio of prepared samples. The detailed Rietveld refinement results are provided in supporting Figure S3 – S5. (c) a -lattice parameter change as a function of anti-site ratio. The inset figure is shown the unit cell volume change as a function of anti-site ratio. Red line : trend line, blue line : confidence band, green line : prediction band. The interval coverage probability is set as 95 %. The star points symbolized stand for hydrothermal synthesized LiFePO_4 and electrochemically treated LiFePO_4 . The data are taken from references 20, 30, 40 and 42. (d) FT-IR results of prepared samples PO_4^{3-} spectra.

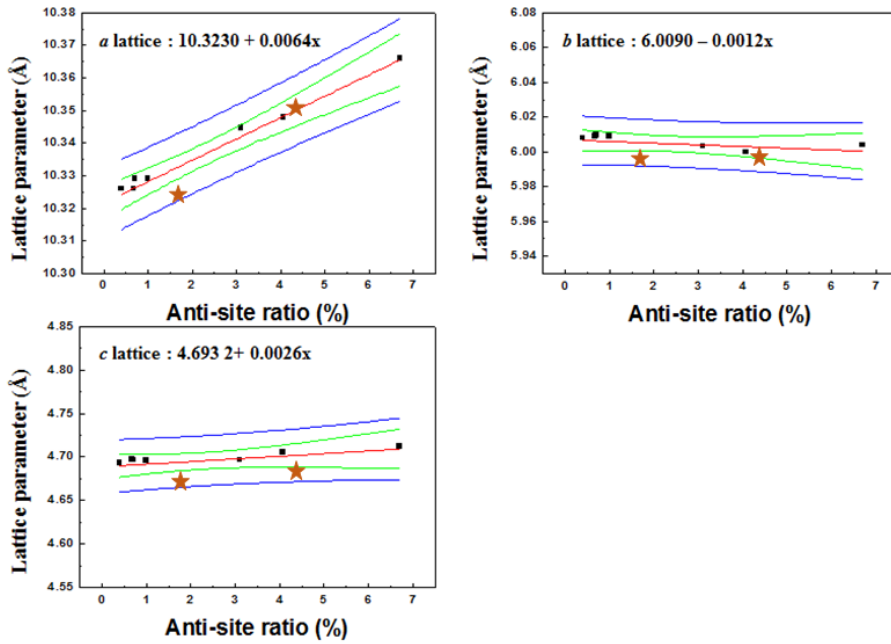


Figure 2-10. Lattice parameter with change modification with anti-site ratio at room temperature. Red line : trend line, blue line : confidence band, green line : prediction band. The interval coverage probability is set as 95 %. This figure used reference number 25, 35, 47 and 49.

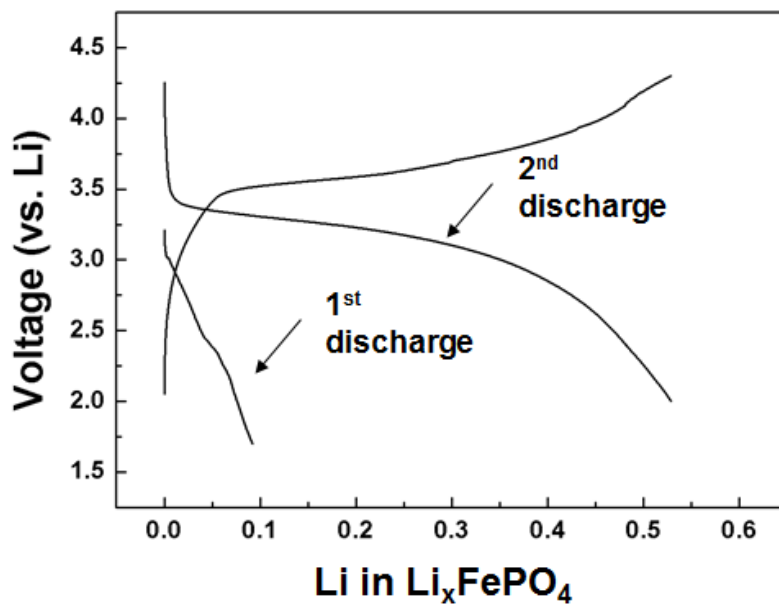


Figure 2-11. The electrochemical profile of solid-solution $\text{Li}_{0.9}\text{FePO}_4$ at $\text{C}/100$. The 1st discharge profile showed unexpected high polarization, however, the 2nd profile did not show overpotential during charging/discharging

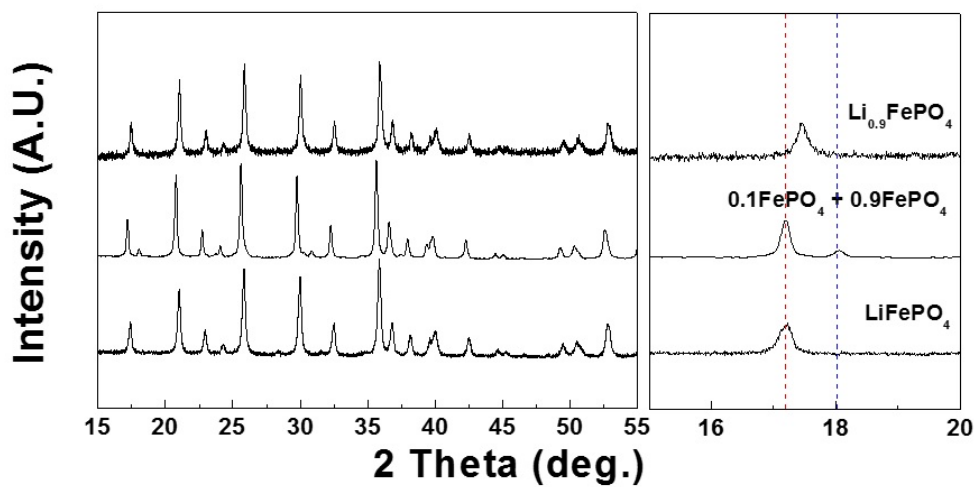


Figure 2-12. 15 ~ 55° XRD patterns of prepared by solid-state method samples (left) and magnified (200) peak of samples (right). red line : (200) peak of LiFePO₄, blue line : (200) peak of FePO₄. All samples are well synthesized without remarkable impurities.

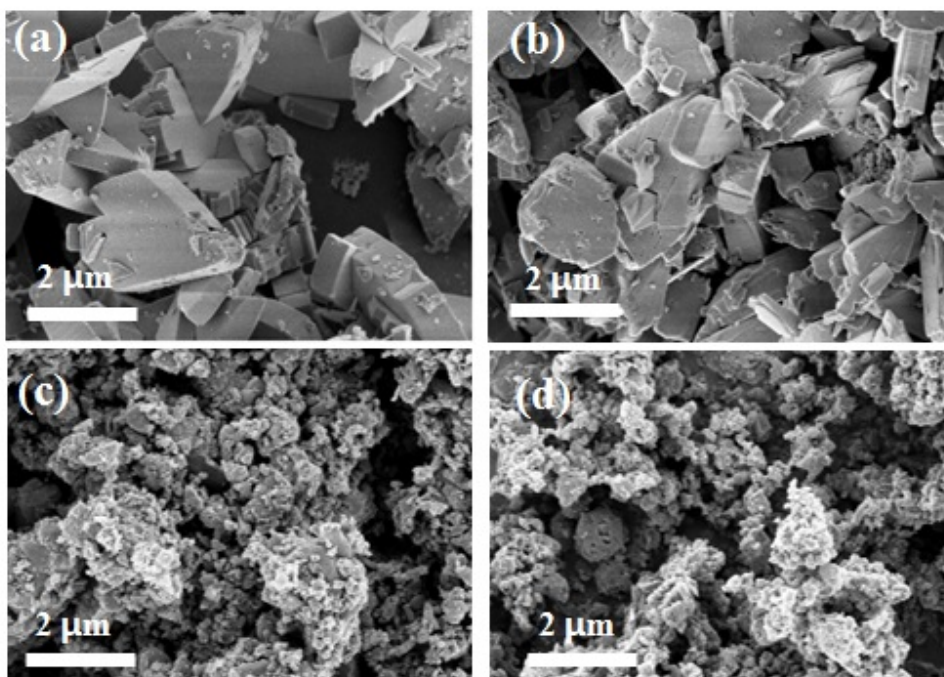


Figure 2-13. SEM image of prepared LiFePO_4 . (a) Hydrothermal synthesis LiFePO_4 (b) 380 °C heated hydrothermal synthesis $\text{Li}_{0.9}\text{FePO}_4$ (c) 600 °C solid-state synthesis LiFePO_4 (d) 380 °C heated solid-state 600 °C synthesis $\text{Li}_{0.9}\text{FePO}_4$.

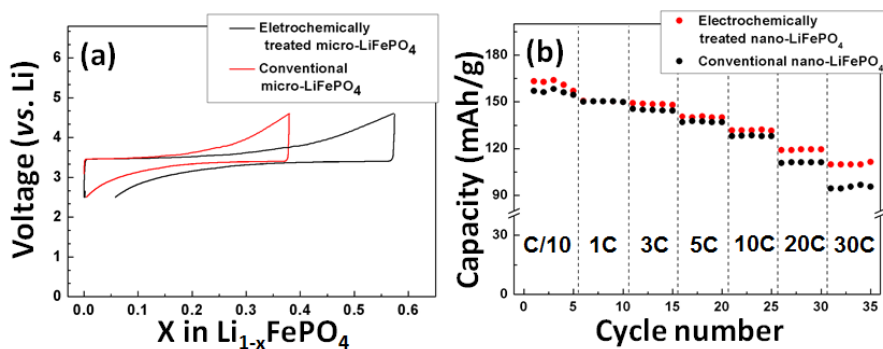


Figure 2-14. (a) First charge/discharge profile at C/200 of electrochemically treated micro-LiFePO₄ and hydrothermally grown micro-LiFePO₄. (b) C-rate capability of electrochemically treated nano-LiFePO₄ (red) and conventional nano-LiFePO₄ (black).

2.4 Conclusion

In this chapter, researcher introduced a new way to reduce defects in crystals with a case study of olivine LiFePO_4 . Fe_{Li} defects in the olivine structure were reduced using a room-temperature electrochemical annealing process. The defect annihilation mechanism was proposed from first principles calculations, which indicated that the introduction of vacancies and excess charge carriers lowered the activation barrier for defect recombination. Using this new method, we demonstrated that defective LiFePO_4 , including both micro- and nano-size particles, can be ‘healed,’ recovering power capabilities. The defect-annihilation mechanism suggested here may be broadly applicable in making defect-less materials, and is expected to help in understanding defect behavior in various materials.

2.5 References

1. Sammalkorpi, M., et al., Mechanical properties of carbon nanotubes with vacancies and related defects. *Physical Review B*, 2004. **70**(24): p. 245416.
2. Kuo, J.H., H.U. Anderson, and D.M. Sparlin, Oxidation-reduction behavior of undoped and Sr-doped LaMnO₃: Defect structure, electrical conductivity, and thermoelectric power. *Journal of Solid State Chemistry*, 1990. **87**(1): p. 55-63.
3. Malik, R., et al., Particle Size Dependence of the Ionic Diffusivity. *Nano Letters*, 2010. **10**(10): p. 4123-4127.
4. Penn, R.L. and J.F. Banfield, Imperfect Oriented Attachment: Dislocation Generation in Defect-Free Nanocrystals. *Science*, 1998. **281**(5379): p. 969-971.
5. Esch, F., et al., Electron Localization Determines Defect Formation on Ceria Substrates. *Science*, 2005. **309**(5735): p. 752-755.
6. Wendt, S., et al., The Role of Interstitial Sites in the Ti3d Defect State in the Band Gap of Titania. *Science*, 2008. **320**(5884): p. 1755-1759.
7. Bikondoa, O., et al., Direct visualization of defect-mediated dissociation of water on TiO₂(110). *Nat Mater*, 2006. **5**(3): p. 189-192.
8. Vlasov, Y.A., et al., On-chip natural assembly of silicon photonic

- bandgap crystals. *Nature*, 2001. **414**(6861): p. 289-293.
9. Philip, J., et al., Carrier-controlled ferromagnetism in transparent oxide semiconductors. *Nat Mater*, 2006. **5**(4): p. 298-304.
 10. Johansson, J., et al., Structural properties of [lang]111[rang]B - oriented III-V nanowires. *Nat Mater*, 2006. **5**(7): p. 574-580.
 11. Pertsinidis, A. and X.S. Ling, Diffusion of point defects in two-dimensional colloidal crystals. *Nature*, 2001. **413**(6852): p. 147-150.
 12. Dathar, G.K.P., et al., Calculations of Li-Ion Diffusion in Olivine Phosphates. *Chemistry of Materials*, 2011. **23**(17): p. 4032-4037.
 13. Fahey, P.M., P.B. Griffin, and J.D. Plummer, Point defects and dopant diffusion in silicon. *Reviews of Modern Physics*, 1989. **61**(2): p. 289-384.
 14. Chung, S.-Y., J.T. Bloking, and Y.-M. Chiang, Electronically conductive phospho-olivines as lithium storage electrodes. *Nat Mater*, 2002. **1**(2): p. 123-128.
 15. Bracht, H., et al., Large disparity between gallium and antimony self-diffusion in gallium antimonide. *Nature*, 2000. **408**(6808): p. 69-72.
 16. Allen, J.E., et al., High-resolution detection of Au catalyst atoms in Si nanowires. *Nat Nano*, 2008. **3**(3): p. 168-173.
 17. Islam, M.S., et al., Atomic-Scale Investigation of Defects, Dopants, and Lithium Transport in the LiFePO₄ Olivine-Type Battery Material. *Chemistry of Materials*, 2005. **17**(20): p. 5085-5092.

18. Chung, S.-Y., et al., Atomic-Scale Visualization of Antisite Defects in LiFePO_4 . *Physical Review Letters*, 2008. **100**(12): p. 125502.
19. Kang, K., et al., Electrodes with High Power and High Capacity for Rechargeable Lithium Batteries. *Science*, 2006. **311**(5763): p. 977-980.
20. Padhi, A.K., K.S. Nanjundaswamy, and J.B. Goodenough, Phospho-olivines as Positive-Electrode Materials for Rechargeable Lithium Batteries. *Journal of The Electrochemical Society*, 1997. **144**(4): p. 1188-1194.
21. Padhi, A.K., et al., Effect of Structure on the $\text{Fe}^{3+} / \text{Fe}^{2+}$ Redox Couple in Iron Phosphates. *Journal of The Electrochemical Society*, 1997. **144**(5): p. 1609-1613.
22. Yamada, A., S.C. Chung, and K. Hinokuma Optimized LiFePO_4 for Lithium Battery Cathodes. *Journal of The Electrochemical Society*, 2001. **148**(3): p. A224-A229.
23. Delacourt, C., et al., The existence of a temperature-driven solid solution in Li_xFePO_4 for $0 \leq x \leq 1$. *Nat Mater*, 2005. **4**(3): p. 254-260.
24. Chen, G., X. Song, and T.J. Richardson, Metastable Solid-Solution Phases in the $\text{LiFePO}_4/\text{FePO}_4$ System. *Journal of The Electrochemical Society*, 2007. **154**(7): p. A627-A632.
25. Wang, Y., P. He, and H. Zhou, Olivine LiFePO_4 : development and future. *Energy & Environmental Science*, 2011. **4**(3): p. 805-817.
26. Xie, H.M., et al., Optimized LiFePO_4 -Polyacene Cathode Material

- for Lithium-Ion Batteries. *Advanced Materials*, 2006. **18**(19): p. 2609-2613.
27. Morgan, D., A. Van der Ven, and G. Ceder, Li Conductivity in Li_xMPO_4 ($\text{M} = \text{Mn}, \text{Fe}, \text{Co}, \text{Ni}$) Olivine Materials. *Electrochemical and Solid-State Letters*, 2004. **7**(2): p. A30-A32.
28. Kang, K., D. Morgan, and G. Ceder, First principles study of Li diffusion in LiFePO_4 structure. *Physical Review B*, 2009. **79**(1): p. 014305.
29. Kang, K. and G. Ceder, Factors that affect Li mobility in layered lithium transition metal oxides. *Physical Review B*, 2006. **74**(9): p. 094105.
30. Yamada, A., et al., Olivine-type cathodes: Achievements and problems. *Journal of Power Sources*, 2003. **119–121**(0): p. 232-238.
31. Yang, M.-R., T.-H. Teng, and S.-H. Wu, LiFePO_4 /carbon cathode materials prepared by ultrasonic spray pyrolysis. *Journal of Power Sources*, 2006. **159**(1): p. 307-311.
32. Qin, X., et al., Hydrothermally synthesized LiFePO_4 crystals with enhanced electrochemical properties: simultaneous suppression of crystal growth along [010] and antisite defect formation. *Physical Chemistry Chemical Physics*, 2012. **14**(8): p. 2669-2677.
33. Delmas, C., et al., Lithium deintercalation in LiFePO_4 nanoparticles via a domino-cascade model. *Nat Mater*, 2008. **7**(8): p. 665-671.
34. Perdew, J.P., K. Burke, and M. Ernzerhof, Generalized Gradient Approximation Made Simple. *Physical Review Letters*, 1996. **77**(18): p.

3865-3868.

35. Kresse, G. and J. Furthmüller, Efficiency of ab-initio total energy calculations for metals and semiconductors using a plane-wave basis set. *Computational Materials Science*, 1996. **6**(1): p. 15-50.

36. Anisimov, V.I., J. Zaanen, and O.K. Andersen, Band theory and Mott insulators: Hubbard U instead of Stoner I. *Physical Review B*, 1991. **44**(3): p. 943-954.

37. Wang, L., T. Maxisch, and G. Ceder, Oxidation energies of transition metal oxides within the GGA+U framework. *Physical Review B*, 2006. **73**(19): p. 195107.

38. Van der Ven, A., et al., Nondilute diffusion from first principles: Li diffusion in Li_xTiS_2 . *Physical Review B*, 2008. **78**(10): p. 104306.

39. Henkelman, G., B.P. Uberuaga, and H. Jonsson, A climbing image nudged elastic band method for finding saddle points and minimum energy paths. *The Journal of Chemical Physics*, 2000. **113**(22): p. 9901-9904.

40. Carvajal, J., FULLPROF: A Program for Rietveld Refinement and Pattern Matching Analysis. Abstracts of the Satellite Meeting on Powder Diffraction of the XV Congress of the IUCr, 1990.

41. Tealdi, C., C. Spreatico, and P. Mustarelli, Lithium diffusion in $\text{Li}_{1-x}\text{FePO}_4$: the effect of cationic disorder. *Journal of Materials Chemistry*, 2012. **22**(47): p. 24870-24876.

42. Chen, J. and J. Graetz, Study of Antisite Defects in Hydrothermally Prepared LiFePO₄ by in Situ X-ray Diffraction. ACS Applied Materials & Interfaces, 2011. **3**(5): p. 1380-1384.
43. Yang, S., et al., Reactivity, stability and electrochemical behavior of lithium iron phosphates. Electrochemistry Communications, 2002. **4**(3): p. 239-244.
44. Yamada, A., et al., Room-temperature miscibility gap in Li_xFePO₄. Nat Mater, 2006. **5**(5): p. 357-360.
45. Burba, C.M. and R. Frech, Raman and FTIR Spectroscopic Study of Li_xFePO₄ (0 ≤ x ≤ 1) Journal of The Electrochemical Society, 2004. **151**(7): p. A1032-A1038.
46. Cho, M.-Y., et al., Defect-free solvothermally assisted synthesis of microspherical mesoporous LiFePO₄/C. RSC Advances, 2013. **3**(10): p. 3421-3427.
47. Badi, S.-P., et al., Direct synthesis of nanocrystalline Li_{0.90}FePO₄: observation of phase segregation of anti-site defects on delithiation. Journal of Materials Chemistry, 2011. **21**(27): p. 10085-10093.
48. Ouyang, C., et al., First-principles study of Li ion diffusion in LiFePO₄ structure. Physical Review B, 2004. **69**(10): p. 104303.

Chapter 3. Lithium-excess olivine for zero F_{eLi} defect

(The content of 3 and 4 chapters share the introduction and references. Also, these contents are now in preparation to be submitted to scientific journals.)

3.1 Introduction

The basic principle of modern rechargeable batteries relies on the reversible intercalation of guest ions in the electrode materials. The intercalation reaction is possible because numerous guest ions can diffuse in and out of the electrode crystal.[1] The diffusivity of the guest ions in the electrode, therefore, strongly affects the electrochemical properties, such as the power density, round-trip efficiency, and energy density. The crystal structure primarily determines the diffusivity of guest ions, providing specific diffusion paths. However, a deviation of the local atomic configuration around the guest ions also sensitively affects the ionic mobility.[2, 3] For example, the presence of immobile defects in the diffusion paths, which may originate from impurities or anti-site defects, can significantly retard the mobility of ions. In particular, crystals with only one-dimensional diffusion pathways are susceptible to the presence of defects that may significantly impede Li-ion diffusion. In this respect, careful selection of the synthesis route or post-treatment of electrode materials is often required to control the defect

concentration.[4-6]

LFP has been intensely studied for the last two decades as a practically important cathode material for lithium rechargeable batteries and as a model system for thermodynamic and kinetic studies of lithium intercalation.[7-14] In the ideal case, LFP can deliver a specific capacity of 169 mAh g⁻¹ via relatively fast lithium diffusion through a channel along the [010] direction of the crystal structure (*Pnma*).[13, 15, 16] However, in practice, approximately 5 % Li-Fe cation site exchange (Li_{Fe}-Fe_{Li} anti-site defect) typically occurs, depending on the synthetic routes, which results in immobile Fe_{Li} ions in the lithium diffusion channel.[3, 17-22] Malik *et al.* demonstrated that the presence of 0.1 % Li_{Fe}-Fe_{Li} anti-site defects in a micron-sized LFP particle statistically reduced its energy density to almost half of the original value[5, 17] and decreased the lithium ionic conductivity by two or three orders of magnitude.[17] In this respect, many researchers have attempted to minimize Fe_{Li} anti-site defects or form positive defects in LFP resulting from the synthesis procedure.[5, 17, 23-25] Among these researchers, the Whittingham group succeeded in systematically analyzing Li_{Fe}-Fe_{Li} anti-site defects in LFP by controlling various synthetic conditions such as the hydrothermal methods and demonstrated that LFPs with high Li_{Fe}-Fe_{Li} anti-site contents suffer from inferior electrochemical performances.[20, 22] Also, Hoang and Johannes investigated on various point defects in LFP, calculating

that lithium-rich and iron-poor LFP could have relatively the high Fe_{Li} defect formation energy from DFT calculation.[26] Masquelier group attempted to synthesize highly defective LFP powder through modified synthetic procedure, showing unexpected electrochemical behaviors. They revealed that high concentration of defect could provide alternative lithium ion diffusion paths offering stable electrochemical performance based on distinct reaction mechanisms.[27-29] Although the nano-sizing of LFP is an indirect approach to reducing the effect of immobile Fe_{Li} anti-site defects because of the shortened diffusion length, the nano-synthesis leads to other problems, such as reducing the tap density of the electrode,[23] generating more surface defects accompanying side reactions because of the large surface area,[30, 31] and creating additional cost problems in the synthesis and electrode fabrication.[32]

Incorporating additional charge-carrying guest ions in a crystal structure sometimes leads to unexpected results in their electrochemical properties,[33, 34] which was recently demonstrated in layered-type lithium transition metal oxides. Armstrong *et al.* demonstrated that a slight excess of lithium ($x = \sim 3\%$) in $\text{Li}_{1+x}\text{V}_{1-x}\text{O}_2$ could switch on lithium-ion intercalation, delivering a higher theoretical specific capacity and volumetric energy density than graphite, whereas pristine LiVO_2 exhibits no evidence of intercalation into its structure.[33] In addition, lithium-excess derivatives of

$\text{Li}(\text{Ni},\text{Co},\text{Mn},\text{Ru},\text{Sn})\text{O}_2$ layered-type electrode materials, *i.e.*, $\text{Li}_{1+x}(\text{Ni},\text{Co},\text{Mn},\text{Ru},\text{Sn})_{1-x}\text{O}_2$, exhibit distinctive electrochemical responses during battery cycling, triggering oxygen redox reactions and delivering extra capacity beyond the expected value for the pristine materials.[35-40] Furthermore, most recently, Lee *et al.* revealed that even fully disordered lithium transition metal oxides (100% anti-site ratio in the layered structure) can utilize the de/intercalation of almost all the lithium in the structure if a sufficient amount of excess lithium is present in the structure to provide a percolation path for lithium diffusion.[41] Also, the earlier attempts on synthesizing $\text{Li}_{1+x}\text{FePO}_4$ ($x < 0.03$) exhibited better electrochemical properties than pristine LiFePO_4 . [42, 43] This series of new findings in lithium-excess layered electrode materials naturally motivated us to examine the strategy of lithium excessiveness in the olivine with $\text{Li}_{1+x}\text{Fe}_{1-x}\text{PO}_4$ compositions, which is an important electrode material and a class of crystals that could be more vulnerable to lithium kinetics because of the restricted diffusion path.

3.2 Experimental

The LFPs with various compositions were synthesized using Li_2CO_3 (Sigma Aldrich, 99.9%), $\text{FeC}_2\text{O}_4 \cdot \text{H}_2\text{O}$ (Sigma Aldrich, 99%), $(\text{NH}_4)_2\text{HPO}_4$ (Aldrich, 98%). Each precursor was pulverized as fine as possible, separately using high energy ball-milling at Ar atmosphere to avoid the oxidation. The fine precursors were mixed by wet ball milling using acetone more than 24 hours. After drying the mixture, the powder was, again, pulverized as fine as possible using dry ball milling to obtain uniformity and calcinated at 350°C with $5 \sim 6^\circ\text{C}/\text{min}$ heating rate for 10 hours. The calcinated powders were reground and pelletized under more than 300 bar. The final sintering process was conducted with heating rate as a $5 \sim 6^\circ\text{C}/\text{min}$ rate in Ar atmosphere for 10 hours.

High-resolution powder diffraction patterns were recorded using synchrotron X-ray radiation (the 8C2-HRPD beam-line at the Pohang Accelerator Laboratory, Korea). ND data were collected using a high-resolution powder diffractometer (HRPD) at the HANARO facility of the Korea Atomic Energy Research Institute.

First principle calculations were performed using the Perdew–Burke–Ernzerhof exchange–correlation parameterization to density functional theory (DFT) with the spin-polarized generalized gradient approximation (GGA).[34] A plane-wave basis set and the projector-augmented wave (PAW) method, as implemented in the Vienna *ab initio* simulation package (VASP), were used. Hubbard parameters (GGA+U) were added to correct the incomplete cancellation of the self-interaction of GGA.[35, 36] A U value of 4.3 eV (the on-site Coulomb term) and a J value of 1.0 eV (the exchange term) were used for the Fe atoms.[37] To study the defect configuration in Li_xFePO_4 ($x = 1/16$), we considered all possible orderings within the $1 \times 2 \times 2$ supercell of LiFePO_4 (112 atoms) generated with the CASM program, which contains defects of one Li in the M2 site, one Fe in the M1 site, and one vacancy in the M1 site.[38] All plausible configurations of Li-Fe cation site-exchange and a Li-vacancy within the 16-formula unit were considered. Activation energies for the ionic diffusion were calculated using the nudged-elastic-band (NEB) method.[39] Appropriate replicate systems were used as starting points for the NEB method, with linear interpolation between the initial and final states of the diffusion pathways.

3.3 Results and Discussion

3.3.1 Structural characterization of lithium-excess olivine

Based on this simple question, we attempted to adapt the lithium-excess concept to LFP ($\text{Li}_{1+x}\text{Fe}_{1-x}\text{PO}_4$) and successfully synthesized the lithium-excess olivine phase by carefully controlling the synthetic conditions. (See the supporting information in Figure 3-1 for details.) First, samples containing various lithium-excess compositions (0, 2.5, 5, 7.5, and 10 %) were synthesized using solid-state methods at 600 °C in an Ar atmosphere to determine how much excess lithium could be incorporated in the olivine structure. Although less than 5 % lithium-excess LFP compositions result in a pure olivine phase without any crystalline impurities, compositions containing more than 7.5 % excess lithium begin to develop a second phase corresponding to $\text{Li}_3\text{Fe}_2(\text{PO}_4)_3$, as observed in the X-ray diffraction (XRD) patterns in Figure 3-1. To verify the presence of additional lithium in the LFP crystal, more detailed analysis was conducted using both high-resolution synchrotron XRD and neutron diffraction (ND), and the results were compared with those for normal LFP. Neutron analysis is necessary to trace the lithium occupancy in the crystal because of its low scattering with X-rays.[44] Figure 3-2(b) presents the ND pattern of 5% lithium-excess LFP along with a calculated pattern using the olivine structure model, which shows

low Bragg R-factors, indicating the reliability of the structural refinements. Detailed structural information from the refinements is provided in Figure 3-3 (a-c). In addition, as a reference, an ND pattern of the normal LFP along with the results of the refinement are presented in Figure 3-3. Note that the 5 % lithium-excess targeted LFP contains 4.2 (2) % lithium in Fe octahedral sites (Li_{Fe}), and all the lithium sites are occupied solely by lithium (Li_{Li}) according to the neutron refinements in Figure 3-2 (c). On the other hand, the normal LFP contains ~0.6 (2) % $\text{Li}_{\text{Fe}}\text{-Fe}_{\text{Li}}$ anti-site defects according to the refinements under the identical condition, which agrees well with previously reported values of $\text{Li}_{\text{Fe}}\text{-Fe}_{\text{Li}}$ anti-site defects in conventional LFPs.[15, 16] The refinements of two samples using high-resolution XRD reproduced the same result for the two samples, as demonstrated in Figure 3-4. The systematic modeling of the relative intensities of the XRD peaks as a function of the excess amount of lithium also agrees with the ND results in Figure 3-5. For a better comparison of the two samples, a few physical properties are tabulated in Figure 3-2 (c). The compositional analysis of two samples using inductively coupled plasma (ICP) supported the presence of the extra amount of lithium for the lithium-excess LFP phase, revealing a Li:Fe:P ratio of 1.08 (3):0.94 (1):1.00 (0) and 0.99 (2):0.98 (2):1.00 (0) for the lithium-excess and normal LFPs, respectively. The surface area is comparable for both samples but is slightly smaller for the lithium-excess LFP according to the Brunauer–

Emmett–Teller (BET) measurements. The scanning electron microscopy (SEM) images in Figure 3-6 show that the particle size of the lithium-excess LFP is slightly larger (~150 nm) than that of the normal LFP (~100 nm).

The excess amount of lithium in LFP leads to a slightly higher oxidation state of the transition metal (Fe) in the sample to maintain charge neutrality based on the substitution of the monovalent Li^+ for divalent Fe^{2+} ($\text{Li}(\text{Li}_{0.05}^+\text{Fe}_{0.95}^{+2.053})\text{PO}_4$). The X-ray absorption near edge structure (XANES) analysis in Figure 3-7 compares the oxidation states of Fe in three samples of $\text{Li}(\text{Li}_{0.05}\text{Fe}_{0.95})\text{PO}_4$, $\text{LiFe}^{+2}\text{PO}_4$, and $\text{Fe}^{+3}\text{PO}_4$. Although the quantitative determination of the Fe valence in $\text{Li}(\text{Li}_{0.05}\text{Fe}_{0.95})\text{PO}_4$ was not trivial, it was clear that the profile of the lithium-excess olivine lies between those of LiFePO_4 and FePO_4 , indicative of a Fe valence higher than +2. The higher oxidation state of Fe of the sample also serves as indirect evidence of the excess lithium present in the structure.

Even though the crystallographic information and compositional analysis indicate the presence of the excess lithium in the olivine, the possibility of the formation of an amorphous impurity phase remains. According to previous reports, the synthesis of LFP using a slightly off-stoichiometric amount of precursors can result in LFP coated with a highly conductive amorphous

phase, enhancing the rate capability.[45-47] To identify any possible amorphous phase, we conducted surface analysis of the lithium-excess LFP using high-resolution transmission electron microscopy (HR-TEM), X-ray photoelectron spectroscopy (XPS), and Fourier-transform infrared spectroscopy (FT-IR). The HR-TEM images (Figure 3-8) reveal the high crystallinity of the lithium-excess LFP both at the surface and in the bulk without an amorphous phase on the surface. In addition, the XPS and FT-IR results show no difference between the surface and bulk of the lithium-excess LFP. Both the pristine and 10-nm surface-deep-etched lithium-excess LFPs exhibited identical XPS and FT-IR profiles, as observed in Figure 3-9 and Figure 3-10, respectively, implying no traceable amount of the amorphous phase on the lithium-excess LFP surface.

a

Method	Li : Fe : P ratio	Temperature (°C)	Reaction Time (hour)	Atmosphere	Crystalline impurity
Solid-state	1.025 : 0.975 : 1	600	10	Ar	-
Solid-state	1.05 : 0.95 : 1	600	10	Ar	-
Solid-state	1.075 : 0.925 : 1	600	10	Ar	$\text{Li}_3\text{Fe}_2(\text{PO}_4)_3$
Solid-state	1.1 : 0.90 : 1	600	10	Ar	$\text{Li}_3\text{PO}_4/\text{Li}_3\text{Fe}_2(\text{PO}_4)_3$
Solid-state	1.05 : 0.95 : 1	700	10	Ar	$\text{Li}_3\text{PO}_4/\text{Li}_3\text{Fe}_2(\text{PO}_4)_3$
Solid-state	1.05 : 0.95 : 1	800	10	Ar	$\text{Li}_3\text{PO}_4/\text{Li}_3\text{Fe}_2(\text{PO}_4)_3$
Hydrothermal	3.0 : 0.95 : 1	180	4	Ar	$\text{Li}_3\text{PO}_4/\text{Li}_3\text{Fe}_2(\text{PO}_4)_3$
Hydrothermal	3.0 : 0.95 : 1	200	4	Ar	$\text{Li}_3\text{PO}_4/\text{Li}_3\text{Fe}_2(\text{PO}_4)_3$
Hydrothermal	3.0 : 0.95 : 1	220	4	Ar	Li_3PO_4 /Unkwn impurity

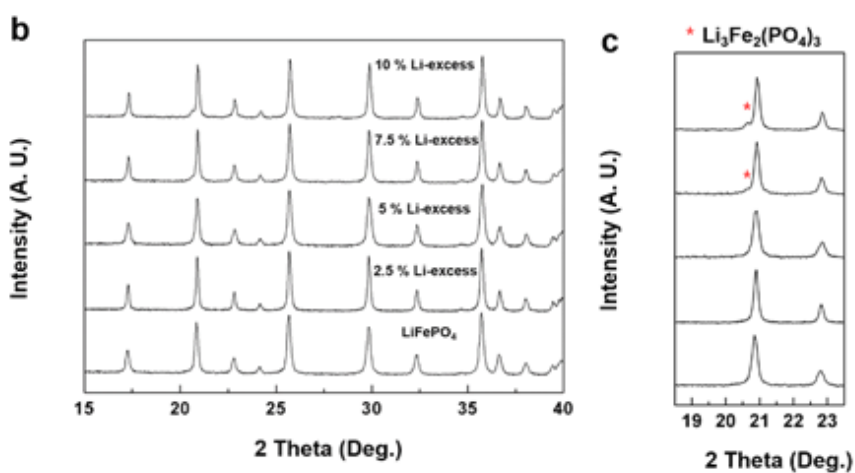


Figure 3-1. Various synthetic condition and the impurity (a) Various synthetic condition and the impurity of each conditions (b) XRD patterns of 0, 2.5, 5, 7.5 and 10 % Li-excess composition of olivine synthesized through solid-state method. (c) Magnified of 18 ~ 24 ° of XRD patterns. The stoichiometric (0% Li-excess) and 5 % Li-excess composition show no crystalline impurities, but the 7.5 % and 10 % contain $\text{Li}_3\text{Fe}_2(\text{PO}_4)_3$ impurities. (Measurement condition: range 15 ~ 40 °, step size 0.02 °, by D2 phaser, Bruker)

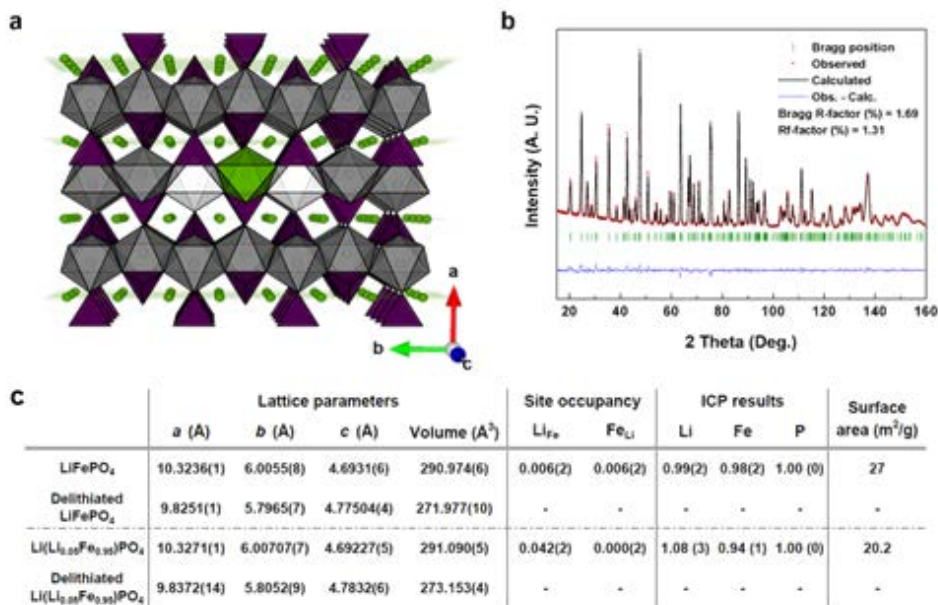
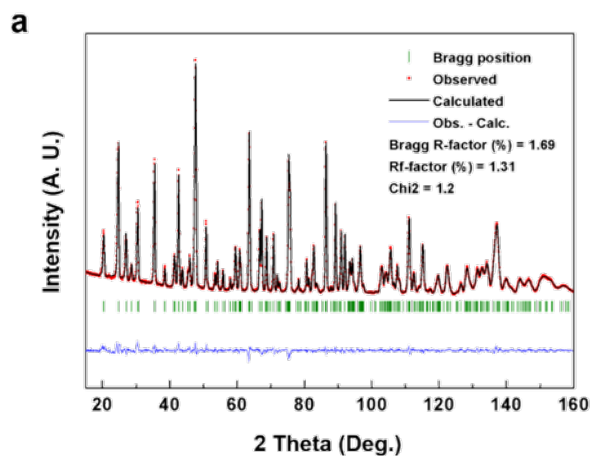


Figure 3-2 Structure characterization results of lithium-excess LFP (a)

Schematic picture of crystalline lithium-excess LFP. Green: Li atoms, purple: PO₄ tetrahedral unit, dark gray: Fe²⁺O₆ octahedral unit, gray: Fe^{2-x+}O₆ octahedral unit. (b) Rietveld refinement of neutron diffraction pattern of lithium-excess LFP. (c) Lattice parameters, M1 and M2 site occupancy, ICP results and surface area of lithium-excess and normal LFPs (d) TEM image of lithium-excess LFP surface.

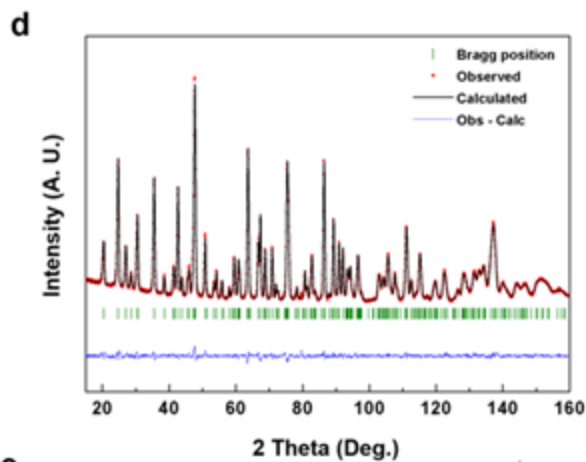


b

	$U_{11} / \text{\AA}^2$	$U_{22} / \text{\AA}^2$	$U_{33} / \text{\AA}^2$	$U_{12} / \text{\AA}^2$	$U_{13} / \text{\AA}^2$	$U_{23} / \text{\AA}^2$	Isotropic therm. Fact
Li	61.1	58.4	127.8	10.6	-9.3	-27.8	1.137
S. D.	4.6	11.8	21.6	5.5	12	12.7	74
Li_{Fe}	10.6	59.1	27.7	0	-0.2	0	0.436
S. D.	0.8	2.4	4.4	0	1.6	0	12
Fe	10.6	59.1	27.7	0	-0.2	0	0.436
S. D.	0.8	2.4	4.4	0	1.6	0	12
Fe_{Li}	61.1	58.4	127.8	10.6	-9.3	-27.8	1.137
S. D.	4.6	11.8	21.6	5.5	12	12.7	74
P1	31.2	63.6	91.9	0	6.5	0	0.729
S. D.	1.7	4.1	7.8	0	3.3	0	23
O1	30.7	60.9	81.8	0	-6.5	0	0.652
S. D.	1.3	3.8	6.8	0	2.8	0	20
O2	29.7	89.4	107.1	0	11.3	0	0.771
S. D.	1.6	4.3	8.7	0	2.9	0	24
O3	27.8	75.3	107.1	10	16.1	-7.7	0.782
S. D.	1	2.5	5.3	1.6	2	3.1	15

c

Name	x (Å)	y (Å)	z (Å)	Occ.
Li	0	0	0	1.000(2)
Li_{Fe}	0.28184(9)	0.25	0.9732(3)	0.042(2)
Fe	0.28184(9)	0.25	0.9732(3)	0.958(2)
Fe_{Li}	0	0	0	0.000(2)
P1	0.09444(17)	0.25	0.4177(3)	1
O1	0.09791(17)	0.25	0.7402(4)	1
O2	0.45748(15)	0.25	0.2043(4)	1
O3	0.16493(14)	0.04736(19)	0.2848(2)	1



e

	U ₂₃ / Å ²	U ₂₂ / Å ²	U ₃₃ / Å ²	U ₁₂ / Å ²	U ₁₃ / Å ²	U ₂₃ / Å ²	Isotropic therm. Fact
Li	37.5	83.9	33.6	7.4	13.1	-2.5	1.063(80)
S. D.	5.3	15.4	23.6	6.5	13.8	15.5	
Li _{Fe}	7.7	46.3	76.3	0	-0.6	0	0.628(13)
S. D.	0.9	2.8	4.7	0	1.8	0	
Fe	7.7	46.3	76.3	0	-0.6	0	0.628(13)
S. D.	0.9	2.8	4.7	0	1.8	0	
Fe _{Li}	37.5	83.9	33.6	7.4	13.1	-2.5	1.063(80)
S. D.	5.3	15.4	23.6	6.5	13.8	15.5	
P1	15.3	30.3	37.6	0	4.5	0	0.415(20)
S. D.	1.8	4.6	8.4	0	3.7	0	
O1	10.9	18	21.8	0	-3.3	0	0.508(25)
S. D.	1.3	4.1	7.4	0	3	0	
O2	10.6	28.9	33.6	0	-2.6	0	0.583(15)
S. D.	1.7	4.6	9.5	0	3.1	0	
O3	10.8	35.5	41.6	11.2	7.7	-2.7	0.628(13)
S. D.	1.1	2.7	5.8	1.8	2.2	3.4	

f

Name	x (Å)	y (Å)	z (Å)	Occ.
Li	0	0	0	0.994(2)
Li _{Fe}	0.28201(10)	0.25	0.9738(3)	0.006(2)
Fe	0.28218(6)	0.25	0.97469(15)	0.994(2)
Fe _{Li}	0	0	0	0.006(2)
P1	0.09515(19)	0.25	0.4175(4)	1
O1	0.09758(19)	0.25	0.7406(4)	1
O2	0.45744(16)	0.25	0.2048(4)	1
O3	0.16476(15)	0.0472(2)	0.2850(3)	1

g

Sample	Li-LiFePO ₄	Li-Li _{1.01} Fe _{0.99} PO ₄
Crystal system		Orthorhombic
Space group		Pnma (No. 62)
Lattice parameters		
<i>a</i> (Å)	10.32369(13)	10.32719(11)
<i>b</i> (Å)	6.00555(8)	6.00707(7)
<i>c</i> (Å)	4.69318(6)	4.69227(5)
Unit cell volume (Å ³)	290.974(6)	291.090(5)
Source		Neutron
Temperature (K)		300
Wavelength (Å)		1.83432
2θ range		0 - 160 °
Number of data positions		3200
Bragg R-factor (%)	1.35	1.58
Rf-factor (%)	0.847	1.09
Chi ²	2.3	2.99

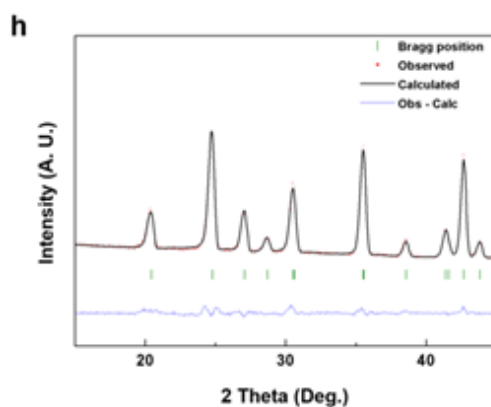
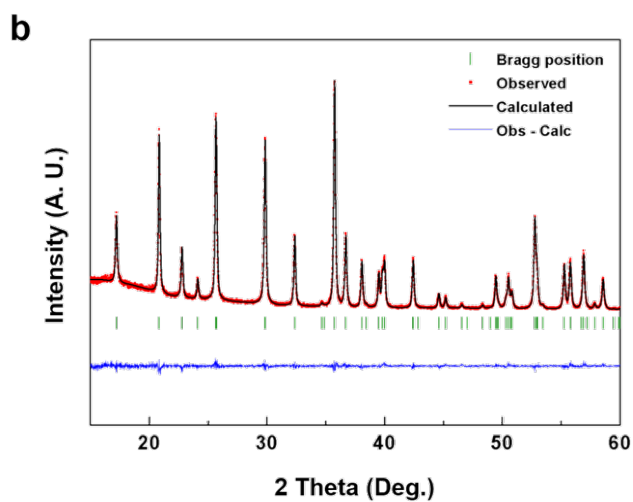
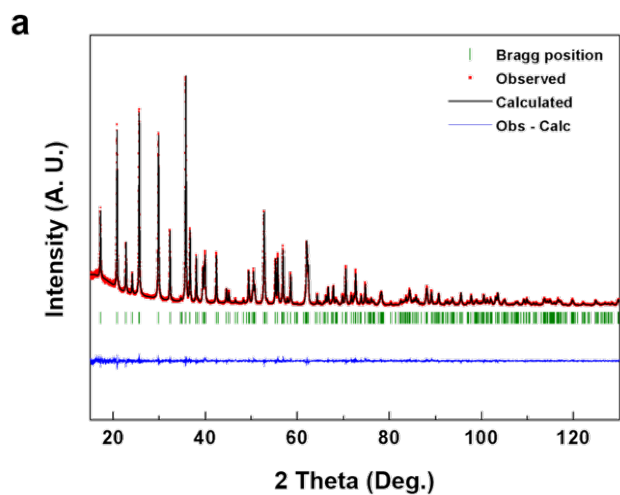
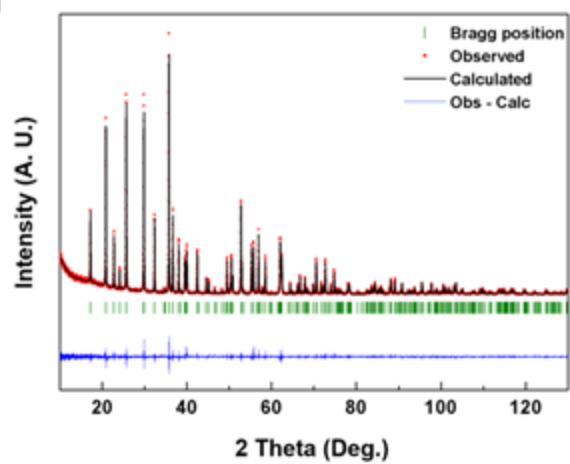


Figure 3-3 Neutron diffraction (ND) Rietveld refinement results of (a) - (c) lithium-excess LFP and (d) - (f) normal LFP. Figure (g) shows overall crystal structure factors and refinement information. The excessive Li ions are positioned at M2 octahedral site with 4.2 % occupancy. Also, the anti-site is not observed at Li-excess LFP. Figure (h) shows zoomed-in figure of (a). (Wyckoff of each sites; Li and Fe_{Li}: 4*a*; Fe, Li_{Fe}, P, O1 and O2: 4*c*; O3: 8*d*)



c

Name	x (Å)	y (Å)	z (Å)	B factor	Occ.
Li	0	0	0	1.299(141)	1.000(0)
Li _{Fe}	0.28213(6)	0.25	0.97434(15)	0.459(10)	0.958(0)
Fe	0.28213(6)	0.25	0.97434(15)	0.459(10)	0.000(0)
Fe _{Li}	0	0	0	1.299(141)	0.042(0)
P1	0.09522(11)	0.25	0.41796(23)	0.647(20)	1
O1	0.09682(29)	0.25	0.74342(55)	0.841(58)	1
O2	0.45622(33)	0.25	0.20930(56)	0.936(62)	1
O3	0.1568(23)	0.04478(33)	0.28349(36)	0.816(41)	1

d**e**

Name	x (Å)	y (Å)	z (Å)	B factor	Occ.
Li	0	0	0	1.189(192)	0.992(1)
Li _{Fe}	0.28217(6)	0.25	0.97469(15)	0.334(13)	0.008(1)
Fe	0.28218(6)	0.25	0.97469(15)	0.334(13)	0.992(1)
Fe _{Li}	0	0	0	1.189(192)	0.008(1)
P1	0.09520(11)	0.25	0.41805(23)	0.308(28)	1
O1	0.09683(30)	0.25	0.74520(55)	0.620(83)	1
O2	0.45625(32)	0.25	0.20551(57)	0.586(82)	1
O3	0.16632(24)	0.04665(34)	0.28463(37)	0.336(54)	1

f

Sample	LiFePO ₄	Li _{1.02} Fe _{0.95} PO ₄
Crystal system	Orthorhombic	
Space group	Pnma (No. 62)	
Lattice parameters		
<i>a</i> (Å)	10.32576(3)	10.32212(4)
<i>b</i> (Å)	6.00648(1)	6.00463(2)
<i>c</i> (Å)	4.69188(1)	4.69394(2)
Unit cell volume (Å ³)	290.997(1)	290.933(2)
Source	Synchrotron (X-ray)	
Temperature (K)	300	
Wavelength (Å)	1.5474	
2θ range	10 - 130.1°	
Number of data positions	12051	
Bragg R-factor (%)	2.9	1.69
Rf-factor (%)	2.1	1.31
Chi ²	1.5	1.2

Figure 3-4. XRD Rietveld refinement results of (a) - (c) lithium-excess LFP and (d) - (e) normal LFP. Figure (f) shows overall crystal structure factors and refinement information. The high resolution XRD Rietveld refinement results are consistent with ND refinement results of zero anti-site in Li-excess phase. (Wyckoff of each sites; Li and Fe_{Li}: 4*a*; Fe, Li_{Fe}, P, O1 and O2: 4*c*; O3: 8*d*)

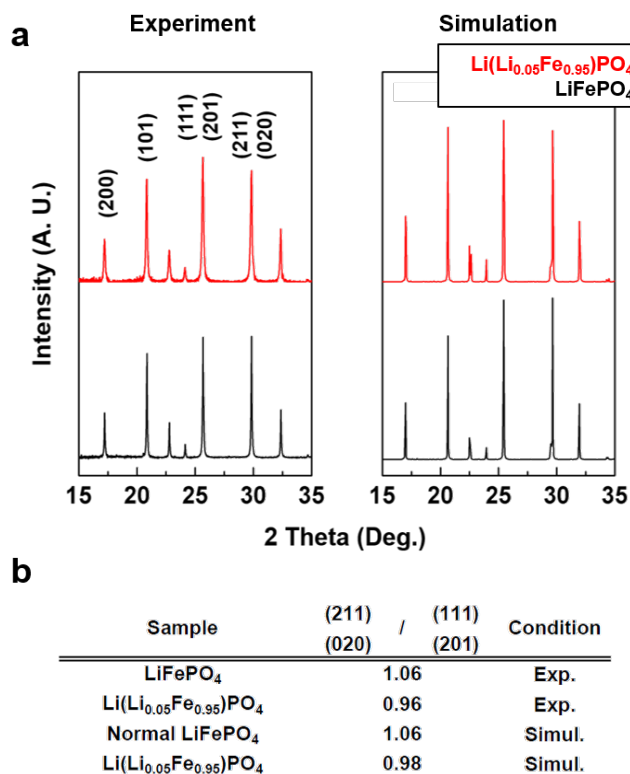


Figure 3-5. High resolution XRD experiment and simulation results (a).

We conduct XRD simulation for confirming how the XRD peak intensity ratio change at lithium-excess LFP with zero anti-site. Left figure in (a) shows the experiment result and right figure shows the simulation result. The intensity ratio of (111)(201) and (211)(020) is mainly change at both experiment and simulation results as exhibited in table (b).

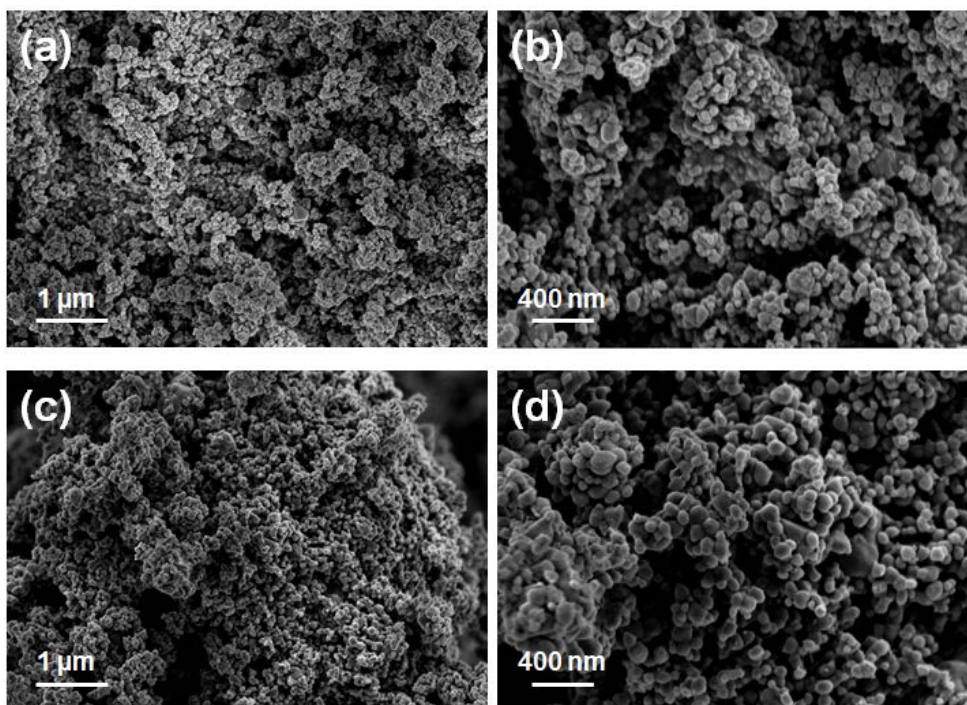


Figure 3-6. SEM image of normal and 5 % lithium-excess LFPs. The figure (a) and (b) show normal LFP. The figure (c) and (d) show 5 % lithium-excess LFP. The particle size of Li-excess LFP (~ 150 nm) is slightly higher than normal LFP (~ 100 nm).

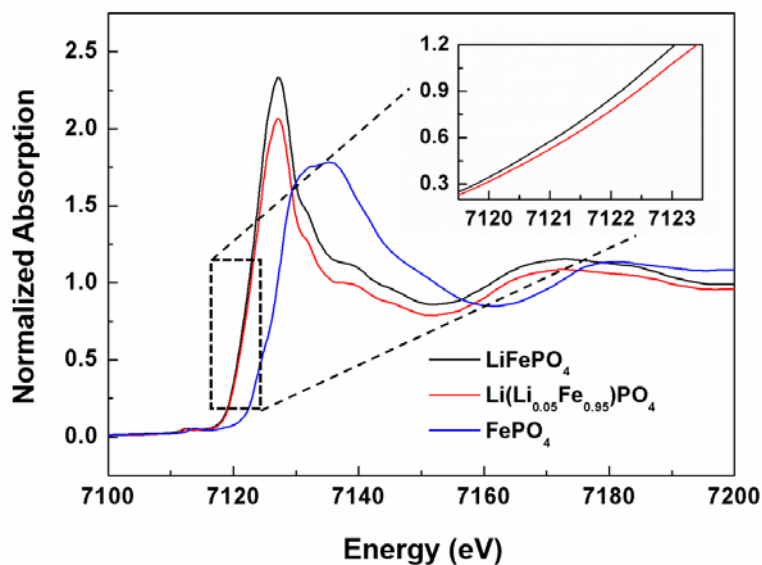


Figure 3-7. Fe XANES measurements for three samples of lithium-excess LFP, normal LFP and normal FP (delithiated LFP). The lithium-excess LFP olivine shows a slightly higher Fe oxidation state than that in the normal LFP.

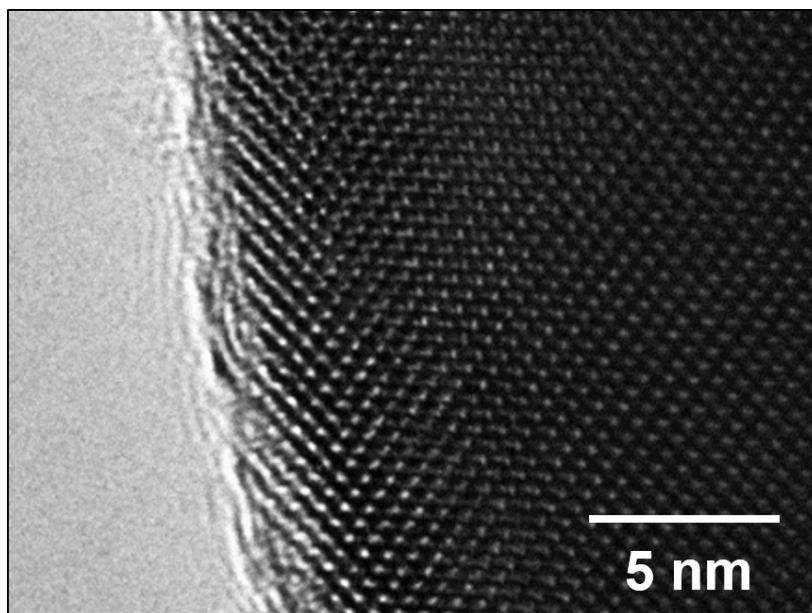


Figure 3-8. TEM image of lithium-excess LFP surface

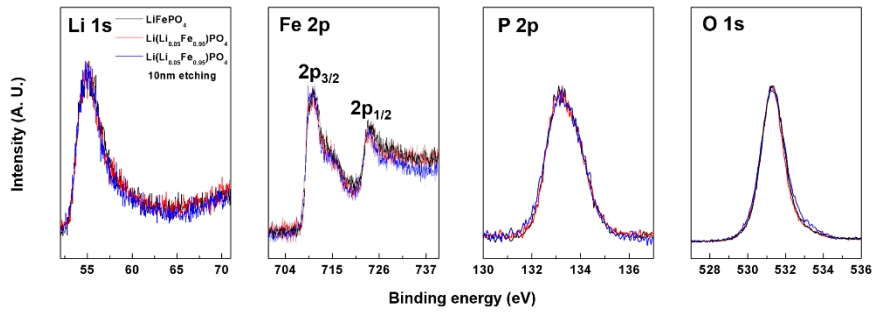


Figure 3-9. Surface analysis on 5 % lithium-excess LFP (red line) and normal LFP. (black line) 10 nm etched surface of lithium-excess LFP is marked by blue lines.(left to right, Li 1s, Fe 2p, P 2p and O 1s XPS)

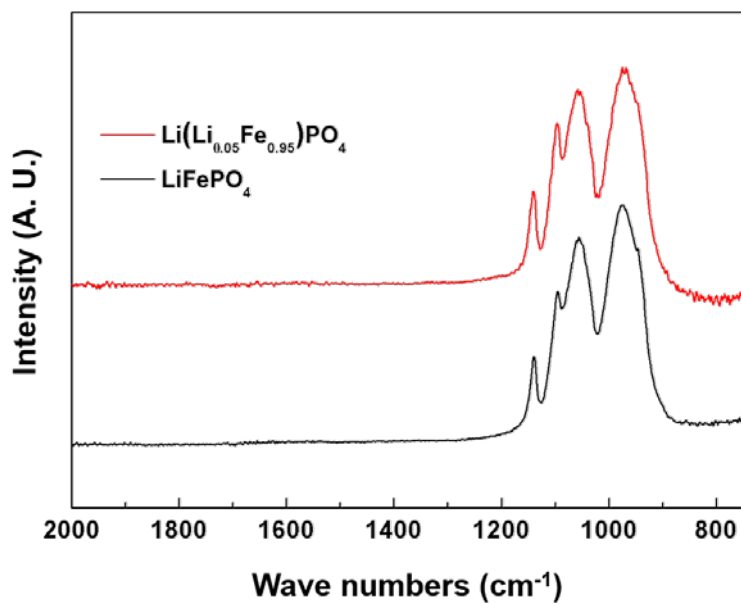


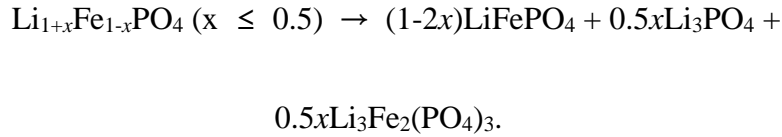
Figure 3-10. Fourier transform infrared spectroscopy (FT-IR) results of lithium-excess (red) and normal LFPs (black). Both materials does not show any impurities signal.

3.3.2 Local atomic configuration and origin of zero Fe anti-site of lithium-excess olivine

Further confirmation of the excess lithium in the LFP could be obtained from the ${}^6\text{Li}$ -NMR measurement using ${}^6\text{Li}$ -labeled samples. Figure 3-11 (a) presents the NMR spectra of ${}^6\text{LiFePO}_4$ and ${}^6\text{Li}({}^6\text{Li}_{0.05}\text{Fe}_{0.95})\text{PO}_4$. Except for the side bands marked with asterisks, a single Li signal is observed between 0 to -100 ppm for both samples. In the zoomed-in view in Figure 3-11 (b), the normal LFP shows a lithium signal at -49 ppm, which is in good agreement with previous reports.[48, 49] However, a less-negative-shifted major NMR signal is observed for lithium-excess LFP at -18 ppm. In addition, the asymmetric nature of the major signal strongly suggests that a small positive-shifted minor peak (+ 47 ppm) is present based on the spectral deconvolution. In the olivine LiFePO_4 crystal, the Li_{Li} (octahedral, M1 site) is coordinated with six oxygen atoms, which also coordinate with six different iron atoms (octahedral, M2 site), as illustrated in Figure 3-12 (a). The Li-O-Fe bonds around Li_{Li} result in near-90° Li-O-Fe angle contacts, inducing a strong paramagnetic interaction (marked by the red dashed line in Figure 3-12 (a)), and 120°-angle contacts, inducing a relatively weak paramagnetic interaction (marked by the blue dashed line in Figure 3-12 (a)). The major NMR peak at -49 ppm in normal LFP or -18 ppm in lithium-excess LFP primarily originates

from the strong near-90° Li-O-Fe interaction resulting from the geometry-dependent delocalization of the unpaired electron spin density of Fe^{2+} . [48, 49] However, the less-negative shift of the major peak for lithium-excess LFP (-18 ppm) is most likely due to the slightly higher average oxidation state of Fe ions around Li_{Li} . Previous NMR reports on LiFePO_4 , $\text{Li}_{0.6}\text{FePO}_4$, and $\text{Li}_{0.54}\text{FePO}_4$ indicated that the major NMR peak gradually shifts to higher frequency (less negative values) with decreasing lithium content and increasing Fe^{3+} content in the olivine, which is consistent with our results. [48, 50-52] The excess lithium residing in the Fe site (Li_{Fe} anti-site) results in the additional minor peak at +47 ppm in the lithium-excess LFP. According to the previous NMR report on the normal LFP that contains a significant amount of $\text{Li}_{\text{Fe}}\text{-Fe}_{\text{Li}}$ anti-site defects, the lithium in Fe sites (M2) with a similar environment to the Li_{Fe} ions in our lithium-excess LFP exhibited a positive NMR peak shift at +75 ppm. [50] Our density functional theory (DFT) calculations (Figure 3-13) indicated that the oxidized Fe ions are mainly localized near Li_{Fe} with the oxidation state of $\text{Fe}^{2.x+}$ ($0 < x < 0.5$), which results in the four $\text{Fe}^{2.x+}$ ($0 < x < 0.5$) ions surrounding the lithium octahedron (Figure 3-12 (b)). All four $\text{Fe}^{2.x+}$ ions are bonded with a near-120° Li-O-Fe angle, whose configuration leads to the comparatively weak paramagnetic shift. This unique environment of Li_{Fe} ions generates relatively less of a paramagnetic shift, yielding a positive chemical shift at +47 ppm.

To understand the thermodynamic feasibility of the lithium-excess LFP phase, we attempted to estimate its relative formation energy against the segregation into thermodynamically stable phases of LiFePO_4 , Li_3PO_4 , and $\text{Li}_3\text{Fe}_2(\text{PO}_4)_3$ as follows:



Based on this equation, we calculated the formation energy of 5% lithium-excess LFP using the $\text{Li}_{24/24}(\text{Li}_{1/24}\text{Fe}_{23/24}(\text{PO}_4)_{24})$ model (192 atoms in a unit cell) at zero temperature excluding the entropic effect. The formation energy for one excess lithium (Li_{Fe}), was observed to be approximately 440 meV per event, indicating that the excess lithium ions formed as a ‘anti-site defect’ state in their structure. Considering the relationship between the defect formation energy and its concentration, the comparison of the various defect formation energies would provide a rough idea of the feasibility of the excess lithium ‘defect’ in the olivine, particularly for defects in an olivine framework.[2] It is noteworthy that the formation energy of $\text{Li}_{\text{Fe}}\text{-Fe}_{\text{Li}}$ anti-site

defect in typical olivine LiFePO_4 is approximately 420 meV per event, and depending on the synthetic routes, olivine LFPs with ~5 % anti-site defect concentration can be easily synthesized.[5] Thus, the synthesis of the olivine LFP with ~5 % excess lithium, which requires ~440 meV defect formation energy, may be plausible. As the concentration of $\text{Li}_{\text{Fe}}\text{-Fe}_{\text{Li}}$ anti-site defect in normal LFP decreases with higher post heat treatments because the materials reach the thermodynamically more stable crystalline state,[5, 53] we also observed that a phase separation into thermodynamically stable phases occurs for lithium-excess LFP above 700 °C based on the temperature-controlled *in-situ* XRD results (see Figure 3-14).

Given the structural analysis of the lithium-excess LFP, most notably, it contains zero Fe_{Li} anti-sites in the M1 sites. Although the excess content of lithium can statistically reduce the probability of transition metal (Fe) occupancy in Li sites, which is similarly observed in lithium-excess $\text{Li}(\text{Li}_x, (\text{Ni}, \text{Mn})_{1-x})\text{O}_2$ ($x > \sim 0.2$) with less Li/Ni site disorder up to 2 %, [54] the complete disappearance of Fe ions in the lithium diffusion channel with only 5% excess lithium is quite remarkable. To further understand the role of the excess lithium present in the structure in reducing the concentration of Fe_{Li} defects, we calculated the defects formation energies on various defects configuration containing Fe_{Li} defect around the excess lithium (Li_{Fe}) using

DFT calculations. (Note that the possible anti-site defects containing Fe_{Li} anti-site in lithium-excess LFP are only $\text{Li}_{\text{Fe}}\text{-Fe}_{\text{Li}}$ paired anti-site configuration.) In this calculation, we considered 17 different $\text{Li}_{\text{Fe}}\text{-Fe}_{\text{Li}}$ anti-site configurations around the excess lithium up to second-nearest transition metal neighbors along each axis (Figure 3-15 shows the detailed atomic configurations). All the defect formation energies of the 17 different configurations are shown as a function of the distance from excess Li_{Fe} ion in Figure 3-17. It is observed that the $\text{Li}_{\text{Fe}}\text{-Fe}_{\text{Li}}$ anti-site energy generally increases as it approaches the excess lithium, indicating that the presence of excess lithium energetically disfavors the formation of an anti-site defect near itself. We also observed that even the lowest defect formation energy (Figure 3-18) was as high as 0.823 eV, which is 2 times larger than the typical $\text{Li}_{\text{Fe}}\text{-Fe}_{\text{Li}}$ anti-site formation energy (0.42 eV, see Figure 3-16) observed in normal LFPs.[3] Because the defect formation is inversely proportional to the exponential value of the formation energy, an increase in the formation energy by ~ 0.4 eV would reduce the probability of the anti-site formation near the excess lithium (Li_{Fe}) by 7 orders of magnitude at room temperature. This remarkable reduction arises from the unfavorable electrostatic interaction among Fe ions around the excess lithium (Li_{Fe}), as shown in Figure 3-18. When the $\text{Li}_{\text{Fe}}\text{-Fe}_{\text{Li}}$ anti-site is introduced near the excess lithium (Li_{Fe}), the neighboring Fe ion becomes oxidized to Fe^{3+} in the locally lithium-rich region.

In addition, under this condition, the site-exchanged Fe^{2+} ion (Fe_{Li}) suffers from a stronger repulsion force from the neighboring Fe^{3+} ion (Figure 3-18, red arrow), which significantly increases the formation energy of the Fe_{Li} anti-site. Considering that the one excess lithium event affects at least 17 neighboring Fe ion sites among the second-nearest neighbors we considered, approximately 4 % excess lithium would result in all the Fe ions sites being affected if the excess lithium ions were homogeneously distributed in the olivine crystal. Thus, the overall $\text{Li}_{\text{Fe}}\text{-Fe}_{\text{Li}}$ anti-site concentration in the lithium-excess LFP would be 1.2×10^{-7} times less than that in the normal LFP at room temperature. This finding implies that the excess lithium in the olivine reduces the Fe_{Li} anti-site defects not only by statistically lowering the probability of Fe occupancy in Li sites from the excessive amount of lithium but also by energetically disfavoring the formation of anti-sites, suggesting that this approach could be effective in producing a zero anti-site olivine. Our results also partly agree with a previous work by Hoang and Johannes, where they reported that the formation energies of Li_{Fe} and Fe_{Li} anti-site defects could be sensitively affected by the presence of lithium-rich phases.[26]

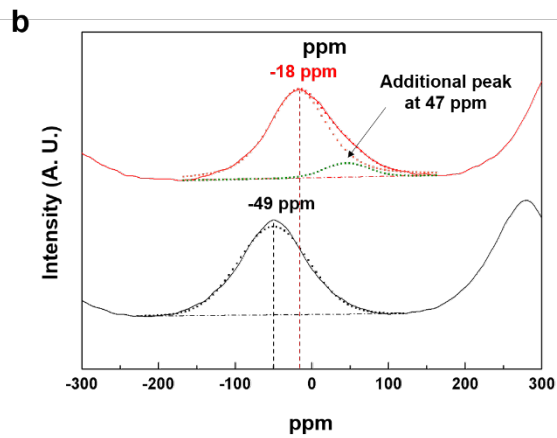
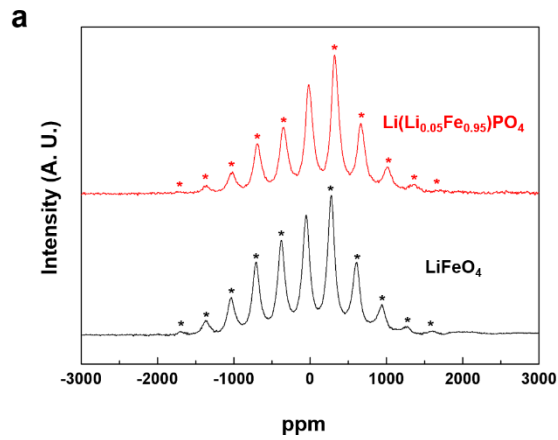


Figure 3-11. ${}^6\text{Li}$ NMR resonance (a) ${}^6\text{Li}$ NMR resonance of lithium-excess LFP (red) and normal LFP (black) with side bands (asterisk). (b) Spectral deconvolution of ${}^6\text{Li}$ NMR peaks. The normal LFP contains single resonance at -49 ppm, and the lithium-excess LFP contains two resonances at -18 and +47 ppm.

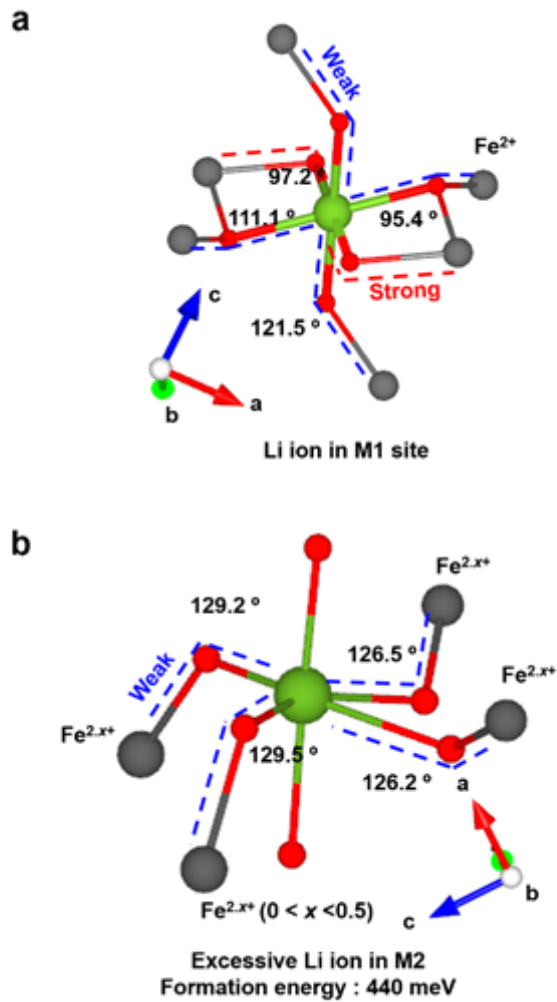


Figure 3-12. Local atomic configurations (c) Local atomic configuration around Li ion in M1 site in normal LFP and (d) excess Li ion in M2 in lithium-excess LFP calculated by DFT method. The red and blue dashed lines indicate strong and weak paramagnetic interactions between Li and Fe ions, respectively.

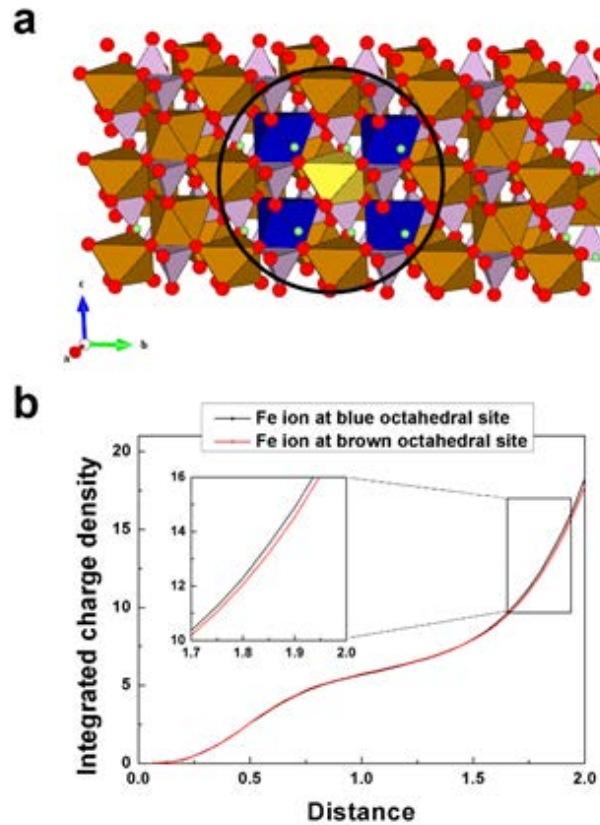


Figure 3-13. Local Fe ion oxidation state (a) The most stable lithium-excess configuration calculated by DFT calculation tool. (yellow octahedral: Li_{Fe} (Li-excess ion), blue octahedral: $\text{Fe}^{2.x+}$ ($0 < x < 0.5$) ion and brown octahedral: Fe^{2+} octahedral). (b) The integrated charge density as a function of distance from center of Fe ion. The Fe ions positioning in blue octahedral site contain additional electron compared with other Fe ions. (brown octahedral) The Fe oxidation state that the charge is delocalized in four $\text{Fe}^{2.x+}$ ($0 < x < 0.5$) ions surround excessive Li_{Fe} is distinct from that of conventional LFP

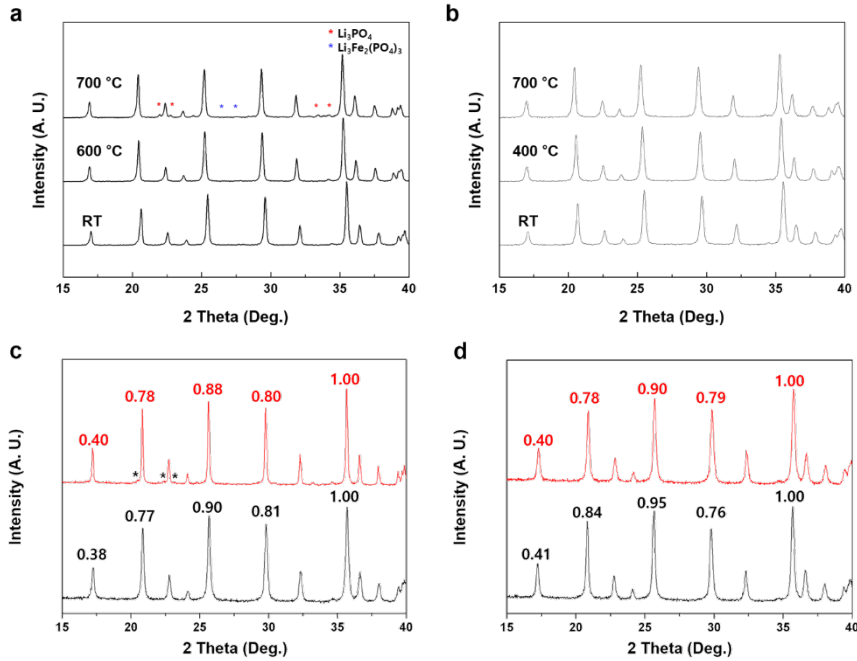
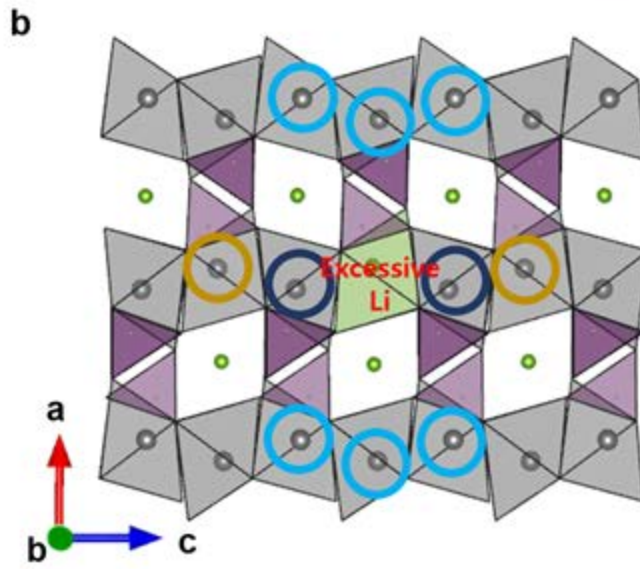
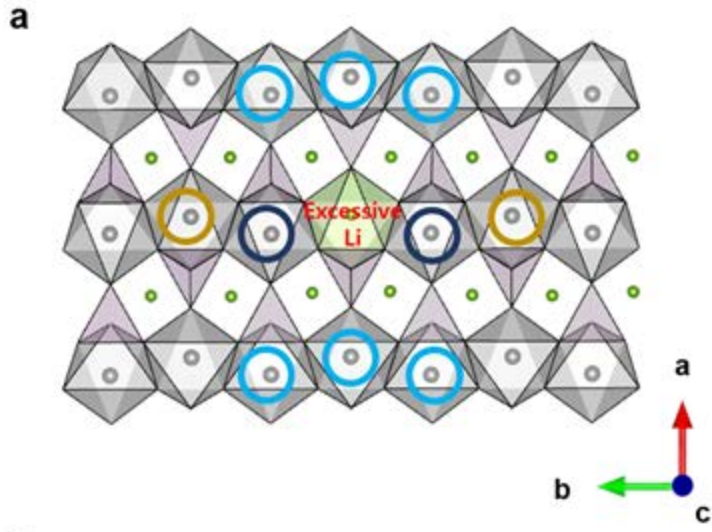
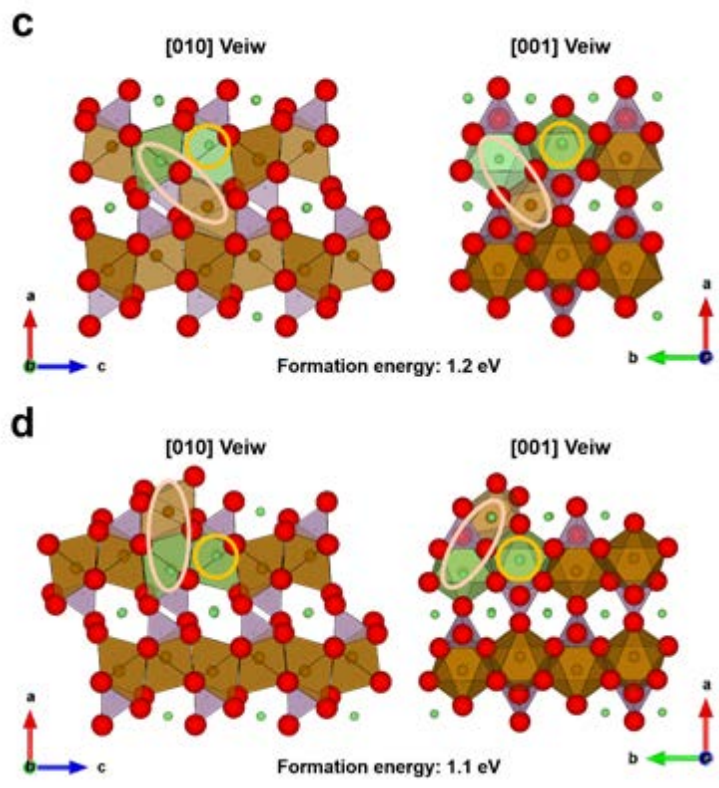


Figure 3-14. In-situ temperature controlled XRD patterns at Ar condition of (a) 5 % lithium-excess LFP and (b) normal LFP. Over the 700 °C, the lithium-excess LFP shows Li_3PO_4 and $\text{Li}_3\text{Fe}_2(\text{PO}_4)_3$ impurities marked by asterisks. Figure (c) and (d) show the intensity ratio change before (black) and after (red) heat treatment at 700 °C of lithium-excess (c) and normal LFPs (d) at room temperature respectively. Before treatment, the intensity ratios of both samples (black lines) are quite different, however, after treatment, these become similar. (red lines) It indicates that the lithium-excess LFP decomposed to stable normal LFP phase and impurities after 700 °C heat treatment.



-  First neighbor Fe ions (4)
-  Second neighbor Fe ions along *a*-axis (9)
-  Second neighbor Fe ions along *b*- or *c*- axis (9)



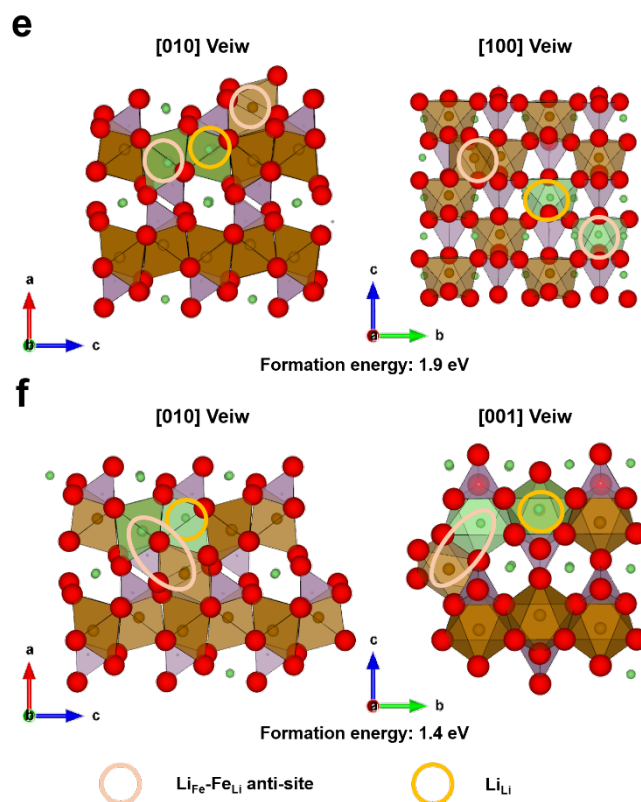


Figure 3-15. Possible cation exchange sites (LiFe-FeLi anti-site) at lithium-excess phase. Each figures shows a plane schematic figure of lithium-excess LFP along (a) c -axis and (b) b -axis. The sites are categorized by 3 kinds; i) First neighbor Fe ions, (marked by deep blue circle) ii) second neighbor Fe ions along a -axis (marked by sky blue circle) and iii) second neighbor Fe ions along b - or c -axis (marked by earthy yellow) of excessive Li ion. The numbers in parentheses indicate number of possible sites. (c), (d), (e) and (f) exhibit the representative $\text{Li}_{\text{Fe}}\text{-Fe}_{\text{Li}}$ pairing anti-site configuration in lithium-excess LFP which are calculated at our work. The pink and yellow circles indicate $\text{Li}_{\text{Fe}}\text{-Fe}_{\text{Li}}$ pairing anti-site and excess lithium ion respectively.

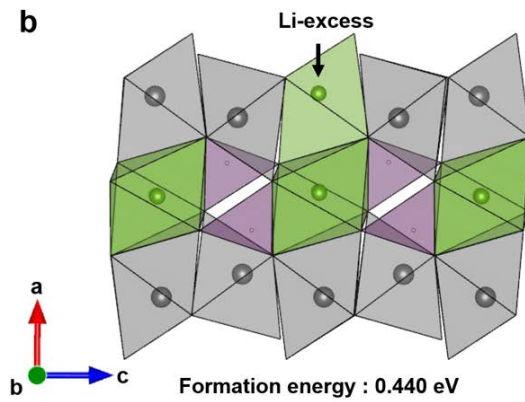
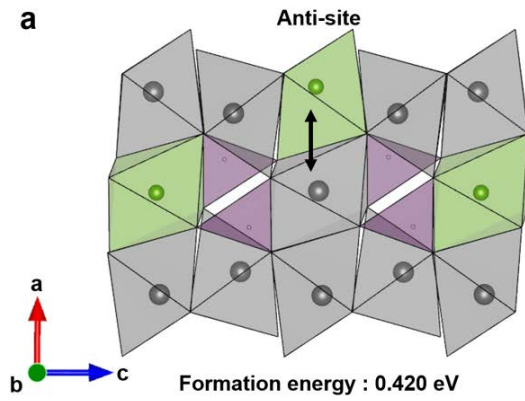


Figure 3-16. Anti-site configuration and its formation energy (a) Typical anti-site configuration and formation energy in normal LFP phase and (b) lithium-excess local configuration and formation energy.

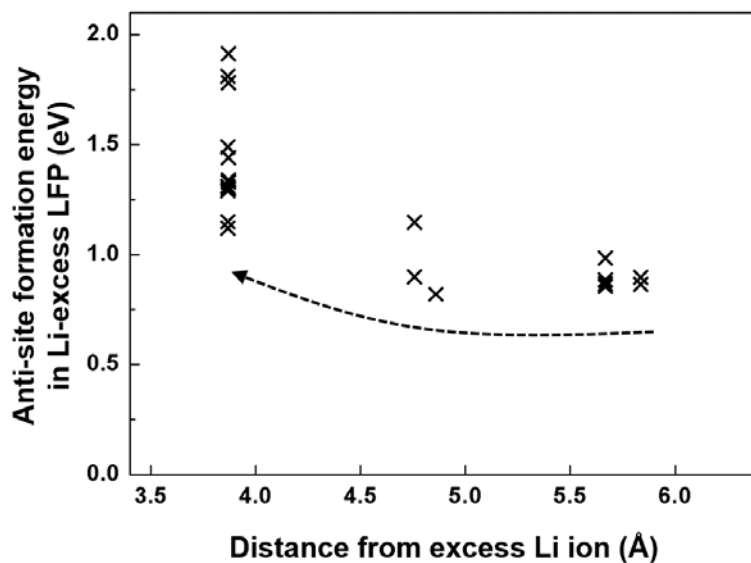


Figure 3-17. Anti-site defect formation energies at lithium-excess LFP as a function of distance from Li_{Fe} .

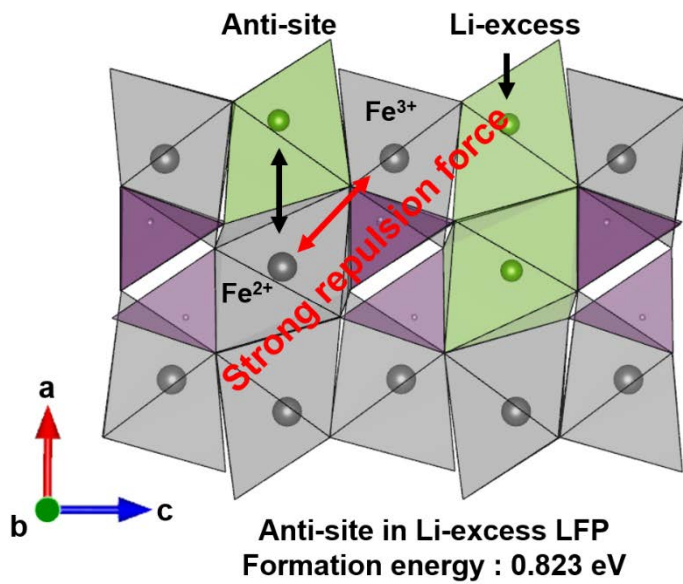


Figure 3-18. The most stable anti-site configuration in lithium-excess LFP.
Site exchanged Fe²⁺ ion (anti-site) and Fe³⁺ ion positioning near excess Li ion make a strong electrostatic repulsion.

3.3.3 New [101] diffusion path of lithium-excess olivine

The occupancy of excess lithium in the Fe site can open up a new lithium diffusion pathway by connecting the nearby lithium channels. It is well known that the olivine crystal has only one diffusion channel along the [010] direction with a low activation barrier (~ 0.44 eV), whereas lithium diffusion across the channels in other directions such as [101] or [001] requires too high of an activation barrier because of the strong electrostatic repulsion from the Fe and insufficient space for lithium hopping, as listed in Figure 3-19.[55, 56] The replacement of the high-valent Fe ions by lithium ions reduces the electrostatic repulsion, thus facilitating lithium hopping around the lithium (Li_{Fe}), as observed in the reduction of the activation barriers along [001] and [010]. Also, the lowered lithium ion diffusion activation energies could be confirmed by electrochemical impedance spectroscopy (EIS) measurement. (See Figure 3-20) Most remarkable is that the excess lithium in the Fe site is also mobile and can diffuse into the nearby lithium channel along [101], participating in the overall diffusion process in the crystal. Our DFT calculations reveal that the presence of lithium in the Fe site opens up a new alternative diffusion path along the [101] direction with a significantly reduced activation barrier of ~ 0.82 eV (Figure 3-22) compared with more than 2 eV for normal LFP (Figure 3-23) along the same direction.[57] The

calculated activation barrier is also similar with the value reported by Dathar et. al. along the [101] diffusion channel containing $\text{Fe}_{\text{Li}}\text{-Li}_{\text{Fe}}$ pairing anti-site.[58] Figure 3-24 and Figure 3-25 present a schematic illustration of lithium hopping along the [101] direction and the corresponding energy profile for normal and lithium-excess LFPs. In the normal LFP, the lithium hopping along the [101] direction is under severe electrostatic repulsion from the nearby corner-sharing Fe ions, and the lithium ion is forced to pass through the oxygen dumbbell, as shown in Figure 3-25. The narrow space between the two oxygens ($\sim 3.05 \text{ \AA}$) disfavors the lithium hopping, resulting in the activation barrier of more than 2 eV. In the lithium-excess LFP, however, the corner-sharing Fe is replaced with lithium, which also participates in the diffusion. Thus, the diffusing lithium ion no longer needs to bypass the high-valent Fe and can hop through the space provided by Li_{Fe} (Figure 3-24). The rate-limiting step during lithium hopping along the [101] direction in the lithium-excess LFP also lies in the step of passing through the Li_{Fe} site. Compared with normal LFP, where the lithium ion squeezes into the narrow oxygen dumbbell, the new intermediate state offered by the Li_{Fe} site provides sufficient space, thus lowering the activation barrier for hopping.

The activation barrier of $\sim 0.82 \text{ meV}$ is slightly higher than that observed for fast lithium pathways but is comparable to that of diffusion paths observed

for NaFeSO₄F[59] and LiMnPO₄[60], implying feasible lithium diffusion along the new path. The [101] route may not be a main diffusion path during fast charge/discharge cycling at room temperature considering the higher activation energy compared with that of the [010] diffusion path and relatively low concentration of lithium-excess, but would support the main [010] diffusion channel as an alternative route, particularly in the presence of immobile impurities in the [010] channel. As Malik *et al.* noted,[17] the immobile impurities in the [010] channel force lithium ions to detour through high-activation-barrier paths such as [101], which reduces the room-temperature specific capacity and ionic conductivity. Thus, the availability of even a small number of low-activation-barrier detour paths would support the overall lithium diffusivity in the defect-containing LFP. It is noteworthy that a similar phenomenon was observed in the rock-salt-type lithium-excess Li_{1.211}Mo_{0.467}Cr_{0.3}O₂, which exhibited remarkably enhanced ionic conductivity and capacity with the introduction of an excess amount of lithium, implying that the ‘excess-lithium strategy’ can be used as a general method to open multiple new lithium diffusion paths in solid-state lithium ionic conductors.[41]

Direction	Activation barrier (meV)	
	LiFePO ₄	Li(Li _{0.05} Fe _{0.95})PO ₄
[010]	444	328
[001]	2187	1850
[101]	2186	819

Figure 3-19. Activation barriers for lithium ion hopping for normal and lithium-excess LFPs.

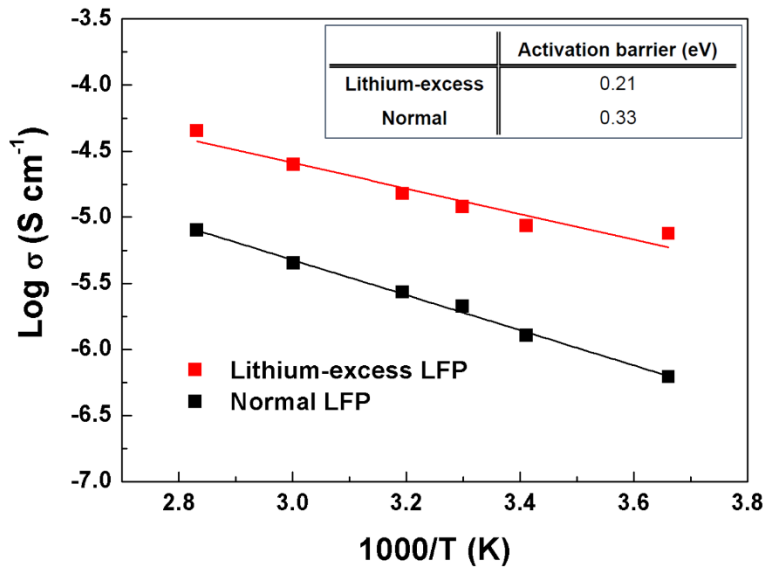


Figure 3-20. Conductivity change of Li-excess and normal LFPs at 0, 20, 30, 40, 60 and 80 °C. The EIS measurements were conducted with 3 MHz ~ 0.1 Hz using Ag/sample/Ag symmetric cells. The Li ion diffusion activation barrier is calculated based on thermal driven conductivities. The activation barriers are obtained as 210 and 330 meV for lithium-excess and normal LFP, respectively.

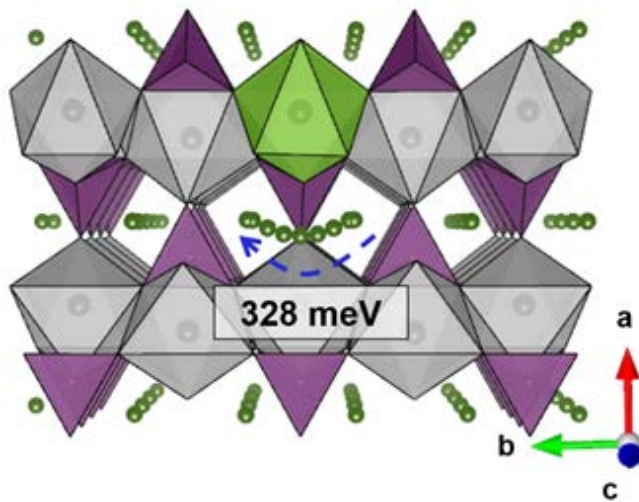


Figure 3-21. The schematics of Li ion diffusion along [010] direction in lithium-excess LFP.

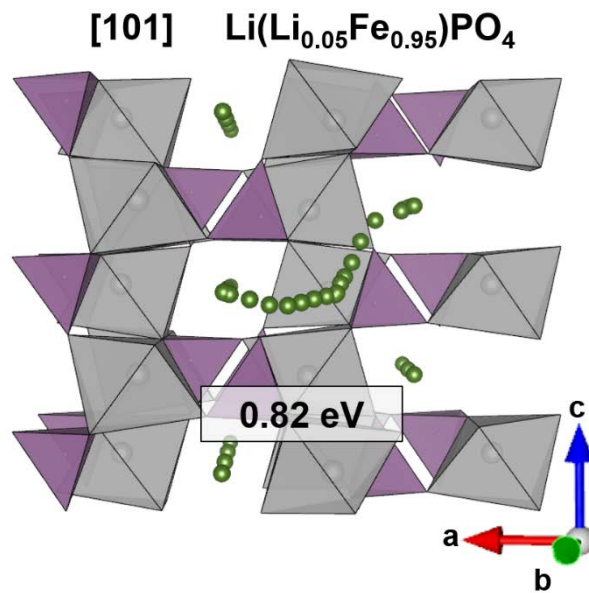


Figure 3-22 The schematics of Li ion diffusion along [101] direction in lithium-excess LFP

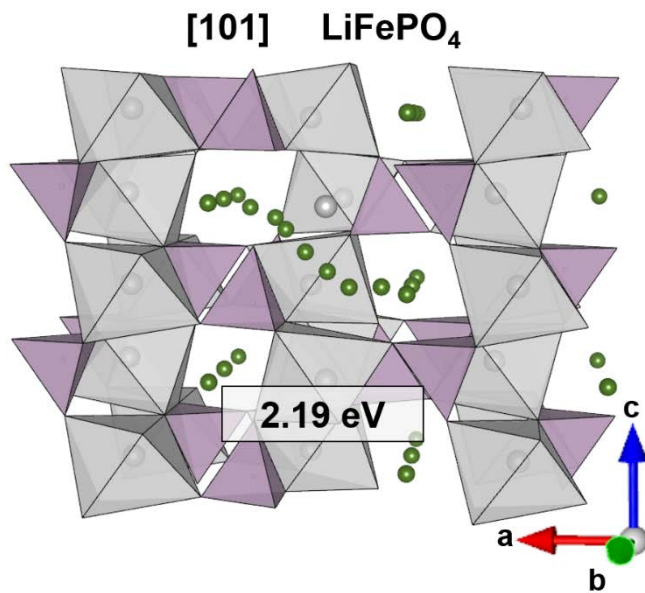


Figure 3-23. The schematics of Li ion diffusion along [101] direction in normal LFP

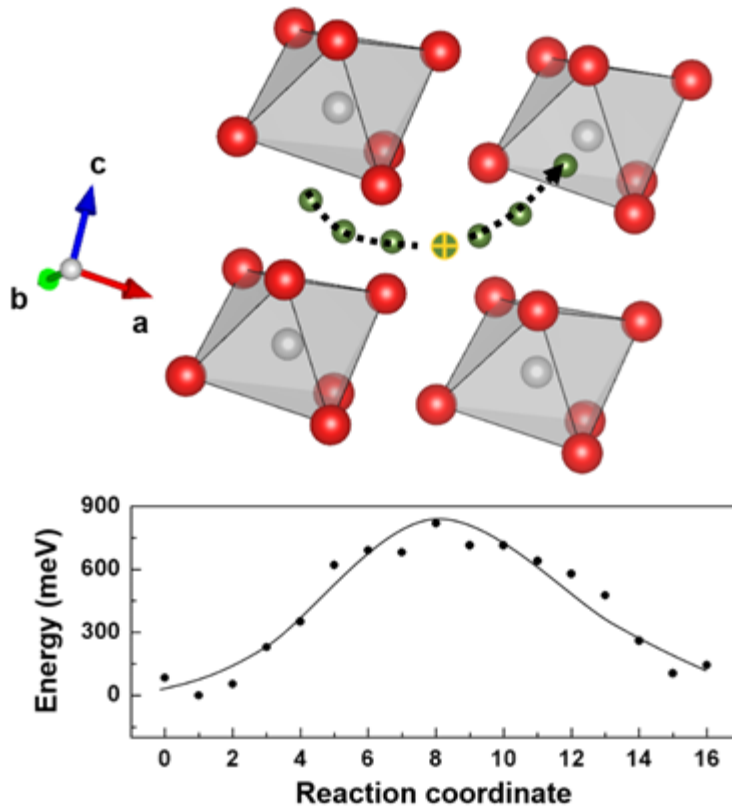


Figure 3-24. [101] activation barrier of lithium-excess LFP. It show the close view of lithium diffusion along with the energy profiles. (Li ions in the highest energy state marked by yellow)

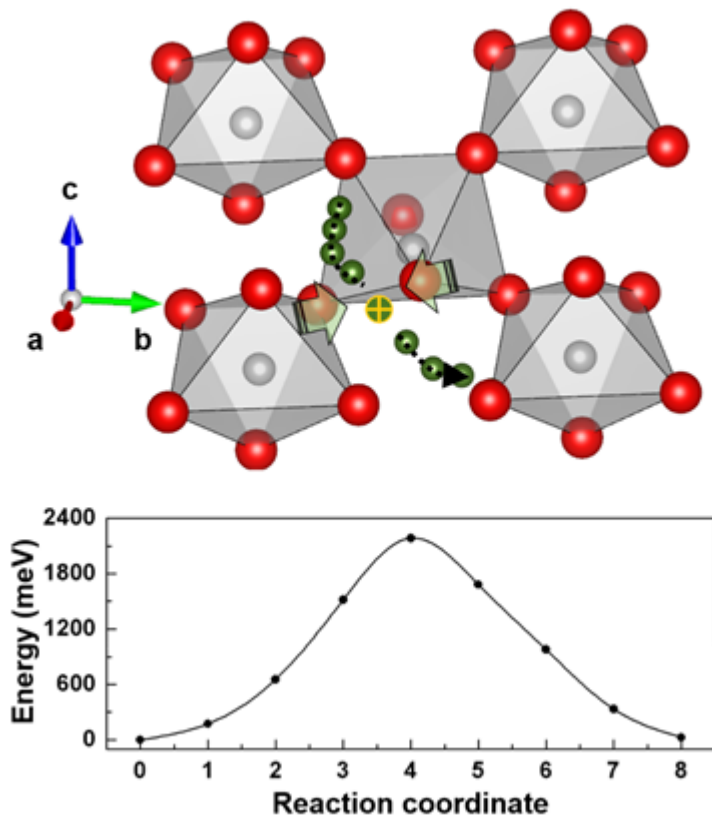


Figure 3-25. [101] activation barrier of normal LFP. It show the close view of lithium diffusion along with the energy profiles. (Li ions in the highest energy state marked by yellow)

3.3.4 Electrochemical properties

The electrochemical properties of lithium-excess LFP were investigated using a Li metal counter electrode in a 2032 coin-type cell. (Figure 3-26 (a)) presents the galvanostatic electrochemical profiles of lithium-excess LFP compared with that of normal LFP at a 10 mA g^{-1} current rate (red: lithium-excess LFP, black: normal LFP). The lithium-excess LFP electrode delivers a slightly lower capacity of $\sim 157 \text{ mAh g}^{-1}$ compared with the normal LFP, $\sim 166 \text{ mA g}^{-1}$, which is due to the higher oxidation state of Fe and the smaller number of available $\text{Fe}^{2+/3+}$ redox couples in $\text{Li}^{1+}(\text{Li}^{1+}_{0.05}[\text{Fe}^{2+}_{0.90}\text{Fe}^{3+}_{0.05}])\text{PO}_4$. Nevertheless, it is notable that a lower polarization gap between charge and discharge was observed for lithium-excess LFP compared with normal LFP under the same electrochemical conditions. The smaller polarization was consistently observed with varying current densities from 30 mA g^{-1} to 0.17 mA g^{-1} , corresponding to a C/1000 rate of LFP, as shown in Figure 3-26 (b). With the extrapolation of the curve toward zero current, the minimum values of the hysteresis gaps reach 20 mV and 30 mV for lithium-excess and normal LFPs, respectively. As the near-zero-current polarization of LFP is related to the delithiation mechanism of single-particle LFP and has been regarded as a thermodynamic property, the different values of the two LFPs imply the distinguishable delithiation behaviors, as will be discussed in further detail.

Additional experiments and discussion regarding the zero-current polarization is provided in the Figure 3-27.

The rate capabilities of lithium-excess LFP were measured at various current rates as shown in Figure 3-28. (The charge/discharge profiles are provided in Figure 3-29) The lithium-excess LFP electrode exhibited a notably improved rate capability compared with that of the normal LFP even though the particle size of lithium-excess LFP is slightly larger, as previously illustrated. Lithium-excess LFP delivers a discharge capacity of 78 mAh g⁻¹ at a current density of 8 A g⁻¹, which is equivalent to approximately 50 C (Figure 3-28). Compared with normal LFP electrodes, this value represents an approximately 2-times-higher capacity. The specific power density calculated at 8 A g⁻¹ is approximately 20 kW kg⁻¹, which is higher than that of other previously reported LFPs that have undergone surface chemical modification or nano-sizing processes, as shown in Figure 3-30.[61-64] After 500 cycles at 0.5 A g⁻¹, the lithium-excess LFP still exhibited 82 % retention of the initial capacity, maintaining a high charge/discharge efficiency in Figure 3-31.

3.4 Conclusion

We successfully synthesized a lithium-excess LFP, $\text{Li}(\text{Li}_{0.05}\text{Fe}_{0.95})\text{PO}_4$, using a solid-state method. The new LFP exhibited unexpected physical and chemical properties that are remarkably distinguishable from those of normal LFP, which is primarily due to the zero Fe_{Li} anti-site defects. The origin of the zero Fe_{Li} anti-site defects is attributed to not only the excess lithium that statistically precludes the occupancy of Fe in lithium sites but also the enlarged anti-site formation energy resulting from the stronger repulsion from higher-valent Fe. We demonstrated that the local lithium-excess configuration (i) provides additional lithium diffusion paths along the [101] directions.

3.5 References

1. Armand, M. and J.M. Tarascon, Building better batteries. *Nature*, 2008. **451**(7179): p. 652-657.
2. Vineyard, G.H. and G.J. Dienes, The Theory of Defect Concentration in Crystals. *Physical Review*, 1954. **93**(2): p. 265-268.
3. Islam, M.S., et al., Atomic-Scale Investigation of Defects, Dopants, and Lithium Transport in the LiFePO₄ Olivine-Type Battery Material. *Chemistry of Materials*, 2005. **17**(20): p. 5085-5092.
4. Wang, J., et al., Size-dependent surface phase change of lithium iron phosphate during carbon coating. *Nat Commun*, 2014. **5**.
5. Chen, J. and J. Graetz, Study of Antisite Defects in Hydrothermally Prepared LiFePO₄ by in Situ X-ray Diffraction. *ACS Applied Materials & Interfaces*, 2011. **3**(5): p. 1380-1384.
6. Delmas, C., et al., On the behavior of the Li_xNiO₂ system: an electrochemical and structural overview. *Journal of Power Sources*, 1997. **68**(1): p. 120-125.
7. Sasaki, T., Y. Ukyo, and P. Novák, Memory effect in a lithium-ion battery. *Nat Mater*, 2013. **12**(6): p. 569-575.
8. Li, Y., et al., Current-induced transition from particle-by-particle to concurrent intercalation in phase-separating battery electrodes. *Nat Mater*,

2014. **13**(12): p. 1149-1156.

9. Gibot, P., et al., Room-temperature single-phase Li insertion/extraction in nanoscale Li_xFePO_4 . *Nat Mater*, 2008. **7**(9): p. 741-747.

10. Delmas, C., et al., Lithium deintercalation in LiFePO_4 nanoparticles via a domino-cascade model. *Nat Mater*, 2008. **7**(8): p. 665-671.

11. Bai, P. and M.Z. Bazant, Charge transfer kinetics at the solid–solid interface in porous electrodes. *Nat Commun*, 2014. **5**.

12. Delacourt, C., et al., The existence of a temperature-driven solid solution in Li_xFePO_4 for $0 < x < 1$. *Nat Mater*, 2005. **4**(3): p. 254-260.

13. Padhi, A.K., K.S. Nanjundaswamy, and J.B. Goodenough, Phospho-olivines as Positive-Electrode Materials for Rechargeable Lithium Batteries. *Journal of The Electrochemical Society*, 1997. **144**(4): p. 1188-1194.

14. Nishijima, M., et al., Accelerated discovery of cathode materials with prolonged cycle life for lithium-ion battery. *Nat Commun*, 2014. **5**.

15. Yamada, A., S.C. Chung, and K. Hinokuma Optimized LiFePO_4 for Lithium Battery Cathodes. *Journal of The Electrochemical Society*, 2001. **148**(3): p. A224-A229.

16. Nishimura, S.-i., et al., Experimental visualization of lithium diffusion in Li_xFePO_4 . *Nat Mater*, 2008. **7**(9): p. 707-711.

17. Malik, R., et al., Particle Size Dependence of the Ionic Diffusivity.

Nano Letters, 2010. **10**(10): p. 4123-4127.

18. Tealdi, C., C. Spreatico, and P. Mustarelli, Lithium diffusion in $\text{Li}_{1-x}\text{FePO}_4$: the effect of cationic disorder. *Journal of Materials Chemistry*, 2012. **22**(47): p. 24870-24876.

19. Chung, S.-Y., et al., Atomic-Scale Visualization of Antisite Defects in LiFePO_4 . *Physical Review Letters*, 2008. **100**(12): p. 125502.

20. Chen, J., et al., The hydrothermal synthesis and characterization of olivines and related compounds for electrochemical applications. *Solid State Ionics*, 2008. **178**(31–32): p. 1676-1693.

21. Yang, S., P.Y. Zavalij, and M. Stanley Whittingham, Hydrothermal synthesis of lithium iron phosphate cathodes. *Electrochemistry Communications*, 2001. **3**(9): p. 505-508.

22. Chen, J. and M.S. Whittingham, Hydrothermal synthesis of lithium iron phosphate. *Electrochemistry Communications*, 2006. **8**(5): p. 855-858.

23. Park, K.-Y., et al., Anti-Site Reordering in LiFePO_4 : Defect Annihilation on Charge Carrier Injection. *Chemistry of Materials*, 2014. **26**(18): p. 5345-5351.

24. Radhamani, A.V., et al., Suppression of antisite defects in fluorine-doped LiFePO_4 . *Scripta Materialia*, 2013. **69**(1): p. 96-99.

25. Yuan, S. and K. Dai, Heat-rate-controlled hydrothermal synthesis of LiFePO_4 achieved by different heating sources. *Russian Journal of*

Electrochemistry, 2014. **50**(4): p. 385-389.

26. Hoang, K. and M. Johannes, Tailoring Native Defects in LiFePO₄: Insights from First-Principles Calculations. Chemistry of Materials, 2011. **23**(11): p. 3003-3013.

27. Amisse, R., et al., Nonstoichiometry in LiFe_{0.5}Mn_{0.5}PO₄: Structural and Electrochemical Properties. Journal of The Electrochemical Society, 2013. **160**(9): p. A1446-A1450.

28. Hamelet, S., et al., Existence of Superstructures Due to Large Amounts of Fe Vacancies in the LiFePO₄-Type Framework. Chemistry of Materials, 2011. **23**(1): p. 32-38.

29. Amisse, R., et al., Singular Structural and Electrochemical Properties in Highly Defective LiFePO₄ Powders. Chemistry of Materials, 2015. **27**(12): p. 4261-4273.

30. Chung, S.-Y., et al., Surface-Orientation-Dependent Distribution of Subsurface Cation-Exchange Defects in Olivine-Phosphate Nanocrystals. ACS Nano, 2015. **9**(1): p. 850-859.

31. Schuster, M.E., et al., Charging and Discharging Behavior of Solvothermal LiFePO₄ Cathode Material Investigated by Combined EELS/NEXAFS Study. Chemistry of Materials, 2013. **26**(2): p. 1040-1047.

32. Julien, C.M., A. Mauger, and K. Zaghib, Surface effects on electrochemical properties of nano-sized LiFePO₄. Journal of Materials

Chemistry, 2011. **21**(27): p. 9955-9968.

33. Armstrong, A.R., et al., The lithium intercalation process in the low-voltage lithium battery anode $\text{Li}_{1+x}\text{V}_{1-x}\text{O}_2$. *Nat Mater*, 2011. **10**(3): p. 223-229.

34. Lu, Z., D.D. MacNeil, and J.R. Dahn, Layered Cathode Materials $\text{Li}[\text{Ni}_x\text{Li}(1/3 - 2x/3)\text{Mn}(2/3 - x/3)]\text{O}_2$ for Lithium-Ion Batteries. *Electrochemical and Solid-State Letters*, 2001. **4**(11): p. A191-A194.

35. Yabuuchi, N., et al., Detailed Studies of a High-Capacity Electrode Material for Rechargeable Batteries, $\text{Li}_2\text{MnO}_3\text{-LiCo}_{1/3}\text{Ni}_{1/3}\text{Mn}_{1/3}\text{O}_2$. *Journal of the American Chemical Society*, 2011. **133**(12): p. 4404-4419.

36. Salager, E., et al., Solid-State NMR of the Family of Positive Electrode Materials $\text{Li}_2\text{Ru}_{1-y}\text{Sn}_y\text{O}_3$ for Lithium-Ion Batteries. *Chemistry of Materials*, 2014. **26**(24): p. 7009-7019.

37. Sathiya, M., et al., High Performance $\text{Li}_2\text{Ru}_{1-y}\text{Mn}_y\text{O}_3$ ($0.2 \leq y \leq 0.8$) Cathode Materials for Rechargeable Lithium-Ion Batteries: Their Understanding. *Chemistry of Materials*, 2013. **25**(7): p. 1121-1131.

38. Ma, J., et al., Feasibility of Using Li_2MoO_3 in Constructing Li-Rich High Energy Density Cathode Materials. *Chemistry of Materials*, 2014. **26**(10): p. 3256-3262.

39. Sathiya, M., et al., Origin of voltage decay in high-capacity layered oxide electrodes. *Nat Mater*, 2015. **14**(2): p. 230-238.

40. Sathiya, M., et al., Reversible anionic redox chemistry in high-capacity layered-oxide electrodes. *Nat Mater*, 2013. **12**(9): p. 827-835.
41. Lee, J., et al., Unlocking the Potential of Cation-Disordered Oxides for Rechargeable Lithium Batteries. *Science*, 2014. **343**(6170): p. 519-522.
42. Yoon, M.-S., et al., Synthesis of Li excess LiFePO₄/C using iron chloride extracted from steel scrap pickling. *Metals and Materials International*, 2014. **20**(4): p. 785-791.
43. Huang, W., Q. Cheng, and X. Qin, Effect of Li excess content and Ti dopants on electrochemical properties of LiFePO₄ prepared by thermal reduction method. *Russian Journal of Electrochemistry*, 2010. **46**(3): p. 359-362.
44. Kim, H., et al., Neutron and X-ray Diffraction Study of Pyrophosphate-Based Li_{2-x}MP₂O₇ (M = Fe, Co) for Lithium Rechargeable Battery Electrodes. *Chemistry of Materials*, 2011. **23**(17): p. 3930-3937.
45. Kang, B. and G. Ceder, Battery materials for ultrafast charging and discharging. *Nature*, 2009. **458**(7235): p. 190-193.
46. Zaghbi, K., et al., Unsupported claims of ultrafast charging of LiFePO₄ Li-ion batteries. *Journal of Power Sources*, 2009. **194**(2): p. 1021-1023.
47. Ceder, G. and B. Kang, Response to “unsupported claims of ultrafast charging of Li-ion batteries”. *Journal of Power Sources*, 2009. **194**(2): p.

1024-1028.

48. Cabana, J., et al., MAS NMR Study of the Metastable Solid Solutions Found in the LiFePO₄/FePO₄ System. *Chemistry of Materials*, 2010. **22**(3): p. 1249-1262.

49. Tucker, M.C., et al., Hyperfine Fields at the Li Site in LiFePO₄-Type Olivine Materials for Lithium Rechargeable Batteries: A ⁷Li MAS NMR and SQUID Study. *Journal of the American Chemical Society*, 2002. **124**(15): p. 3832-3833.

50. Upreti, S., et al., Crystal Structure, Physical Properties, and Electrochemistry of Copper Substituted LiFePO₄ Single Crystals. *Chemistry of Materials*, 2011. **24**(1): p. 166-173.

51. Davis, L.J.M., I. Heinmaa, and G.R. Goward, Study of Lithium Dynamics in Monoclinic Li₃Fe₂(PO₄)₃ using ⁶Li VT and 2D Exchange MAS NMR Spectroscopy. *Chemistry of Materials*, 2010. **22**(3): p. 769-775.

52. Hamelet, S., et al., The effects of moderate thermal treatments under air on LiFePO₄-based nano powders. *Journal of Materials Chemistry*, 2009. **19**(23): p. 3979-3991.

53. Omenya, F., et al., Can Vanadium Be Substituted into LiFePO₄? *Chemistry of Materials*, 2011. **23**(21): p. 4733-4740.

54. Armstrong, A.R., et al., Demonstrating Oxygen Loss and Associated Structural Reorganization in the Lithium Battery Cathode

- Li[Ni_{0.2}Li_{0.2}Mn_{0.6}]O₂. Journal of the American Chemical Society, 2006. **128**(26): p. 8694-8698.
55. Morgan, D., A. Van der Ven, and G. Ceder, Li Conductivity in Li_x MPO₄ (M = Mn , Fe , Co , Ni) Olivine Materials. Electrochemical and Solid-State Letters, 2004. **7**(2): p. A30-A32.
56. Kang, K. and G. Ceder, Factors that affect Li mobility in layered lithium transition metal oxides. Physical Review B, 2006. **74**(9): p. 094105.
57. Van der Ven, A. and G. Ceder, Lithium Diffusion in Layered Li_x CoO₂. Electrochemical and Solid-State Letters, 2000. **3**(7): p. 301-304.
58. Dathar, G.K.P., et al., Calculations of Li-Ion Diffusion in Olivine Phosphates. Chemistry of Materials, 2011. **23**(17): p. 4032-4037.
59. Tripathi, R., et al., Alkali-ion Conduction Paths in LiFeSO₄F and NaFeSO₄F Tavorite-Type Cathode Materials. Chemistry of Materials, 2011. **23**(8): p. 2278-2284.
60. Rissouli, K., et al., Electrical conductivity in lithium orthophosphates. Materials Science and Engineering: B, 2003. **98**(3): p. 185-189.
61. Choi, D. and P.N. Kumta, Surfactant based sol-gel approach to nanostructured LiFePO₄ for high rate Li-ion batteries. Journal of Power Sources, 2007. **163**(2): p. 1064-1069.
62. Zhu, C., et al., Electrospinning of Highly Electroactive Carbon-Coated Single-Crystalline LiFePO₄ Nanowires. Angewandte Chemie

International Edition, 2011. **50**(28): p. 6278-6282.

63. Oh, S.W., et al., Double Carbon Coating of LiFePO₄ as High Rate Electrode for Rechargeable Lithium Batteries. *Advanced Materials*, 2010. **22**(43): p. 4842-4845.

64. Lepage, D., et al., A Soft Chemistry Approach to Coating of LiFePO₄ with a Conducting Polymer. *Angewandte Chemie International Edition*, 2011. **50**(30): p. 6884-6887.

65. Malik, R., F. Zhou, and G. Ceder, Kinetics of non-equilibrium lithium incorporation in LiFePO₄. *Nat Mater*, 2011. **10**(8): p. 587-590.

66. Dreyer, W., et al., The thermodynamic origin of hysteresis in insertion batteries. *Nat Mater*, 2010. **9**(5): p. 448-453.

67. Bai, P., D.A. Cogswell, and M.Z. Bazant, Suppression of Phase Separation in LiFePO₄ Nanoparticles During Battery Discharge. *Nano Letters*, 2011. **11**(11): p. 4890-4896.

68. Perdew, J.P., K. Burke, and M. Ernzerhof, Generalized Gradient Approximation Made Simple. *Physical Review Letters*, 1996. **77**(18): p. 3865-3868.

69. Kresse, G. and J. Furthmüller, Efficiency of ab-initio total energy calculations for metals and semiconductors using a plane-wave basis set. *Computational Materials Science*, 1996. **6**(1): p. 15-50.

70. Anisimov, V.I., J. Zaanen, and O.K. Andersen, Band theory and Mott

insulators: Hubbard U instead of Stoner I. Physical Review B, 1991. **44**(3): p. 943-954.

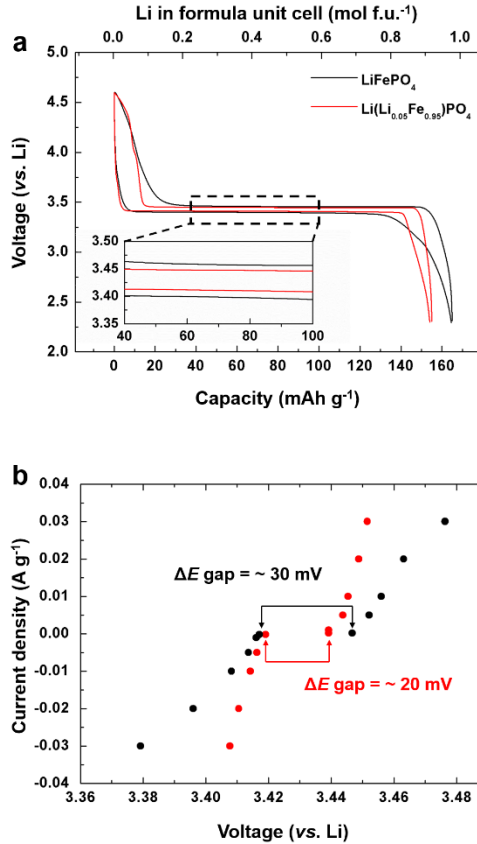


Figure 3-26 Electrochemical properties of lithium-excess and normal LFPS (a) Charge/discharge curves of normal LFP (black) and lithium-excess LFP (red) at a current density 10 mA g^{-1} . Inset figure exhibits magnified charge/discharge curves near plateau region. The lithium-excess LFP shows lower polarization than normal LFP. (b) Hysteresis gap of normal LFP (black) and lithium-excess LFP (red) at various current density. Zero-current hysteresis gap of normal and lithium-excess LFPs are obtained at around 30 mV and 20 mV, respectively.

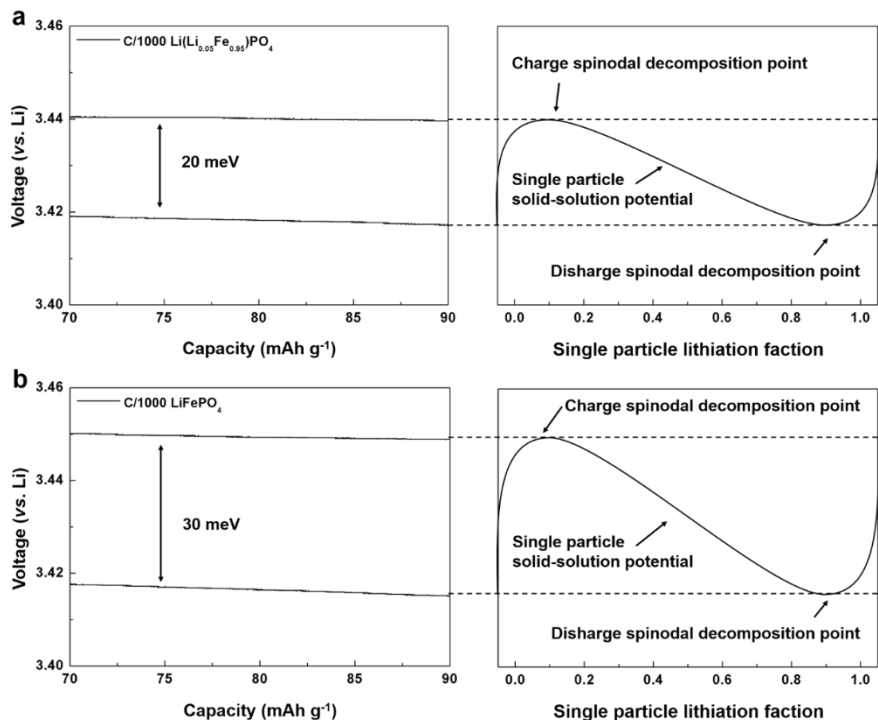


Figure 3-27. Hysteresis gap of electrodes (a) and (b) show the relationship between CC profiles with a C/1000 current density and single particle solid-solution behavior of lithium-excess and normal LFP electrodes, respectively. The voltage gaps between charge and discharge with a near-zero current density is explained by many-body particle models with single particle solid-solution behavior.¹ The highest of del/lithiation spinodal decomposition points (phase transition activation barrier) are strongly related with positive energy penalties induced from coherency/interfacial energies at a moderate particle size. Recently, there is growing evidence that the phase transition barrier could be decreased by nano-sizing, doping and transition metal substitution.

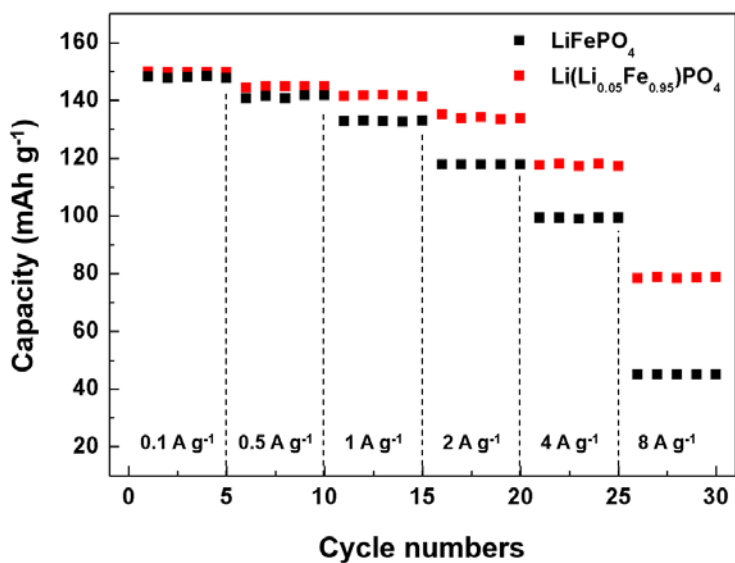


Figure 3-28. Rate capability of lithium-excess LFP (red) and normal LFP (black).

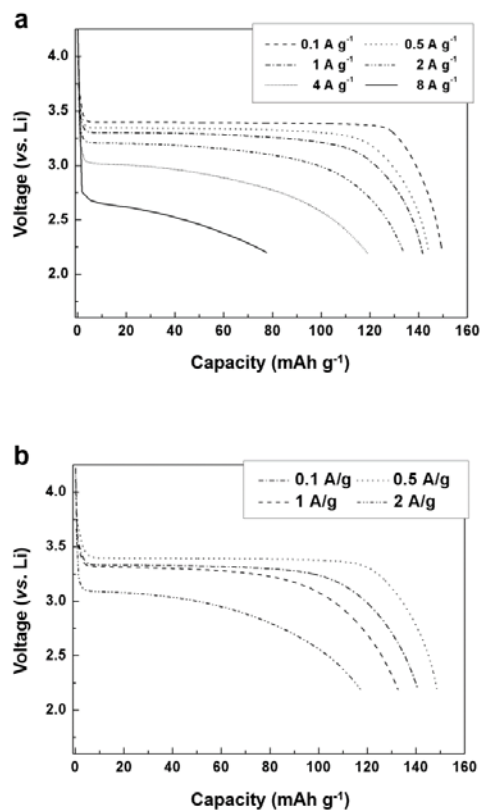


Figure 3-29. Galvanostatic discharge profiles of lithium-excess LFP (a) and normal LFP (b) at various current rates.

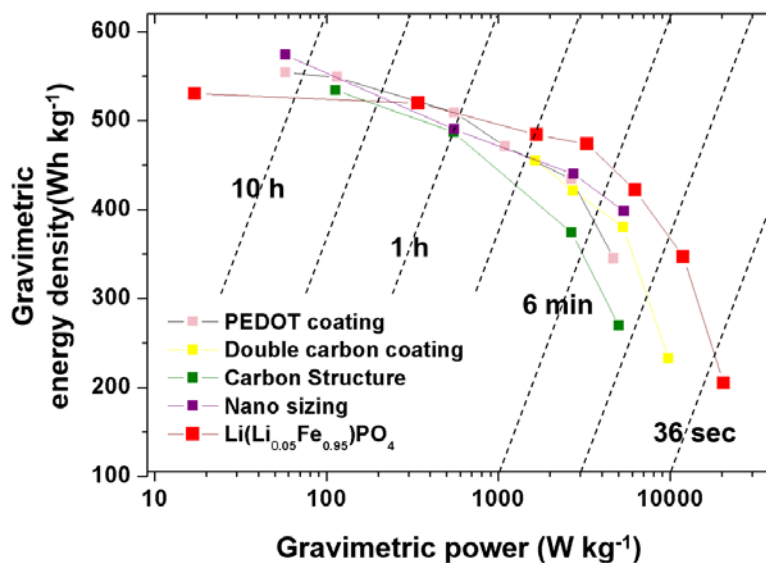


Figure 3-30. Ragone plot of various surface or chemical modified LFPs.

The lithium-excess LFP shows lower gravimetric energy density than other modified LFPs at a low current rate, however, improved energy and power density are exhibited at higher current rates. (refs: Nano-sizing(61), carbon structure(62), double carbon coating(63) and PEDOT coating(64))

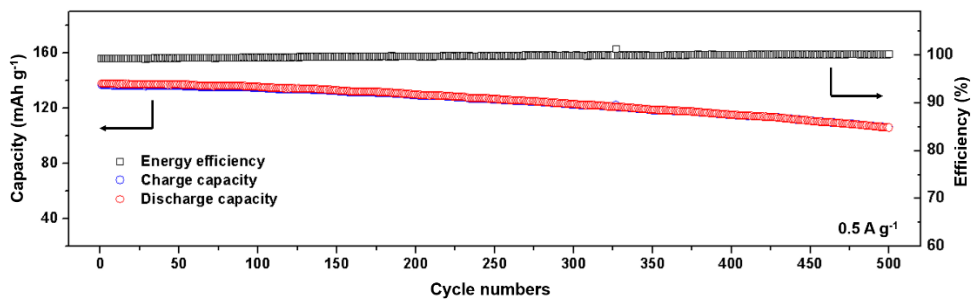


Figure 3-31. Cycle life test of lithium-excess LFP with a current density 0.5 A g^{-1} . (Corresponding with 2.95 C of normal LFP) The capacity after 500 cycles maintained 81.5 % of the initial charge/discharge capacity.

Chapter 4. Thermodynamic and kinetic issues

4.1 Hysteresis gap and Memory effect of LiFePO₄

4.1.1 Experimental section

The LFPs with various compositions were synthesized using Li₂CO₃ (Sigma Aldrich, 99.9%), FeC₂O₄·H₂O (Sigma Aldrich, 99%), (NH₄)₂HPO₄ (Aldrich, 98%). Each precursor was pulverized as fine as possible, separately using high energy ball-milling at Ar atmosphere to avoid the oxidation. The fine precursors were mixed by wet ball milling using acetone more than 24 hours. After drying the mixture, the powder was, again, pulverized as fine as possible using dry ball milling to obtain uniformity and calcinated at 350 °C with 5 ~ 6 °C/min heating rate for 10 hours. The calcinated powders were reground and pelletized under more than 300 bar. The final sintering process was conducted with heating rate as a 5 ~ 6 °C/min rate in Ar atmosphere for 10 hours. An electrode was fabricated by mixing the synthesized powders, pre-mixed with super P (22 wt%) in a ball mill for 24 h, and polyvinylidene fluoride (PVDF, 10 wt%) in N-methyl-2-pyrrolidone (NMP). The mixture was cast on Al foil and dried at 120°C for 2 h. Electrochemical cells were assembled using a CR2016-type coin cell with lithium metal as the counter electrode, a separator (Celgard 2400), and 1 M LiPF₆ in ethyl carbonate/dimethyl carbonate (Panax, EC/DMC, 1:1 v/v) as the electrolyte in

an Ar-filled glove box.

4.1.2 Lowed Spinodal decomposition barrier

The single-particle solid-solution equilibrium model was recently proposed and is now widely accepted for LFP electrode systems.[7, 8, 65, 66] According to the model, the free energy of small-size LFP particles is significantly modified by the interfacial and coherency energy, which comes as a positive energy penalty,[67] leading to the lithium chemical potential profile of LFP single-particles changing from a two-phase- to single-phase-like feature. The collected behavior of single particles in the electrode containing numerous LFP particles is the origin of the thermodynamic hysteresis gap between the charge and discharge.[65, 66] The lower hysteresis gap (~ 20 mV) compared with that of normal LFP (~ 30 mV) that we observed in Figure 3-26 (b) indicates that the lithium-excess LFP is likely to possess a distinct single-particle characteristic. To understand this phenomenon in detail, we investigated the preference toward the single-phase-like behavior changes resulting from the presence of the excess lithium in LFP by calculating the free energy of mixing using DFT methods, as shown in Figure4-1. For reference, the phase mixing energies of normal LFP were taken from the work of the Ceder group in ref 65 (black dots) and plotted together with those of excess-lithium LFP (orange dots) as a function of the

lithium contents. Compared with the minimum mixing free energies of normal LFP at each lithium composition (blue line),^[65] those of the lithium-excess LFP (red line, see Figure4-2 for detailed energy calculations and atomic configurations) lie well below, indicating that the lithium-excess LFP is energetically much closer to the single-phase energy over all the lithium compositions, *i.e.*, it deviates less from the tie-line of the LFP two-phase reaction.^[65] This relation between the energy and lithium contents of Figure4-1 can be roughly converted into a plot with respect to the lithium chemical potential, as presented in Figure4-3. The figure presents a schematic energy profile of a single-particle electrode that undergoes a solid-solution for both cases of lithium-excess (red line) and normal (black line) LFPs. The spinodal energy per lithium to overcome for lithium-excess LFP ($\Delta\mu_{\text{Li-excess LFP}}$) was approximately 6.5 mV according to DFT calculations and ~ 10 mV according to experiments. These values are only two-thirds of those of normal LFP ($\Delta\mu_{\text{LFP}}$, ~ 15 mV),^[65, 66] which implies that the energy to overcome is much less for the single-phase-like reaction in the case of lithium-excess LFP. According to the particle-to-particle intercalation model,^[66] discrete one-by-one filling of many particles occurs, and the energy barrier for the single particle results in the voltage hysteresis between the charge and discharge plateau, as illustrated in Figure4-3. The smaller hysteresis gap in lithium-excess LFP derived from this figure agrees well with the results in Figure 3-27.

It is speculated that the lower phase-transition energy barrier for lithium-excess LFP stems from the defective nature of lithium in the Fe site (Li_{Fe}) that destabilizes the pristine phase and promotes the mixing as a “*phase mixing seed*”. In addition, the reduced lattice misfit between lithium-excess LFP and delithiated lithium-excess LFP as listed in Figure 3-2 (c) is also believed to have affected on reducing the phase transition barrier.[7, 66]

The thermal behavior of partially delithiated phases supports our suggestion of reduced phase mixing energy in the lithium-excess LFP. The thermal phase diagram in Figure4-4 was obtained from temperature-controlled XRD using chemically delithiated lithium-excess phases according to the targeted lithium compositions. (All the *in-situ* XRD patterns are provided in Figure4-5 .) Although previous work by Delacourt *et al.* reported that the partially delithiated normal LFP becomes a solid-solution phase above 350 °C, the complete solid-solution is formed at a 70 °C-lower temperature for the lithium-excess LFP, 280 °C, indicating that the excess-lithium LFP exhibits a stronger tendency for the single-phase reaction with a lower energy barrier for the transition. Moreover, we observed that the partially delithiated lithium-excess LFP forms intermediate phases above 200 °C, similar to the thermal phase behavior of normal LFP. This finding suggests that an intermediate phase with particular lithium ordering is also possible in lithium-

excess LFP. We are conducting a further investigation to verify the lithium orderings and compositions of the intermediate phases.

4.1.3 Less memory effect at new LFP system

Another aspect that we investigated for lithium-excess LFP was how the reduced energy barrier for the transition affects the (i) ‘overshooting’ of voltage during charge/discharge and (ii) the memory effect that has recently been reported for normal LFP.[7] T. Sasaki *et al.* demonstrated that the electrochemical profile of LFP exhibits an anomalous polarization increase depending on the relaxation time and is affected by the history of the cycling.[7] This increase was explained using a particle-by-particle charge/discharge model with non-uniform chemical potentials of LFP single particles after the relaxation.[7] When the LFP electrode stops at certain charge or discharge states, the active LFP particles begin to separate into Li-rich and Li-poor particles. The active particles not reaching the most stable state during relaxation do not show additional polarization, whereas those that have reached this state have to climb up the energy barrier again, inducing higher polarization.[7] We also observed an anomalous polarization increase after relaxation in the galvanostatic intermittent titration technique (GITT) compared with the constant current (CC) measurements for normal LFP, as observed in Figure4-6 (a). Also, consistent with the observation of T. Sasaki

et al., the memory effect is clearly observed for normal LFP after the memory writing cycle (Figure4-6 (b)). However, it was noted that the lithium-excess LFP exhibits a much smaller increase in the polarization after relaxation in the GITT, as observed in Figure4-7 (a), and does not exhibit any detectable memory effect even after we applied the same memory writing cycle as that of the normal LFP electrode, as shown in Figure4-7 (b).

Considering the memory effect model proposed by Sasaki *et al.*, we could infer that the lithium-excess LFP particle has a different relaxation behavior from the normal LFP. To further compare the relaxation behavior and polarization increase of lithium-excess and normal LFP electrodes, we designed an additional experiment of rest-time-dependent partial GITT. Before performing the partial GITT, the open-circuit voltage (OCV) at 50 % state of charge (SOC) was measured during relaxation after charge or discharge with a current rate of 10 mA g⁻¹ as a function of time, as shown in Figure4-8 (a). Although the OCV of normal LFP required more than 100 min to obtain a charge and discharge gap of 30 mV, the OCV gap of lithium-excess LFP was reduced to 10 mV in less than 20 min. This result indicates that the relaxation process occurs much faster for lithium-excess LFP, which is attributed to the higher degree of lithium diffusion in the lithium-excess LFP. For direct comparison, the measurement of the effective lithium diffusivities

and conductivities for the two LFPs was performed as illustrated in Figure4-9 and Figure4-10, indicating that the lithium-excess LFP has one order higher conductive properties than the normal LFP. The difference in the relaxation kinetics affects the behavior of the GITT experiment. Figure4-8 (b) and (c) show the partial GITT profiles of both LFPs during the charge and discharge. The black dotted lines represent the equilibrium voltage of LFP vs. Li/Li^+ . Consistent with the GITT measurement above, the lithium-excess LFP shows considerably lower polarization from the equilibrium potential for both charge and discharge regardless of the duration of the rest time. However, with increasing rest time, the voltage profiles of lithium-excess LFP start to show an overshooting in the charge or discharge. In addition, the overshooting profile becomes more pronounced with additional rest time, as clearly observed in the insets of Figure4-8 (b) and (c). The origin of the overshoot in LFP has not yet been clearly revealed yet, but it is believed that it results from the resistance involved with the Spinodal decomposition or nucleation formation from the pristine and electrochemically activated particles.[7] During the relaxation step, both LFPs would either undergo Spinodal decomposition or relax back to the original state by exchanging lithium among each other or with particles in the Li-poor phase.[7, 66] Since it is reported that the overshoots appears just before the sequential particle-by-particle process occurs and the full relaxation of particles is the triggering

condition of the overshooting, the predominant overshooting is attributed to the faster relaxation kinetics of the lithium-excess LFPs. Nevertheless, the overshoot in lithium-excess LFP is relatively small. It is believed that the energy penalty that the particle needs to climb again would be less for lithium-excess LFP because of the reduced Spinodal decomposition barrier, as indicated in Figure4-3, which would also reduce the overshooting during charge/discharge.

The results of the relaxation time *vs.* polarization experiments give us a hint why the memory effect is not observed in the lithium-excess LFP. Sasaki *et al.* demonstrated that as the rest time increases between the memory writing and memory releasing step, the memory effect is notably reduced because of the sufficient time for homogenization of the lithium chemical potential among LFP particles.[7] This finding implies that how fast the electrode material relaxes to the stable state at zero current will sensitively affect the dominance of the memory effect. Accordingly, we designed an experiment on lithium-excess LFP to impose a shorter interval between the memory writing and releasing cycles. As we systematically decrease the interval from 10 min to 1 min in Figure4-11, the memory effect begins to appear. When the interval time becomes less than 5 min, the signature of the voltage protrusion is observed even though the magnitude is significantly smaller than for normal

LFP under the same condition, indicating that the memory effect is a universal effect in olivine LFPs. However, because the lithium-excess LFP allows much faster lithium kinetics, the homogenization of the lithium chemical potential among particles will also be significantly quicker after the memory writing step. Therefore, within the same interval, the homogenization would be far more efficient for lithium-excess LFP, and the detectable memory effect would not be observed.

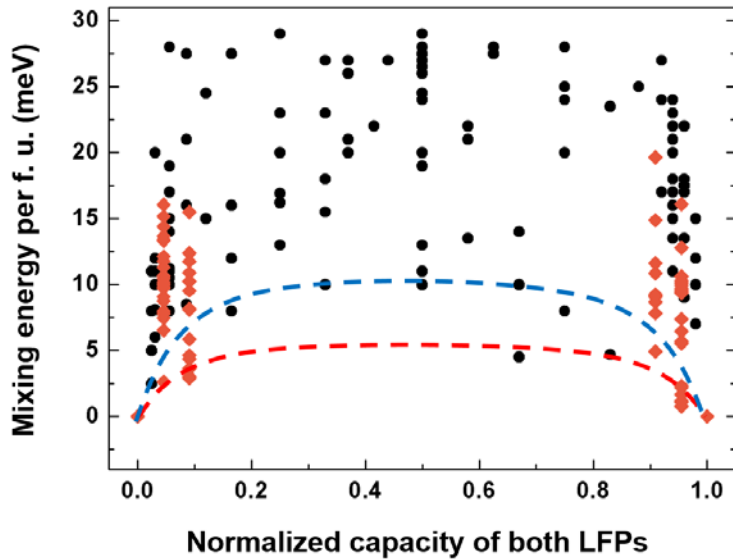


Figure4-1 . Mixing free energy and atomic configuration of lithium-excess LFP (orange) and normal LFP (black, ref 65, copyright 2011, Nature Publishing Group) as a function of lithium contents. Mixing energies of lithium-excess and normal LFP at zero-temperature. Black dots and blue line are taken from the work of Ceder *et al.* [65]. The free energies were calculated by DFT calculation using 245 atoms. The dash line is a predicted curve of whole mixing free energy. (lithium-excess LFP: orange, normal LFP: blue dash line)

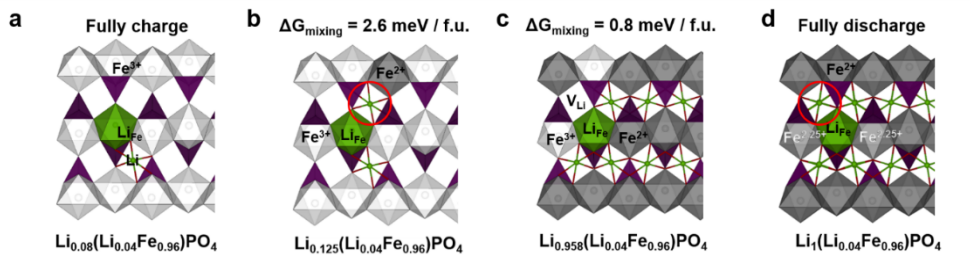


Figure4-2 . Detailed DFT calculation results. It is revealed by DFT calculation that the unique Li-excess atomic configuration has preferred interstitial sites to extract or insert Li ions during Li concentration change. The Figure (a) – (d) show local Li-excess configuration corresponding with the lowest mixing energy at certain Li factions. At the end of charge state, (Figure (a)) Li_{Fe} ion and another Li_{Li} ion remained due to all Fe ions oxidized to 3+ state. And, when an electron is inserted into electrode, the additional Li ion is located at near Li-excess configuration site marked with red circle in Figure (b) with $2.6 \text{ meV f.u.}^{-1}$ mixing energy. Similarly, at the beginning of discharge state, the Li ion marked by red circle in Figure (d) is firstly came out with $0.8 \text{ meV f.u.}^{-1}$ phase mixing energy. (Figure (c)) Although we could not investigate mixing energy for whole Li concentration and precise Li composition of solubility limits due to limitation of DFT calculation, this result elucidates that the lithium-excess LFP has energetic lower alternative diffusional configuration than normal LFP because Li-excess local configuration plays role as a “*phase mixing seed*”.

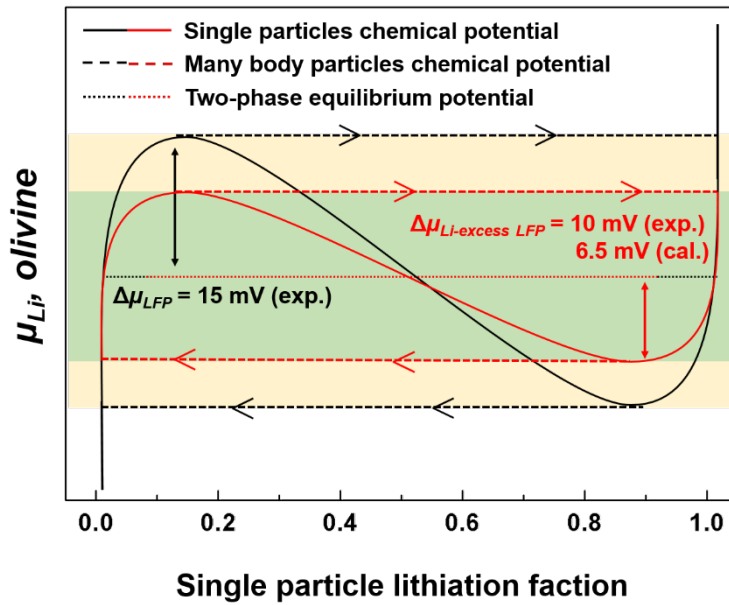


Figure4-3. The single particle chemical potential of normal LFP (black) and lithium-excess LFP (red) as a function of the lithiation fraction. The normal LFP and lithium-excess LFP contain $\sim 15 \text{ mV}$ and $\sim 10 \text{ mV}$ phase transition activation barrier, respectively

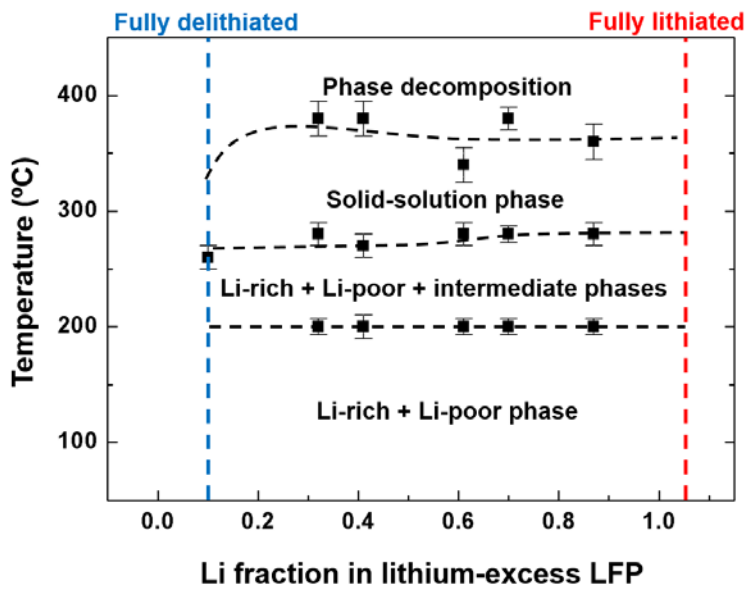
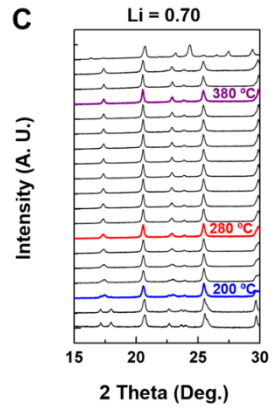
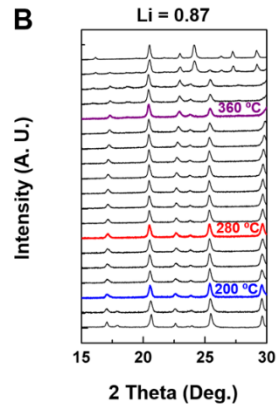
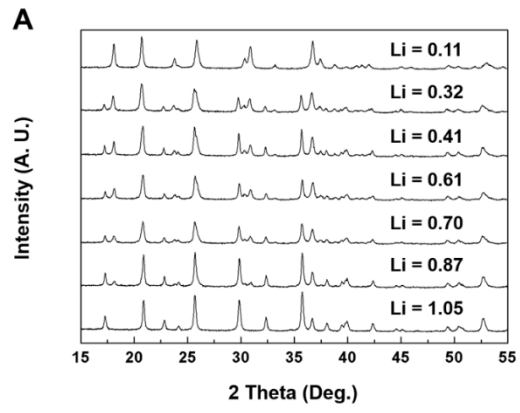


Figure4-4 Thermal phase diagram of lithium-excess LFP



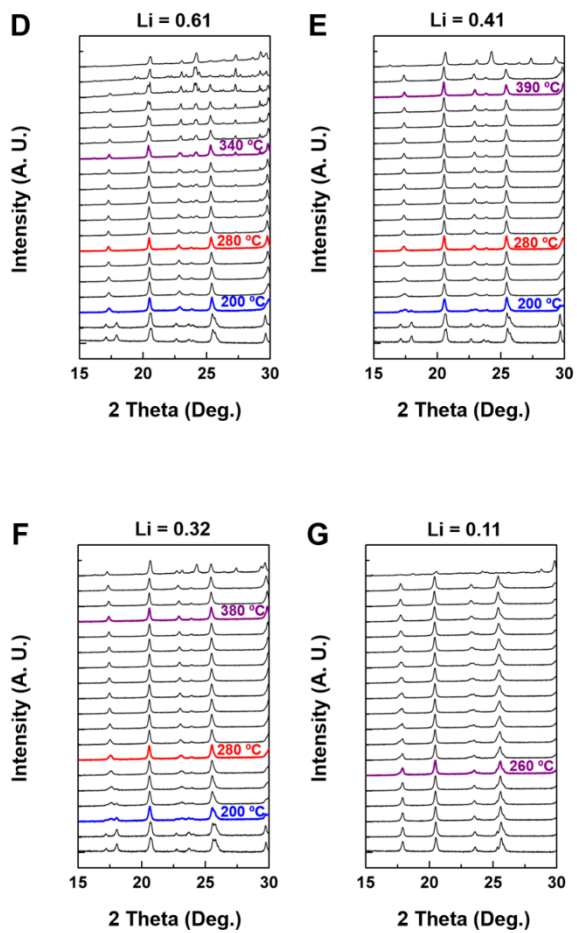


Figure4-5 . Thermal XRD patterns of lithium-excess LFP

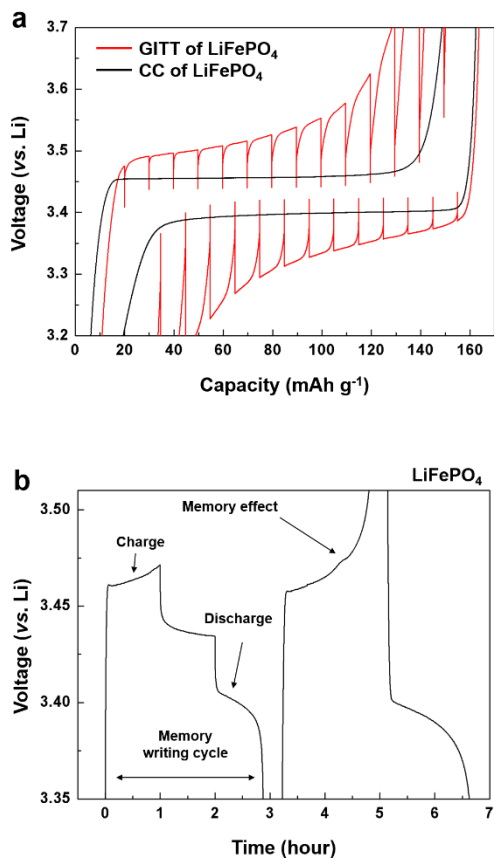


Figure4-6 . Memory effect of normal LFP. Charge and discharge profile in CC (Constant current) and GITT (Galvanostatic intermittent titration technique) modes of (a) normal LFP at a current rate 10 mA g⁻¹. The rest time of GITT is about 20 minutes. (b) show the memory effect test of both LFPs. Memory writing cycles (first cycle) are conducted to SOC 50 % with one hour rest time between charge and discharge. Memory releasing cycles (second cycle) are conducted within 2.5 ~ 4.5 V (vs. Li) with a 80 mA g⁻¹ current rate.

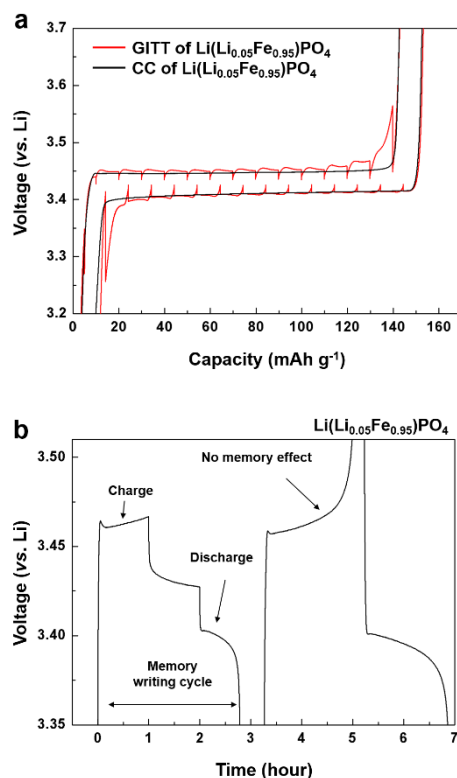


Figure4-7 Memory effect of lithium-excess LFP. Charge and discharge profile in CC (Constant current) and GITT (Galvanostatic intermittent titration technique) modes of (a) excess LFP at a current rate 10 mA g^{-1} . The rest time of GITT is about 20 minutes. (b) show the memory effect test LFPs. Memory writing cycles (first cycle) are conducted to SOC 50 % with one hour rest time between charge and discharge. Memory releasing cycles (second cycle) are conducted within 2.5 ~ 4.5 V (vs. Li) with a 80 mA g^{-1} current rate. The memory effect is not observed in lithium-excess LFP.

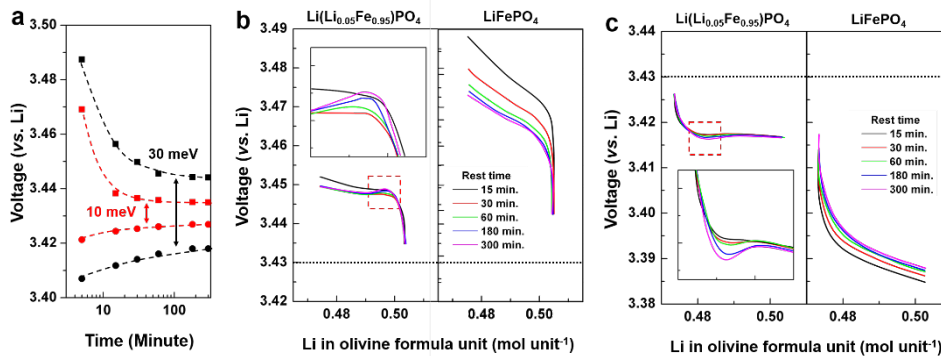


Figure4-8. OCV change of both electrodes. (a) OCV change of lithium-excess and normal LFPs as a function of the rest time. (black: normal LFP and red: lithium-excess LFP) The lithium-excess LFP relaxed faster than normal LFP with reaching 10 mV charge and discharge OCV gap. Partial GITT profile change depending on the rest times at each electrodes during (b) charge and (c) discharge. The each inset figures exhibits the magnified profiles marked by red squares. The black dot line indicates the equilibrium potential of LFP electrode vs. Li/Li^+ .

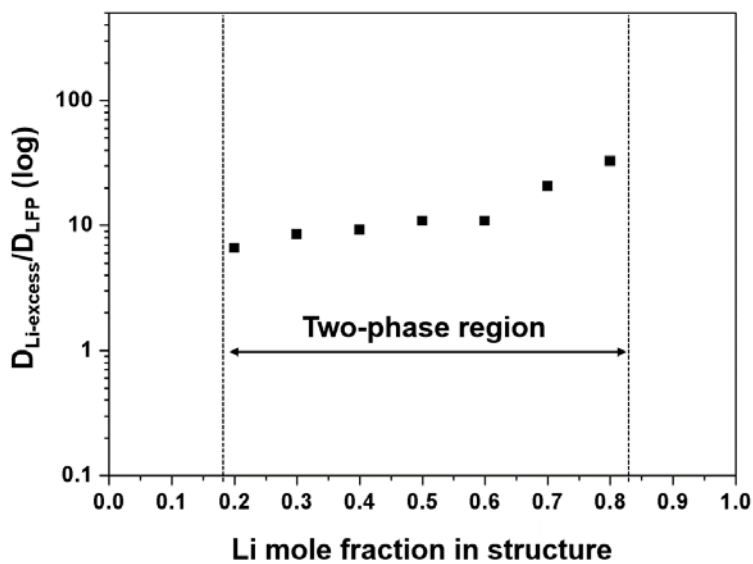
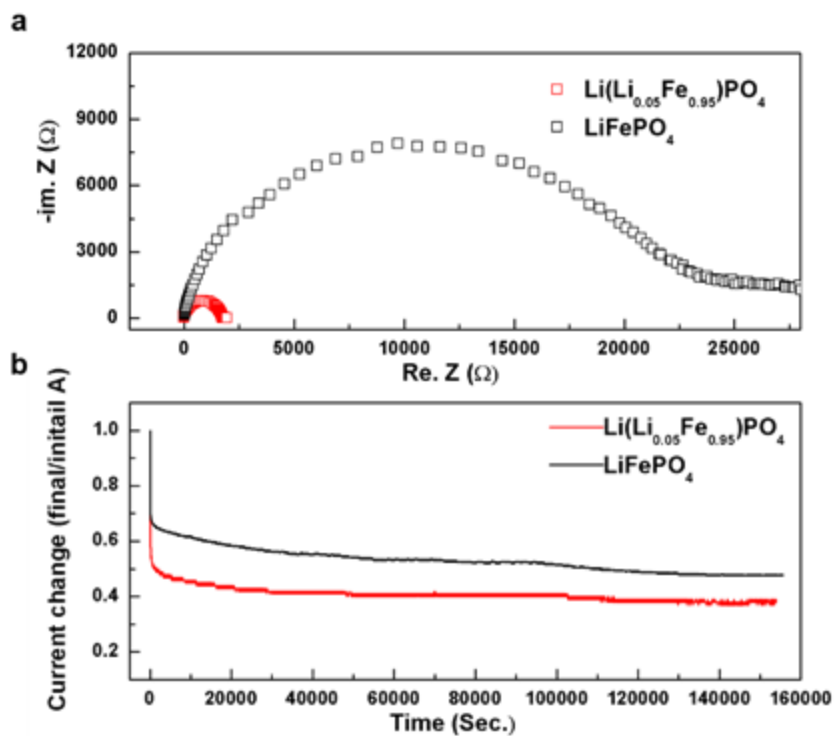


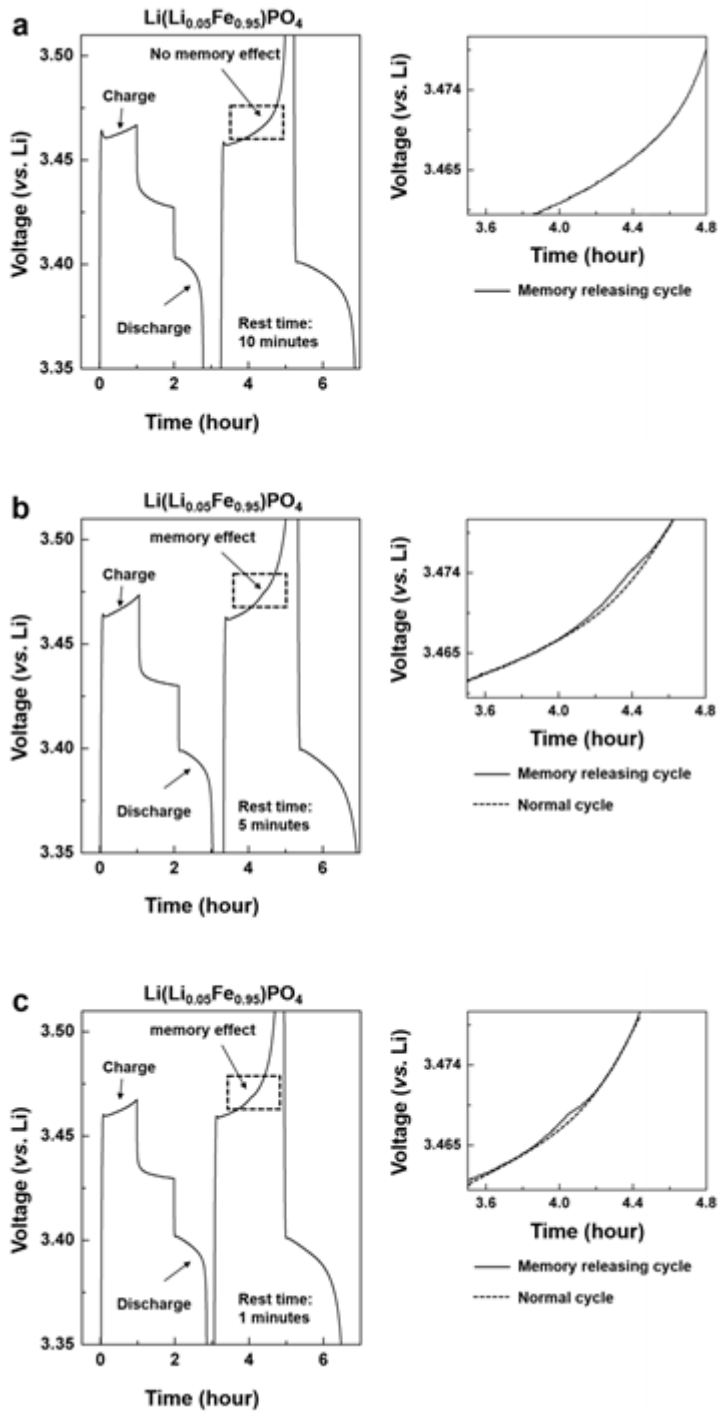
Figure4-9 . The effective diffusivity ratio ($D_{\text{Li-excess}}/D_{\text{LFP}}$) calculated from GITT results with in two-phase reaction region.⁵ The lithium-excess LFP shows statically 10 times higher diffusivity than normal LFP.



c

	σ (S cm ⁻¹)			Carbon (wt %)	Temp. (C°)	Ref.
	Total Con.	Ionic Con.	Elec. Con.			
Normal LFP	2.31×10^{-6}	1.27×10^{-6}	1.04×10^{-6}	2.5 (1)	20	-
Lithium-excess LFP	2.64×10^{-5}	1.63×10^{-5}	1.01×10^{-5}	2.9 (1)	20	-
Normal LFP	-	3.20×10^{-6}	2.00×10^{-10}	-	RT	6
Normal LFP	2.7×10^{-9}	$\sim 10^{-7-8}$	$\sim 10^{-9}$	-	25	7

Figure4-10 . Conductivity measurement (a) EIS measurement results of lithium-excess and normal LFPs. The powders are pelleted under 400 bar as disk shape with ~ 1 mm thickness and sintered at 500 °C for 5 hours in Ar atmosphere. The symmetric cells are assembled with Ag/sample/Ag configuration for measuring total conductivities. The EIS measurements are conducted with 3 MHz ~ 0.1 Hz at room temperature (20 °C). (b) Current change tendency under constant voltage applied (1 V). The currents are saturated over ~ 40 hours, and the electronic conductivity portions are confirmed by ~ 0.4 and 0.53 for lithium-excess and normal LFPs, respectively. The table (c) shows total, ionic, electronic conductivity at 20 °C and residual carbon ratio of normal, lithium-excess LFPs and previous reports. The ionic and electronic conductivities of lithium-excess LFP shows ~ 13 times and 10 times better than normal LFP respectively, and it is consistent with diffusivity measurement at S Fig. 19. The ionic conductivity of normal LFP powder is well matched with previous reports, the electronic conductivities of both powders show much higher ($\sim 10^{-5} \sim -6$) than previous reports ($\sim 10^{-9}$).^{6,7} As shown in Table (c), lithium-excess and normal LFPs contains 2 ~ 3 wt % residual carbon. We conjectured that these residual carbon are produced from carbon containing precursors, such as Li_2CO_3 and $\text{FeC}_2\text{O}_4 \cdot \text{H}_2\text{O}$, and higher electronic conductivities are came from residual carbon.



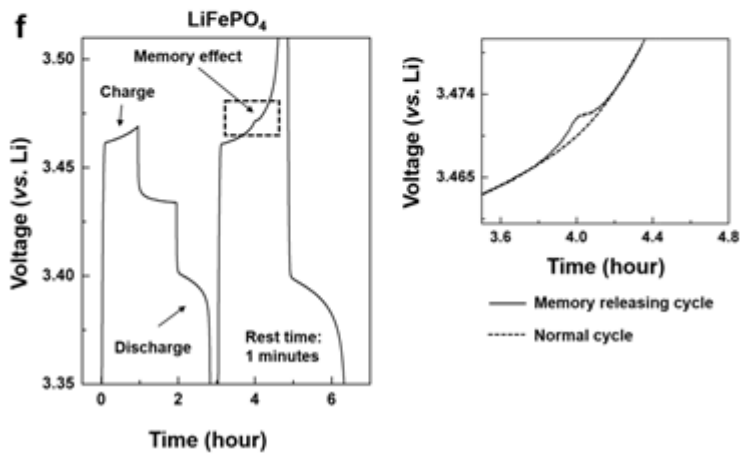
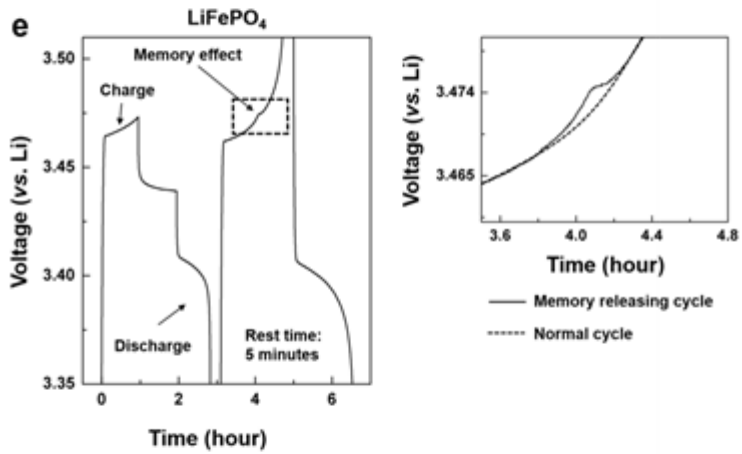
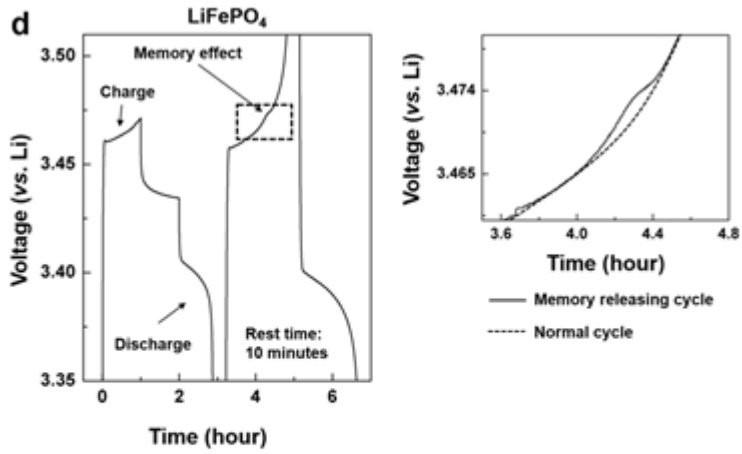


Figure4-11 . Confirmation on memory effect depending on rest time between memory writing (first half charge/discharge) cycle and memory releasing (second full charge/discharge) cycle. The all experiments are conducted with a 80 mA g^{-1} current density and $2.5 \sim 4.5 \text{ V (vs. Li)}$ voltage windows. (a)10 minutes rest time, (b) 5 minutes rest time and (c) 1minute rest time for lithium-excess LFP. (d)10 minutes rest time, (e) 5 minutes rest time and (f) 1minute rest time for normal LFP. The memory effect is reinforced with decreasing rest time between first cycle and second cycle at both LFPs. However, the degree of overshooting of lithium-excess LFP is remarkably lower than counterpart normal LFP electrode, and the overshooting (memory effect) has completely disappeared with more than 10 minutes rest time. We infer that the fast kinetic of lithium-excess configuration makes active particles fast reunion in the relaxation state (rest state), resulting in erasing memory effect as shown in (a). Also, the relatively low phase transition activation energy of lithium-excess LFP could affect on lowering degree of overshooting compared with normal LFP as show in (b) and (c).

4.2 Conclusion

In summary, we show that (i) lowers the spinodal decomposition point and (ii) significantly weakens the memory effect at lithium-excess LFP. We believe that unlocking the restrictive lithium ion diffusion in the olivine electrode is expected to affect other intrinsic thermodynamic and kinetic properties of olivine LFPs, such as the phase boundary configuration, intermediate phase, and relaxation behavior, which requires further investigation. Notably, all of these physical changes in olivine cathodes originate from only a small change in the Li/Fe compositions. Our results suggest that a simple excess ionic carrier concept in the electrode crystal not only enhances the power capability but also brings up unexpected properties for the pristine crystal and offers a novel interesting approach to tune solid-state ionic conductors.

4.3 References

1. Armand, M. and J.M. Tarascon, Building better batteries. *Nature*, 2008. **451**(7179): p. 652-657.
2. Vineyard, G.H. and G.J. Dienes, The Theory of Defect Concentration in Crystals. *Physical Review*, 1954. **93**(2): p. 265-268.
3. Islam, M.S., et al., Atomic-Scale Investigation of Defects, Dopants, and Lithium Transport in the LiFePO₄ Olivine-Type Battery Material. *Chemistry of Materials*, 2005. **17**(20): p. 5085-5092.
4. Wang, J., et al., Size-dependent surface phase change of lithium iron phosphate during carbon coating. *Nat Commun*, 2014. **5**.
5. Chen, J. and J. Graetz, Study of Antisite Defects in Hydrothermally Prepared LiFePO₄ by in Situ X-ray Diffraction. *ACS Applied Materials & Interfaces*, 2011. **3**(5): p. 1380-1384.
6. Delmas, C., et al., On the behavior of the Li_xNiO₂ system: an electrochemical and structural overview. *Journal of Power Sources*, 1997. **68**(1): p. 120-125.
7. Sasaki, T., Y. Ukyo, and P. Novák, Memory effect in a lithium-ion battery. *Nat Mater*, 2013. **12**(6): p. 569-575.
8. Li, Y., et al., Current-induced transition from particle-by-particle to concurrent intercalation in phase-separating battery electrodes. *Nat Mater*,

2014. **13**(12): p. 1149-1156.

9. Gibot, P., et al., Room-temperature single-phase Li insertion/extraction in nanoscale Li_xFePO_4 . *Nat Mater*, 2008. **7**(9): p. 741-747.

10. Delmas, C., et al., Lithium deintercalation in LiFePO_4 nanoparticles via a domino-cascade model. *Nat Mater*, 2008. **7**(8): p. 665-671.

11. Bai, P. and M.Z. Bazant, Charge transfer kinetics at the solid–solid interface in porous electrodes. *Nat Commun*, 2014. **5**.

12. Delacourt, C., et al., The existence of a temperature-driven solid solution in Li_xFePO_4 for $0 < x < 1$. *Nat Mater*, 2005. **4**(3): p. 254-260.

13. Padhi, A.K., K.S. Nanjundaswamy, and J.B. Goodenough, Phospho-olivines as Positive-Electrode Materials for Rechargeable Lithium Batteries. *Journal of The Electrochemical Society*, 1997. **144**(4): p. 1188-1194.

14. Nishijima, M., et al., Accelerated discovery of cathode materials with prolonged cycle life for lithium-ion battery. *Nat Commun*, 2014. **5**.

15. Yamada, A., S.C. Chung, and K. Hinokuma Optimized LiFePO_4 for Lithium Battery Cathodes. *Journal of The Electrochemical Society*, 2001. **148**(3): p. A224-A229.

16. Nishimura, S.-i., et al., Experimental visualization of lithium diffusion in Li_xFePO_4 . *Nat Mater*, 2008. **7**(9): p. 707-711.

17. Malik, R., et al., Particle Size Dependence of the Ionic Diffusivity.

Nano Letters, 2010. **10**(10): p. 4123-4127.

18. Tealdi, C., C. Spreatico, and P. Mustarelli, Lithium diffusion in $\text{Li}_{1-x}\text{FePO}_4$: the effect of cationic disorder. *Journal of Materials Chemistry*, 2012. **22**(47): p. 24870-24876.

19. Chung, S.-Y., et al., Atomic-Scale Visualization of Antisite Defects in LiFePO_4 . *Physical Review Letters*, 2008. **100**(12): p. 125502.

20. Chen, J., et al., The hydrothermal synthesis and characterization of olivines and related compounds for electrochemical applications. *Solid State Ionics*, 2008. **178**(31–32): p. 1676-1693.

21. Yang, S., P.Y. Zavalij, and M. Stanley Whittingham, Hydrothermal synthesis of lithium iron phosphate cathodes. *Electrochemistry Communications*, 2001. **3**(9): p. 505-508.

22. Chen, J. and M.S. Whittingham, Hydrothermal synthesis of lithium iron phosphate. *Electrochemistry Communications*, 2006. **8**(5): p. 855-858.

23. Park, K.-Y., et al., Anti-Site Reordering in LiFePO_4 : Defect Annihilation on Charge Carrier Injection. *Chemistry of Materials*, 2014. **26**(18): p. 5345-5351.

24. Radhamani, A.V., et al., Suppression of antisite defects in fluorine-doped LiFePO_4 . *Scripta Materialia*, 2013. **69**(1): p. 96-99.

25. Yuan, S. and K. Dai, Heat-rate-controlled hydrothermal synthesis of LiFePO_4 achieved by different heating sources. *Russian Journal of*

Electrochemistry, 2014. **50**(4): p. 385-389.

26. Hoang, K. and M. Johannes, Tailoring Native Defects in LiFePO₄: Insights from First-Principles Calculations. Chemistry of Materials, 2011. **23**(11): p. 3003-3013.

27. Amisse, R., et al., Nonstoichiometry in LiFe_{0.5}Mn_{0.5}PO₄: Structural and Electrochemical Properties. Journal of The Electrochemical Society, 2013. **160**(9): p. A1446-A1450.

28. Hamelet, S., et al., Existence of Superstructures Due to Large Amounts of Fe Vacancies in the LiFePO₄-Type Framework. Chemistry of Materials, 2011. **23**(1): p. 32-38.

29. Amisse, R., et al., Singular Structural and Electrochemical Properties in Highly Defective LiFePO₄ Powders. Chemistry of Materials, 2015. **27**(12): p. 4261-4273.

30. Chung, S.-Y., et al., Surface-Orientation-Dependent Distribution of Subsurface Cation-Exchange Defects in Olivine-Phosphate Nanocrystals. ACS Nano, 2015. **9**(1): p. 850-859.

31. Schuster, M.E., et al., Charging and Discharging Behavior of Solvothermal LiFePO₄ Cathode Material Investigated by Combined EELS/NEXAFS Study. Chemistry of Materials, 2013. **26**(2): p. 1040-1047.

32. Julien, C.M., A. Mauger, and K. Zaghib, Surface effects on electrochemical properties of nano-sized LiFePO₄. Journal of Materials

Chemistry, 2011. **21**(27): p. 9955-9968.

33. Armstrong, A.R., et al., The lithium intercalation process in the low-voltage lithium battery anode $\text{Li}_{1+x}\text{V}_{1-x}\text{O}_2$. *Nat Mater*, 2011. **10**(3): p. 223-229.

34. Lu, Z., D.D. MacNeil, and J.R. Dahn, Layered Cathode Materials $\text{Li}[\text{Ni}_x\text{Li}(1/3 - 2x/3)\text{Mn}(2/3 - x/3)]\text{O}_2$ for Lithium-Ion Batteries. *Electrochemical and Solid-State Letters*, 2001. **4**(11): p. A191-A194.

35. Yabuuchi, N., et al., Detailed Studies of a High-Capacity Electrode Material for Rechargeable Batteries, $\text{Li}_2\text{MnO}_3\text{-LiCo}_{1/3}\text{Ni}_{1/3}\text{Mn}_{1/3}\text{O}_2$. *Journal of the American Chemical Society*, 2011. **133**(12): p. 4404-4419.

36. Salager, E., et al., Solid-State NMR of the Family of Positive Electrode Materials $\text{Li}_2\text{Ru}_{1-y}\text{Sn}_y\text{O}_3$ for Lithium-Ion Batteries. *Chemistry of Materials*, 2014. **26**(24): p. 7009-7019.

37. Sathiya, M., et al., High Performance $\text{Li}_2\text{Ru}_{1-y}\text{Mn}_y\text{O}_3$ ($0.2 \leq y \leq 0.8$) Cathode Materials for Rechargeable Lithium-Ion Batteries: Their Understanding. *Chemistry of Materials*, 2013. **25**(7): p. 1121-1131.

38. Ma, J., et al., Feasibility of Using Li_2MoO_3 in Constructing Li-Rich High Energy Density Cathode Materials. *Chemistry of Materials*, 2014. **26**(10): p. 3256-3262.

39. Sathiya, M., et al., Origin of voltage decay in high-capacity layered oxide electrodes. *Nat Mater*, 2015. **14**(2): p. 230-238.

40. Sathiya, M., et al., Reversible anionic redox chemistry in high-capacity layered-oxide electrodes. *Nat Mater*, 2013. **12**(9): p. 827-835.
41. Lee, J., et al., Unlocking the Potential of Cation-Disordered Oxides for Rechargeable Lithium Batteries. *Science*, 2014. **343**(6170): p. 519-522.
42. Yoon, M.-S., et al., Synthesis of Li excess LiFePO₄/C using iron chloride extracted from steel scrap pickling. *Metals and Materials International*, 2014. **20**(4): p. 785-791.
43. Huang, W., Q. Cheng, and X. Qin, Effect of Li excess content and Ti dopants on electrochemical properties of LiFePO₄ prepared by thermal reduction method. *Russian Journal of Electrochemistry*, 2010. **46**(3): p. 359-362.
44. Kim, H., et al., Neutron and X-ray Diffraction Study of Pyrophosphate-Based Li_{2-x}MP₂O₇ (M = Fe, Co) for Lithium Rechargeable Battery Electrodes. *Chemistry of Materials*, 2011. **23**(17): p. 3930-3937.
45. Kang, B. and G. Ceder, Battery materials for ultrafast charging and discharging. *Nature*, 2009. **458**(7235): p. 190-193.
46. Zaghbi, K., et al., Unsupported claims of ultrafast charging of LiFePO₄ Li-ion batteries. *Journal of Power Sources*, 2009. **194**(2): p. 1021-1023.
47. Ceder, G. and B. Kang, Response to “unsupported claims of ultrafast charging of Li-ion batteries”. *Journal of Power Sources*, 2009. **194**(2): p.

1024-1028.

48. Cabana, J., et al., MAS NMR Study of the Metastable Solid Solutions Found in the LiFePO₄/FePO₄ System. *Chemistry of Materials*, 2010. **22**(3): p. 1249-1262.

49. Tucker, M.C., et al., Hyperfine Fields at the Li Site in LiFePO₄-Type Olivine Materials for Lithium Rechargeable Batteries: A ⁷Li MAS NMR and SQUID Study. *Journal of the American Chemical Society*, 2002. **124**(15): p. 3832-3833.

50. Upreti, S., et al., Crystal Structure, Physical Properties, and Electrochemistry of Copper Substituted LiFePO₄ Single Crystals. *Chemistry of Materials*, 2011. **24**(1): p. 166-173.

51. Davis, L.J.M., I. Heinmaa, and G.R. Goward, Study of Lithium Dynamics in Monoclinic Li₃Fe₂(PO₄)₃ using ⁶Li VT and 2D Exchange MAS NMR Spectroscopy. *Chemistry of Materials*, 2010. **22**(3): p. 769-775.

52. Hamelet, S., et al., The effects of moderate thermal treatments under air on LiFePO₄-based nano powders. *Journal of Materials Chemistry*, 2009. **19**(23): p. 3979-3991.

53. Omenya, F., et al., Can Vanadium Be Substituted into LiFePO₄? *Chemistry of Materials*, 2011. **23**(21): p. 4733-4740.

54. Armstrong, A.R., et al., Demonstrating Oxygen Loss and Associated Structural Reorganization in the Lithium Battery Cathode

Li[Ni_{0.2}Li_{0.2}Mn_{0.6}]O₂. Journal of the American Chemical Society, 2006. **128**(26): p. 8694-8698.

55. Morgan, D., A. Van der Ven, and G. Ceder, Li Conductivity in Li_x MPO₄ (M = Mn , Fe , Co , Ni) Olivine Materials. Electrochemical and Solid-State Letters, 2004. **7**(2): p. A30-A32.

56. Kang, K. and G. Ceder, Factors that affect Li mobility in layered lithium transition metal oxides. Physical Review B, 2006. **74**(9): p. 094105.

57. Van der Ven, A. and G. Ceder, Lithium Diffusion in Layered Li_x CoO₂. Electrochemical and Solid-State Letters, 2000. **3**(7): p. 301-304.

58. Dathar, G.K.P., et al., Calculations of Li-Ion Diffusion in Olivine Phosphates. Chemistry of Materials, 2011. **23**(17): p. 4032-4037.

59. Tripathi, R., et al., Alkali-ion Conduction Paths in LiFeSO₄F and NaFeSO₄F Tavorite-Type Cathode Materials. Chemistry of Materials, 2011. **23**(8): p. 2278-2284.

60. Rissouli, K., et al., Electrical conductivity in lithium orthophosphates. Materials Science and Engineering: B, 2003. **98**(3): p. 185-189.

61. Choi, D. and P.N. Kumta, Surfactant based sol-gel approach to nanostructured LiFePO₄ for high rate Li-ion batteries. Journal of Power Sources, 2007. **163**(2): p. 1064-1069.

62. Zhu, C., et al., Electrospinning of Highly Electroactive Carbon-Coated Single-Crystalline LiFePO₄ Nanowires. Angewandte Chemie

International Edition, 2011. **50**(28): p. 6278-6282.

63. Oh, S.W., et al., Double Carbon Coating of LiFePO₄ as High Rate Electrode for Rechargeable Lithium Batteries. *Advanced Materials*, 2010. **22**(43): p. 4842-4845.

64. Lepage, D., et al., A Soft Chemistry Approach to Coating of LiFePO₄ with a Conducting Polymer. *Angewandte Chemie International Edition*, 2011. **50**(30): p. 6884-6887.

65. Malik, R., F. Zhou, and G. Ceder, Kinetics of non-equilibrium lithium incorporation in LiFePO₄. *Nat Mater*, 2011. **10**(8): p. 587-590.

66. Dreyer, W., et al., The thermodynamic origin of hysteresis in insertion batteries. *Nat Mater*, 2010. **9**(5): p. 448-453.

67. Bai, P., D.A. Cogswell, and M.Z. Bazant, Suppression of Phase Separation in LiFePO₄ Nanoparticles During Battery Discharge. *Nano Letters*, 2011. **11**(11): p. 4890-4896.

68. Perdew, J.P., K. Burke, and M. Ernzerhof, Generalized Gradient Approximation Made Simple. *Physical Review Letters*, 1996. **77**(18): p. 3865-3868.

69. Kresse, G. and J. Furthmüller, Efficiency of ab-initio total energy calculations for metals and semiconductors using a plane-wave basis set. *Computational Materials Science*, 1996. **6**(1): p. 15-50.

70. Anisimov, V.I., J. Zaanen, and O.K. Andersen, Band theory and Mott

insulators: Hubbard U instead of Stoner I. Physical Review B, 1991. **44**(3): p. 943-954.

Chapter 5. Summary

Lithium iron phosphate (LFP) has attracted tremendous attention as an electrode material for next-generation lithium rechargeable battery systems due to the use of low-cost iron, long cycle-life and its chemical/electrochemical stability. While the lithium diffusion in LFP, the essential property during battery operation, is relatively fast due to the one-dimensional tunnel present in the olivine crystal structure, the tunnel is inherently vulnerable to immobile anti-site defects which, if any, block the lithium diffusion and lead to the inferior performance. Herein, we demonstrate that the kinetic issue arising from the defects in LFP can be completely eliminated in lithium-excess olivine LFP, which we successfully synthesized for the first time. The presence of excess amount of lithium in the olivine structure reduces the concentration of defects in the tunnel by ~ 7 orders of magnitude. Moreover, it opens up a new lithium diffusion path along the [101] direction making the olivine LFP as a three-dimensional lithium diffuser. We also observe that the intrinsic energy barrier for phase transition is notably reduced in the lithium-excess olivine LFP. The fundamentally different nature of lithium-excess olivine LFP compared with normal LFP additionally induces a faster charging capability, reducing the thermal solid-solution temperature and resulting in a significantly less memory effect. The

excess ionic carrier concept in the electrode crystal brings up unexpected properties for the pristine crystal and offers a novel and interesting approach to enhance the diffusivity by opening up additional diffusion paths in solid-state ionic conductors.

Chapter 6. Abstract in Korean

현재 인류는 화석 연료의 고갈, 산업화에 따른 CO₂ 배출, 지구온난화와 같은 환경 문제에 직면하고 있다. 이 문제를 해결하고자, 기존의 화석 연료를 이용한 에너지 생산 및 이용에서 벗어난 친환경 에너지 생산 기술인 풍력, 수력, 태양열 발전 기술이 주목을 받고 있다. 그러나, 상위 친환경 에너지 발전 기술들은 공간적 혹은 시간적 제약이 존재하며, 간헐적인 발전을 하기 때문에 에너지 수요와 공급이 일치하지 못하는 문제를 가진다. 이 문제를 해결하고자 친환경 발전 기술을 보조할 수 있는 대형 에너지 저장 기술이 각광을 받고 있다. 다양한 에너지 저장 기술 중 리튬 이차전지 기술은 높은 에너지 밀도, 장수명성, 높은 효율성으로 친환경 발전 기술을 보조할 대형 에너지 저장 기술로 큰 주목을 받고 있다.

리튬 이차전지 기술에 사용되는 전극 물질은 대부분 intercalation 반응으로 충전과 방전 반응이 행해지며, 충전 중에는 구조 내에서 전자와 리튬 이온이 결정 구조 외로 탈리, 방전 중에는 결정 구조 내로 전자와 리튬 이온이 삽입이 되는 반응을 한다. 그렇기 때문에 전극 물질의 전기화학 특성은 결정 구조와 화학적 조성에

의해서 결정이 된다. 다양한 전극 물질 중 올리빈계 리튬 인산화 철 양극 물질은 높은 열적 안정성, 장 수명성, 낮은 가격으로 인하여 대형 에너지 저장 기술에 사용 적합한 물질로 주목을 받고 있다. 이론적으로 이 물질은 약 580 Wh Kg^{-1} (용량: 169 mAh g^{-1} , 전압: 3.42 V vs. Li)의 에너지 밀도를 가지고 있으며, 결정 구조에 기인하는 1차원 리튬 이온 확산 경로를 가지고 있다. 그러나, 이러한 결정학적 한계에 의해서 합성 시에 생성이 되는 양이온 자리 교환 결함에 굉장히 취약한 특징을 가진다. 충전과 방전과정에서 움직이지 않는다고 알려진 이 양이온 자리 교환 결함은 리튬 확산 경로에 존재하고 있으며, 통계적으로 약 1%의 자리 교환 결함은 1 마이크로 크기의 상위 전극 물질의 용량을 절반 가량 내놓지 못하게 하며, 리튬 이온의 전도도를 2~3승 이상 저하시키는 것으로 보고되었다.

본 연구는 리튬 이차전지용 양극 소재인 리튬 인산화 철 물질의 양이온 자리 결함의 문제를 해결하고자 진행이 되었으며, 2장에서는 전기화학반응을 이용한 양이온 자리 결함을 제거 하는 방법에 관하여 논한다. 공극이 더해진 결정 구조에서는 양이온 자리 결함이 원래의 자리를 되돌아 갈 수 있는 경로를 제공해

주게 되며, 전자를 삽입하는 과정에서 상위 물질의 양이온 자리 결함이 원래의 결정학적 자리를 찾아가게 되는 효과를 가진다.

3장에서는 상위 양극 물질을 리튬 과량으로 합성하여서 이 문제를 해결하는 방법을 소개한다. 리튬 과량으로 합성된 상위 물질은 결정 구조 내부의 철 이온 자리를 부분적으로 차지 하고 있음을 다양한 결정 분석 방법으로 확인을 하였으며, 전이 금속 산화수 변화로 인해 양이온 자리 교환 결함이 극적으로 사라지게 되는 것을 확인하였다. 뿐만 아니라, 과량 Li 이온은 새로운 확산 경로를 제공하게 되어서 더 이상 1차원 확산이 아닌 3차원 확산을 가능케 한다. 때문에, 기존 물질보다 2배 이상 높은 출력 특성을 보이며 장수명성 또한 뛰어난 것을 확인하였다. 또한, 최근 이슈가 되고 있는 LFP 양극 물질의 열역학적 Spinodal 분해 에너지가 기존보다 낮아지는 것을 확인 하였으며, 이 현상을 ‘*phase mixing seed*’라는 새로운 모델을 제시해 설명을 한다.



저작자표시-비영리-변경금지 2.0 대한민국

이용자는 아래의 조건을 따르는 경우에 한하여 자유롭게

- 이 저작물을 복제, 배포, 전송, 전시, 공연 및 방송할 수 있습니다.

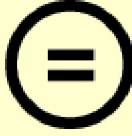
다음과 같은 조건을 따라야 합니다:



저작자표시. 귀하는 원저작자를 표시하여야 합니다.



비영리. 귀하는 이 저작물을 영리 목적으로 이용할 수 없습니다.



변경금지. 귀하는 이 저작물을 개작, 변형 또는 가공할 수 없습니다.

- 귀하는, 이 저작물의 재이용이나 배포의 경우, 이 저작물에 적용된 이용허락조건을 명확하게 나타내어야 합니다.
- 저작권자로부터 별도의 허가를 받으면 이러한 조건들은 적용되지 않습니다.

저작권법에 따른 이용자의 권리는 위의 내용에 의하여 영향을 받지 않습니다.

이것은 [이용허락규약\(Legal Code\)](#)을 이해하기 쉽게 요약한 것입니다.

[Disclaimer](#)

공학박사 학위논문

고성능 리튬이차전지용 올리빈계
양극소재에 관한 연구

Tailoring olivine cathode electrode materials
for high performance lithium secondary battery

2016 년 02 월

서울대학교 대학원

재료공학부

박 규 영

Abstract

Tailoring olivine cathode electrode materials for high performance lithium secondary battery

Kyu-Young Park

Department of Materials Science and Engineering

College of Engineering

Seoul National University

Lithium iron phosphate (LFP) has attracted much attention as a cathode electrode material for next-generation lithium rechargeable battery system because of its superior chemical/thermal stability, long term cycle life from rigid crystal structure, suitable energy density for using large scale energy storage system and use of low-cost element, iron. In the ideal case, the lithium iron phosphate could can release and insert lithium ions on their crystal structure with a theoretical gravimetric energy density specific capacity of 580 Wh kg⁻¹(theoretical capacity of ~ 169 mAh g⁻¹, Fe^{2+/3+} redox voltage of

3.42 V (vs. Li/Li⁺) through the one dimensional lithium diffusion channels being along the [010] direction of crystal structure (*Pnma*). However, the presence of immobile defects in the diffusion paths, which may originate from impurities or Li-Fe cation site exchange defect (anti-site defect), can significantly retard the mobility of ions of lithium iron phosphate. In particular, crystals with only one-dimensional diffusion pathways, such as olivine-type materials lithium iron phosphate, are detrimental with the presence of defects. Depending on synthesis process, approximately 0.5–7 % of the Li-Fe anti-site defect is present in crystal structure, which results in immobile Fe ions in the [010] lithium ion diffusion channel. According to report, the presence of 0.1 % anti-site defects in a micron-sized particle reduces its energy density to almost half of theoretical capacity and decreases the lithium ionic conductivity by two or three orders of magnitude.

Chapter 2 introduce a new method to remove anti-site defects in olivine crystals using electrochemical charge carrier injection process at a room temperature. The Fe anti-site defects in LiFePO₄ are effectively reduced by the electrochemical recombination of Li/Fe anti-sites. The healed crystal structure of lithium iron phosphate recovers its specific capacity and high-power capabilities. In this chapter, various configuration of anti-site defects and its recombination mechanisms are discussed.

Chapter 3 and 4 deals with a new type lithium-excess composition lithium iron phosphate having zero Fe anti-site in their crystal structure. It is confirmed that the Fe anti-site defects are completely removed in lithium-excess composition lithium iron phosphate due to its unique Fe oxidation state, showing superior rate capability and long term cycle ability. In this chapter, not only the structural characterization of lithium-excess lithium iron phosphate with zero Fe anti-site but also electrochemical behavior arising from thermodynamic and kinetic properties, especially Spinodal decomposition behavior and memory effect, will be discussed.

Keywords: Energy storage, Lithium rechargeable battery, cathode, olivine

Table of Contents

Chapter 1. General Introduction	1
1.1 Preface.....	1
1.1.1 General background	1
1.1.2 Spinodal decomposition behavior on electrode.....	4
1.1.3 References.....	8
Chapter 2. Anti-site reordering in LiFePO₄ using charge carrier injection	11
2.1 Introduction.....	11
2.2 Experimental	15
2.3 Results and Discussion.....	18
2.3.1 Anti-site configuration & possible recombination process...	18
2.3.2 Charge carrier injection method to reduce anti-site concentration	25
2.4 Conclusion.....	43
2.5 References	44
Chapter 3. Lithium-excess olivine for zero Fe_{Li} defect	51

3.1 Introduction	51
3.2 Experimental	55
3.3 Results and Discussion	57
3.3.1 Structural characterization of lithium-excess olivine	57
3.3.2 Local atomic configuration and origin of zero Fe anti-site of lithium-excess olivine	75
3.3.3 New [101] diffusion path of lithium-excess olivine	91
3.3.4 Electrochemical properties	101
3.4 Conclusion	103
3.5 References	104
Chapter 4. Thermodynamic and kinetic issues	121
4.1 Hysteresis gap and Memory effect of LiFePO_4	121
4.1.1 Experimental section	121
4.1.2 Lowed Spinodal decomposition barrier	122
4.1.3 Less memory effect at new LFP system	125
4.2 Conclusion	145
4.3 References	146
Chapter 5. Summary	157

Chapter 6. Abstract in Korean	159
Curriculum Vitae.....	163

List of Figures

Figure 2-1. Calculated formation energy of anti-site defect in LiFePO ₄ and its configuration corresponding to the distance between Li ⁺ on Fe ²⁺ site and Fe ²⁺ on Li ⁺ site.	22
Figure 2-2 Formation energies for 45 different vacancy-Fe defect configurations of the single-phase Li _{1-x} FePO ₄ from first principles calculations.	23
Figure 2-3. Energy curve and schematics of the Fe-Li cation site re-ordering process during discharge.	24
Figure 2-4 The 15 ~ 55° high resolution powder diffraction patterns of prepared by hydrothermal synthesis.....	32
Figure 2-5 (a) Magnified (200) peak of high resolution powder diffraction patterns of the prepared samples. (b) Rietveld refinement results of solid-solution Li _{0.9} FePO ₄ . The inset figure is an SEM image of micro-size Li _{0.9} FePO ₄	33
Figure 2-6. Rietveld refinement results of hydrothermally prepared LiFePO ₄	34

Figure 2-7. Rietveld refinement results of solid-solution $\text{Li}_{0.9}\text{FePO}_4$	35
Figure 2-8. Rietveld refinement result of electrochemically treated LiFePO_4	36
Figure 2-9. Defect characterization.....	37
Figure 2-10. Lattice parameter with change modification with anti-site ratio at room temperature	38
Figure 2-11. The electrochemical profile of solid-solution $\text{Li}_{0.9}\text{FePO}_4$ at C/100.....	39
Figure 2-12. $15 \sim 55^\circ$ XRD patterns of prepared by solid-state method samples	40
Figure 2-13. SEM image of prepared LiFePO_4	41
Figure 2-14. (a) First charge/discharge profile at C/200 of electrochemically treated micro- LiFePO_4 and hydrothermally grown micro- LiFePO_4 . (b) C-rate capability of electrochemically treated nano- LiFePO_4 (red) and conventional nano- LiFePO_4 (black).	42
Figure 3-1. Various synthetic condition and the impurity	61

Figure 3-2 Structure characterization results of lithium-excess LFP	62
Figure 3-3 Neutron diffraction (ND) Rietveld refinement results	65
Figure 3-4. XRD Rietveld refinement results	68
Figure 3-5. High resolution XRD experiment and simulation results	69
Figure 3-6. SEM image of normal and 5 % lithium-excess LFPs	70
Figure 3-7. Fe XANES measurements	71
Figure 3-8. TEM image of lithium-excess LFP surface	72
Figure 3-9. Surface analysis on 5 % lithium-excess LFP (red line) and normal LFP. (black line) 10 nm etched surface of lithium-excess LFP	73
Figure 3-10. Fourier transform infrared spectroscopy (FT-IR) results	74
Figure 3-11. ^6Li NMR resonance	81
Figure 3-12. Local atomic configurations	82
Figure 3-13. Local Fe ion oxidation state	83
Figure 3-14. In-situ temperature controlled XRD patterns	84

Figure 3-15. Possible cation exchange sites (LiFe-FeLi anti-site) at lithium-excess phase 87

Figure 3-16. Anti-site configuration and its formation energy 88

Figure 3-17. Anti-site defect formation energies at lithium-excess LFP as a function of distance from Li_{Fe} 89

Figure 3-18. The most stable anti-site configuration..... 90

Figure 3-19. Activation barriers for lithium ion hopping for normal and lithium-excess LFPs. 94

Figure 3-20. Conductivity change of Li-excess and normal LFPs..... 95

Figure 3-21. The schematics of Li ion diffusion along [010] direction in lithium-excess LFP. 96

Figure 3-22 The schematics of Li ion diffusion along [101] direction in lithium-excess LFP 97

Figure 3-23. The schematics of Li ion diffusion along [101] direction in normal LFP 98

Figure 3-24. [101] activation barrier of lithium-excess LFP. 99

Figure 3-25. [101] activation barrier of normal LFP.	100
Figure 3-26 Electrochemical properties of lithium-excess and normal LFPS	114
Figure 3-27. Hysteresis gap of electrodes	115
Figure 3-28. Rate capability of lithium-excess LFP (red) and normal LFP (black).	116
Figure 3-29. Galvanostatic discharge profiles	117
Figure 3-30. Ragone plot of various surface or chemical modified LFPS ·	118
Figure 3-31. Cycle life test of lithium-excess LFP with a current density ·	119
Figure4-1 . Mixing free energy and atomic configuration of lithium-excess LFP (orange) and normal LFP	130
Figure4-2 . Detailed DFT calculation results	131
Figure4-3. The single particle chemical potential	132
Figure4-4 Thermal phase diagram of lithium-excess LFP	133
Figure4-5 . Thermal XRD patterns of lithium-excess LFP	135

Figure4-6 . Memory effect of normal LFP.....	136
Figure4-7 Memory effect of lithium-excess LFP.	137
Figure4-8. OCV change of both electrodes.....	138
Figure4-9 . The effective diffusivity.....	139
Figure4-10 . Conductivity measurement.....	141
Figure4-11 . Confirmation on memory effect depending on rest time	144

Chapter 1. General Introduction

1.1 Preface

1.1.1 General background

Now a days, the global community faces an energy and environmental issues arising from exhaustion of fossil fuel resources, CO₂ emissions and global warming problem.[1] Thus, the energy generation paradigm is moved from fossil fuel based phase to renewable energy generation using sustainable resources, such as wind power, solar and geothermal energy.[1, 2] However, because those sustainable energy generation systems are tied to geometrical and temporal limitations, the energy demands and generation are not always coincident. Therefore, the development of large scale energy storage systems is required to overcome the intermittent energy generation problems. Among the various energy storage systems, the lithium rechargeable battery system is attracted great attentions as a solution of intermittent energy generation problems due to its high energy density, power density and round-trip efficiency.[1, 2]

Most electrode materials for lithium rechargeable batteries store energy based on intercalation mechanism.[1] The guest ions move from thermodynamically stable interstitial sites to out of crystalline host materials with electrons extraction, and the reverse reaction occurs with the injection

of electrons. Therefore, the ability of ion diffusion in the crystal structure strongly affects on the electrochemical properties in terms of energy density, power density and round-trip efficiency.[3-5] The ionic diffusion ability sensitively undergo changes with several factors such as temperature, diffusional activation energy and local atomic configuration. Among them, the defect in crystal structure is one of inevitable factors that determine ionic diffusion ability, therefore, careful choices of synthesis route or post treatment are required to control defect concentration.[6, 7] Especially, the electrode materials having a limited one- (1-D) or two-dimensional (2-D) guest ion diffusion pathway, such as olivine type LiFePO_4 for Li rechargeable electrode, are susceptible to presence of defects that could impede Li ion diffusion.[8-10]

The lithium iron phosphates (LFP) has been intensely investigated for last two decades as a cathode electrode material and model of thermodynamic Li ion intercalation for phase separating electrode materials.[11-14] The LFP shows promising electrochemical properties for applying a large scale energy storage system such as superior thermal stability, low cost, long term cycle stability and suitable theoretical energy density. Theoretically, the LFP could release and insert Li ion on their crystal structure with a theoretical gravimetric energy density of 580 Wh kg^{-1} (theoretical capacity of $\sim 169 \text{ mAh g}^{-1}$, $\text{Fe}^{2+/3+}$ redox voltage of 3.42 V (vs. Li/Li^+)) through the 1-D channels

being along the [010] direction of crystal structure (*Pnma*).[15] However, in practice, the Li-Fe cation site exchange defect (anti-site) in Li diffusion channel always forms with 1 ~ 5 % ratio depending on synthesise route, resulting in denying LFP to reach at a desired energy and power density.[4] For example, the presence of 0.1 % anti-site ratio in micro size LFP makes statically its energy density to almost half of original value and reduces ionic conductivity with two or three orders.[8] Since the nano-sizing[8] or post crystal structural treatment[9] on LFP has been widely applied to avoid immobile Fe anti-site effect, these approaches cannot completely get rid of the anti-site effects from LFP because anti-site still remains under 1% in their structure. In addition, the nano-synthesis leads to other problems, such as lowering tap density of electrode, generating other surface defects, surface side reaction during cycling and additional cost problem at synthesizing.[16, 17] Therefore, it is difficult for these approaches to be an ultimate solutions as satisfying high gravimetric/volumetric energy density and low cost active materials.

1.1.2 Spinodal decomposition behavior on electrode

Since the pioneering work on olivine type electrode materials, the phase behavior during electrochemical cycling of LiFePO_4 compounds is well investigated as the typical phase separation behavior at room temperature. *i. e.* two-phase reaction. [1] At the bulk scale LiFePO_4 , the lithium-rich and lithium-poor phases are coexisted in their crystal structure, forming phase boundary between those phases during cycling. [1-5] However, the recently experimental works on LiFePO_4 revealed that some thermodynamic factors could change the solubility limits of LiFePO_4 , resulting in distinguishable phase behavior with pure bulk one.[11-15] These new insight on the phase behavior open the chance to understanding the intrinsic properties of electrode materials. [12-13] Especially, the Spinodal decomposition behavior, which is one of well-known phase separation mechanism, at nano-sizing olivine materials provides a key clues on solving the unexpected fast charge/discharge behavior of LiFePO_4 . [19] According to the previous research that investigated on how the interfacial energy, coherency strain energy induced by lattice parameter difference between lithium-rich and lithium-poor olivine phases or surface energy modified as decreasing particle size.[ref] This increasing internal coherency energy bring the result of thermodynamic positive energy penalty, resulting in curvature like shape lithium-chemical potential during charge/discharge. The LiFePO_4 operating

with Spinodal decomposition mechanism could exhibit higher rate-capability due to lack of phase boundary movement in a single particle. [12, 19]

Moreover, the Spinodal decomposition with electrode materials exhibits some unique properties. First, it is an origin of ‘hysteresis gap’ between charge/discharge at an ultra-low current density. Theoretically, operation voltage of the lithium ion battery system is based on the thermodynamic phase equilibrium state with counter electrode. Therefore, in ideal case *i.e.* state without polarization came from cell system, such as concentration or resistance polarization, the voltages is only determined by state of charge regardless charge or discharge process. However, the nano-sizing LiFePO₄ exhibit the un-narrow-able polarization gap between charge and discharge even in an ultra-low current density. Previous research revealed that this ‘hysteresis gap’ is came from Spinodal decomposition barrier, providing new insight on lithium-ion battery system which could have ‘thermodynamic polarization. [12]

Second, the Spinodal decomposition chemical potential shape cause the memory effect on lithium-ion battery. As discussed at previous section, because the lithium ion battery is operated based on reversible reactions, the battery system could not ‘memorize’ how much electrode is charged or discharged. However, recently, Sasaki and *et. al*, firstly discovered that the

electrode casted with LiFePO_4 exhibit unexpected voltage bumped phenomena when the cell is re-charged after partially charge/discharge process.[13] They concluded that this strange observation is came from the particle-by-particle phase separating caused by Spinodal decomposition behavior.

Chapter 2 deals with a new defect control method using an electrochemical procedure at room temperature.[18] By tailoring the local environment around defects according to a strategy suggested by first principles calculations, it was found that the energy level of defects and the activation barrier for recombination could be lowered significantly. Experimental verification with a case study of LiFePO_4 revealed that significant defect annihilation occurred from a structural analysis, which substantially boosted the power capability of the material. In this work, an effective way to reduce Li-Fe defects is proposed using a simple electrochemical treatment at room temperature.

Chapter 3 introduces the lithium-excess concept could be expanded from layered type electrode to polyanion-based electrode, especially at olivine type that is one of the most promising cathode electrode materials.[19] The Li-excess LFP shows superior rate performance that it release almost half of

theoretical capacity at a high current density as well as stable electrochemical cycling.

The Chapter 4 introduces that lithium-excess configuration plays role as a “*phase mixing seed*” that reduces thermodynamic phase transition activation energy. The intrinsic thermodynamic and kinetic changes of Li-excess LFP induce lowering thermal solid-solution temperature and less memory effect than stoichiometric LFP.

1.1.3 References

1. Armand, M. and J.M. Tarascon, Building better batteries. *Nature*, 2008. **451**(7179): p. 652-657.
2. Kang, K., et al., Electrodes with High Power and High Capacity for Rechargeable Lithium Batteries. *Science*, 2006. **311**(5763): p. 977-980.
3. Kang, K. and G. Ceder, Factors that affect Li mobility in layered lithium transition metal oxides. *Physical Review B*, 2006. **74**(9): p. 094105.
4. Chen, J. and J. Graetz, Study of Antisite Defects in Hydrothermally Prepared LiFePO₄ by in Situ X-ray Diffraction. *ACS Applied Materials & Interfaces*, 2011. **3**(5): p. 1380-1384.
5. Dathar, G.K.P., et al., Calculations of Li-Ion Diffusion in Olivine Phosphates. *Chemistry of Materials*, 2011. **23**(17): p. 4032-4037.
6. Hoang, K. and M. Johannes, Tailoring Native Defects in LiFePO₄: Insights from First-Principles Calculations. *Chemistry of Materials*, 2011. **23**(11): p. 3003-3013.
7. Van der Ven, A. and G. Ceder, Lithium Diffusion in Layered Li_xCoO₂. *Electrochemical and Solid-State Letters*, 2000. **3**(7): p. 301-304.
8. Malik, R., et al., Particle Size Dependence of the Ionic Diffusivity. *Nano Letters*, 2010. **10**(10): p. 4123-4127.
9. Chen, J. and M.S. Whittingham, Hydrothermal synthesis of lithium

- iron phosphate. *Electrochemistry Communications*, 2006. **8**(5): p. 855-858.
10. Tealdi, C., C. Spreatico, and P. Mustarelli, Lithium diffusion in $\text{Li}_{1-x}\text{FePO}_4$: the effect of cationic disorder. *Journal of Materials Chemistry*, 2012. **22**(47): p. 24870-24876.
 11. Gibot, P., et al., Room-temperature single-phase Li insertion/extraction in nanoscale Li_xFePO_4 . *Nat Mater*, 2008. **7**(9): p. 741-747.
 12. Dreyer, W., et al., The thermodynamic origin of hysteresis in insertion batteries. *Nat Mater*, 2010. **9**(5): p. 448-453.
 13. Sasaki, T., Y. Ukyo, and P. Novák, Memory effect in a lithium-ion battery. *Nat Mater*, 2013. **12**(6): p. 569-575.
 14. Delacourt, C., et al., The existence of a temperature-driven solid solution in Li_xFePO_4 for $0 < x < 1$. *Nat Mater*, 2005. **4**(3): p. 254-260.
 15. Padhi, A.K., K.S. Nanjundaswamy, and J.B. Goodenough, Phospho-olivines as Positive-Electrode Materials for Rechargeable Lithium Batteries. *Journal of The Electrochemical Society*, 1997. **144**(4): p. 1188-1194.
 16. Julien, C.M., A. Mauger, and K. Zaghbi, Surface effects on electrochemical properties of nano-sized LiFePO_4 . *Journal of Materials Chemistry*, 2011. **21**(27): p. 9955-9968.
 17. Wang, J., et al., Size-dependent surface phase change of lithium iron phosphate during carbon coating. *Nat. Commun.*, 2014. **5**.
 18. Park, K.-Y., et al., Anti-Site Reordering in LiFePO_4 : Defect

Annihilation on Charge Carrier Injection. *Chemistry of Materials*, 2014.
26(18): p. 5345-5351.

[19] Delmas. C., et al., Lithium deintercalation in LiFePO₄ nanoparticle via a domino-cascade model. *Nat. Mater.*, 2008. 7, p. 665-671

Chapter 2. Anti-site reordering in LiFePO₄ using charge carrier injection

(The content of this chapter has been published in *Chemistry of Materilas*. Reprinted with permission from K.-Y Park *et al.* Anti-Site Reordering in LiFePO₄: Defect Annihilation on Charge Carrier Injection. *Chem. Mater.*, **2014**, 26 (18) pp. 3545-5351 (DOI: 10.1021/cm502432q). Copyright 2014 American Chemical Society.

2.1 Introduction

Defects in crystals are an important factor governing the intrinsic properties of materials, such as mechanical strength, electronic conductivity, and mass diffusion rates.[1-3] While the concentration of defects in a crystal at a certain temperature and pressure is determined by thermodynamics,[4-6] materials synthesized via non-equilibrium routes generally contain higher concentrations of defects. Careful choices of synthesis conditions or post-treatment methods are needed to control the level of defects and to tune the properties of materials.[7-10] In conventional semiconductor systems, it is known that the type and concentration of defects determine the electronic properties of materials.[11-13] Similarly, in ion mass-transfer systems, they critically affect kinetic properties.[14-16]

Defects in a crystal can impede ion transport by blocking diffusion pathways in one- (1-D) or two-dimensional (2-D) ionic conductors [17-19] LiFePO_4 , an important material in batteries, is a good example of this. While it has been considered a promising electrode material [20-22] due to its stability [23, 24] and relatively high energy density [25, 26], kinetic issues arising from the restrictive diffusion pathways for lithium ions and the low electronic conductivity have been problematic. [27] In particular, lithium ions can diffuse only through a 1-D tunnel in the crystal. Thus, this diffusion is susceptible to the presence of defects that may block the tunnel. [3] Since nano-sizing has been conducted widely for this material, the reduction in diffusion length can partly resolve the low-power problem. However, more importantly, nano-sizing is capable of reducing the detrimental effects of the defects blocking the channel. Malik *et al.* recently revealed that with 0.1% of Li-Fe site exchange in LiFePO_4 , ~45% of Li ions are trapped, statistically, between the defects in a 1- μm LiFePO_4 particle. However, this drops significantly, to ~5% in a 100-nm LiFePO_4 particle. [3] For these trapped lithium ions to participate in the battery reaction, they must diffuse through other unfavorable diffusion pathways that require higher activation barriers ($> 1 \text{ eV}$). [27-29]

Important practical issue with nano-sized LiFePO_4 that needs to be urgently

addressed, nevertheless, is the low electrode tap density, which results in a significant reduction in the volumetric energy density. It is simply because the interactions between nanoparticles make it difficult for them to be packed densely. This issue is more serious for LiFePO_4 , the crystal density of which is only 3.6 g/cm^3 , which is substantially lower than those of commercial electrodes, such as LiCoO_2 (5.1 g/cm^3) and LiMn_2O_4 (4.2 g/cm^3). [30, 31] Using nano- LiFePO_4 , in this regard, can hardly satisfy the requirements for batteries with high volumetric energy density. In this regards, it is increasingly important to develop a micro- LiFePO_4 electrode material that is capable of delivering satisfactory performance with reasonably high gravimetric/volumetric energy density. However, previous studies on large-size LiFePO_4 particles have shown that the material delivers undesirably low specific capacity or power capabilities. [3, 32, 33]

The minimization of defects in micro- LiFePO_4 can contribute to enhancing the transport properties because it reduces the possibility of blocking lithium diffusion tunnels. Since the blocking effect becomes more serious in larger particles, as noted, the control of anti-site defects becomes more critical in developing larger LiFePO_4 particles having fast transport properties. Previous approaches to reducing defects in crystals have mainly used high temperatures, with post heat treatment to recombine defects. [18] Here, we

report a novel way to reduce anti-site (Li-Fe) defects in LiFePO_4 electrochemically at room temperature. In this approach, we intentionally introduced a vacancy in the lithium channel by partial charging, and carried out a deep discharge below the conventional voltage cut-off. As a result, we observed significant Fe_{Li} -defect annihilation, resulting in defect-less LiFePO_4 from a structural analysis. Furthermore, the electrochemical performance could be enhanced markedly in the ‘healed’ sample. Density functional theory calculations suggest that Fe_{Li} -defect migration and annihilation could be facilitated by the introduction of vacancies near defects and the injection of excess electrons during over-discharge, which lowers the migration barrier for Fe defects.

2.2 Experimental

LiFePO₄ with a high concentration of defects was synthesized by a hydrothermal method. LiOH (Sigma Aldrich, 99.9%), FeSO₄·7H₂O (Sigma Aldrich, 99.8%), and H₃PO₄ (Sigma Aldrich, 85 wt% in water base) were used as precursors at a molar ratio of 3:1:1 in deionized water. The mixture was heated to 180°C in an autoclave and maintained for 2 h in an air atmosphere. The synthesized powder was filtered and then moved to a drying oven at 120°C for 24 h to remove water.

The solid-state synthesis of LiFePO₄ used precursors such as Li₂CO₃ (Sigma Aldrich, 99.9%), FeC₂O₄·H₂O (Sigma Aldrich, 99%), NH₃HPO₄ (Aldrich, 98%), and pyromellitic acid hydrate (Fluka, 6 wt%, PA, 99%) as the organic additive. The powders were ball-milled in acetone for 14 h and dried at 70°C. The mixture was first calcined at 500°C in an Ar atmosphere for 10 h. For additional carbon coating, 6 wt% of pyromellitic acid hydrate and 1 wt% of ferrocene (Aldrich, 98%) were mixed with the calcined powder using a ball-mill in acetone for 2 h. The acetone was then evaporated at 70°C in a drying oven. The dried mixture was pelletized under 200 kg cm⁻² pressure in a disk-shaped mold, and then sintered again at 600°C under Ar for 10 h.

The prepared LiFePO₄ powders and NO₂BF₄ powder were mixed in

acetonitrile for 4 h at a molar ratio of 1:0.1 for chemical delithiation. After the drying process, partially de-lithiated powder was heated again to 380°C for 4 h and quenched with liquid N₂. An electrode was fabricated by mixing the synthesized powders, pre-mixed with super P (22 wt%) in a ball mill for 24 h, and polyvinylidene fluoride (PVDF, 10 wt%) in N-methyl-2-pyrrolidone (NMP). The mixture was cast on Al foil and dried at 120°C for 2 h. Electrochemical cells were assembled using a CR2016-type coin cell with lithium metal as the counter electrode, a separator (Celgard 2400), and 1 M LiPF₆ in ethyl carbonate/dimethyl carbonate (Panax, EC/DMC, 1:1 v/v) as the electrolyte in an Ar-filled glove box.

First principle calculations were performed using the Perdew–Burke–Ernzerhof exchange-correlation parameterization to density functional theory (DFT) with the spin-polarized generalized gradient approximation (GGA).[34] A plane-wave basis set and the projector-augmented wave (PAW) method, as implemented in the Vienna *ab initio* simulation package (VASP), were used. Hubbard parameters (GGA+U) were added to correct the incomplete cancellation of the self-interaction of GGA.[35, 36] A U value of 4.3 eV (the on-site Coulomb term) and a J value of 1.0 eV (the exchange term) were used for the Fe atoms.[37] To study the defect configuration in Li_xFePO₄ ($x = 1/16$), we considered all possible orderings within the 1 × 2 × 2 supercell

of LiFePO_4 (112 atoms) generated with the CASM program, which contains defects of one Li in the M2 site, one Fe in the M1 site, and one vacancy in the M1 site.[38] All plausible configurations of Li-Fe cation site-exchange and a Li-vacancy within the 16-formula unit were considered. Activation energies for the ionic diffusion were calculated using the nudged-elastic-band (NEB) method.[39] Appropriate replicate systems were used as starting points for the NEB method, with linear interpolation between the initial and final states of the diffusion pathways.

High-resolution powder diffraction patterns were recorded using synchrotron X-ray radiation (the 8C2-HRPD beam-line at the Pohang Accelerator Laboratory, Korea). The incident X-rays were collimated using a mirror and monochromatized to a wavelength of $\sim 1.5495 \text{ \AA}$ using a Si (111) monochromator. The diffraction data were collected in the 10 to 130° range with a step size of 0.01° . Rietveld refinement of the HRPD results was conducted using the “Fullprof” program.[40] The size and morphology of the powders were observed using field emission scanning electron microscopy (FE-SEM, Philips, XL 30 FEG).

2.3 Results and Discussion

2.3.1 Anti-site configuration & possible recombination process

In perfect olivine LiFePO_4 , all Li and Fe ions occupy M1 and M2 octahedral sites, respectively. However, Li/Fe cation site exchange may lead to Li ions in M2 sites and Fe ions in M1 sites.[20, 41] This type of cation disorder can be an edge-shared Li/Fe defect or a corner-shared Li/Fe defect, as shown in Figure 2-1.[17, 41] Calculation of the defect formation energies indicates that both defects are comparable in energy, but the edge-shared Li/Fe defect (~ 390 meV) is slightly more probable than the corner-shared one (~ 490 meV), consistent with previous observations.[17] It has also been noted that the defect formation energy tends to decrease as the $\text{Fe}_{\text{Li}} - \text{Li}_{\text{Fe}}$ distance decreases among the types of anti-site. This indicates that an effectively attractive interaction does exist between Fe_{Li} and Li_{Fe} defects (see the formation energies for various defect types in Figure 2-1). Generally, it is known that these types of Li/Fe site exchange do not recombine during charging/discharging process or at room temperature due to the relatively high activation energy for recombination.[41]

The types of stable anti-site configurations differ with the introduction of a lithium vacancy, *i.e.*, $\text{Li}_{1-x}\text{FePO}_4$. DFT calculations on various anti-site

configurations showed that the corner-shared Li/Fe defect becomes more probable in Li-deficient olivine, even though both corner-shared (Figure 2-2 (a)) and edge-shared Figure 2-2 (b)) Li/Fe defects are comparably stable. However, it has been noted that all the stable anti-site configurations contain the vacancy as the first nearest neighbor to the Fe defect at the M1 octahedral site along the *b*-direction. It is believed that the relatively high valent Fe³⁺ exhibits stronger electrostatic repulsion, and thus prefers a vacancy to Li⁺ as its neighbor. As a consequence of the reduction in the electrostatic repulsion, the defect formation energy becomes lower in Li_{1-x}FePO₄ (~100 to 200 meV) than in LiFePO₄ (~400 to 500 meV; Figure 2-2). Furthermore, defect formation is energetically more stable than the defect-free Li_{15/16}FePO₄ phase (dotted line in Figure 2-2). This suggests that a meta-stable Li_{15/16}FePO₄ phase, if any, is likely to contain appreciable amounts of Li/Fe site exchange, although the most stable state is the two-phase coexistence of LiFePO₄ and FePO₄.

Close examination of the stable anti-site configurations revealed that the major defect type (corner-shared defect, Fig. 1(a)) has a plausible re-ordering route. In the possible route, shown in Figure 2-3, Li migrates to the vacant M1 site (inset 1, 2), then Fe moves sequentially to the M2 site (inset 3, 4), annihilating the defect. To assess this possible defect recombination, we

calculated the activation energy following the hypothetical migration path using NEB calculations. Figure 2-3 illustrates the energy profile along the recombination path. The recombination involved a relatively high activation energy of ~ 1.4 eV. When the lithium ion diffuses from M2 to the vacant M1 site, the system becomes destabilized gradually by ~ 1 eV (inset 2 of Figure 2-3) and iron migration carries an additional ~ 400 meV barrier (inset 3 of Figure 2-3). The high activation barrier of ~ 1.4 eV is attributable to the strong electrostatic repulsion among cations during the migration, and implies that the recombination of the defect in such conditions is unlikely to occur at room temperature.[28, 29] However, we found that a slight reduction of the system can significantly lower the activation barrier. When we intentionally injected excess electrons into the system, Fe^{3+} in the M2 site becomes reduced locally to Fe^{2+} , leading to a decrease in the activation barrier of iron migration from ~ 1.4 eV to ~ 0.8 eV. Considering that the activation barriers in many operable electrodes at room temperature range within several hundreds meV,[12, 28, 41] this indicates that recombination of the defect at room temperature is quite plausible in this case. While the injection of excess charge into the system is purely artificial in the calculations, we suggest that it can occur in the dynamic circumstances of charging or discharging of the electrode in electrochemical systems. A local charge imbalance due to the differing mobilities of the cation (Li ion) and electron during discharge can also induce such a situation.

However, the second major defect type, the edge-shared defect (Figure 2-2(b)), does not have an apparent re-ordering route, indicating that an edge-shared defect would not recombine and would remain, even with this healing process, which we will discuss further below.

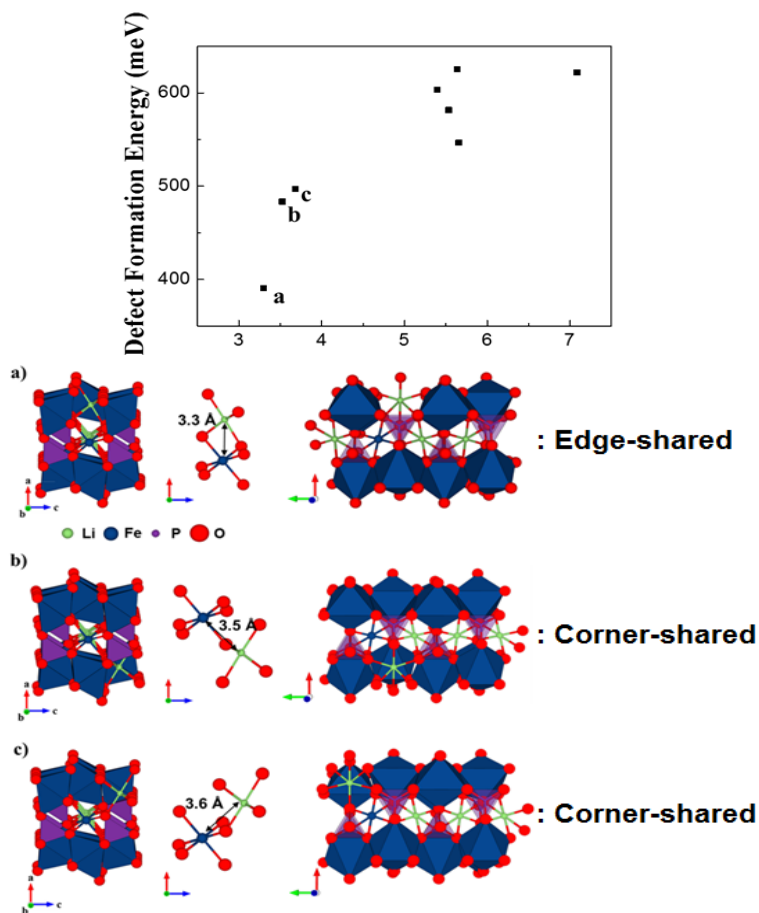


Figure 2-1. Calculated formation energy of anti-site defect in LiFePO₄ and its configuration corresponding to the distance between Li⁺ on Fe²⁺ site and Fe²⁺ on Li⁺ site. Near anti-site defect has lower formation energy. (a) Edge-shared anti-site defect with the lowest formation energy (about 390 meV) (b), (c) Corner-shared anti-site defect with the formation energy of about 490 meV.

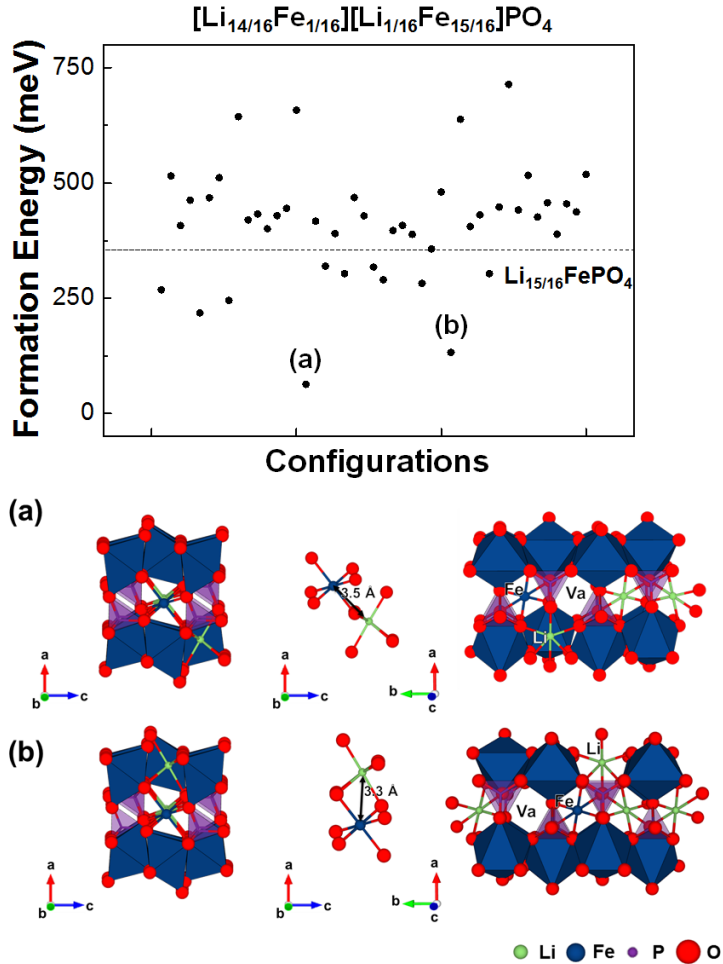


Figure 2-2 Formation energies for 45 different vacancy-Fe defect configurations of the single-phase $\text{Li}_{1-x}\text{FePO}_4$ from first principles calculations. The most stable energy is observed in (a) the corner-shared configuration and the second most stable configurations is shown as (b) the edge-shared configuration.

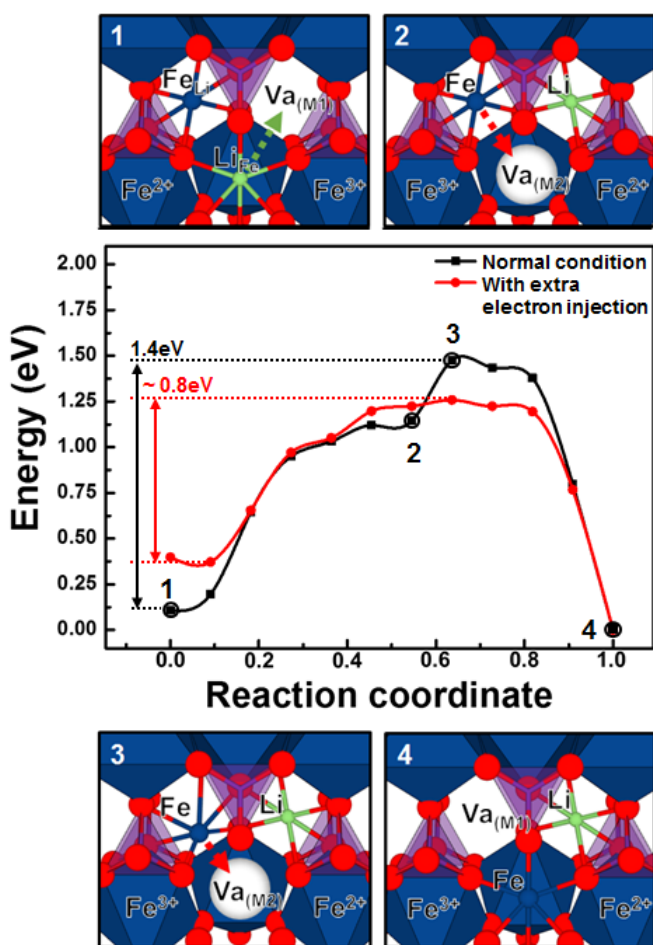


Figure 2-3. Energy curve and schematics of the Fe-Li cation site re-ordering process during discharge. The black line is the Fe/Li recombination route with no charge carrier injection. The red line is the hypothetical Fe/Li recombination route with a charge carrier (electron) injection. Schematics 1 – 4 schematics are Fe-Li cation site re-ordering processes at each point.

2.3.2 Charge carrier injection method to reduce anti-site concentration

Inspired by these theoretical results, we prepared a vacancy-introduced LiFePO_4 , *i.e.*, $\text{Li}_{0.9}\text{FePO}_4$, in the form of solid solution from a defective LiFePO_4 . First, the LiFePO_4 was synthesized hydrothermally and delithiated chemically to obtain a mixture of LiFePO_4 and FePO_4 with a molar ratio of 9:1 (high-resolution powder X-ray diffraction (HRPD) patterns are provided in Figure 2-4). The two-phase mixture was heated and quenched to retain a $\text{Li}_{0.9}\text{FePO}_4$ solid-solution phase. Figure 2-5 shows that the (200) peak of FePO_4 can be detected at $\sim 18^\circ$ in the mixture, which disappears after heating and quenching. The shift of the (200) peak confirms the formation of solid-solution $\text{Li}_{0.9}\text{FePO}_4$. Rietveld refinements of the $\text{Li}_{0.9}\text{FePO}_4$ in Figure 2-5 (b) show that the solid-solution phase was obtained successfully with $a = 10.328 \text{ \AA}$, $b = 6.007 \text{ \AA}$, and $c = 4.706 \text{ \AA}$. Comparison with pristine LiFePO_4 indicated that the lattice parameters decreased after the delithiation, in good agreement with previous reports.[42] The LiFePO_4 and $\text{Li}_{0.9}\text{FePO}_4$ contain $\sim 4.2\%$ and $\sim 4.0\%$ Li-Fe site exchange, respectively (detailed refinement results are provided in Figure 2-6 and 2-7). Those values match well with previous reports that hydrothermally prepared LiFePO_4 generally contains approximately ~ 3 to 4% defects, which are maintained even at the low post-heat-treatment temperature[42, 43] The particle size of the sample

was $\sim 2 \mu\text{m}$, as shown in the inset of Figure 3(b).

By constructing an electrochemical cell using the defective $\text{Li}_{0.9}\text{FePO}_4$, we then attempted to mimic the theoretical results of Li/Fe anti-site recombination. Figure 2-9 (a) shows the galvanostatic intermittent titrations (GITT) discharge profile of $\text{Li}_{0.9}\text{FePO}_4$. While the $\text{Li}_{0.9}\text{FePO}_4$ was capable of lithiating 0.1 Li up to $\sim 1.6 \text{ V}$ discharge, notably high polarization was observed in the profile. However, the open-circuit voltage (OCV) after the relaxation matched that of conventional $\text{Li}_{0.9}\text{FePO}_4$, indicating that the lithium insertion into $\text{Li}_{0.9}\text{FePO}_4$ solid solution occurred with a large kinetic barrier. The high polarization of $\text{Li}_{0.9}\text{FePO}_4$ at this stage will be discussed later.

After imposing the dynamic situation where lithium ions and electrons were injected into the defective $\text{Li}_{0.9}\text{FePO}_4$, we detected an unusual change in structural parameters. The tables in Figure 2-9 (b) and 2-10 compare the structural parameters obtained from the careful refinements of HRPDs for pristine LiFePO_4 and $\text{Li}_{0.9}\text{FePO}_4$ before and after electrochemical treatment. The first remarkable observation is that the lithiation of the defective $\text{Li}_{0.9}\text{FePO}_4$, following the protocol above (recombined LiFePO_4 in the Table) resulted in a significant *reduction* in the c lattice, along with the a lattice and

the volume. This is in contrast to the general trend with lithiation into olivine where the a and b lattice parameters and volumes *increase*, and the c lattice parameter decreases.[42] Also, the concentration of anti-site defects decreased from 4.0% to 1.86%. This unusual behavior indicated that not only the lithium content but also other structural rearrangement(s) affected the lattice parameters in the new LiFePO_4 . [44] At this point, it should be mentioned that the complete annihilation of the defects was not possible even after multiple electrochemical annealing, which we believe is due to the presence of edge-shared Li/Fe defect. As noted above, the edge-shared defect is also comparably probable with the corner-shared defect in the sample, but cannot be recombined due to the absence of the reordering routes.

From comparisons with previous reports on lattice parameters, we found that lattice parameters of olivines are sensitive to the concentration of defects and that the observed change was likely due to a decrease in Fe_{Li} defects, consistent with our theoretical predictions. In Figure 2-9 (c), we plot the previously reported lattice parameters of LiFePO_4 as a function of the refined value of Li/Fe site exchange.[20, 32, 42, 44] This revealed that as the Fe_{Li} defect concentration increased, the a lattice and volume of the olivine increased, following an almost linear relationship. To our surprise, the refined lattice parameters before and after the electrochemical healing of our

defective LiFePO_4 (denoted with stars) also showed a similar trend, suggesting that the Li/Fe site exchange had decreased after the healing. Figure 2-10 shows that the b and c lattice parameters followed the same trend, further confirming the decrease in anti-site defects.

Fourier transform infrared spectroscopy (FT-IR) spectra analyses also supported the decrease in the Fe_{Li} defect concentration in the new LiFePO_4 . Previous theoretical and experimental works have indicated that the IR absorption of PO_4^{3-} is sensitive to the presence of defects in the olivine crystal.[32, 45] Defect-free LiFePO_4 shows the PO_4^{3-} absorption typically at ~ 956 to 963 cm^{-1} , whereas LiFePO_4 with a high defect concentration has a PO_4^{3-} signal at ~ 983 to 1003 cm^{-1} . [32, 45, 46] In our FT-IR measurements, we found that the PO_4^{3-} absorption varied considerably, depending on the sample. Figure 2-9 (d) shows that the absorption bands of the P-O symmetric stretching vibration of the LiFePO_4 (anti-sites $\sim 4.2\%$) and $\text{Li}_{0.9}\text{FePO}_4$ (anti-sites $\sim 4.0\%$) were observed at $\sim 985 \text{ cm}^{-1}$. In contrast, electrochemically treated LiFePO_4 (anti-sites $\sim 1.8\%$) and the reference LiFePO_4 (anti-sites $\sim 1.0\%$) showed absorption at $\sim 960 \text{ cm}^{-1}$, suggesting that the new LiFePO_4 contained fewer Fe-Li cation site exchanges after our experiment, mimicking the charge carrier injection process. Our result is in contrast to previous reports that the recombination of Fe_{Li} defects in LiFePO_4 is only possible

above $\sim 500^\circ\text{C}$ with heat treatment⁴⁰ and not during a charging/discharging process.[47]

An unusually high polarization was observed during the initial lithiation of the defective $\text{Li}_{0.9}\text{FePO}_4$ during the electrochemical treatment. Nevertheless, the OCV after relaxation, which was close to ~ 3.42 V, agreed well with the average redox potential of $\text{Fe}^{2+}/\text{Fe}^{3+}$. This indicates that the lithiation process of the defective $\text{Li}_{0.9}\text{FePO}_4$ was a significantly sluggish process that required a high over-potential. We believe that this kinetic barrier was related to the recombination process of the Li/Fe site exchange. As shown before, the recombination required an activation barrier of ~ 0.8 eV, which is higher than that of typical lithium diffusion in conventional LiFePO_4 (~ 0.3 eV).[48] Thus, it would require a high over-potential once it occurs at room temperature in an electrochemical cell. The large polarization was only observed during the initial discharge process, and disappeared subsequently in this region (Figure 2-11). This supports the idea that the polarization stems from a structural rearrangement involving the defect recombination.

Using this electrochemical recombination process, we prepared two kinds of defect-less LiFePO_4 : one starting from hydrothermally synthesized micro- LiFePO_4 , and the other from nano- LiFePO_4 obtained with a conventional

solid-state synthesis. The synthesis and characterization of samples are illustrated in the supporting materials (Figure 2-12 and 2-13). Although highly defective LiFePO_4 with micron-size particles usually shows very small capacity at room temperature, the reduction in Li/Fe site exchange could enhance electrochemical performance markedly. Figure 2-14 (a) shows that the reversible capacity of micro- LiFePO_4 could be increased considerably after the recombination process. About ~ 0.2 Li ion capacity could be additionally achievable even with micron-sized LiFePO_4 . It is believed that the reduction of anti-site defect from 4.0% to 1.86% could liberate those amounts of trapped lithium ions. The full utilization of Li in micro- LiFePO_4 was not possible due to the presence of edge-shared Li/Fe defects. The effect of defect reduction was also observable in the nano- LiFePO_4 electrodes. Figure 2-14 (b) shows that the electrochemical recombination could enhance the power capability of the conventional nano- LiFePO_4 synthesized from a solid-solution reaction (~ 100 to 200 nm; SEM images in Figure 2-13 (c) and (d)). The electrochemically treated nano- LiFePO_4 delivered ~ 9.3 to 12.3% higher capacity at higher current rates than its counterpart. At a 30-C rate, the electrochemically annealed sample could achieve ~ 115 mAh/g, ~ 20 mAh/g higher than that of conventional nano- LiFePO_4 . This confirms that the simple electrochemical treatment described can result in the enhancement of the power capability of defective crystalline electrode materials regardless of the

particle sizes. We believe that the suggested defect recombination mechanism may be broadly applicable to electrode materials that typically suffer from restrained diffusion paths in crystals due to the presence of defects[3, 42]

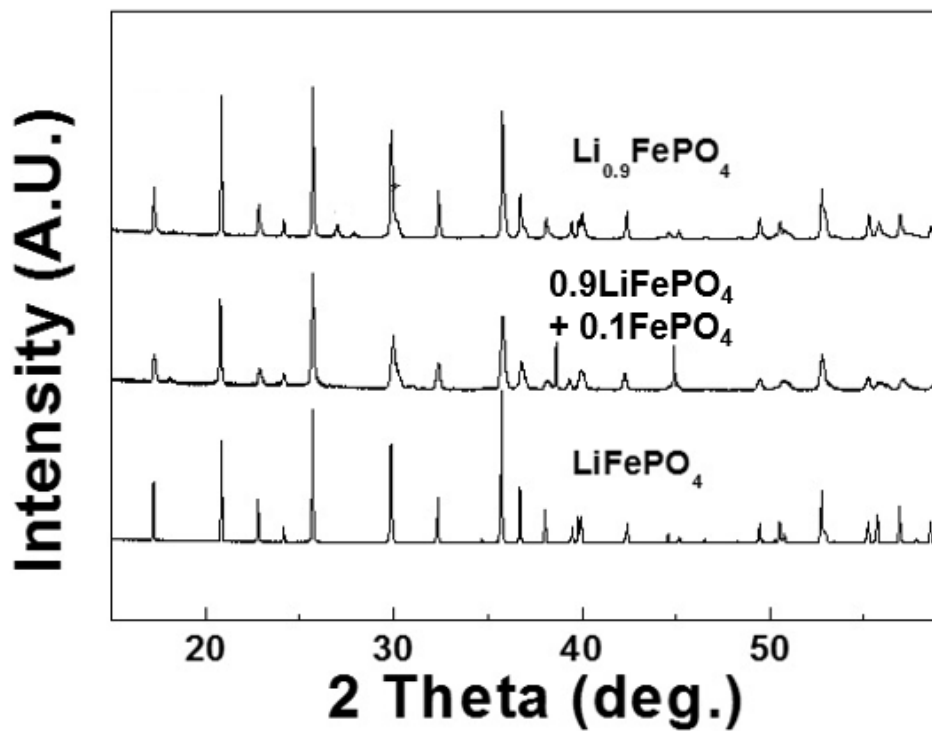


Figure 2-4 The 15 ~ 55° high resolution powder diffraction patterns of prepared by hydrothermal synthesis

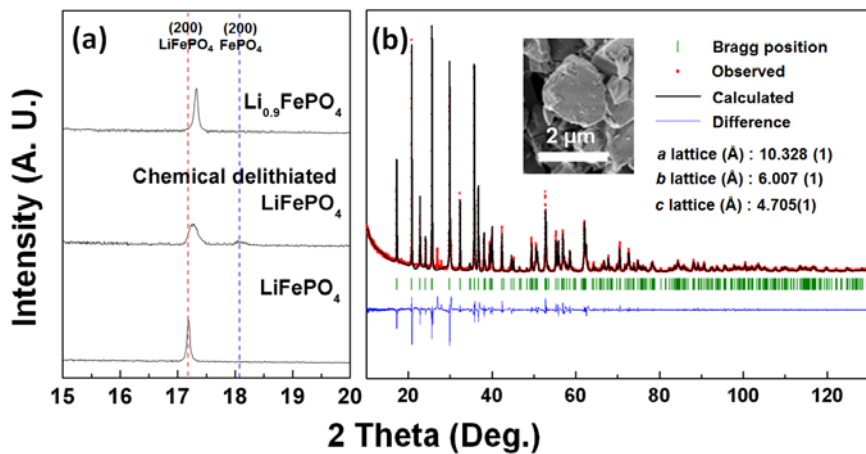
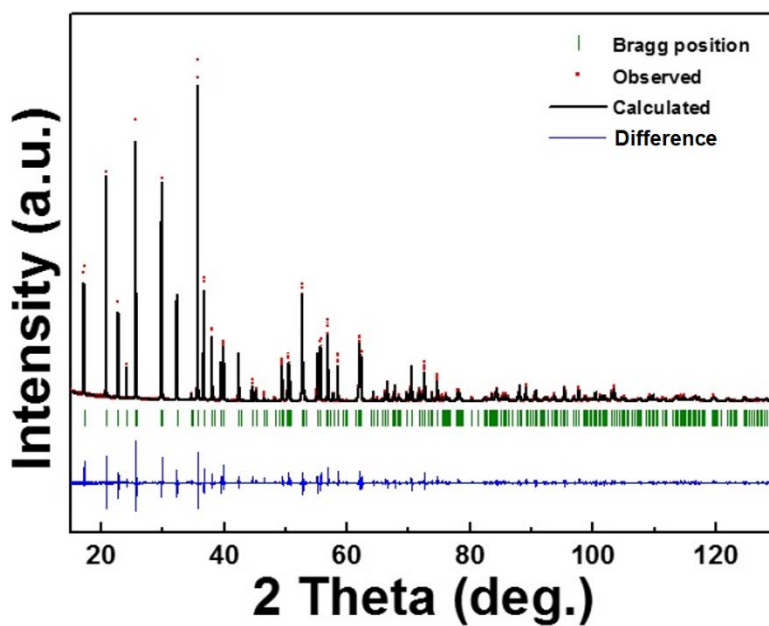


Figure 2-5 (a) Magnified (200) peak of high resolution powder diffraction patterns of the prepared samples. (b) Rietveld refinement results of solid-solution $\text{Li}_{0.9}\text{FePO}_4$. The inset figure is an SEM image of micro-size $\text{Li}_{0.9}\text{FePO}_4$

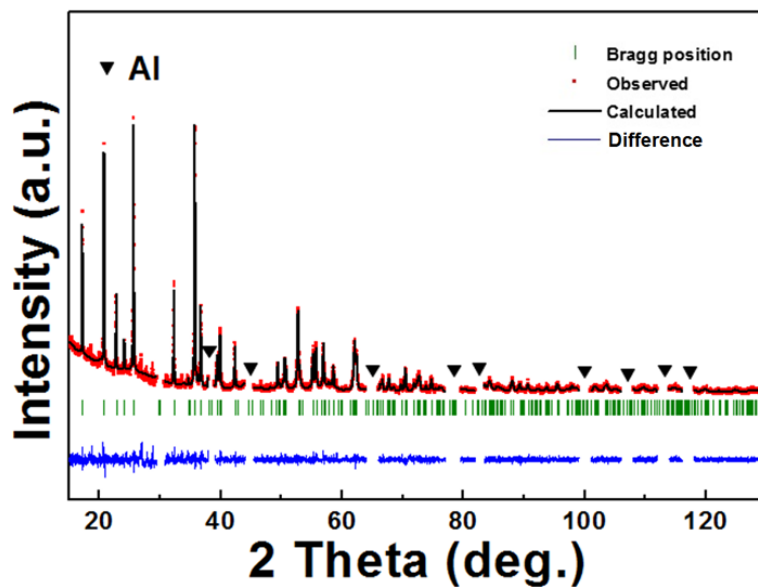


Atom	X	Y	Z	Biso	Mult.	Occ.		
Li	0.00000(0)	0.00000(0)	0.00000(0)	1.49	4	0.479	Chi ²	5.49
Fe	0.28189(7)	0.25000(0)	0.97522(17)	0.395	4	0.479	R _p	11
Li _{Fe}	0.28189(7)	0.25000(0)	0.97522(17)	1.49	4	0.021	R _I	5.02
Fe _{Li}	0.00000(0)	0.00000(0)	0.00000(0)	0.395	4	0.021	R _f	3.44
P	0.09524(13)	0.25000(0)	0.41750(26)	0.282	4	0.500	Unit cell V.	292.640(1)
O1	0.09721(34)	0.25000(0)	0.74437(64)	0.495	4	0.500	Lattice a(Å)	10.35027(3)
O2	0.45596(36)	0.25000(0)	0.20695(65)	0.482	4	0.500	Lattice b(Å)	6.01304(2)
O3	0.16747(28)	0.04299(38)	0.28245(42)	0.518	8	1.000	Lattice b(Å)	4.70205(1)

Figure 2-6. Rietveld refinement results of hydrothermally prepared LiFePO₄.

Atom	X	Y	Z	Biso	Mult.	Occ.		
Li	0.00000(0)	0.00000(0)	0.00000(0)	1.49	4	0.430	Chi ²	9.65
Fe	0.28139(13)	0.25000(0)	0.97462(35)	0.395	4	0.480	R _p	14.2
Li _{Fe}	0.28139(13)	0.25000(0)	0.97462(35)	1.49	4	0.020	R _I	7.71
Fe _{Li}	0.00000(0)	0.00000(0)	0.00000(0)	0.395	4	0.020	R _f	4.71
P	0.09592(23)	0.25000(0)	0.41781(48)	0.282	4	0.500	Unit cell V.	291.998(5)
O1	0.10082(60)	0.25000(0)	0.74909(113)	0.495	4	0.500	Lattice a(Å)	10.32877(8)
O2	0.45482(66)	0.25000(0)	0.20070(109)	0.482	4	0.500	Lattice b(Å)	6.00752(6)
O3	0.16566(49)	0.03936(72)	0.27621(71)	0.518	8	1.000	Lattice b(Å)	4.70582(4)

Figure 2-7. Rietveld refinement results of solid-solution Li_{0.9}FePO₄.



Atom	X	Y	Z	Biso	Mult.	Occ.		
Li	0.00000(0)	0.00000(0)	0.00000(0)	1.375(90)	4	0.4907(8)	Chi ²	1.50
Fe	0.28166(15)	0.25000(0)	0.97498(43)	0.369(20)	4	0.4907(8)	R _p	6.67
Li _{Fe}	0.28166(15)	0.25000(0)	0.97498(43)	0.280(90)	4	0.0093(8)	R _i	3.94
Fe _{Ti}	0.00000(0)	0.00000(0)	0.00000(0)	1.464(20)	4	0.0093(8)	R _f	2.74
P	0.09816(29)	0.25000(0)	0.41935(49)	0.356(41)	4	0.500	Unit cell V.	290.637(4)
O1	0.09531(71)	0.25000(0)	0.74595(118)	0.590(142)	4	0.500	Lattice a(Å)	10.32416(8)
O2	0.44798(82)	0.25000(0)	0.21221(109)	0.192(126)	4	0.500	Lattice b(Å)	5.99040(6)
O3	0.16480(53)	0.04815(79)	0.28282(81)	0.676(90)	8	1.000	Lattice b(Å)	4.66938(4)

Figure 2-8. Rietveld refinement result of electrochemically treated LiFePO₄

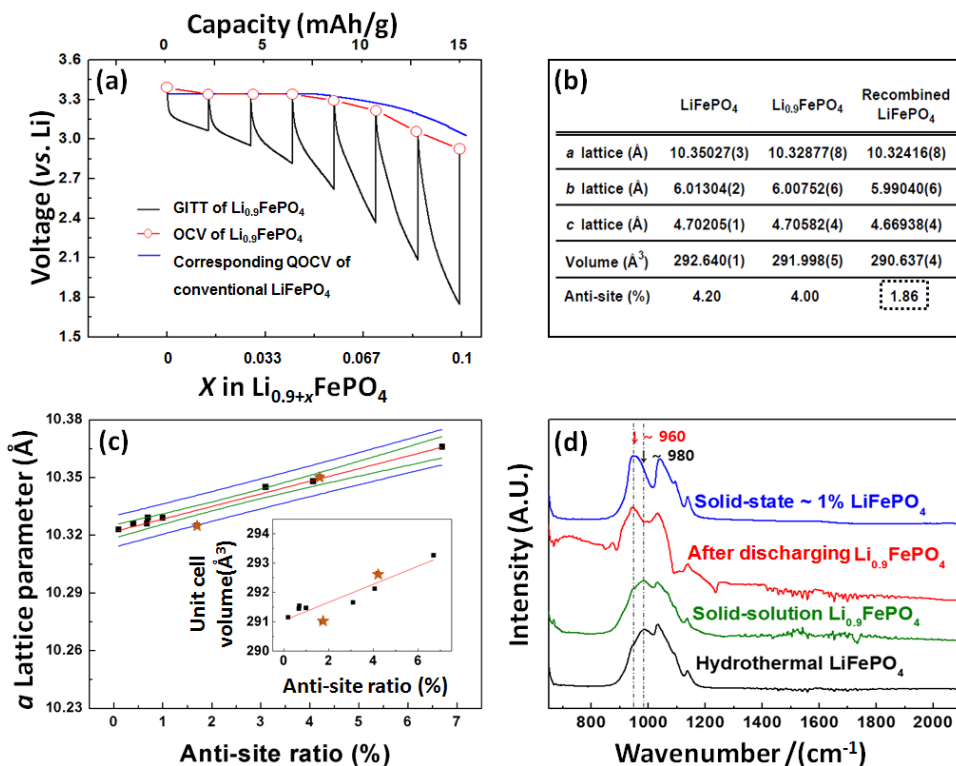


Figure 2-9. Defect characterization (a) Black: GITT result of $\text{Li}_{0.9}\text{FePO}_4$, red: quasi-OCV result of $\text{Li}_{0.9}\text{FePO}_4$, blue: quasi-OCV of conventional LiFePO_4 . (b) Lattice parameters, volume and anti-site ratio of prepared samples. The detailed Rietveld refinement results are provided in supporting Figure S3 – S5. (c) a -lattice parameter change as a function of anti-site ratio. The inset figure is shown the unit cell volume change as a function of anti-site ratio. Red line : trend line, blue line : confidence band, green line : prediction band. The interval coverage probability is set as 95 %. The star points symbolized stand for hydrothermal synthesized LiFePO_4 and electrochemically treated LiFePO_4 . The data are taken from references 20, 30, 40 and 42. (d) FT-IR results of prepared samples PO_4^{3-} spectra.

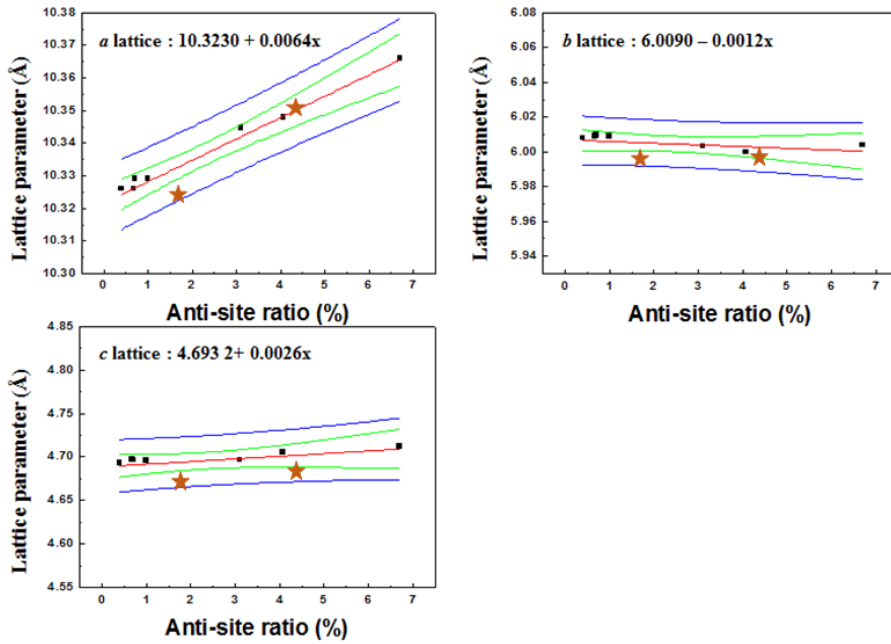


Figure 2-10. Lattice parameter with change modification with anti-site ratio at room temperature. Red line : trend line, blue line : confidence band, green line : prediction band. The interval coverage probability is set as 95 %. This figure used reference number 25, 35, 47 and 49.

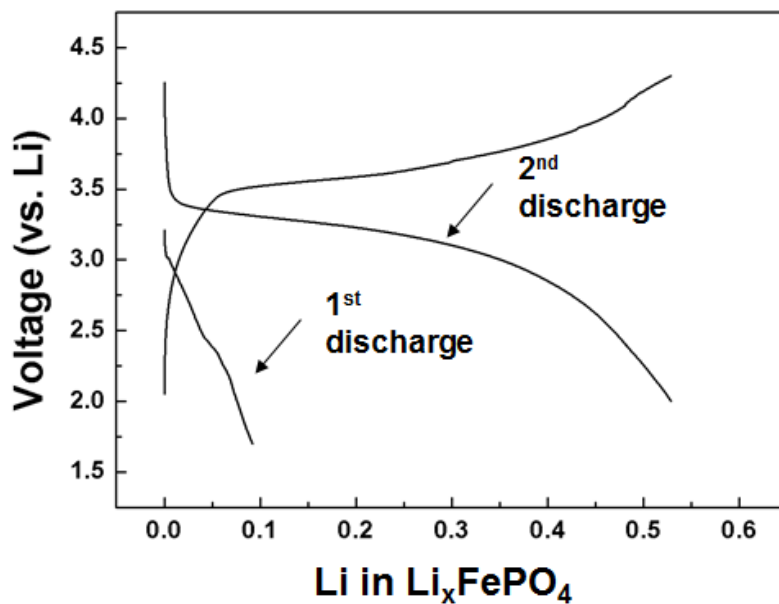


Figure 2-11. The electrochemical profile of solid-solution $\text{Li}_{0.9}\text{FePO}_4$ at $\text{C}/100$. The 1st discharge profile showed unexpected high polarization, however, the 2nd profile did not show overpotential during charging/discharging

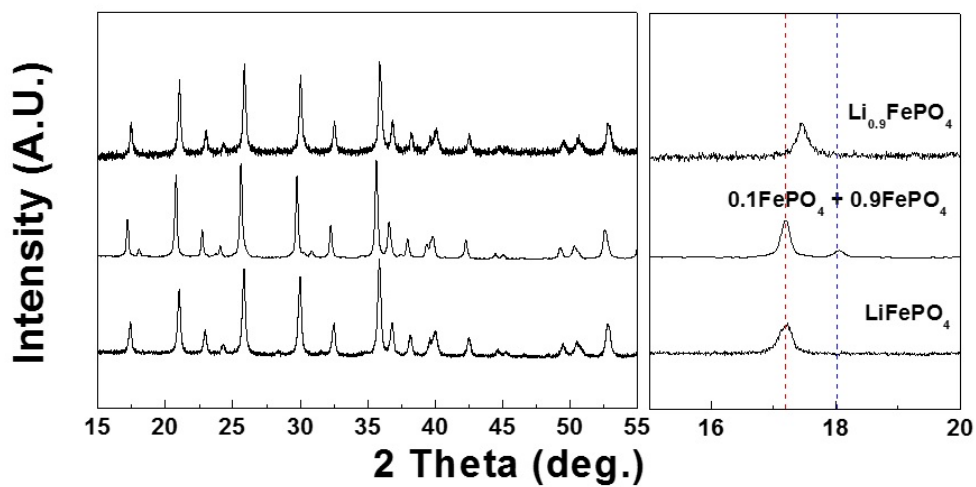


Figure 2-12. 15 ~ 55° XRD patterns of prepared by solid-state method samples (left) and magnified (200) peak of samples (right). red line : (200) peak of LiFePO₄, blue line : (200) peak of FePO₄. All samples are well synthesized without remarkable impurities.

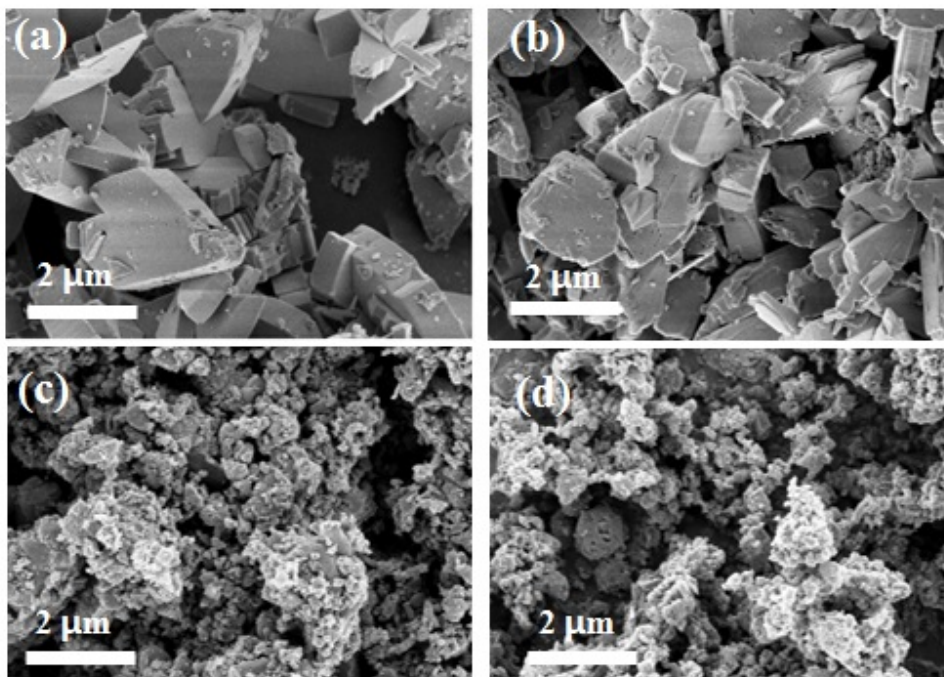


Figure 2-13. SEM image of prepared LiFePO_4 . (a) Hydrothermal synthesis LiFePO_4 (b) 380 °C heated hydrothermal synthesis $\text{Li}_{0.9}\text{FePO}_4$ (c) 600 °C solid-state synthesis LiFePO_4 (d) 380 °C heated solid-state 600 °C synthesis $\text{Li}_{0.9}\text{FePO}_4$.

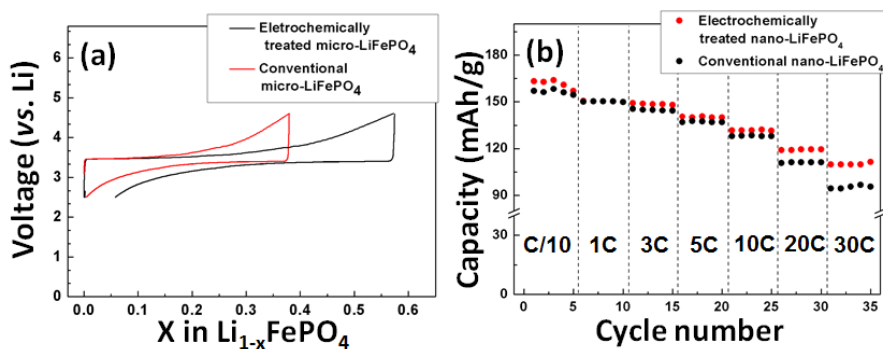


Figure 2-14. (a) First charge/discharge profile at C/200 of electrochemically treated micro-LiFePO₄ and hydrothermally grown micro-LiFePO₄. (b) C-rate capability of electrochemically treated nano-LiFePO₄ (red) and conventional nano-LiFePO₄ (black).

2.4 Conclusion

In this chapter, researcher introduced a new way to reduce defects in crystals with a case study of olivine LiFePO_4 . Fe_{Li} defects in the olivine structure were reduced using a room-temperature electrochemical annealing process. The defect annihilation mechanism was proposed from first principles calculations, which indicated that the introduction of vacancies and excess charge carriers lowered the activation barrier for defect recombination. Using this new method, we demonstrated that defective LiFePO_4 , including both micro- and nano-size particles, can be ‘healed,’ recovering power capabilities. The defect-annihilation mechanism suggested here may be broadly applicable in making defect-less materials, and is expected to help in understanding defect behavior in various materials.

2.5 References

1. Sammalkorpi, M., et al., Mechanical properties of carbon nanotubes with vacancies and related defects. *Physical Review B*, 2004. **70**(24): p. 245416.
2. Kuo, J.H., H.U. Anderson, and D.M. Sparlin, Oxidation-reduction behavior of undoped and Sr-doped LaMnO₃: Defect structure, electrical conductivity, and thermoelectric power. *Journal of Solid State Chemistry*, 1990. **87**(1): p. 55-63.
3. Malik, R., et al., Particle Size Dependence of the Ionic Diffusivity. *Nano Letters*, 2010. **10**(10): p. 4123-4127.
4. Penn, R.L. and J.F. Banfield, Imperfect Oriented Attachment: Dislocation Generation in Defect-Free Nanocrystals. *Science*, 1998. **281**(5379): p. 969-971.
5. Esch, F., et al., Electron Localization Determines Defect Formation on Ceria Substrates. *Science*, 2005. **309**(5735): p. 752-755.
6. Wendt, S., et al., The Role of Interstitial Sites in the Ti3d Defect State in the Band Gap of Titania. *Science*, 2008. **320**(5884): p. 1755-1759.
7. Bikondoa, O., et al., Direct visualization of defect-mediated dissociation of water on TiO₂(110). *Nat Mater*, 2006. **5**(3): p. 189-192.
8. Vlasov, Y.A., et al., On-chip natural assembly of silicon photonic

- bandgap crystals. *Nature*, 2001. **414**(6861): p. 289-293.
9. Philip, J., et al., Carrier-controlled ferromagnetism in transparent oxide semiconductors. *Nat Mater*, 2006. **5**(4): p. 298-304.
 10. Johansson, J., et al., Structural properties of [lang]111[rang]B - oriented III-V nanowires. *Nat Mater*, 2006. **5**(7): p. 574-580.
 11. Pertsinidis, A. and X.S. Ling, Diffusion of point defects in two-dimensional colloidal crystals. *Nature*, 2001. **413**(6852): p. 147-150.
 12. Dathar, G.K.P., et al., Calculations of Li-Ion Diffusion in Olivine Phosphates. *Chemistry of Materials*, 2011. **23**(17): p. 4032-4037.
 13. Fahey, P.M., P.B. Griffin, and J.D. Plummer, Point defects and dopant diffusion in silicon. *Reviews of Modern Physics*, 1989. **61**(2): p. 289-384.
 14. Chung, S.-Y., J.T. Bloking, and Y.-M. Chiang, Electronically conductive phospho-olivines as lithium storage electrodes. *Nat Mater*, 2002. **1**(2): p. 123-128.
 15. Bracht, H., et al., Large disparity between gallium and antimony self-diffusion in gallium antimonide. *Nature*, 2000. **408**(6808): p. 69-72.
 16. Allen, J.E., et al., High-resolution detection of Au catalyst atoms in Si nanowires. *Nat Nano*, 2008. **3**(3): p. 168-173.
 17. Islam, M.S., et al., Atomic-Scale Investigation of Defects, Dopants, and Lithium Transport in the LiFePO₄ Olivine-Type Battery Material. *Chemistry of Materials*, 2005. **17**(20): p. 5085-5092.

18. Chung, S.-Y., et al., Atomic-Scale Visualization of Antisite Defects in LiFePO_4 . *Physical Review Letters*, 2008. **100**(12): p. 125502.
19. Kang, K., et al., Electrodes with High Power and High Capacity for Rechargeable Lithium Batteries. *Science*, 2006. **311**(5763): p. 977-980.
20. Padhi, A.K., K.S. Nanjundaswamy, and J.B. Goodenough, Phospho-olivines as Positive-Electrode Materials for Rechargeable Lithium Batteries. *Journal of The Electrochemical Society*, 1997. **144**(4): p. 1188-1194.
21. Padhi, A.K., et al., Effect of Structure on the $\text{Fe}^{3+} / \text{Fe}^{2+}$ Redox Couple in Iron Phosphates. *Journal of The Electrochemical Society*, 1997. **144**(5): p. 1609-1613.
22. Yamada, A., S.C. Chung, and K. Hinokuma Optimized LiFePO_4 for Lithium Battery Cathodes. *Journal of The Electrochemical Society*, 2001. **148**(3): p. A224-A229.
23. Delacourt, C., et al., The existence of a temperature-driven solid solution in Li_xFePO_4 for $0 \leq x \leq 1$. *Nat Mater*, 2005. **4**(3): p. 254-260.
24. Chen, G., X. Song, and T.J. Richardson, Metastable Solid-Solution Phases in the $\text{LiFePO}_4/\text{FePO}_4$ System. *Journal of The Electrochemical Society*, 2007. **154**(7): p. A627-A632.
25. Wang, Y., P. He, and H. Zhou, Olivine LiFePO_4 : development and future. *Energy & Environmental Science*, 2011. **4**(3): p. 805-817.
26. Xie, H.M., et al., Optimized LiFePO_4 -Polyacene Cathode Material

- for Lithium-Ion Batteries. *Advanced Materials*, 2006. **18**(19): p. 2609-2613.
27. Morgan, D., A. Van der Ven, and G. Ceder, Li Conductivity in Li_xMPO_4 ($M = \text{Mn}, \text{Fe}, \text{Co}, \text{Ni}$) Olivine Materials. *Electrochemical and Solid-State Letters*, 2004. **7**(2): p. A30-A32.
28. Kang, K., D. Morgan, and G. Ceder, First principles study of Li diffusion in LiFePO_4 structure. *Physical Review B*, 2009. **79**(1): p. 014305.
29. Kang, K. and G. Ceder, Factors that affect Li mobility in layered lithium transition metal oxides. *Physical Review B*, 2006. **74**(9): p. 094105.
30. Yamada, A., et al., Olivine-type cathodes: Achievements and problems. *Journal of Power Sources*, 2003. **119–121**(0): p. 232-238.
31. Yang, M.-R., T.-H. Teng, and S.-H. Wu, LiFePO_4 /carbon cathode materials prepared by ultrasonic spray pyrolysis. *Journal of Power Sources*, 2006. **159**(1): p. 307-311.
32. Qin, X., et al., Hydrothermally synthesized LiFePO_4 crystals with enhanced electrochemical properties: simultaneous suppression of crystal growth along [010] and antisite defect formation. *Physical Chemistry Chemical Physics*, 2012. **14**(8): p. 2669-2677.
33. Delmas, C., et al., Lithium deintercalation in LiFePO_4 nanoparticles via a domino-cascade model. *Nat Mater*, 2008. **7**(8): p. 665-671.
34. Perdew, J.P., K. Burke, and M. Ernzerhof, Generalized Gradient Approximation Made Simple. *Physical Review Letters*, 1996. **77**(18): p.

3865-3868.

35. Kresse, G. and J. Furthmüller, Efficiency of ab-initio total energy calculations for metals and semiconductors using a plane-wave basis set. *Computational Materials Science*, 1996. **6**(1): p. 15-50.

36. Anisimov, V.I., J. Zaanen, and O.K. Andersen, Band theory and Mott insulators: Hubbard U instead of Stoner I. *Physical Review B*, 1991. **44**(3): p. 943-954.

37. Wang, L., T. Maxisch, and G. Ceder, Oxidation energies of transition metal oxides within the GGA+U framework. *Physical Review B*, 2006. **73**(19): p. 195107.

38. Van der Ven, A., et al., Nondilute diffusion from first principles: Li diffusion in Li_xTiS_2 . *Physical Review B*, 2008. **78**(10): p. 104306.

39. Henkelman, G., B.P. Uberuaga, and H. Jonsson, A climbing image nudged elastic band method for finding saddle points and minimum energy paths. *The Journal of Chemical Physics*, 2000. **113**(22): p. 9901-9904.

40. Carvajal, J., FULLPROF: A Program for Rietveld Refinement and Pattern Matching Analysis. Abstracts of the Satellite Meeting on Powder Diffraction of the XV Congress of the IUCr, 1990.

41. Tealdi, C., C. Spreatico, and P. Mustarelli, Lithium diffusion in $\text{Li}_{1-x}\text{FePO}_4$: the effect of cationic disorder. *Journal of Materials Chemistry*, 2012. **22**(47): p. 24870-24876.

42. Chen, J. and J. Graetz, Study of Antisite Defects in Hydrothermally Prepared LiFePO₄ by in Situ X-ray Diffraction. ACS Applied Materials & Interfaces, 2011. **3**(5): p. 1380-1384.
43. Yang, S., et al., Reactivity, stability and electrochemical behavior of lithium iron phosphates. Electrochemistry Communications, 2002. **4**(3): p. 239-244.
44. Yamada, A., et al., Room-temperature miscibility gap in Li_xFePO₄. Nat Mater, 2006. **5**(5): p. 357-360.
45. Burba, C.M. and R. Frech, Raman and FTIR Spectroscopic Study of Li_xFePO₄ (0 ≤ x ≤ 1) Journal of The Electrochemical Society, 2004. **151**(7): p. A1032-A1038.
46. Cho, M.-Y., et al., Defect-free solvothermally assisted synthesis of microspherical mesoporous LiFePO₄/C. RSC Advances, 2013. **3**(10): p. 3421-3427.
47. Badi, S.-P., et al., Direct synthesis of nanocrystalline Li_{0.90}FePO₄: observation of phase segregation of anti-site defects on delithiation. Journal of Materials Chemistry, 2011. **21**(27): p. 10085-10093.
48. Ouyang, C., et al., First-principles study of Li ion diffusion in LiFePO₄ structure. Physical Review B, 2004. **69**(10): p. 104303.

Chapter 3. Lithium-excess olivine for zero F_{Li} defect

(The content of 3 and 4 chapters share the introduction and references. Also, these contents are now in preparation to be submitted to scientific journals.)

3.1 Introduction

The basic principle of modern rechargeable batteries relies on the reversible intercalation of guest ions in the electrode materials. The intercalation reaction is possible because numerous guest ions can diffuse in and out of the electrode crystal.[1] The diffusivity of the guest ions in the electrode, therefore, strongly affects the electrochemical properties, such as the power density, round-trip efficiency, and energy density. The crystal structure primarily determines the diffusivity of guest ions, providing specific diffusion paths. However, a deviation of the local atomic configuration around the guest ions also sensitively affects the ionic mobility.[2, 3] For example, the presence of immobile defects in the diffusion paths, which may originate from impurities or anti-site defects, can significantly retard the mobility of ions. In particular, crystals with only one-dimensional diffusion pathways are susceptible to the presence of defects that may significantly impede Li-ion diffusion. In this respect, careful selection of the synthesis route or post-treatment of electrode materials is often required to control the defect

concentration.[4-6]

LFP has been intensely studied for the last two decades as a practically important cathode material for lithium rechargeable batteries and as a model system for thermodynamic and kinetic studies of lithium intercalation.[7-14] In the ideal case, LFP can deliver a specific capacity of 169 mAh g⁻¹ via relatively fast lithium diffusion through a channel along the [010] direction of the crystal structure (*Pnma*).[13, 15, 16] However, in practice, approximately 5 % Li-Fe cation site exchange (Li_{Fe}-Fe_{Li} anti-site defect) typically occurs, depending on the synthetic routes, which results in immobile Fe_{Li} ions in the lithium diffusion channel.[3, 17-22] Malik *et al.* demonstrated that the presence of 0.1 % Li_{Fe}-Fe_{Li} anti-site defects in a micron-sized LFP particle statistically reduced its energy density to almost half of the original value[5, 17] and decreased the lithium ionic conductivity by two or three orders of magnitude.[17] In this respect, many researchers have attempted to minimize Fe_{Li} anti-site defects or form positive defects in LFP resulting from the synthesis procedure.[5, 17, 23-25] Among these researchers, the Whittingham group succeeded in systematically analyzing Li_{Fe}-Fe_{Li} anti-site defects in LFP by controlling various synthetic conditions such as the hydrothermal methods and demonstrated that LFPs with high Li_{Fe}-Fe_{Li} anti-site contents suffer from inferior electrochemical performances.[20, 22] Also, Hoang and Johannes investigated on various point defects in LFP, calculating

that lithium-rich and iron-poor LFP could have relatively the high Fe_{Li} defect formation energy from DFT calculation.[26] Masquelier group attempted to synthesize highly defective LFP powder through modified synthetic procedure, showing unexpected electrochemical behaviors. They revealed that high concentration of defect could provide alternative lithium ion diffusion paths offering stable electrochemical performance based on distinct reaction mechanisms.[27-29] Although the nano-sizing of LFP is an indirect approach to reducing the effect of immobile Fe_{Li} anti-site defects because of the shortened diffusion length, the nano-synthesis leads to other problems, such as reducing the tap density of the electrode,[23] generating more surface defects accompanying side reactions because of the large surface area,[30, 31] and creating additional cost problems in the synthesis and electrode fabrication.[32]

Incorporating additional charge-carrying guest ions in a crystal structure sometimes leads to unexpected results in their electrochemical properties,[33, 34] which was recently demonstrated in layered-type lithium transition metal oxides. Armstrong *et al.* demonstrated that a slight excess of lithium ($x = \sim 3\%$) in $\text{Li}_{1+x}\text{V}_{1-x}\text{O}_2$ could switch on lithium-ion intercalation, delivering a higher theoretical specific capacity and volumetric energy density than graphite, whereas pristine LiVO_2 exhibits no evidence of intercalation into its structure.[33] In addition, lithium-excess derivatives of

$\text{Li}(\text{Ni},\text{Co},\text{Mn},\text{Ru},\text{Sn})\text{O}_2$ layered-type electrode materials, *i.e.*, $\text{Li}_{1+x}(\text{Ni},\text{Co},\text{Mn},\text{Ru},\text{Sn})_{1-x}\text{O}_2$, exhibit distinctive electrochemical responses during battery cycling, triggering oxygen redox reactions and delivering extra capacity beyond the expected value for the pristine materials.[35-40] Furthermore, most recently, Lee *et al.* revealed that even fully disordered lithium transition metal oxides (100% anti-site ratio in the layered structure) can utilize the de/intercalation of almost all the lithium in the structure if a sufficient amount of excess lithium is present in the structure to provide a percolation path for lithium diffusion.[41] Also, the earlier attempts on synthesizing $\text{Li}_{1+x}\text{FePO}_4$ ($x < 0.03$) exhibited better electrochemical properties than pristine LiFePO_4 . [42, 43] This series of new findings in lithium-excess layered electrode materials naturally motivated us to examine the strategy of lithium excessiveness in the olivine with $\text{Li}_{1+x}\text{Fe}_{1-x}\text{PO}_4$ compositions, which is an important electrode material and a class of crystals that could be more vulnerable to lithium kinetics because of the restricted diffusion path.

3.2 Experimental

The LFPs with various compositions were synthesized using Li_2CO_3 (Sigma Aldrich, 99.9%), $\text{FeC}_2\text{O}_4 \cdot \text{H}_2\text{O}$ (Sigma Aldrich, 99%), $(\text{NH}_4)_2\text{HPO}_4$ (Aldrich, 98%). Each precursor was pulverized as fine as possible, separately using high energy ball-milling at Ar atmosphere to avoid the oxidation. The fine precursors were mixed by wet ball milling using acetone more than 24 hours. After drying the mixture, the powder was, again, pulverized as fine as possible using dry ball milling to obtain uniformity and calcinated at 350°C with $5 \sim 6^\circ\text{C}/\text{min}$ heating rate for 10 hours. The calcinated powders were reground and pelletized under more than 300 bar. The final sintering process was conducted with heating rate as a $5 \sim 6^\circ\text{C}/\text{min}$ rate in Ar atmosphere for 10 hours.

High-resolution powder diffraction patterns were recorded using synchrotron X-ray radiation (the 8C2-HRPD beam-line at the Pohang Accelerator Laboratory, Korea). ND data were collected using a high-resolution powder diffractometer (HRPD) at the HANARO facility of the Korea Atomic Energy Research Institute.

First principle calculations were performed using the Perdew–Burke–Ernzerhof exchange–correlation parameterization to density functional theory (DFT) with the spin-polarized generalized gradient approximation (GGA).[34] A plane-wave basis set and the projector-augmented wave (PAW) method, as implemented in the Vienna *ab initio* simulation package (VASP), were used. Hubbard parameters (GGA+U) were added to correct the incomplete cancellation of the self-interaction of GGA.[35, 36] A U value of 4.3 eV (the on-site Coulomb term) and a J value of 1.0 eV (the exchange term) were used for the Fe atoms.[37] To study the defect configuration in Li_xFePO_4 ($x = 1/16$), we considered all possible orderings within the $1 \times 2 \times 2$ supercell of LiFePO_4 (112 atoms) generated with the CASM program, which contains defects of one Li in the M2 site, one Fe in the M1 site, and one vacancy in the M1 site.[38] All plausible configurations of Li-Fe cation site-exchange and a Li-vacancy within the 16-formula unit were considered. Activation energies for the ionic diffusion were calculated using the nudged-elastic-band (NEB) method.[39] Appropriate replicate systems were used as starting points for the NEB method, with linear interpolation between the initial and final states of the diffusion pathways.

3.3 Results and Discussion

3.3.1 Structural characterization of lithium-excess olivine

Based on this simple question, we attempted to adapt the lithium-excess concept to LFP ($\text{Li}_{1+x}\text{Fe}_{1-x}\text{PO}_4$) and successfully synthesized the lithium-excess olivine phase by carefully controlling the synthetic conditions. (See the supporting information in Figure 3-1 for details.) First, samples containing various lithium-excess compositions (0, 2.5, 5, 7.5, and 10 %) were synthesized using solid-state methods at 600 °C in an Ar atmosphere to determine how much excess lithium could be incorporated in the olivine structure. Although less than 5 % lithium-excess LFP compositions result in a pure olivine phase without any crystalline impurities, compositions containing more than 7.5 % excess lithium begin to develop a second phase corresponding to $\text{Li}_3\text{Fe}_2(\text{PO}_4)_3$, as observed in the X-ray diffraction (XRD) patterns in Figure 3-1. To verify the presence of additional lithium in the LFP crystal, more detailed analysis was conducted using both high-resolution synchrotron XRD and neutron diffraction (ND), and the results were compared with those for normal LFP. Neutron analysis is necessary to trace the lithium occupancy in the crystal because of its low scattering with X-rays.[44] Figure 3-2(b) presents the ND pattern of 5% lithium-excess LFP along with a calculated pattern using the olivine structure model, which shows

low Bragg R-factors, indicating the reliability of the structural refinements. Detailed structural information from the refinements is provided in Figure 3-3 (a-c). In addition, as a reference, an ND pattern of the normal LFP along with the results of the refinement are presented in Figure 3-3. Note that the 5 % lithium-excess targeted LFP contains 4.2 (2) % lithium in Fe octahedral sites (Li_{Fe}), and all the lithium sites are occupied solely by lithium (Li_{Li}) according to the neutron refinements in Figure 3-2 (c). On the other hand, the normal LFP contains ~0.6 (2) % $\text{Li}_{\text{Fe}}\text{-Fe}_{\text{Li}}$ anti-site defects according to the refinements under the identical condition, which agrees well with previously reported values of $\text{Li}_{\text{Fe}}\text{-Fe}_{\text{Li}}$ anti-site defects in conventional LFPs.[15, 16] The refinements of two samples using high-resolution XRD reproduced the same result for the two samples, as demonstrated in Figure 3-4. The systematic modeling of the relative intensities of the XRD peaks as a function of the excess amount of lithium also agrees with the ND results in Figure 3-5. For a better comparison of the two samples, a few physical properties are tabulated in Figure 3-2 (c). The compositional analysis of two samples using inductively coupled plasma (ICP) supported the presence of the extra amount of lithium for the lithium-excess LFP phase, revealing a Li:Fe:P ratio of 1.08 (3):0.94 (1):1.00 (0) and 0.99 (2):0.98 (2):1.00 (0) for the lithium-excess and normal LFPs, respectively. The surface area is comparable for both samples but is slightly smaller for the lithium-excess LFP according to the Brunauer–

Emmett–Teller (BET) measurements. The scanning electron microscopy (SEM) images in Figure 3-6 show that the particle size of the lithium-excess LFP is slightly larger (~150 nm) than that of the normal LFP (~100 nm).

The excess amount of lithium in LFP leads to a slightly higher oxidation state of the transition metal (Fe) in the sample to maintain charge neutrality based on the substitution of the monovalent Li^+ for divalent Fe^{2+} ($\text{Li}(\text{Li}_{0.05}^+\text{Fe}_{0.95}^{+2.053})\text{PO}_4$). The X-ray absorption near edge structure (XANES) analysis in Figure 3-7 compares the oxidation states of Fe in three samples of $\text{Li}(\text{Li}_{0.05}\text{Fe}_{0.95})\text{PO}_4$, $\text{LiFe}^{+2}\text{PO}_4$, and $\text{Fe}^{+3}\text{PO}_4$. Although the quantitative determination of the Fe valence in $\text{Li}(\text{Li}_{0.05}\text{Fe}_{0.95})\text{PO}_4$ was not trivial, it was clear that the profile of the lithium-excess olivine lies between those of LiFePO_4 and FePO_4 , indicative of a Fe valence higher than +2. The higher oxidation state of Fe of the sample also serves as indirect evidence of the excess lithium present in the structure.

Even though the crystallographic information and compositional analysis indicate the presence of the excess lithium in the olivine, the possibility of the formation of an amorphous impurity phase remains. According to previous reports, the synthesis of LFP using a slightly off-stoichiometric amount of precursors can result in LFP coated with a highly conductive amorphous

phase, enhancing the rate capability.[45-47] To identify any possible amorphous phase, we conducted surface analysis of the lithium-excess LFP using high-resolution transmission electron microscopy (HR-TEM), X-ray photoelectron spectroscopy (XPS), and Fourier-transform infrared spectroscopy (FT-IR). The HR-TEM images (Figure 3-8) reveal the high crystallinity of the lithium-excess LFP both at the surface and in the bulk without an amorphous phase on the surface. In addition, the XPS and FT-IR results show no difference between the surface and bulk of the lithium-excess LFP. Both the pristine and 10-nm surface-deep-etched lithium-excess LFPs exhibited identical XPS and FT-IR profiles, as observed in Figure 3-9 and Figure 3-10, respectively, implying no traceable amount of the amorphous phase on the lithium-excess LFP surface.

a

Method	Li : Fe : P ratio	Temperature (°C)	Reaction Time (hour)	Atmosphere	Crystalline impurity
Solid-state	1.025 : 0.975 : 1	600	10	Ar	-
Solid-state	1.05 : 0.95 : 1	600	10	Ar	-
Solid-state	1.075 : 0.925 : 1	600	10	Ar	$\text{Li}_3\text{Fe}_2(\text{PO}_4)_3$
Solid-state	1.1 : 0.90 : 1	600	10	Ar	$\text{Li}_3\text{PO}_4/\text{Li}_3\text{Fe}_2(\text{PO}_4)_3$
Solid-state	1.05 : 0.95 : 1	700	10	Ar	$\text{Li}_3\text{PO}_4/\text{Li}_3\text{Fe}_2(\text{PO}_4)_3$
Solid-state	1.05 : 0.95 : 1	800	10	Ar	$\text{Li}_3\text{PO}_4/\text{Li}_3\text{Fe}_2(\text{PO}_4)_3$
Hydrothermal	3.0 : 0.95 : 1	180	4	Ar	$\text{Li}_3\text{PO}_4/\text{Li}_3\text{Fe}_2(\text{PO}_4)_3$
Hydrothermal	3.0 : 0.95 : 1	200	4	Ar	$\text{Li}_3\text{PO}_4/\text{Li}_3\text{Fe}_2(\text{PO}_4)_3$
Hydrothermal	3.0 : 0.95 : 1	220	4	Ar	Li_3PO_4 /Unkwn impurity

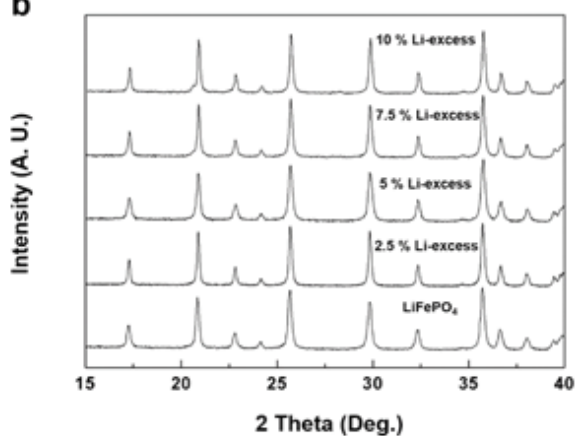
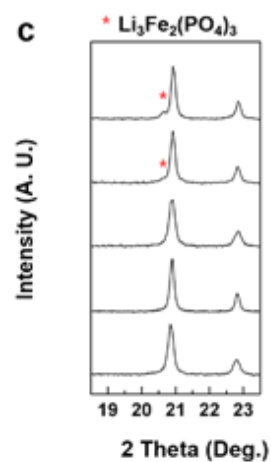
b**c**

Figure 3-1. Various synthetic condition and the impurity (a) Various synthetic condition and the impurity of each conditions (b) XRD patterns of 0, 2.5, 5, 7.5 and 10 % Li-excess composition of olivine synthesized through solid-state method. (c) Magnified of 18 ~ 24 ° of XRD patterns. The stoichiometric (0% Li-excess) and 5 % Li-excess composition show no crystalline impurities, but the 7.5 % and 10 % contain $\text{Li}_3\text{Fe}_2(\text{PO}_4)_3$ impurities. (Measurement condition: range 15 ~ 40 °, step size 0.02 °, by D2 phaser, Bruker)

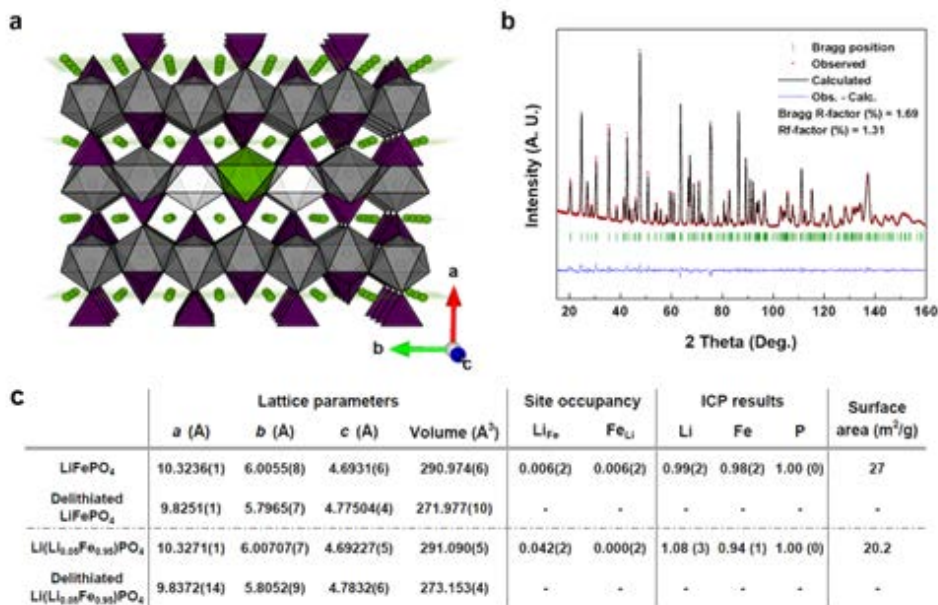
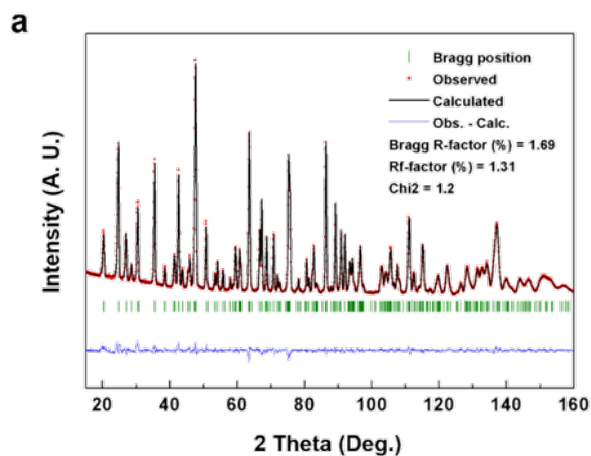


Figure 3-2 Structure characterization results of lithium-excess LFP (a)

Schematic picture of crystalline lithium-excess LFP. Green: Li atoms, purple: PO₄ tetrahedral unit, dark gray: Fe²⁺O₆ octahedral unit, gray: Fe^{2-x+}O₆ octahedral unit. (b) Rietveld refinement of neutron diffraction pattern of lithium-excess LFP. (c) Lattice parameters, M1 and M2 site occupancy, ICP results and surface area of lithium-excess and normal LFPs (d) TEM image of lithium-excess LFP surface.

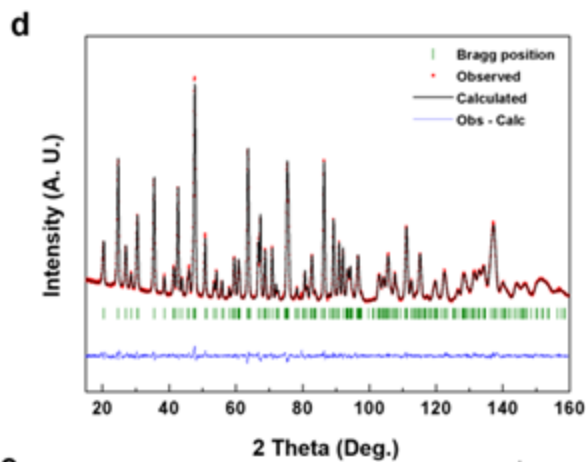


b

	$U_{11} / \text{\AA}^2$	$U_{22} / \text{\AA}^2$	$U_{33} / \text{\AA}^2$	$U_{12} / \text{\AA}^2$	$U_{13} / \text{\AA}^2$	$U_{23} / \text{\AA}^2$	Isotropic therm. Fact
Li	61.1	58.4	127.8	10.6	-9.3	-27.8	1.137
S. D.	4.6	11.8	21.6	5.5	12	12.7	74
Li_{Fe}	10.6	59.1	27.7	0	-0.2	0	0.436
S. D.	0.8	2.4	4.4	0	1.6	0	12
Fe	10.6	59.1	27.7	0	-0.2	0	0.436
S. D.	0.8	2.4	4.4	0	1.6	0	12
Fe_{Li}	61.1	58.4	127.8	10.6	-9.3	-27.8	1.137
S. D.	4.6	11.8	21.6	5.5	12	12.7	74
P1	31.2	63.6	91.9	0	6.5	0	0.729
S. D.	1.7	4.1	7.8	0	3.3	0	23
O1	30.7	60.9	81.8	0	-6.5	0	0.652
S. D.	1.3	3.8	6.8	0	2.8	0	20
O2	29.7	89.4	107.1	0	11.3	0	0.771
S. D.	1.6	4.3	8.7	0	2.9	0	24
O3	27.8	75.3	107.1	10	16.1	-7.7	0.782
S. D.	1	2.5	5.3	1.6	2	3.1	15

c

Name	x (Å)	y (Å)	z (Å)	Occ.
Li	0	0	0	1.000(2)
Li_{Fe}	0.28184(9)	0.25	0.9732(3)	0.042(2)
Fe	0.28184(9)	0.25	0.9732(3)	0.958(2)
Fe_{Li}	0	0	0	0.000(2)
P1	0.09444(17)	0.25	0.4177(3)	1
O1	0.09791(17)	0.25	0.7402(4)	1
O2	0.45748(15)	0.25	0.2043(4)	1
O3	0.16493(14)	0.04736(19)	0.2848(2)	1



e

	U ₂₃ / Å ²	U ₂₂ / Å ²	U ₃₃ / Å ²	U ₁₂ / Å ²	U ₁₃ / Å ²	U ₂₃ / Å ²	Isotropic therm. Fact
Li	37.5	83.9	33.6	7.4	13.1	-2.5	1.063(80)
S. D.	5.3	15.4	23.6	6.5	13.8	15.5	
Li _{Fe}	7.7	46.3	76.3	0	-0.6	0	0.628(13)
S. D.	0.9	2.8	4.7	0	1.8	0	
Fe	7.7	46.3	76.3	0	-0.6	0	0.628(13)
S. D.	0.9	2.8	4.7	0	1.8	0	
Fe _{Li}	37.5	83.9	33.6	7.4	13.1	-2.5	1.063(80)
S. D.	5.3	15.4	23.6	6.5	13.8	15.5	
P1	15.3	30.3	37.6	0	4.5	0	0.415(20)
S. D.	1.8	4.6	8.4	0	3.7	0	
O1	10.9	18	21.8	0	-3.3	0	0.508(25)
S. D.	1.3	4.1	7.4	0	3	0	
O2	10.6	28.9	33.6	0	-2.6	0	0.583(15)
S. D.	1.7	4.6	9.5	0	3.1	0	
O3	10.8	35.5	41.6	11.2	7.7	-2.7	0.628(13)
S. D.	1.1	2.7	5.8	1.8	2.2	3.4	

f

Name	x (Å)	y (Å)	z (Å)	Occ.
Li	0	0	0	0.994(2)
Li _{Fe}	0.28201(10)	0.25	0.9738(3)	0.006(2)
Fe	0.28218(6)	0.25	0.97469(15)	0.994(2)
Fe _{Li}	0	0	0	0.006(2)
P1	0.09515(19)	0.25	0.4175(4)	1
O1	0.09758(19)	0.25	0.7406(4)	1
O2	0.45744(16)	0.25	0.2048(4)	1
O3	0.16476(15)	0.0472(2)	0.2850(3)	1

g

Sample	Li-LiFePO ₄	Li-Li _{1.01} Fe _{0.99} PO ₄
Crystal system	Orthorhombic	
Space group	Pnma (No. 62)	
Lattice parameters		
<i>a</i> (Å)	10.32369(13)	10.32719(11)
<i>b</i> (Å)	6.00555(8)	6.00707(7)
<i>c</i> (Å)	4.69318(6)	4.69227(5)
Unit cell volume (Å ³)	290.974(6)	291.090(5)
Source	Neutron	
Temperature (K)	300	
Wavelength (Å)	1.83432	
2θ range	0 - 160 °	
Number of data positions	3200	
Bragg R-factor (%)	1.35	1.58
Rf-factor (%)	0.847	1.09
Chi ²	2.3	2.99

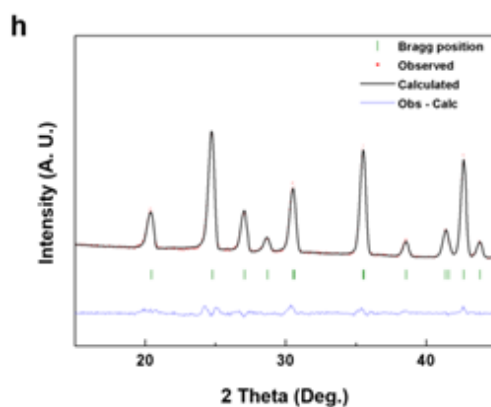
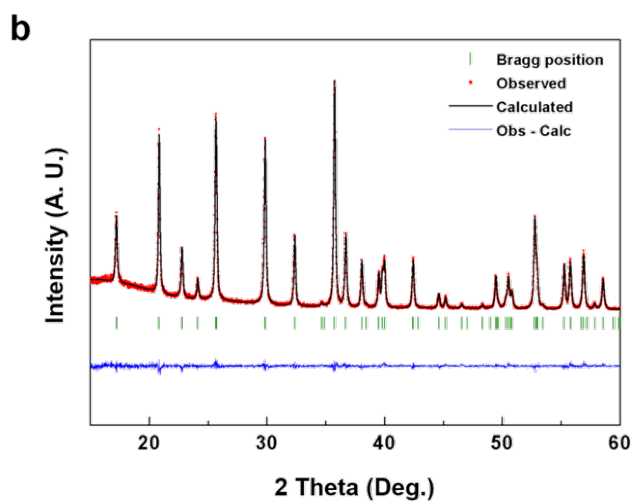
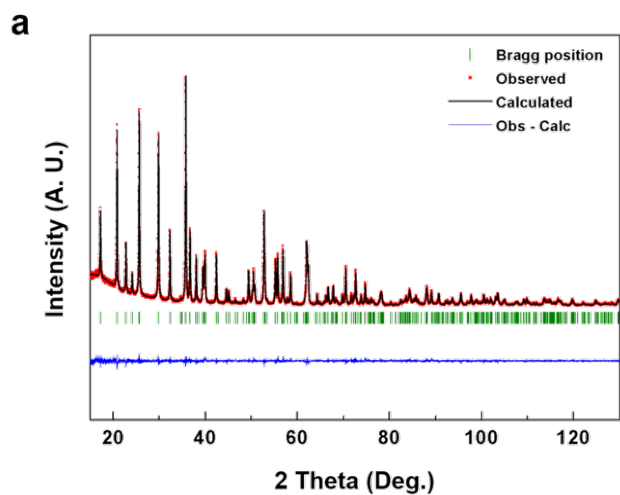
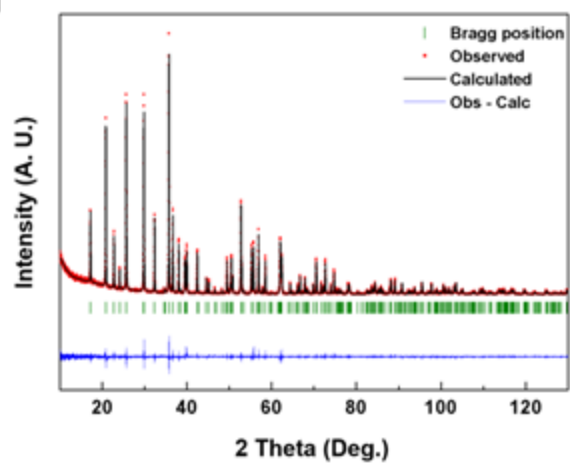


Figure 3-3 Neutron diffraction (ND) Rietveld refinement results of (a) - (c) lithium-excess LFP and (d) - (f) normal LFP. Figure (g) shows overall crystal structure factors and refinement information. The excessive Li ions are positioned at M2 octahedral site with 4.2 % occupancy. Also, the anti-site is not observed at Li-excess LFP. Figure (h) shows zoomed-in figure of (a). (Wyckoff of each sites; Li and Fe_{Li}: 4*a*; Fe, Li_{Fe}, P, O1 and O2: 4*c*; O3: 8*d*)



c

Name	x (Å)	y (Å)	z (Å)	B factor	Occ.
Li	0	0	0	1.299(141)	1.000(0)
Li _{Fe}	0.28213(6)	0.25	0.97434(15)	0.459(10)	0.958(0)
Fe	0.28213(6)	0.25	0.97434(15)	0.459(10)	0.000(0)
Fe _{Li}	0	0	0	1.299(141)	0.042(0)
P1	0.09522(11)	0.25	0.41796(23)	0.647(20)	1
O1	0.09682(29)	0.25	0.74342(55)	0.841(58)	1
O2	0.45622(33)	0.25	0.20930(56)	0.936(62)	1
O3	0.1568(23)	0.04478(33)	0.28349(36)	0.816(41)	1

d**e**

Name	x (Å)	y (Å)	z (Å)	B factor	Occ.
Li	0	0	0	1.189(192)	0.992(1)
Li _{Fe}	0.28217(6)	0.25	0.97469(15)	0.334(13)	0.008(1)
Fe	0.28218(6)	0.25	0.97469(15)	0.334(13)	0.992(1)
Fe _{Li}	0	0	0	1.189(192)	0.008(1)
P1	0.09520(11)	0.25	0.41805(23)	0.308(28)	1
O1	0.09683(30)	0.25	0.74520(55)	0.620(83)	1
O2	0.45625(32)	0.25	0.20551(57)	0.586(82)	1
O3	0.16632(24)	0.04665(34)	0.28463(37)	0.336(54)	1

f

Sample	LiFePO ₄	Li _{1.02} Fe _{0.95} PO ₄
Crystal system	Orthorhombic	
Space group	Pnma (No. 62)	
Lattice parameters		
<i>a</i> (Å)	10.32576(3)	10.32212(4)
<i>b</i> (Å)	6.00648(1)	6.00463(2)
<i>c</i> (Å)	4.69188(1)	4.69394(2)
Unit cell volume (Å ³)	290.997(1)	290.933(2)
Source	Synchrotron (X-ray)	
Temperature (K)	300	
Wavelength (Å)	1.5474	
2θ range	10 - 130.1°	
Number of data positions	12051	
Bragg R-factor (%)	2.9	1.69
Rf-factor (%)	2.1	1.31
Chi ²	1.5	1.2

Figure 3-4. XRD Rietveld refinement results of (a) - (c) lithium-excess LFP and (d) - (e) normal LFP. Figure (f) shows overall crystal structure factors and refinement information. The high resolution XRD Rietveld refinement results are consistent with ND refinement results of zero anti-site in Li-excess phase. (Wyckoff of each sites; Li and Fe_{Li}: 4*a*; Fe, Li_{Fe}, P, O1 and O2: 4*c*; O3: 8*d*)

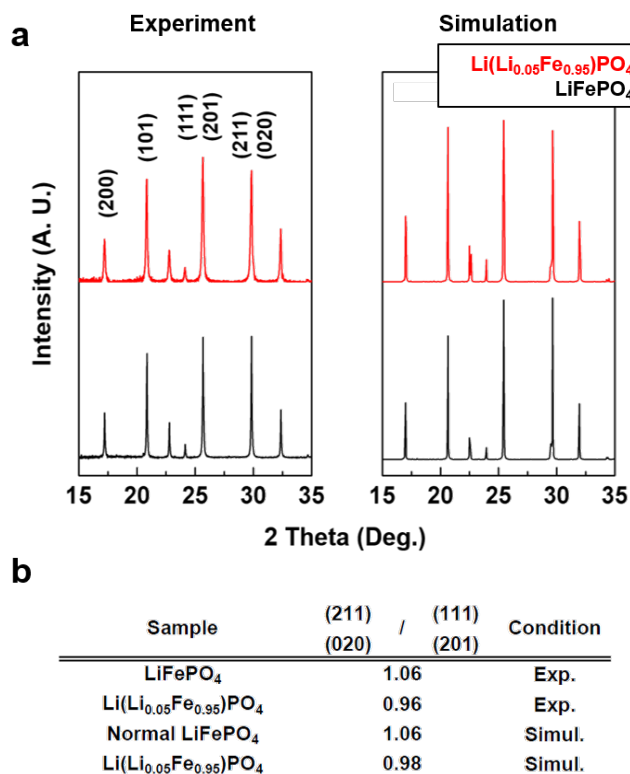


Figure 3-5. High resolution XRD experiment and simulation results (a).

We conduct XRD simulation for confirming how the XRD peak intensity ratio change at lithium-excess LFP with zero anti-site. Left figure in (a) shows the experiment result and right figure shows the simulation result. The intensity ratio of (111)(201) and (211)(020) is mainly change at both experiment and simulation results as exhibited in table (b).

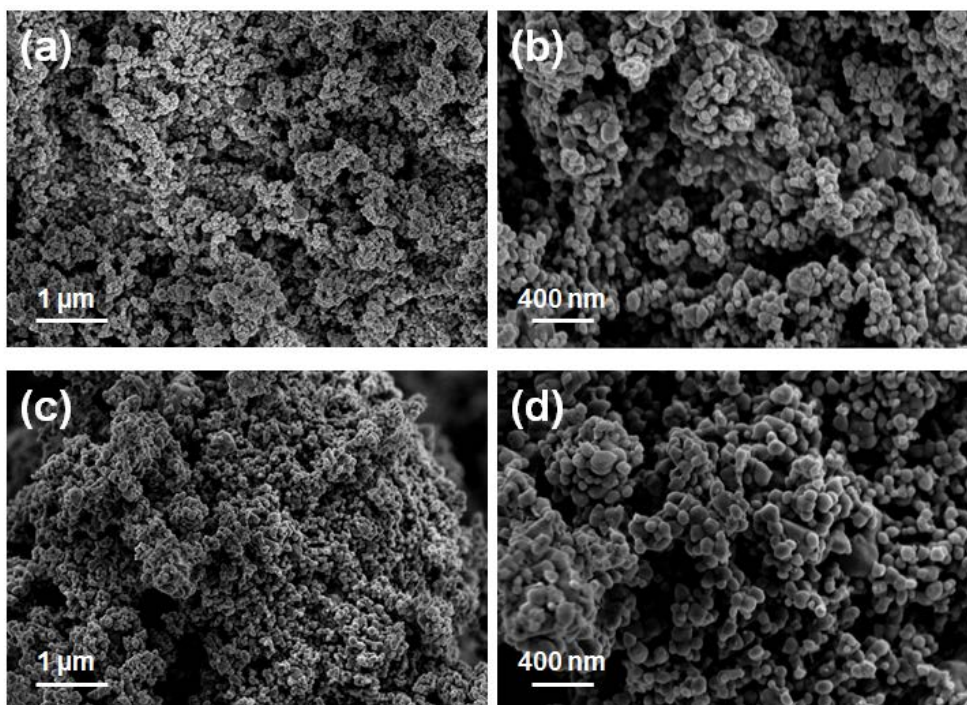


Figure 3-6. SEM image of normal and 5 % lithium-excess LFPs. The figure (a) and (b) show normal LFP. The figure (c) and (d) show 5 % lithium-excess LFP. The particle size of Li-excess LFP (~ 150 nm) is slightly higher than normal LFP (~ 100 nm).

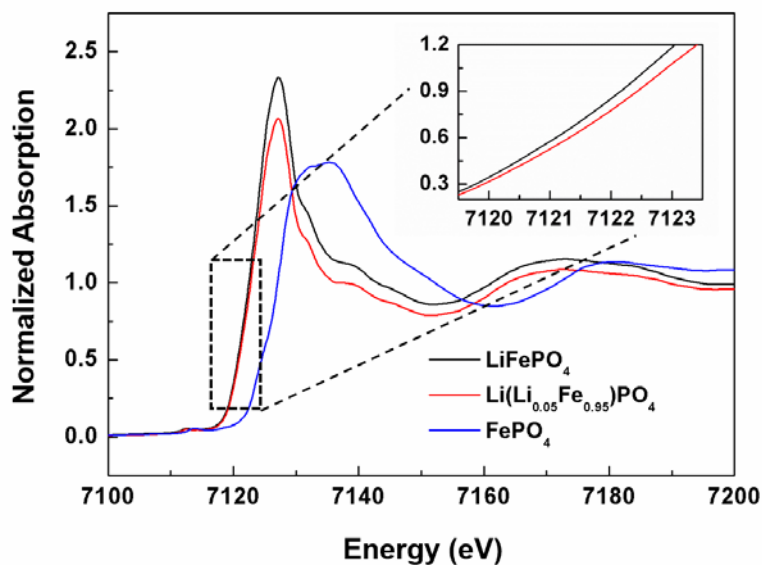


Figure 3-7. Fe XANES measurements for three samples of lithium-excess LFP, normal LFP and normal FP (delithiated LFP). The lithium-excess LFP olivine shows a slightly higher Fe oxidation state than that in the normal LFP.

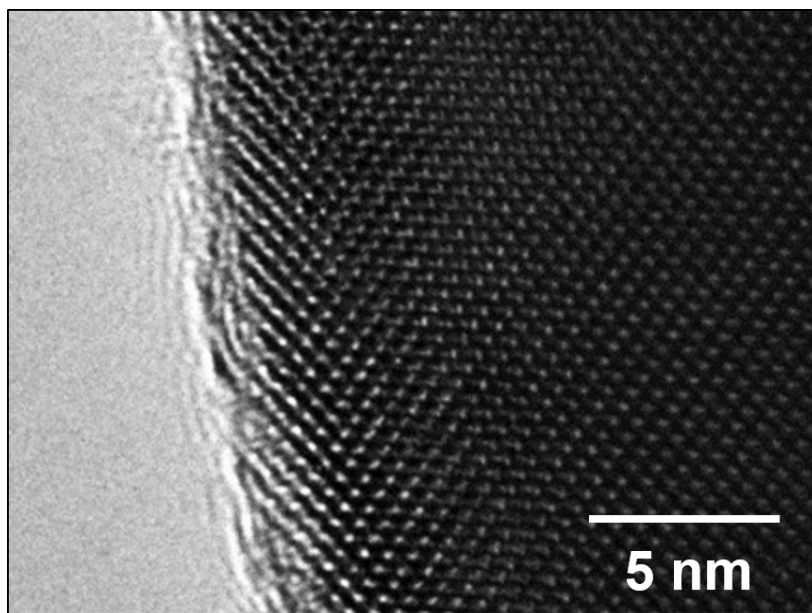


Figure 3-8. TEM image of lithium-excess LFP surface

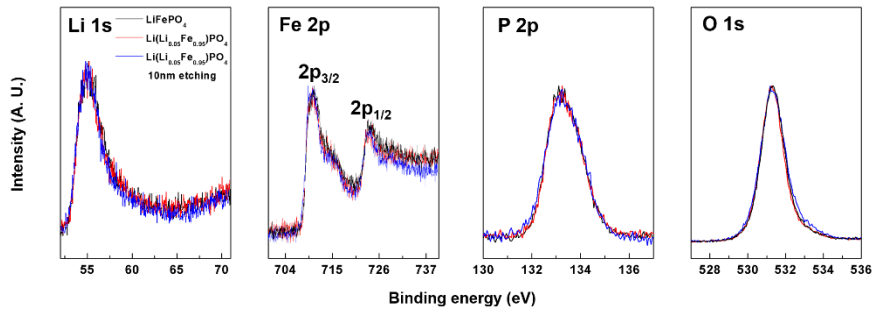


Figure 3-9. Surface analysis on 5 % lithium-excess LFP (red line) and normal LFP. (black line) 10 nm etched surface of lithium-excess LFP is marked by blue lines.(left to right, Li 1s, Fe 2p, P 2p and O 1s XPS)

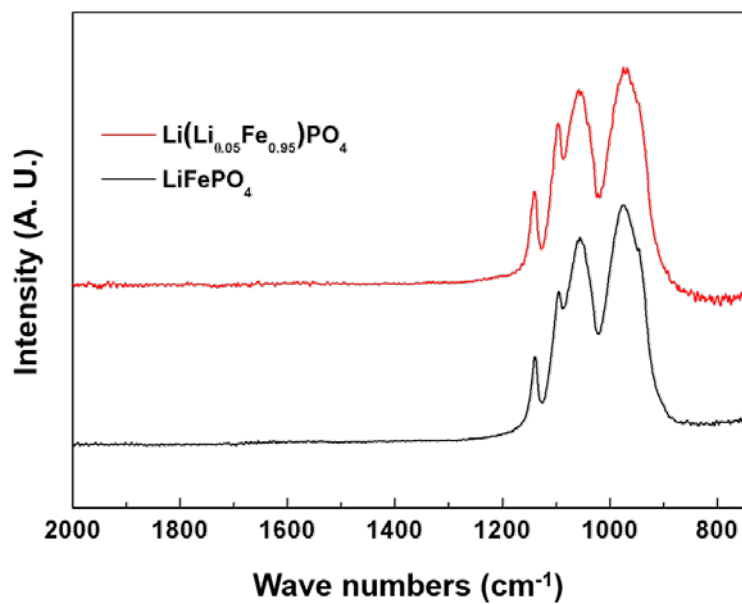


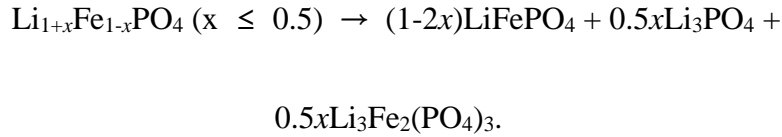
Figure 3-10. Fourier transform infrared spectroscopy (FT-IR) results of lithium-excess (red) and normal LFPs (black). Both materials does not show any impurities signal.

3.3.2 Local atomic configuration and origin of zero Fe anti-site of lithium-excess olivine

Further confirmation of the excess lithium in the LFP could be obtained from the ${}^6\text{Li}$ -NMR measurement using ${}^6\text{Li}$ -labeled samples. Figure 3-11 (a) presents the NMR spectra of ${}^6\text{LiFePO}_4$ and ${}^6\text{Li}({}^6\text{Li}_{0.05}\text{Fe}_{0.95})\text{PO}_4$. Except for the side bands marked with asterisks, a single Li signal is observed between 0 to -100 ppm for both samples. In the zoomed-in view in Figure 3-11 (b), the normal LFP shows a lithium signal at -49 ppm, which is in good agreement with previous reports.[48, 49] However, a less-negative-shifted major NMR signal is observed for lithium-excess LFP at -18 ppm. In addition, the asymmetric nature of the major signal strongly suggests that a small positive-shifted minor peak (+ 47 ppm) is present based on the spectral deconvolution. In the olivine LiFePO_4 crystal, the Li_{Li} (octahedral, M1 site) is coordinated with six oxygen atoms, which also coordinate with six different iron atoms (octahedral, M2 site), as illustrated in Figure 3-12 (a). The Li-O-Fe bonds around Li_{Li} result in near-90° Li-O-Fe angle contacts, inducing a strong paramagnetic interaction (marked by the red dashed line in Figure 3-12 (a)), and 120°-angle contacts, inducing a relatively weak paramagnetic interaction (marked by the blue dashed line in Figure 3-12 (a)). The major NMR peak at -49 ppm in normal LFP or -18 ppm in lithium-excess LFP primarily originates

from the strong near-90° Li-O-Fe interaction resulting from the geometry-dependent delocalization of the unpaired electron spin density of Fe^{2+} . [48, 49] However, the less-negative shift of the major peak for lithium-excess LFP (-18 ppm) is most likely due to the slightly higher average oxidation state of Fe ions around Li_{Li} . Previous NMR reports on LiFePO_4 , $\text{Li}_{0.6}\text{FePO}_4$, and $\text{Li}_{0.54}\text{FePO}_4$ indicated that the major NMR peak gradually shifts to higher frequency (less negative values) with decreasing lithium content and increasing Fe^{3+} content in the olivine, which is consistent with our results. [48, 50-52] The excess lithium residing in the Fe site (Li_{Fe} anti-site) results in the additional minor peak at +47 ppm in the lithium-excess LFP. According to the previous NMR report on the normal LFP that contains a significant amount of $\text{Li}_{\text{Fe}}\text{-Fe}_{\text{Li}}$ anti-site defects, the lithium in Fe sites (M2) with a similar environment to the Li_{Fe} ions in our lithium-excess LFP exhibited a positive NMR peak shift at +75 ppm. [50] Our density functional theory (DFT) calculations (Figure 3-13) indicated that the oxidized Fe ions are mainly localized near Li_{Fe} with the oxidation state of $\text{Fe}^{2.x+}$ ($0 < x < 0.5$), which results in the four $\text{Fe}^{2.x+}$ ($0 < x < 0.5$) ions surrounding the lithium octahedron (Figure 3-12 (b)). All four $\text{Fe}^{2.x+}$ ions are bonded with a near-120° Li-O-Fe angle, whose configuration leads to the comparatively weak paramagnetic shift. This unique environment of Li_{Fe} ions generates relatively less of a paramagnetic shift, yielding a positive chemical shift at +47 ppm.

To understand the thermodynamic feasibility of the lithium-excess LFP phase, we attempted to estimate its relative formation energy against the segregation into thermodynamically stable phases of LiFePO_4 , Li_3PO_4 , and $\text{Li}_3\text{Fe}_2(\text{PO}_4)_3$ as follows:



Based on this equation, we calculated the formation energy of 5% lithium-excess LFP using the $\text{Li}_{24/24}(\text{Li}_{1/24}\text{Fe}_{23/24}(\text{PO}_4)_{24})$ model (192 atoms in a unit cell) at zero temperature excluding the entropic effect. The formation energy for one excess lithium (Li_{Fe}), was observed to be approximately 440 meV per event, indicating that the excess lithium ions formed as a ‘anti-site defect’ state in their structure. Considering the relationship between the defect formation energy and its concentration, the comparison of the various defect formation energies would provide a rough idea of the feasibility of the excess lithium ‘defect’ in the olivine, particularly for defects in an olivine framework.[2] It is noteworthy that the formation energy of $\text{Li}_{\text{Fe}}\text{-Fe}_{\text{Li}}$ anti-site

defect in typical olivine LiFePO_4 is approximately 420 meV per event, and depending on the synthetic routes, olivine LFPs with ~5 % anti-site defect concentration can be easily synthesized.[5] Thus, the synthesis of the olivine LFP with ~5 % excess lithium, which requires ~440 meV defect formation energy, may be plausible. As the concentration of $\text{Li}_{\text{Fe}}\text{-Fe}_{\text{Li}}$ anti-site defect in normal LFP decreases with higher post heat treatments because the materials reach the thermodynamically more stable crystalline state,[5, 53] we also observed that a phase separation into thermodynamically stable phases occurs for lithium-excess LFP above 700 °C based on the temperature-controlled *in-situ* XRD results (see Figure 3-14).

Given the structural analysis of the lithium-excess LFP, most notably, it contains zero Fe_{Li} anti-sites in the M1 sites. Although the excess content of lithium can statistically reduce the probability of transition metal (Fe) occupancy in Li sites, which is similarly observed in lithium-excess $\text{Li}(\text{Li}_x, (\text{Ni}, \text{Mn})_{1-x})\text{O}_2$ ($x > \sim 0.2$) with less Li/Ni site disorder up to 2 %, [54] the complete disappearance of Fe ions in the lithium diffusion channel with only 5% excess lithium is quite remarkable. To further understand the role of the excess lithium present in the structure in reducing the concentration of Fe_{Li} defects, we calculated the defects formation energies on various defects configuration containing Fe_{Li} defect around the excess lithium (Li_{Fe}) using

DFT calculations. (Note that the possible anti-site defects containing Fe_{Li} anti-site in lithium-excess LFP are only $\text{Li}_{\text{Fe}}\text{-Fe}_{\text{Li}}$ paired anti-site configuration.) In this calculation, we considered 17 different $\text{Li}_{\text{Fe}}\text{-Fe}_{\text{Li}}$ anti-site configurations around the excess lithium up to second-nearest transition metal neighbors along each axis (Figure 3-15 shows the detailed atomic configurations). All the defect formation energies of the 17 different configurations are shown as a function of the distance from excess Li_{Fe} ion in Figure 3-17. It is observed that the $\text{Li}_{\text{Fe}}\text{-Fe}_{\text{Li}}$ anti-site energy generally increases as it approaches the excess lithium, indicating that the presence of excess lithium energetically disfavors the formation of an anti-site defect near itself. We also observed that even the lowest defect formation energy (Figure 3-18) was as high as 0.823 eV, which is 2 times larger than the typical $\text{Li}_{\text{Fe}}\text{-Fe}_{\text{Li}}$ anti-site formation energy (0.42 eV, see Figure 3-16) observed in normal LFPs.[3] Because the defect formation is inversely proportional to the exponential value of the formation energy, an increase in the formation energy by ~ 0.4 eV would reduce the probability of the anti-site formation near the excess lithium (Li_{Fe}) by 7 orders of magnitude at room temperature. This remarkable reduction arises from the unfavorable electrostatic interaction among Fe ions around the excess lithium (Li_{Fe}), as shown in Figure 3-18. When the $\text{Li}_{\text{Fe}}\text{-Fe}_{\text{Li}}$ anti-site is introduced near the excess lithium (Li_{Fe}), the neighboring Fe ion becomes oxidized to Fe^{3+} in the locally lithium-rich region.

In addition, under this condition, the site-exchanged Fe^{2+} ion (Fe_{Li}) suffers from a stronger repulsion force from the neighboring Fe^{3+} ion (Figure 3-18, red arrow), which significantly increases the formation energy of the Fe_{Li} anti-site. Considering that the one excess lithium event affects at least 17 neighboring Fe ion sites among the second-nearest neighbors we considered, approximately 4 % excess lithium would result in all the Fe ions sites being affected if the excess lithium ions were homogeneously distributed in the olivine crystal. Thus, the overall $\text{Li}_{\text{Fe}}\text{-Fe}_{\text{Li}}$ anti-site concentration in the lithium-excess LFP would be 1.2×10^{-7} times less than that in the normal LFP at room temperature. This finding implies that the excess lithium in the olivine reduces the Fe_{Li} anti-site defects not only by statistically lowering the probability of Fe occupancy in Li sites from the excessive amount of lithium but also by energetically disfavoring the formation of anti-sites, suggesting that this approach could be effective in producing a zero anti-site olivine. Our results also partly agree with a previous work by Hoang and Johannes, where they reported that the formation energies of Li_{Fe} and Fe_{Li} anti-site defects could be sensitively affected by the presence of lithium-rich phases.[26]

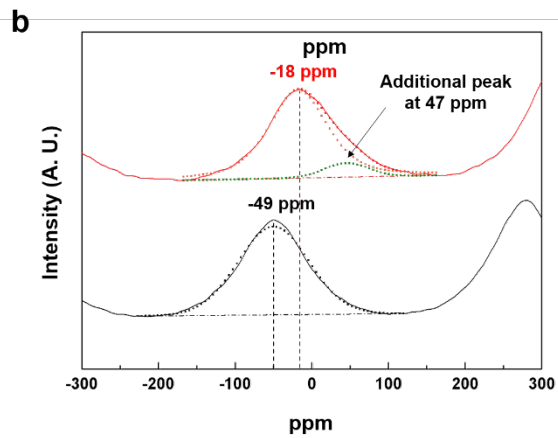
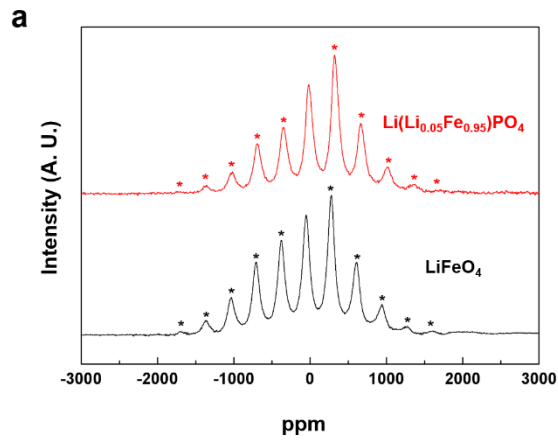


Figure 3-11. ${}^6\text{Li}$ NMR resonance (a) ${}^6\text{Li}$ NMR resonance of lithium-excess LFP (red) and normal LFP (black) with side bands (asterisk). (b) Spectral deconvolution of ${}^6\text{Li}$ NMR peaks. The normal LFP contains single resonance at -49 ppm, and the lithium-excess LFP contains two resonances at -18 and +47 ppm.

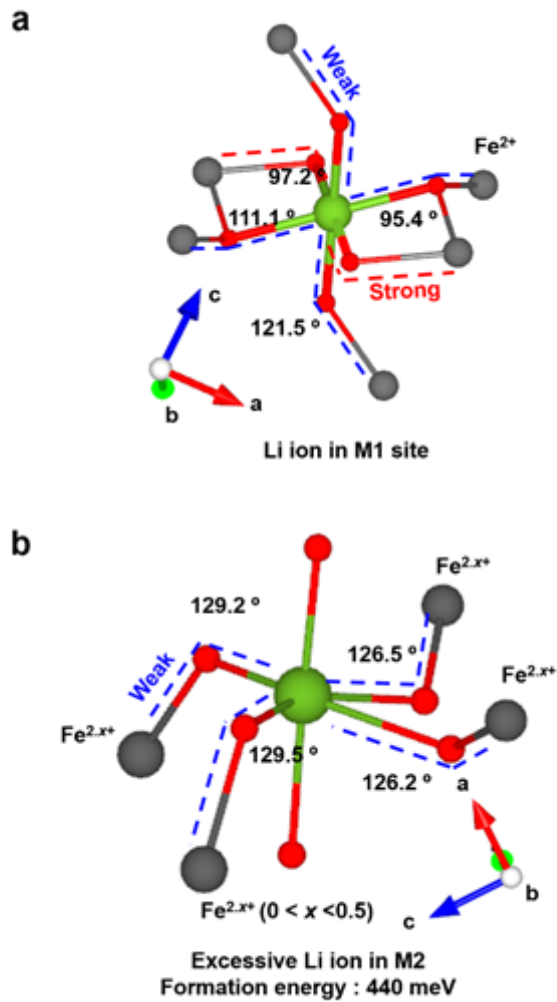


Figure 3-12. Local atomic configurations (c) Local atomic configuration around Li ion in M1 site in normal LFP and (d) excess Li ion in M2 in lithium-excess LFP calculated by DFT method. The red and blue dashed lines indicate strong and weak paramagnetic interactions between Li and Fe ions, respectively.

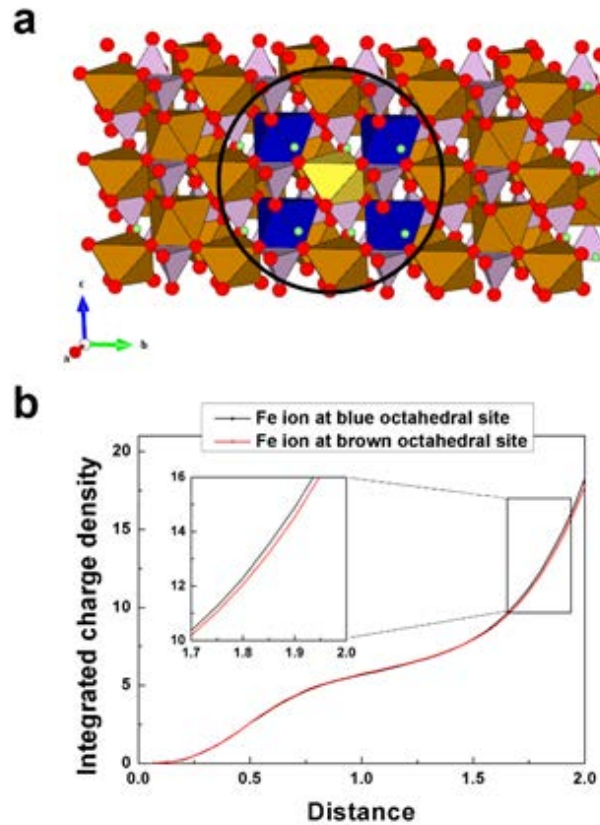


Figure 3-13. Local Fe ion oxidation state (a) The most stable lithium-excess configuration calculated by DFT calculation tool. (yellow octahedral: Li_{Fe} (Li-excess ion), blue octahedral: $\text{Fe}^{2.x+}$ ($0 < x < 0.5$) ion and brown octahedral: Fe^{2+} octahedral). (b) The integrated charge density as a function of distance from center of Fe ion. The Fe ions positioning in blue octahedral site contain additional electron compared with other Fe ions. (brown octahedral) The Fe oxidation state that the charge is delocalized in four $\text{Fe}^{2.x+}$ ($0 < x < 0.5$) ions surround excessive Li_{Fe} is distinct from that of conventional LFP

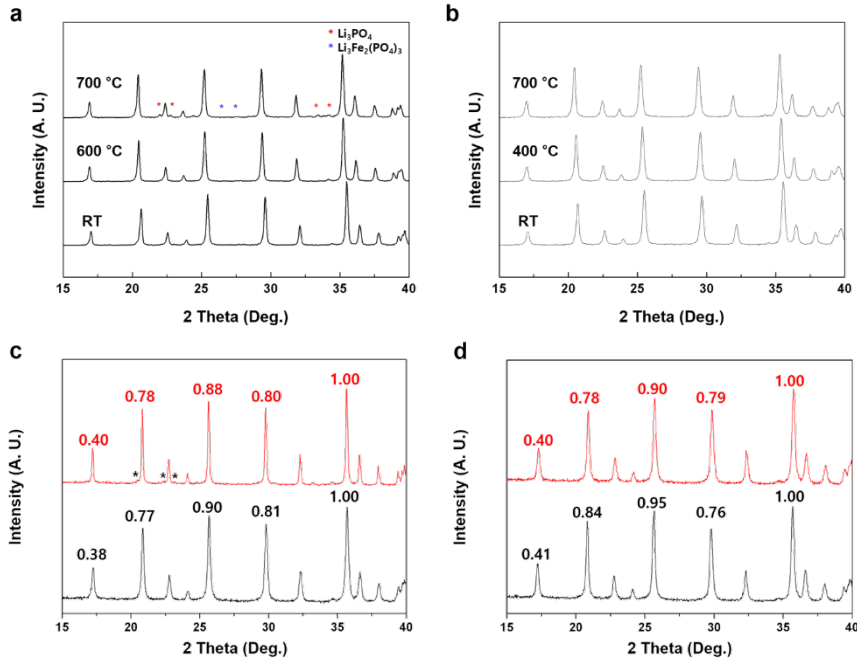
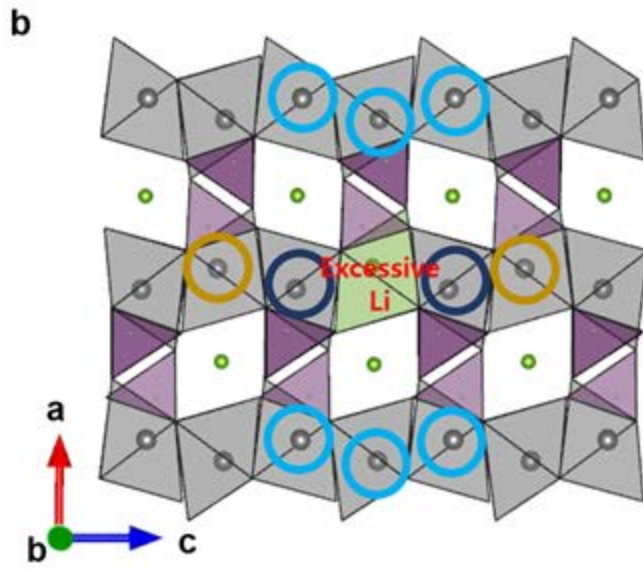
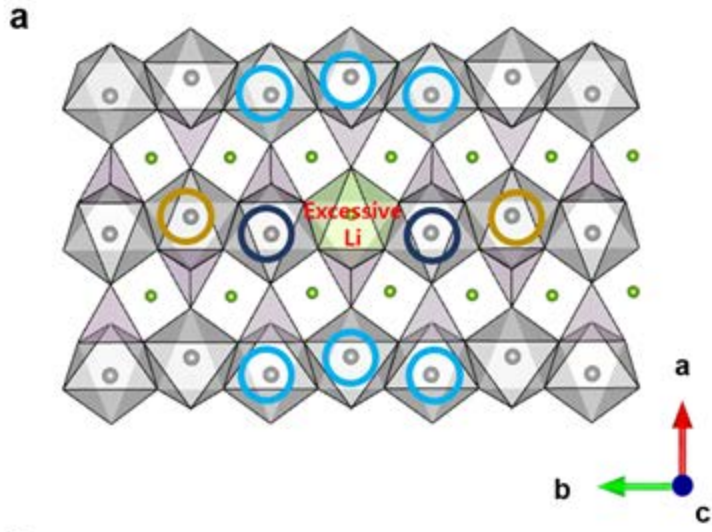
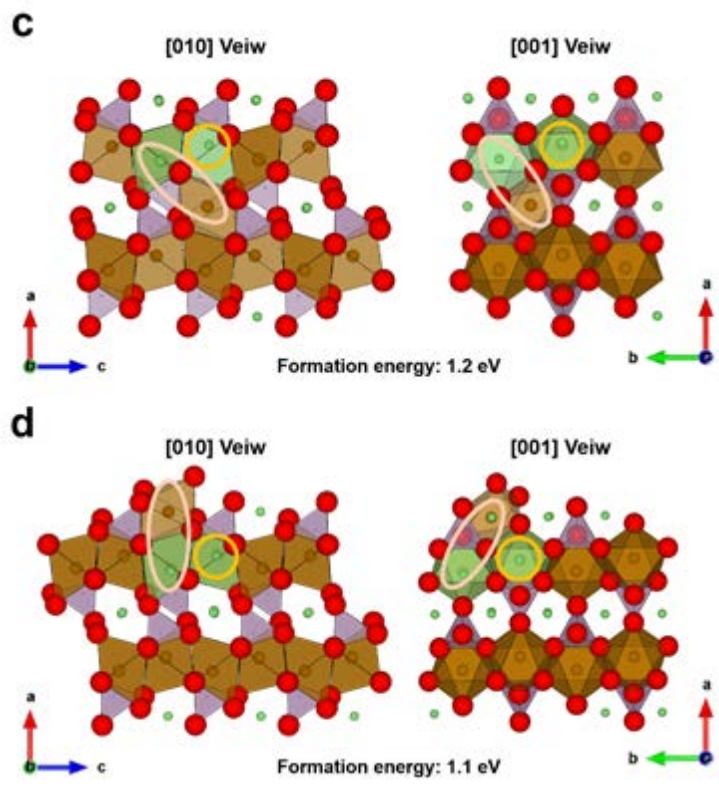


Figure 3-14. In-situ temperature controlled XRD patterns at Ar condition of (a) 5 % lithium-excess LFP and (b) normal LFP. Over the 700 °C, the lithium-excess LFP shows Li_3PO_4 and $\text{Li}_3\text{Fe}_2(\text{PO}_4)_3$ impurities marked by asterisks. Figure (c) and (d) show the intensity ratio change before (black) and after (red) heat treatment at 700 °C of lithium-excess (c) and normal LFPs (d) at room temperature respectively. Before treatment, the intensity ratios of both samples (black lines) are quite different, however, after treatment, these become similar. (red lines) It indicates that the lithium-excess LFP decomposed to stable normal LFP phase and impurities after 700 °C heat treatment.



-  First neighbor Fe ions (4)
-  Second neighbor Fe ions along *a*-axis (9)
-  Second neighbor Fe ions along *b*- or *c*- axis (9)



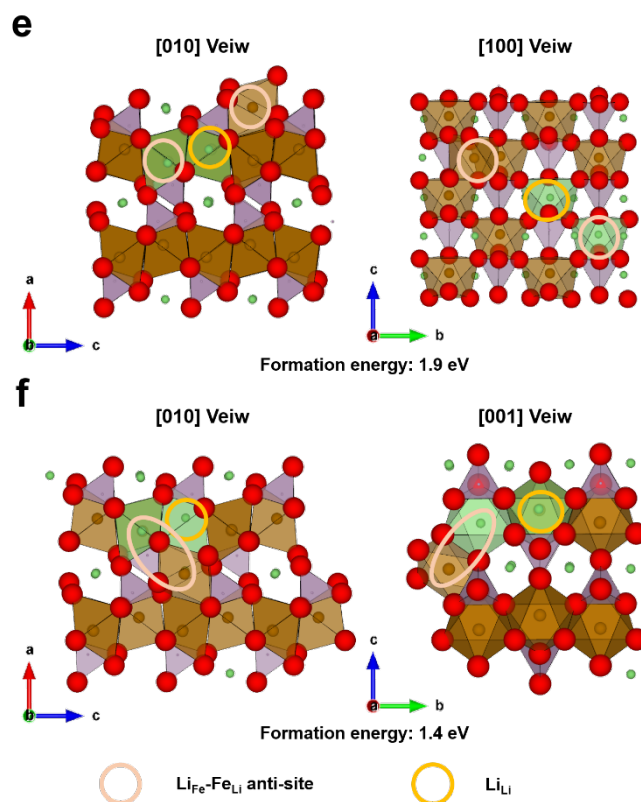


Figure 3-15. Possible cation exchange sites (LiFe-FeLi anti-site) at lithium-excess phase. Each figures shows a plane schematic figure of lithium-excess LFP along (a) c -axis and (b) b -axis. The sites are categorized by 3 kinds; i) First neighbor Fe ions, (marked by deep blue circle) ii) second neighbor Fe ions along a -axis (marked by sky blue circle) and iii) second neighbor Fe ions along b - or c -axis (marked by earthy yellow) of excessive Li ion. The numbers in parentheses indicate number of possible sites. (c), (d), (e) and (f) exhibit the representative $\text{Li}_{\text{Fe}}\text{-Fe}_{\text{Li}}$ pairing anti-site configuration in lithium-excess LFP which are calculated at our work. The pink and yellow circles indicate $\text{Li}_{\text{Fe}}\text{-Fe}_{\text{Li}}$ pairing anti-site and excess lithium ion respectively.

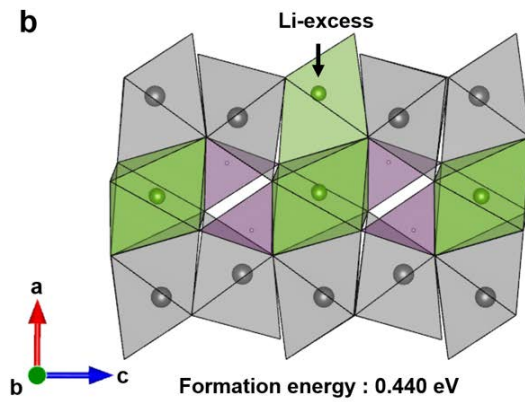
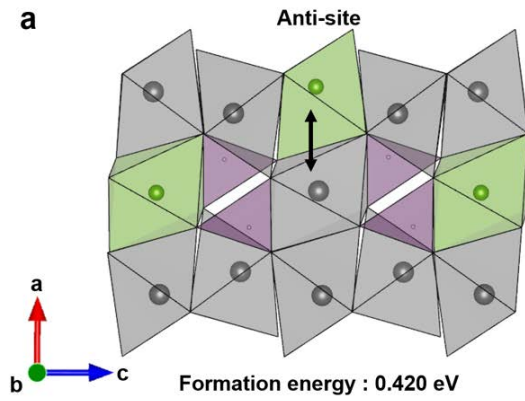


Figure 3-16. Anti-site configuration and its formation energy (a) Typical anti-site configuration and formation energy in normal LFP phase and (b) lithium-excess local configuration and formation energy.

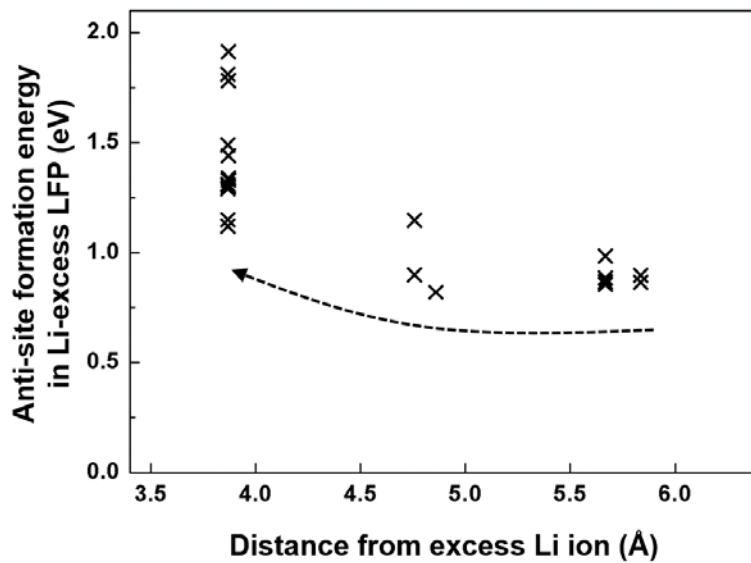


Figure 3-17. Anti-site defect formation energies at lithium-excess LFP as a function of distance from Li_{Fe} .

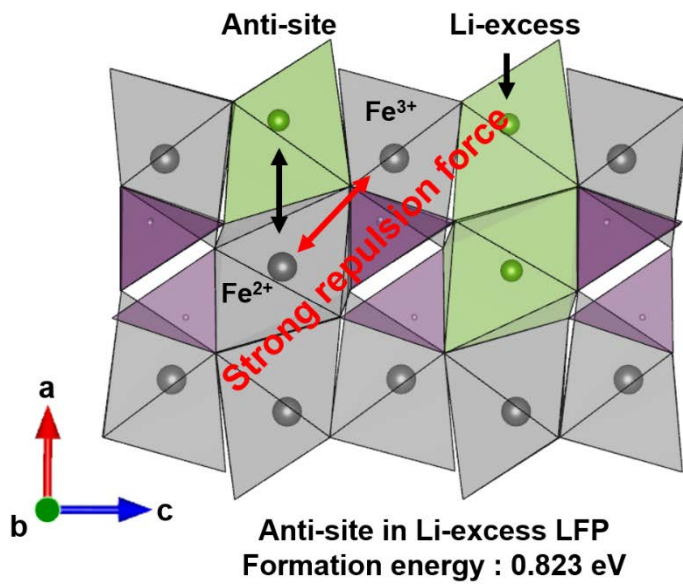


Figure 3-18. The most stable anti-site configuration in lithium-excess LFP. Site exchanged Fe^{2+} ion (anti-site) and Fe^{3+} ion positioning near excess Li ion make a strong electrostatic repulsion.

3.3.3 New [101] diffusion path of lithium-excess olivine

The occupancy of excess lithium in the Fe site can open up a new lithium diffusion pathway by connecting the nearby lithium channels. It is well known that the olivine crystal has only one diffusion channel along the [010] direction with a low activation barrier (~ 0.44 eV), whereas lithium diffusion across the channels in other directions such as [101] or [001] requires too high of an activation barrier because of the strong electrostatic repulsion from the Fe and insufficient space for lithium hopping, as listed in Figure 3-19.[55, 56] The replacement of the high-valent Fe ions by lithium ions reduces the electrostatic repulsion, thus facilitating lithium hopping around the lithium (Li_{Fe}), as observed in the reduction of the activation barriers along [001] and [010]. Also, the lowered lithium ion diffusion activation energies could be confirmed by electrochemical impedance spectroscopy (EIS) measurement. (See Figure 3-20) Most remarkable is that the excess lithium in the Fe site is also mobile and can diffuse into the nearby lithium channel along [101], participating in the overall diffusion process in the crystal. Our DFT calculations reveal that the presence of lithium in the Fe site opens up a new alternative diffusion path along the [101] direction with a significantly reduced activation barrier of ~ 0.82 eV (Figure 3-22) compared with more than 2 eV for normal LFP (Figure 3-23) along the same direction.[57] The

calculated activation barrier is also similar with the value reported by Dathar et. al. along the [101] diffusion channel containing $\text{Fe}_{\text{Li}}\text{-Li}_{\text{Fe}}$ pairing anti-site.[58] Figure 3-24 and Figure 3-25 present a schematic illustration of lithium hopping along the [101] direction and the corresponding energy profile for normal and lithium-excess LFPs. In the normal LFP, the lithium hopping along the [101] direction is under severe electrostatic repulsion from the nearby corner-sharing Fe ions, and the lithium ion is forced to pass through the oxygen dumbbell, as shown in Figure 3-25. The narrow space between the two oxygens ($\sim 3.05 \text{ \AA}$) disfavors the lithium hopping, resulting in the activation barrier of more than 2 eV. In the lithium-excess LFP, however, the corner-sharing Fe is replaced with lithium, which also participates in the diffusion. Thus, the diffusing lithium ion no longer needs to bypass the high-valent Fe and can hop through the space provided by Li_{Fe} (Figure 3-24). The rate-limiting step during lithium hopping along the [101] direction in the lithium-excess LFP also lies in the step of passing through the Li_{Fe} site. Compared with normal LFP, where the lithium ion squeezes into the narrow oxygen dumbbell, the new intermediate state offered by the Li_{Fe} site provides sufficient space, thus lowering the activation barrier for hopping.

The activation barrier of $\sim 0.82 \text{ meV}$ is slightly higher than that observed for fast lithium pathways but is comparable to that of diffusion paths observed

for NaFeSO_4F [59] and LiMnPO_4 [60], implying feasible lithium diffusion along the new path. The [101] route may not be a main diffusion path during fast charge/discharge cycling at room temperature considering the higher activation energy compared with that of the [010] diffusion path and relatively low concentration of lithium-excess, but would support the main [010] diffusion channel as an alternative route, particularly in the presence of immobile impurities in the [010] channel. As Malik *et al.* noted,[17] the immobile impurities in the [010] channel force lithium ions to detour through high-activation-barrier paths such as [101], which reduces the room-temperature specific capacity and ionic conductivity. Thus, the availability of even a small number of low-activation-barrier detour paths would support the overall lithium diffusivity in the defect-containing LFP. It is noteworthy that a similar phenomenon was observed in the rock-salt-type lithium-excess $\text{Li}_{1.211}\text{Mo}_{0.467}\text{Cr}_{0.3}\text{O}_2$, which exhibited remarkably enhanced ionic conductivity and capacity with the introduction of an excess amount of lithium, implying that the ‘excess-lithium strategy’ can be used as a general method to open multiple new lithium diffusion paths in solid-state lithium ionic conductors.[41]

Direction	Activation barrier (meV)	
	LiFePO ₄	Li(Li _{0.05} Fe _{0.95})PO ₄
[010]	444	328
[001]	2187	1850
[101]	2186	819

Figure 3-19. Activation barriers for lithium ion hopping for normal and lithium-excess LFPs.

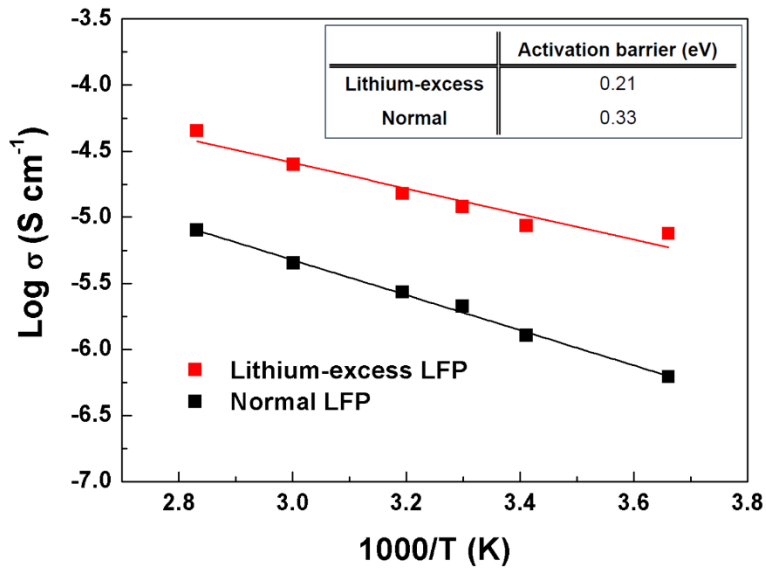


Figure 3-20. Conductivity change of Li-excess and normal LFPs at 0, 20, 30, 40, 60 and 80 °C. The EIS measurements were conducted with 3 MHz ~ 0.1 Hz using Ag/sample/Ag symmetric cells. The Li ion diffusion activation barrier is calculated based on thermal driven conductivities. The activation barriers are obtained as 210 and 330 meV for lithium-excess and normal LFP, respectively.

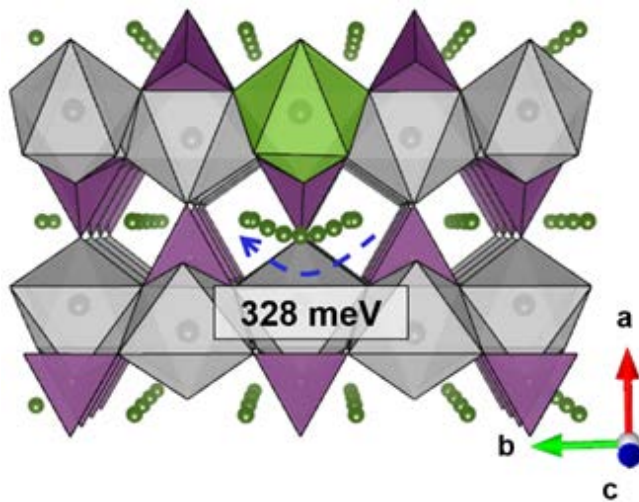


Figure 3-21. The schematics of Li ion diffusion along [010] direction in lithium-excess LFP.

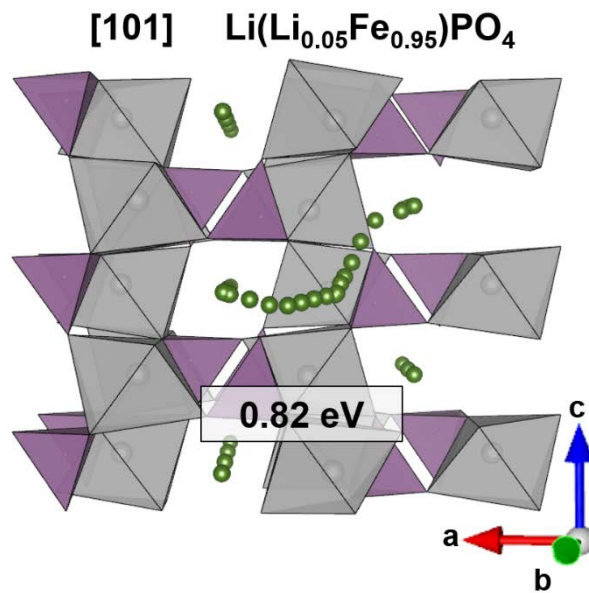


Figure 3-22 The schematics of Li ion diffusion along [101] direction in lithium-excess LFP

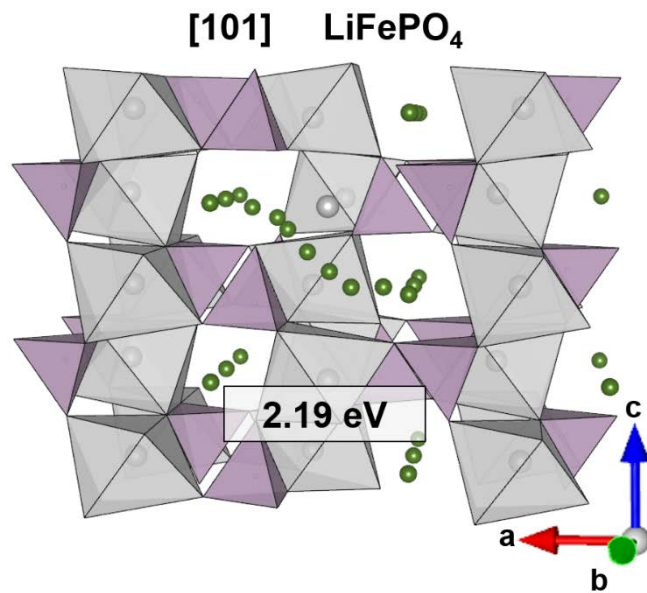


Figure 3-23. The schematics of Li ion diffusion along [101] direction in normal LFP

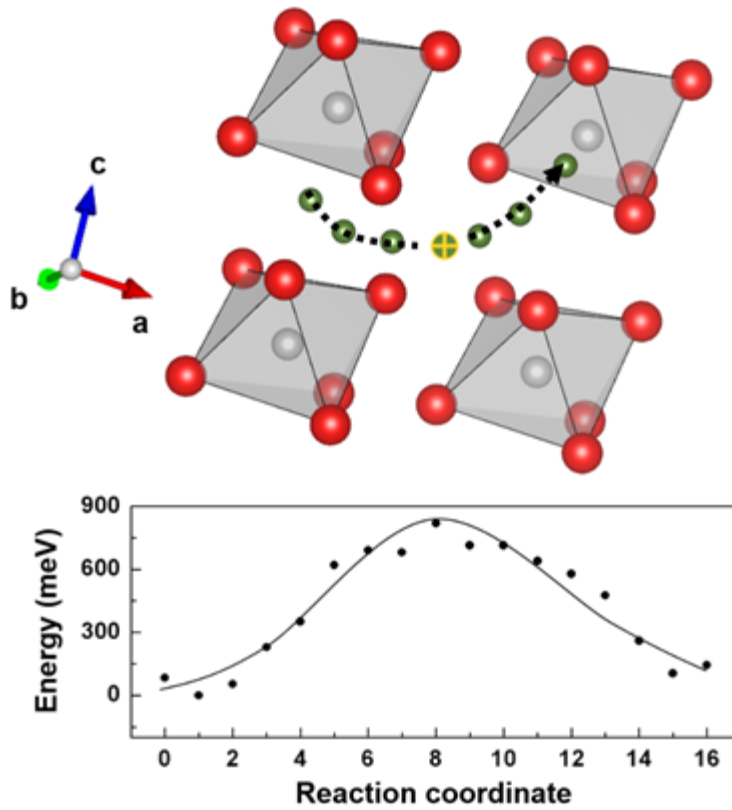


Figure 3-24. [101] activation barrier of lithium-excess LFP. It show the close view of lithium diffusion along with the energy profiles. (Li ions in the highest energy state marked by yellow)

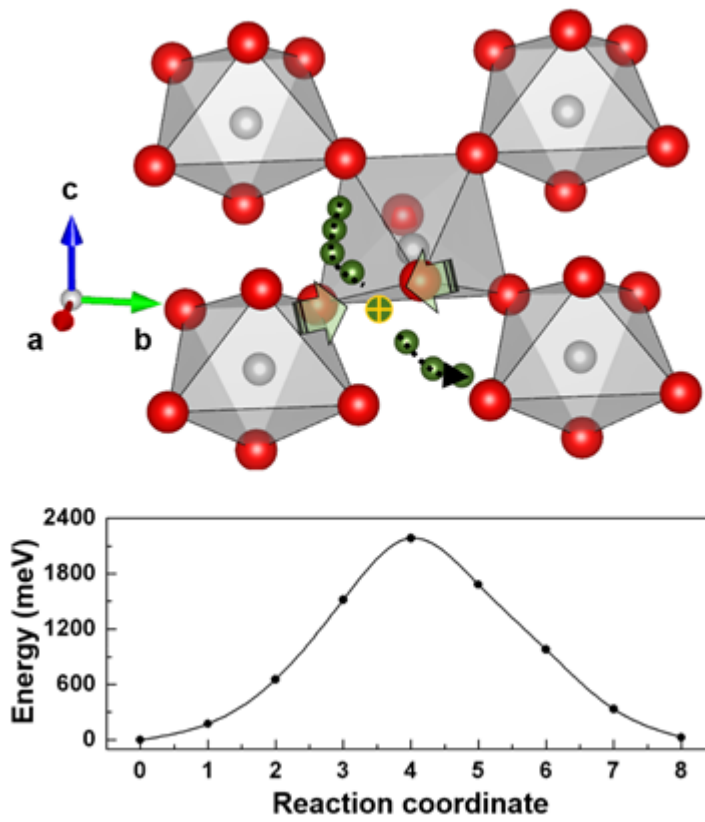


Figure 3-25. [101] activation barrier of normal LFP. It show the close view of lithium diffusion along with the energy profiles. (Li ions in the highest energy state marked by yellow)

3.3.4 Electrochemical properties

The electrochemical properties of lithium-excess LFP were investigated using a Li metal counter electrode in a 2032 coin-type cell. (Figure 3-26 (a)) presents the galvanostatic electrochemical profiles of lithium-excess LFP compared with that of normal LFP at a 10 mA g^{-1} current rate (red: lithium-excess LFP, black: normal LFP). The lithium-excess LFP electrode delivers a slightly lower capacity of $\sim 157 \text{ mAh g}^{-1}$ compared with the normal LFP, $\sim 166 \text{ mA g}^{-1}$, which is due to the higher oxidation state of Fe and the smaller number of available $\text{Fe}^{2+/3+}$ redox couples in $\text{Li}^{1+}(\text{Li}^{1+}_{0.05}[\text{Fe}^{2+}_{0.90}\text{Fe}^{3+}_{0.05}])\text{PO}_4$. Nevertheless, it is notable that a lower polarization gap between charge and discharge was observed for lithium-excess LFP compared with normal LFP under the same electrochemical conditions. The smaller polarization was consistently observed with varying current densities from 30 mA g^{-1} to 0.17 mA g^{-1} , corresponding to a C/1000 rate of LFP, as shown in Figure 3-26 (b). With the extrapolation of the curve toward zero current, the minimum values of the hysteresis gaps reach 20 mV and 30 mV for lithium-excess and normal LFPs, respectively. As the near-zero-current polarization of LFP is related to the delithiation mechanism of single-particle LFP and has been regarded as a thermodynamic property, the different values of the two LFPs imply the distinguishable delithiation behaviors, as will be discussed in further detail.

Additional experiments and discussion regarding the zero-current polarization is provided in the Figure 3-27.

The rate capabilities of lithium-excess LFP were measured at various current rates as shown in Figure 3-28. (The charge/discharge profiles are provided in Figure 3-29) The lithium-excess LFP electrode exhibited a notably improved rate capability compared with that of the normal LFP even though the particle size of lithium-excess LFP is slightly larger, as previously illustrated. Lithium-excess LFP delivers a discharge capacity of 78 mAh g⁻¹ at a current density of 8 A g⁻¹, which is equivalent to approximately 50 C (Figure 3-28). Compared with normal LFP electrodes, this value represents an approximately 2-times-higher capacity. The specific power density calculated at 8 A g⁻¹ is approximately 20 kW kg⁻¹, which is higher than that of other previously reported LFPs that have undergone surface chemical modification or nano-sizing processes, as shown in Figure 3-30.[61-64] After 500 cycles at 0.5 A g⁻¹, the lithium-excess LFP still exhibited 82 % retention of the initial capacity, maintaining a high charge/discharge efficiency in Figure 3-31.

3.4 Conclusion

We successfully synthesized a lithium-excess LFP, $\text{Li}(\text{Li}_{0.05}\text{Fe}_{0.95})\text{PO}_4$, using a solid-state method. The new LFP exhibited unexpected physical and chemical properties that are remarkably distinguishable from those of normal LFP, which is primarily due to the zero Fe_{Li} anti-site defects. The origin of the zero Fe_{Li} anti-site defects is attributed to not only the excess lithium that statistically precludes the occupancy of Fe in lithium sites but also the enlarged anti-site formation energy resulting from the stronger repulsion from higher-valent Fe. We demonstrated that the local lithium-excess configuration (i) provides additional lithium diffusion paths along the [101] directions.

3.5 References

1. Armand, M. and J.M. Tarascon, Building better batteries. *Nature*, 2008. **451**(7179): p. 652-657.
2. Vineyard, G.H. and G.J. Dienes, The Theory of Defect Concentration in Crystals. *Physical Review*, 1954. **93**(2): p. 265-268.
3. Islam, M.S., et al., Atomic-Scale Investigation of Defects, Dopants, and Lithium Transport in the LiFePO₄ Olivine-Type Battery Material. *Chemistry of Materials*, 2005. **17**(20): p. 5085-5092.
4. Wang, J., et al., Size-dependent surface phase change of lithium iron phosphate during carbon coating. *Nat Commun*, 2014. **5**.
5. Chen, J. and J. Graetz, Study of Antisite Defects in Hydrothermally Prepared LiFePO₄ by in Situ X-ray Diffraction. *ACS Applied Materials & Interfaces*, 2011. **3**(5): p. 1380-1384.
6. Delmas, C., et al., On the behavior of the Li_xNiO₂ system: an electrochemical and structural overview. *Journal of Power Sources*, 1997. **68**(1): p. 120-125.
7. Sasaki, T., Y. Ukyo, and P. Novák, Memory effect in a lithium-ion battery. *Nat Mater*, 2013. **12**(6): p. 569-575.
8. Li, Y., et al., Current-induced transition from particle-by-particle to concurrent intercalation in phase-separating battery electrodes. *Nat Mater*,

2014. **13**(12): p. 1149-1156.

9. Gibot, P., et al., Room-temperature single-phase Li insertion/extraction in nanoscale Li_xFePO_4 . *Nat Mater*, 2008. **7**(9): p. 741-747.

10. Delmas, C., et al., Lithium deintercalation in LiFePO_4 nanoparticles via a domino-cascade model. *Nat Mater*, 2008. **7**(8): p. 665-671.

11. Bai, P. and M.Z. Bazant, Charge transfer kinetics at the solid–solid interface in porous electrodes. *Nat Commun*, 2014. **5**.

12. Delacourt, C., et al., The existence of a temperature-driven solid solution in Li_xFePO_4 for $0 < x < 1$. *Nat Mater*, 2005. **4**(3): p. 254-260.

13. Padhi, A.K., K.S. Nanjundaswamy, and J.B. Goodenough, Phospho-olivines as Positive-Electrode Materials for Rechargeable Lithium Batteries. *Journal of The Electrochemical Society*, 1997. **144**(4): p. 1188-1194.

14. Nishijima, M., et al., Accelerated discovery of cathode materials with prolonged cycle life for lithium-ion battery. *Nat Commun*, 2014. **5**.

15. Yamada, A., S.C. Chung, and K. Hinokuma Optimized LiFePO_4 for Lithium Battery Cathodes. *Journal of The Electrochemical Society*, 2001. **148**(3): p. A224-A229.

16. Nishimura, S.-i., et al., Experimental visualization of lithium diffusion in Li_xFePO_4 . *Nat Mater*, 2008. **7**(9): p. 707-711.

17. Malik, R., et al., Particle Size Dependence of the Ionic Diffusivity.

Nano Letters, 2010. **10**(10): p. 4123-4127.

18. Tealdi, C., C. Spreatico, and P. Mustarelli, Lithium diffusion in $\text{Li}_{1-x}\text{FePO}_4$: the effect of cationic disorder. *Journal of Materials Chemistry*, 2012. **22**(47): p. 24870-24876.

19. Chung, S.-Y., et al., Atomic-Scale Visualization of Antisite Defects in LiFePO_4 . *Physical Review Letters*, 2008. **100**(12): p. 125502.

20. Chen, J., et al., The hydrothermal synthesis and characterization of olivines and related compounds for electrochemical applications. *Solid State Ionics*, 2008. **178**(31–32): p. 1676-1693.

21. Yang, S., P.Y. Zavalij, and M. Stanley Whittingham, Hydrothermal synthesis of lithium iron phosphate cathodes. *Electrochemistry Communications*, 2001. **3**(9): p. 505-508.

22. Chen, J. and M.S. Whittingham, Hydrothermal synthesis of lithium iron phosphate. *Electrochemistry Communications*, 2006. **8**(5): p. 855-858.

23. Park, K.-Y., et al., Anti-Site Reordering in LiFePO_4 : Defect Annihilation on Charge Carrier Injection. *Chemistry of Materials*, 2014. **26**(18): p. 5345-5351.

24. Radhamani, A.V., et al., Suppression of antisite defects in fluorine-doped LiFePO_4 . *Scripta Materialia*, 2013. **69**(1): p. 96-99.

25. Yuan, S. and K. Dai, Heat-rate-controlled hydrothermal synthesis of LiFePO_4 achieved by different heating sources. *Russian Journal of*

Electrochemistry, 2014. **50**(4): p. 385-389.

26. Hoang, K. and M. Johannes, Tailoring Native Defects in LiFePO₄: Insights from First-Principles Calculations. Chemistry of Materials, 2011. **23**(11): p. 3003-3013.

27. Amisse, R., et al., Nonstoichiometry in LiFe_{0.5}Mn_{0.5}PO₄: Structural and Electrochemical Properties. Journal of The Electrochemical Society, 2013. **160**(9): p. A1446-A1450.

28. Hamelet, S., et al., Existence of Superstructures Due to Large Amounts of Fe Vacancies in the LiFePO₄-Type Framework. Chemistry of Materials, 2011. **23**(1): p. 32-38.

29. Amisse, R., et al., Singular Structural and Electrochemical Properties in Highly Defective LiFePO₄ Powders. Chemistry of Materials, 2015. **27**(12): p. 4261-4273.

30. Chung, S.-Y., et al., Surface-Orientation-Dependent Distribution of Subsurface Cation-Exchange Defects in Olivine-Phosphate Nanocrystals. ACS Nano, 2015. **9**(1): p. 850-859.

31. Schuster, M.E., et al., Charging and Discharging Behavior of Solvothermal LiFePO₄ Cathode Material Investigated by Combined EELS/NEXAFS Study. Chemistry of Materials, 2013. **26**(2): p. 1040-1047.

32. Julien, C.M., A. Mauger, and K. Zaghib, Surface effects on electrochemical properties of nano-sized LiFePO₄. Journal of Materials

Chemistry, 2011. **21**(27): p. 9955-9968.

33. Armstrong, A.R., et al., The lithium intercalation process in the low-voltage lithium battery anode $\text{Li}_{1+x}\text{V}_{1-x}\text{O}_2$. *Nat Mater*, 2011. **10**(3): p. 223-229.

34. Lu, Z., D.D. MacNeil, and J.R. Dahn, Layered Cathode Materials $\text{Li}[\text{Ni}_x\text{Li}(1/3 - 2x/3)\text{Mn}(2/3 - x/3)]\text{O}_2$ for Lithium-Ion Batteries. *Electrochemical and Solid-State Letters*, 2001. **4**(11): p. A191-A194.

35. Yabuuchi, N., et al., Detailed Studies of a High-Capacity Electrode Material for Rechargeable Batteries, $\text{Li}_2\text{MnO}_3\text{-LiCo}_{1/3}\text{Ni}_{1/3}\text{Mn}_{1/3}\text{O}_2$. *Journal of the American Chemical Society*, 2011. **133**(12): p. 4404-4419.

36. Salager, E., et al., Solid-State NMR of the Family of Positive Electrode Materials $\text{Li}_2\text{Ru}_{1-y}\text{Sn}_y\text{O}_3$ for Lithium-Ion Batteries. *Chemistry of Materials*, 2014. **26**(24): p. 7009-7019.

37. Sathiya, M., et al., High Performance $\text{Li}_2\text{Ru}_{1-y}\text{Mn}_y\text{O}_3$ ($0.2 \leq y \leq 0.8$) Cathode Materials for Rechargeable Lithium-Ion Batteries: Their Understanding. *Chemistry of Materials*, 2013. **25**(7): p. 1121-1131.

38. Ma, J., et al., Feasibility of Using Li_2MoO_3 in Constructing Li-Rich High Energy Density Cathode Materials. *Chemistry of Materials*, 2014. **26**(10): p. 3256-3262.

39. Sathiya, M., et al., Origin of voltage decay in high-capacity layered oxide electrodes. *Nat Mater*, 2015. **14**(2): p. 230-238.

40. Sathiya, M., et al., Reversible anionic redox chemistry in high-capacity layered-oxide electrodes. *Nat Mater*, 2013. **12**(9): p. 827-835.
41. Lee, J., et al., Unlocking the Potential of Cation-Disordered Oxides for Rechargeable Lithium Batteries. *Science*, 2014. **343**(6170): p. 519-522.
42. Yoon, M.-S., et al., Synthesis of Li excess LiFePO₄/C using iron chloride extracted from steel scrap pickling. *Metals and Materials International*, 2014. **20**(4): p. 785-791.
43. Huang, W., Q. Cheng, and X. Qin, Effect of Li excess content and Ti dopants on electrochemical properties of LiFePO₄ prepared by thermal reduction method. *Russian Journal of Electrochemistry*, 2010. **46**(3): p. 359-362.
44. Kim, H., et al., Neutron and X-ray Diffraction Study of Pyrophosphate-Based Li_{2-x}MP₂O₇ (M = Fe, Co) for Lithium Rechargeable Battery Electrodes. *Chemistry of Materials*, 2011. **23**(17): p. 3930-3937.
45. Kang, B. and G. Ceder, Battery materials for ultrafast charging and discharging. *Nature*, 2009. **458**(7235): p. 190-193.
46. Zaghbi, K., et al., Unsupported claims of ultrafast charging of LiFePO₄ Li-ion batteries. *Journal of Power Sources*, 2009. **194**(2): p. 1021-1023.
47. Ceder, G. and B. Kang, Response to “unsupported claims of ultrafast charging of Li-ion batteries”. *Journal of Power Sources*, 2009. **194**(2): p.

1024-1028.

48. Cabana, J., et al., MAS NMR Study of the Metastable Solid Solutions Found in the LiFePO₄/FePO₄ System. *Chemistry of Materials*, 2010. **22**(3): p. 1249-1262.

49. Tucker, M.C., et al., Hyperfine Fields at the Li Site in LiFePO₄-Type Olivine Materials for Lithium Rechargeable Batteries: A ⁷Li MAS NMR and SQUID Study. *Journal of the American Chemical Society*, 2002. **124**(15): p. 3832-3833.

50. Upreti, S., et al., Crystal Structure, Physical Properties, and Electrochemistry of Copper Substituted LiFePO₄ Single Crystals. *Chemistry of Materials*, 2011. **24**(1): p. 166-173.

51. Davis, L.J.M., I. Heinmaa, and G.R. Goward, Study of Lithium Dynamics in Monoclinic Li₃Fe₂(PO₄)₃ using ⁶Li VT and 2D Exchange MAS NMR Spectroscopy. *Chemistry of Materials*, 2010. **22**(3): p. 769-775.

52. Hamelet, S., et al., The effects of moderate thermal treatments under air on LiFePO₄-based nano powders. *Journal of Materials Chemistry*, 2009. **19**(23): p. 3979-3991.

53. Omenya, F., et al., Can Vanadium Be Substituted into LiFePO₄? *Chemistry of Materials*, 2011. **23**(21): p. 4733-4740.

54. Armstrong, A.R., et al., Demonstrating Oxygen Loss and Associated Structural Reorganization in the Lithium Battery Cathode

- Li[Ni_{0.2}Li_{0.2}Mn_{0.6}]O₂. Journal of the American Chemical Society, 2006. **128**(26): p. 8694-8698.
55. Morgan, D., A. Van der Ven, and G. Ceder, Li Conductivity in Li_x MPO₄ (M = Mn , Fe , Co , Ni) Olivine Materials. Electrochemical and Solid-State Letters, 2004. **7**(2): p. A30-A32.
56. Kang, K. and G. Ceder, Factors that affect Li mobility in layered lithium transition metal oxides. Physical Review B, 2006. **74**(9): p. 094105.
57. Van der Ven, A. and G. Ceder, Lithium Diffusion in Layered Li_x CoO₂. Electrochemical and Solid-State Letters, 2000. **3**(7): p. 301-304.
58. Dathar, G.K.P., et al., Calculations of Li-Ion Diffusion in Olivine Phosphates. Chemistry of Materials, 2011. **23**(17): p. 4032-4037.
59. Tripathi, R., et al., Alkali-ion Conduction Paths in LiFeSO₄F and NaFeSO₄F Tavorite-Type Cathode Materials. Chemistry of Materials, 2011. **23**(8): p. 2278-2284.
60. Rissouli, K., et al., Electrical conductivity in lithium orthophosphates. Materials Science and Engineering: B, 2003. **98**(3): p. 185-189.
61. Choi, D. and P.N. Kumta, Surfactant based sol-gel approach to nanostructured LiFePO₄ for high rate Li-ion batteries. Journal of Power Sources, 2007. **163**(2): p. 1064-1069.
62. Zhu, C., et al., Electrospinning of Highly Electroactive Carbon-Coated Single-Crystalline LiFePO₄ Nanowires. Angewandte Chemie

International Edition, 2011. **50**(28): p. 6278-6282.

63. Oh, S.W., et al., Double Carbon Coating of LiFePO₄ as High Rate Electrode for Rechargeable Lithium Batteries. *Advanced Materials*, 2010. **22**(43): p. 4842-4845.

64. Lepage, D., et al., A Soft Chemistry Approach to Coating of LiFePO₄ with a Conducting Polymer. *Angewandte Chemie International Edition*, 2011. **50**(30): p. 6884-6887.

65. Malik, R., F. Zhou, and G. Ceder, Kinetics of non-equilibrium lithium incorporation in LiFePO₄. *Nat Mater*, 2011. **10**(8): p. 587-590.

66. Dreyer, W., et al., The thermodynamic origin of hysteresis in insertion batteries. *Nat Mater*, 2010. **9**(5): p. 448-453.

67. Bai, P., D.A. Cogswell, and M.Z. Bazant, Suppression of Phase Separation in LiFePO₄ Nanoparticles During Battery Discharge. *Nano Letters*, 2011. **11**(11): p. 4890-4896.

68. Perdew, J.P., K. Burke, and M. Ernzerhof, Generalized Gradient Approximation Made Simple. *Physical Review Letters*, 1996. **77**(18): p. 3865-3868.

69. Kresse, G. and J. Furthmüller, Efficiency of ab-initio total energy calculations for metals and semiconductors using a plane-wave basis set. *Computational Materials Science*, 1996. **6**(1): p. 15-50.

70. Anisimov, V.I., J. Zaanen, and O.K. Andersen, Band theory and Mott

insulators: Hubbard U instead of Stoner I. Physical Review B, 1991. **44**(3): p. 943-954.

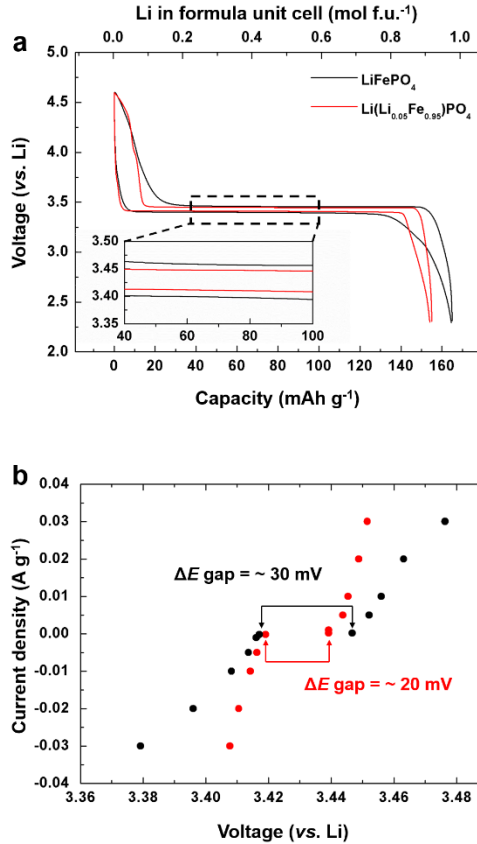


Figure 3-26 Electrochemical properties of lithium-excess and normal LFPS (a) Charge/discharge curves of normal LFP (black) and lithium-excess LFP (red) at a current density 10 mA g^{-1} . Inset figure exhibits magnified charge/discharge curves near plateau region. The lithium-excess LFP shows lower polarization than normal LFP. (b) Hysteresis gap of normal LFP (black) and lithium-excess LFP (red) at various current density. Zero-current hysteresis gap of normal and lithium-excess LFPs are obtained at around 30 mV and 20 mV, respectively.

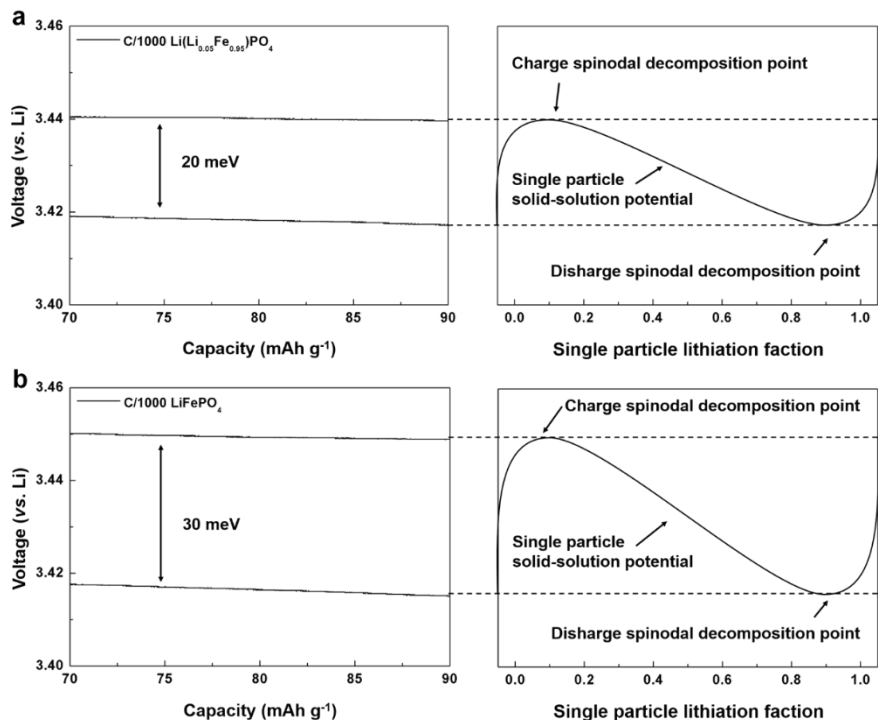


Figure 3-27. Hysteresis gap of electrodes (a) and (b) show the relationship between CC profiles with a C/1000 current density and single particle solid-solution behavior of lithium-excess and normal LFP electrodes, respectively. The voltage gaps between charge and discharge with a near-zero current density is explained by many-body particle models with single particle solid-solution behavior.¹ The highest of del/lithiation spinodal decomposition points (phase transition activation barrier) are strongly related with positive energy penalties induced from coherency/interfacial energies at a moderate particle size. Recently, there is growing evidence that the phase transition barrier could be decreased by nano-sizing, doping and transition metal substitution.

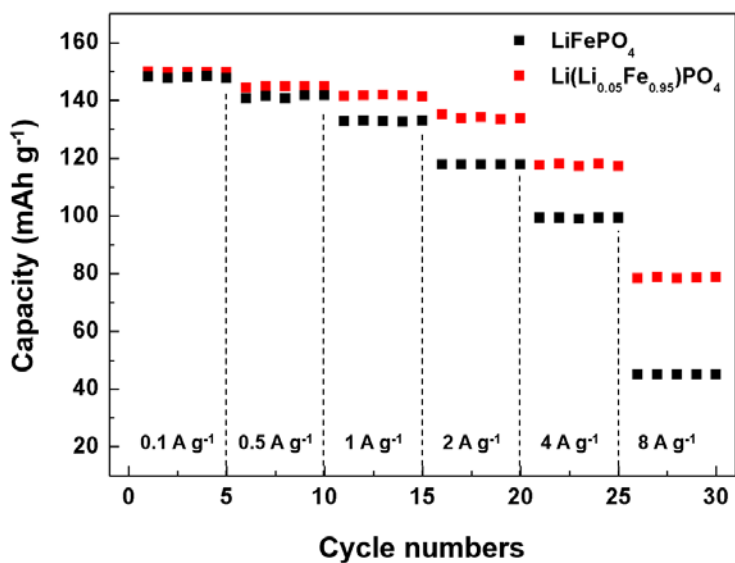


Figure 3-28. Rate capability of lithium-excess LFP (red) and normal LFP (black).

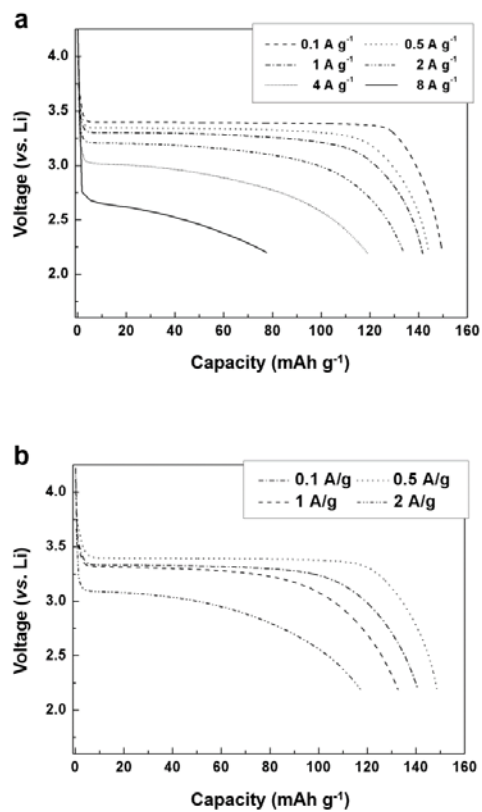


Figure 3-29. Galvanostatic discharge profiles of lithium-excess LFP (a) and normal LFP (b) at various current rates.

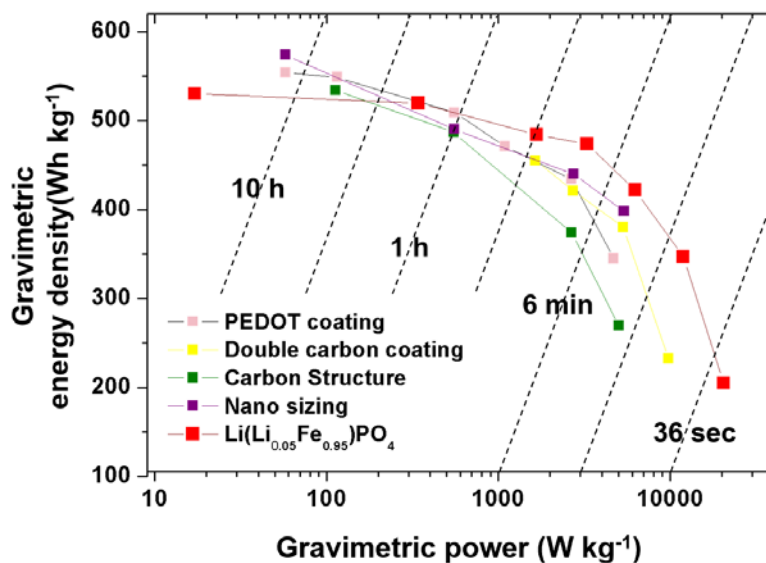


Figure 3-30. Ragone plot of various surface or chemical modified LFPs.

The lithium-excess LFP shows lower gravimetric energy density than other modified LFPs at a low current rate, however, improved energy and power density are exhibited at higher current rates. (refs: Nano-sizing(61), carbon structure(62), double carbon coating(63) and PEDOT coating(64))

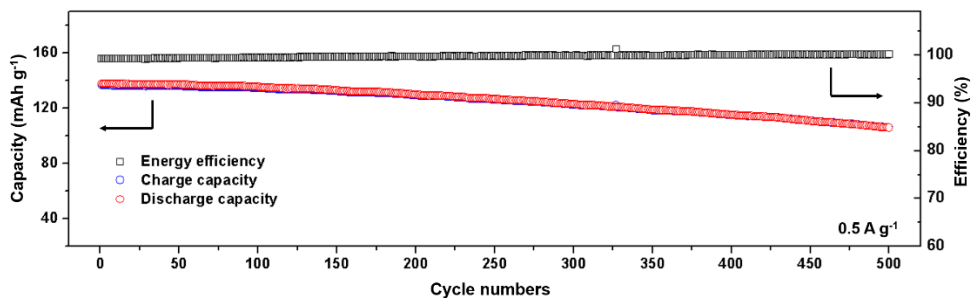


Figure 3-31. Cycle life test of lithium-excess LFP with a current density 0.5 A g^{-1} . (Corresponding with 2.95 C of normal LFP) The capacity after 500 cycles maintained 81.5 % of the initial charge/discharge capacity.

Chapter 4. Thermodynamic and kinetic issues

4.1 Hysteresis gap and Memory effect of LiFePO₄

4.1.1 Experimental section

The LFPs with various compositions were synthesized using Li₂CO₃ (Sigma Aldrich, 99.9%), FeC₂O₄·H₂O (Sigma Aldrich, 99%), (NH₄)₂HPO₄ (Aldrich, 98%). Each precursor was pulverized as fine as possible, separately using high energy ball-milling at Ar atmosphere to avoid the oxidation. The fine precursors were mixed by wet ball milling using acetone more than 24 hours. After drying the mixture, the powder was, again, pulverized as fine as possible using dry ball milling to obtain uniformity and calcinated at 350 °C with 5 ~ 6 °C/min heating rate for 10 hours. The calcinated powders were reground and pelletized under more than 300 bar. The final sintering process was conducted with heating rate as a 5 ~ 6 °C/min rate in Ar atmosphere for 10 hours. An electrode was fabricated by mixing the synthesized powders, pre-mixed with super P (22 wt%) in a ball mill for 24 h, and polyvinylidene fluoride (PVDF, 10 wt%) in N-methyl-2-pyrrolidone (NMP). The mixture was cast on Al foil and dried at 120°C for 2 h. Electrochemical cells were assembled using a CR2016-type coin cell with lithium metal as the counter electrode, a separator (Celgard 2400), and 1 M LiPF₆ in ethyl carbonate/dimethyl carbonate (Panax, EC/DMC, 1:1 v/v) as the electrolyte in

an Ar-filled glove box.

4.1.2 Lowed Spinodal decomposition barrier

The single-particle solid-solution equilibrium model was recently proposed and is now widely accepted for LFP electrode systems.[7, 8, 65, 66] According to the model, the free energy of small-size LFP particles is significantly modified by the interfacial and coherency energy, which comes as a positive energy penalty,[67] leading to the lithium chemical potential profile of LFP single-particles changing from a two-phase- to single-phase-like feature. The collected behavior of single particles in the electrode containing numerous LFP particles is the origin of the thermodynamic hysteresis gap between the charge and discharge.[65, 66] The lower hysteresis gap (~ 20 mV) compared with that of normal LFP (~ 30 mV) that we observed in Figure 3-26 (b) indicates that the lithium-excess LFP is likely to possess a distinct single-particle characteristic. To understand this phenomenon in detail, we investigated the preference toward the single-phase-like behavior changes resulting from the presence of the excess lithium in LFP by calculating the free energy of mixing using DFT methods, as shown in Figure4-1. For reference, the phase mixing energies of normal LFP were taken from the work of the Ceder group in ref 65 (black dots) and plotted together with those of excess-lithium LFP (orange dots) as a function of the

lithium contents. Compared with the minimum mixing free energies of normal LFP at each lithium composition (blue line),^[65] those of the lithium-excess LFP (red line, see Figure4-2 for detailed energy calculations and atomic configurations) lie well below, indicating that the lithium-excess LFP is energetically much closer to the single-phase energy over all the lithium compositions, *i.e.*, it deviates less from the tie-line of the LFP two-phase reaction.^[65] This relation between the energy and lithium contents of Figure4-1 can be roughly converted into a plot with respect to the lithium chemical potential, as presented in Figure4-3. The figure presents a schematic energy profile of a single-particle electrode that undergoes a solid-solution for both cases of lithium-excess (red line) and normal (black line) LFPs. The spinodal energy per lithium to overcome for lithium-excess LFP ($\Delta\mu_{\text{Li-excess LFP}}$) was approximately 6.5 mV according to DFT calculations and ~ 10 mV according to experiments. These values are only two-thirds of those of normal LFP ($\Delta\mu_{\text{LFP}}$, ~ 15 mV),^[65, 66] which implies that the energy to overcome is much less for the single-phase-like reaction in the case of lithium-excess LFP. According to the particle-to-particle intercalation model,^[66] discrete one-by-one filling of many particles occurs, and the energy barrier for the single particle results in the voltage hysteresis between the charge and discharge plateau, as illustrated in Figure4-3. The smaller hysteresis gap in lithium-excess LFP derived from this figure agrees well with the results in Figure 3-27.

It is speculated that the lower phase-transition energy barrier for lithium-excess LFP stems from the defective nature of lithium in the Fe site (Li_{Fe}) that destabilizes the pristine phase and promotes the mixing as a “*phase mixing seed*”. In addition, the reduced lattice misfit between lithium-excess LFP and delithiated lithium-excess LFP as listed in Figure 3-2 (c) is also believed to have affected on reducing the phase transition barrier.[7, 66]

The thermal behavior of partially delithiated phases supports our suggestion of reduced phase mixing energy in the lithium-excess LFP. The thermal phase diagram in Figure4-4 was obtained from temperature-controlled XRD using chemically delithiated lithium-excess phases according to the targeted lithium compositions. (All the *in-situ* XRD patterns are provided in Figure4-5 .) Although previous work by Delacourt *et al.* reported that the partially delithiated normal LFP becomes a solid-solution phase above 350 °C, the complete solid-solution is formed at a 70 °C-lower temperature for the lithium-excess LFP, 280 °C, indicating that the excess-lithium LFP exhibits a stronger tendency for the single-phase reaction with a lower energy barrier for the transition. Moreover, we observed that the partially delithiated lithium-excess LFP forms intermediate phases above 200 °C, similar to the thermal phase behavior of normal LFP. This finding suggests that an intermediate phase with particular lithium ordering is also possible in lithium-

excess LFP. We are conducting a further investigation to verify the lithium orderings and compositions of the intermediate phases.

4.1.3 Less memory effect at new LFP system

Another aspect that we investigated for lithium-excess LFP was how the reduced energy barrier for the transition affects the (i) ‘overshooting’ of voltage during charge/discharge and (ii) the memory effect that has recently been reported for normal LFP.[7] T. Sasaki *et al.* demonstrated that the electrochemical profile of LFP exhibits an anomalous polarization increase depending on the relaxation time and is affected by the history of the cycling.[7] This increase was explained using a particle-by-particle charge/discharge model with non-uniform chemical potentials of LFP single particles after the relaxation.[7] When the LFP electrode stops at certain charge or discharge states, the active LFP particles begin to separate into Li-rich and Li-poor particles. The active particles not reaching the most stable state during relaxation do not show additional polarization, whereas those that have reached this state have to climb up the energy barrier again, inducing higher polarization.[7] We also observed an anomalous polarization increase after relaxation in the galvanostatic intermittent titration technique (GITT) compared with the constant current (CC) measurements for normal LFP, as observed in Figure4-6 (a). Also, consistent with the observation of T. Sasaki

et al., the memory effect is clearly observed for normal LFP after the memory writing cycle (Figure4-6 (b)). However, it was noted that the lithium-excess LFP exhibits a much smaller increase in the polarization after relaxation in the GITT, as observed in Figure4-7 (a), and does not exhibit any detectable memory effect even after we applied the same memory writing cycle as that of the normal LFP electrode, as shown in Figure4-7 (b).

Considering the memory effect model proposed by Sasaki *et al.*, we could infer that the lithium-excess LFP particle has a different relaxation behavior from the normal LFP. To further compare the relaxation behavior and polarization increase of lithium-excess and normal LFP electrodes, we designed an additional experiment of rest-time-dependent partial GITT. Before performing the partial GITT, the open-circuit voltage (OCV) at 50 % state of charge (SOC) was measured during relaxation after charge or discharge with a current rate of 10 mA g⁻¹ as a function of time, as shown in Figure4-8 (a). Although the OCV of normal LFP required more than 100 min to obtain a charge and discharge gap of 30 mV, the OCV gap of lithium-excess LFP was reduced to 10 mV in less than 20 min. This result indicates that the relaxation process occurs much faster for lithium-excess LFP, which is attributed to the higher degree of lithium diffusion in the lithium-excess LFP. For direct comparison, the measurement of the effective lithium diffusivities

and conductivities for the two LFPs was performed as illustrated in Figure4-9 and Figure4-10, indicating that the lithium-excess LFP has one order higher conductive properties than the normal LFP. The difference in the relaxation kinetics affects the behavior of the GITT experiment. Figure4-8 (b) and (c) show the partial GITT profiles of both LFPs during the charge and discharge. The black dotted lines represent the equilibrium voltage of LFP vs. Li/Li^+ . Consistent with the GITT measurement above, the lithium-excess LFP shows considerably lower polarization from the equilibrium potential for both charge and discharge regardless of the duration of the rest time. However, with increasing rest time, the voltage profiles of lithium-excess LFP start to show an overshooting in the charge or discharge. In addition, the overshooting profile becomes more pronounced with additional rest time, as clearly observed in the insets of Figure4-8 (b) and (c). The origin of the overshoot in LFP has not yet been clearly revealed yet, but it is believed that it results from the resistance involved with the Spinodal decomposition or nucleation formation from the pristine and electrochemically activated particles.[7] During the relaxation step, both LFPs would either undergo Spinodal decomposition or relax back to the original state by exchanging lithium among each other or with particles in the Li-poor phase.[7, 66] Since it is reported that the overshoots appears just before the sequential particle-by-particle process occurs and the full relaxation of particles is the triggering

condition of the overshooting, the predominant overshooting is attributed to the faster relaxation kinetics of the lithium-excess LFPs. Nevertheless, the overshoot in lithium-excess LFP is relatively small. It is believed that the energy penalty that the particle needs to climb again would be less for lithium-excess LFP because of the reduced Spinodal decomposition barrier, as indicated in Figure4-3, which would also reduce the overshooting during charge/discharge.

The results of the relaxation time *vs.* polarization experiments give us a hint why the memory effect is not observed in the lithium-excess LFP. Sasaki *et al.* demonstrated that as the rest time increases between the memory writing and memory releasing step, the memory effect is notably reduced because of the sufficient time for homogenization of the lithium chemical potential among LFP particles.[7] This finding implies that how fast the electrode material relaxes to the stable state at zero current will sensitively affect the dominance of the memory effect. Accordingly, we designed an experiment on lithium-excess LFP to impose a shorter interval between the memory writing and releasing cycles. As we systematically decrease the interval from 10 min to 1 min in Figure4-11, the memory effect begins to appear. When the interval time becomes less than 5 min, the signature of the voltage protrusion is observed even though the magnitude is significantly smaller than for normal

LFP under the same condition, indicating that the memory effect is a universal effect in olivine LFPs. However, because the lithium-excess LFP allows much faster lithium kinetics, the homogenization of the lithium chemical potential among particles will also be significantly quicker after the memory writing step. Therefore, within the same interval, the homogenization would be far more efficient for lithium-excess LFP, and the detectable memory effect would not be observed.

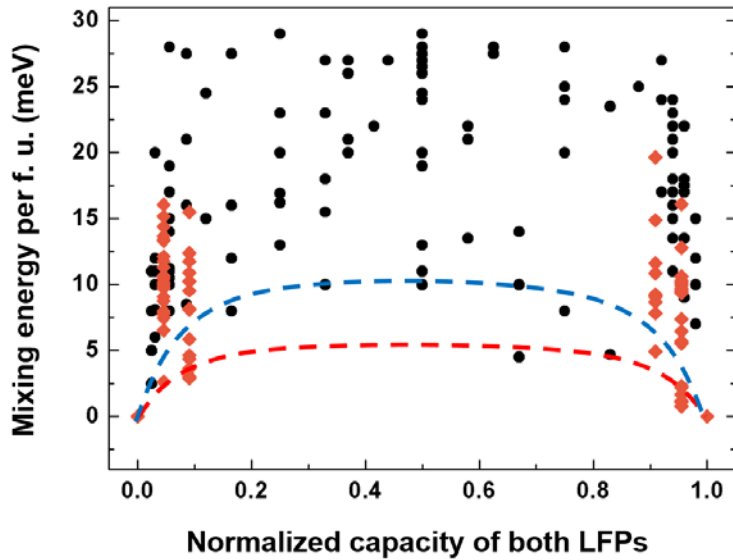


Figure4-1 . Mixing free energy and atomic configuration of lithium-excess LFP (orange) and normal LFP (black, ref 65, copyright 2011, Nature Publishing Group) as a function of lithium contents. Mixing energies of lithium-excess and normal LFP at zero-temperature. Black dots and blue line are taken from the work of Ceder *et al.* [65]. The free energies were calculated by DFT calculation using 245 atoms. The dash line is a predicted curve of whole mixing free energy. (lithium-excess LFP: orange, normal LFP: blue dash line)

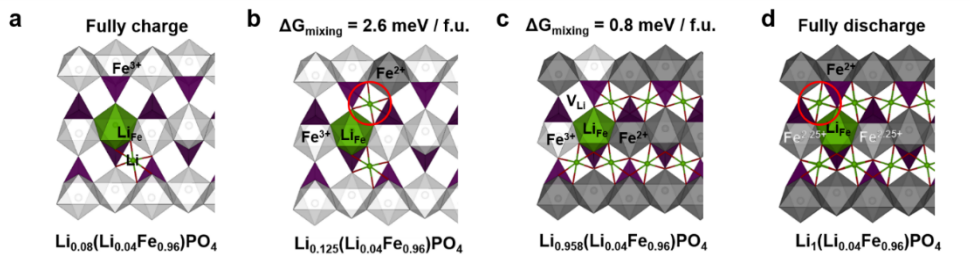


Figure4-2 . Detailed DFT calculation results. It is revealed by DFT calculation that the unique Li-excess atomic configuration has preferred interstitial sites to extract or insert Li ions during Li concentration change. The Figure (a) – (d) show local Li-excess configuration corresponding with the lowest mixing energy at certain Li factions. At the end of charge state, (Figure (a)) Li_{Fe} ion and another Li_{Li} ion remained due to all Fe ions oxidized to 3+ state. And, when an electron is inserted into electrode, the additional Li ion is located at near Li-excess configuration site marked with red circle in Figure (b) with $2.6 \text{ meV f.u.}^{-1}$ mixing energy. Similarly, at the beginning of discharge state, the Li ion marked by red circle in Figure (d) is firstly came out with $0.8 \text{ meV f.u.}^{-1}$ phase mixing energy. (Figure (c)) Although we could not investigate mixing energy for whole Li concentration and precise Li composition of solubility limits due to limitation of DFT calculation, this result elucidates that the lithium-excess LFP has energetic lower alternative diffusional configuration than normal LFP because Li-excess local configuration plays role as a “*phase mixing seed*”.

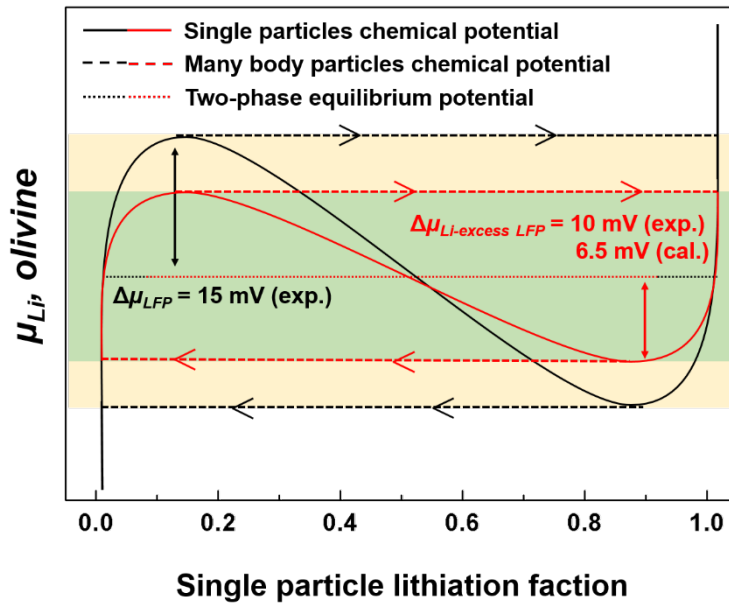


Figure4-3. The single particle chemical potential of normal LFP (black) and lithium-excess LFP (red) as a function of the lithiation fraction. The normal LFP and lithium-excess LFP contain ~ 15 mV and ~ 10 mV phase transition activation barrier, respectively

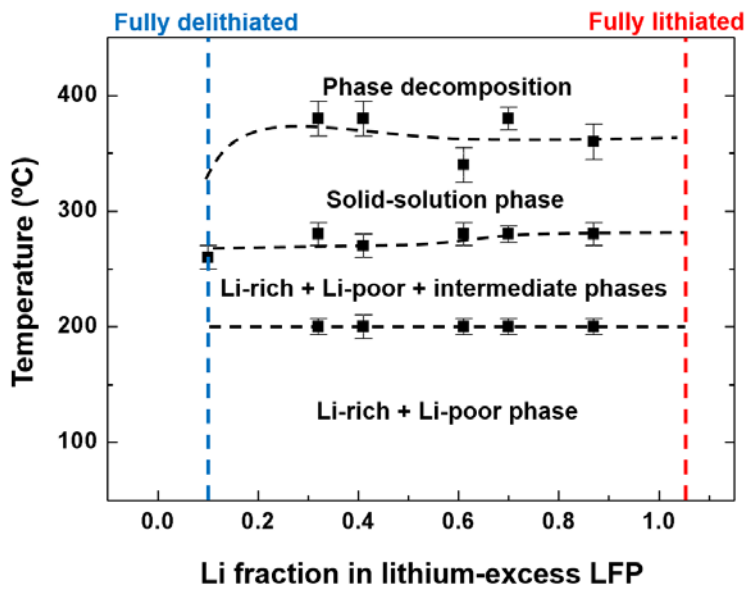
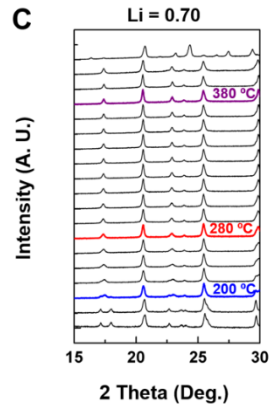
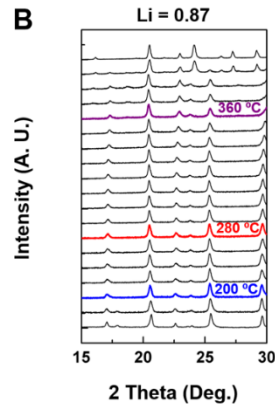
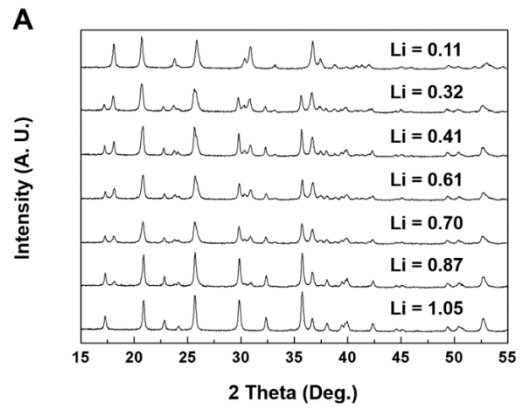


Figure4-4 Thermal phase diagram of lithium-excess LFP



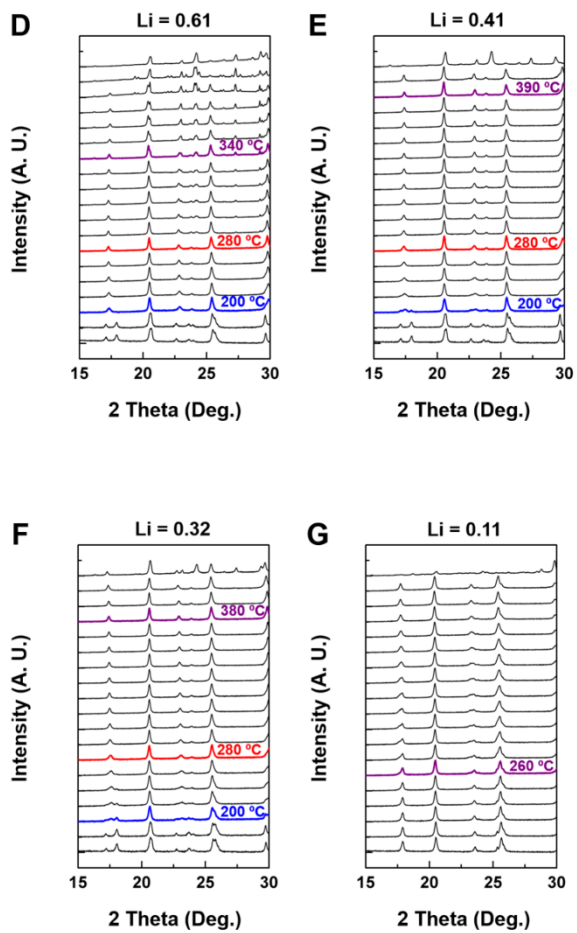


Figure4-5 . Thermal XRD patterns of lithium-excess LFP

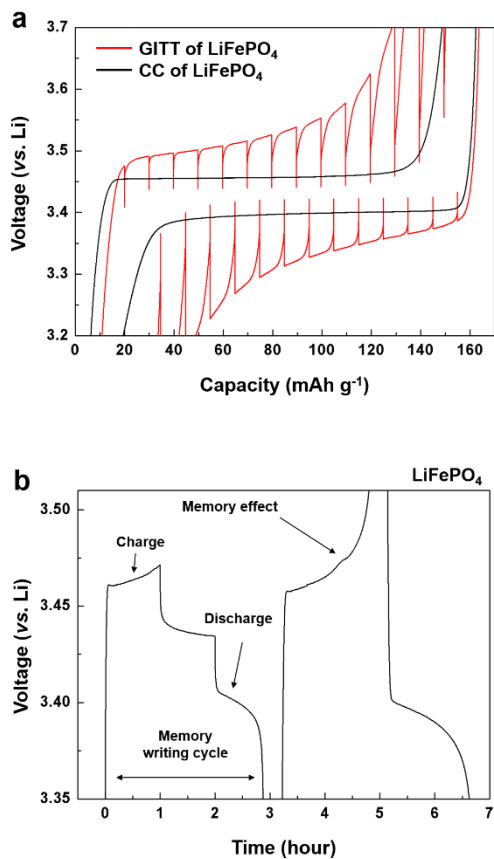


Figure4-6 . Memory effect of normal LFP. Charge and discharge profile in CC (Constant current) and GITT (Galvanostatic intermittent titration technique) modes of (a) normal LFP at a current rate 10 mA g⁻¹. The rest time of GITT is about 20 minutes. (b) show the memory effect test of both LFPs. Memory writing cycles (first cycle) are conducted to SOC 50 % with one hour rest time between charge and discharge. Memory releasing cycles (second cycle) are conducted within 2.5 ~ 4.5 V (vs. Li) with a 80 mA g⁻¹ current rate.

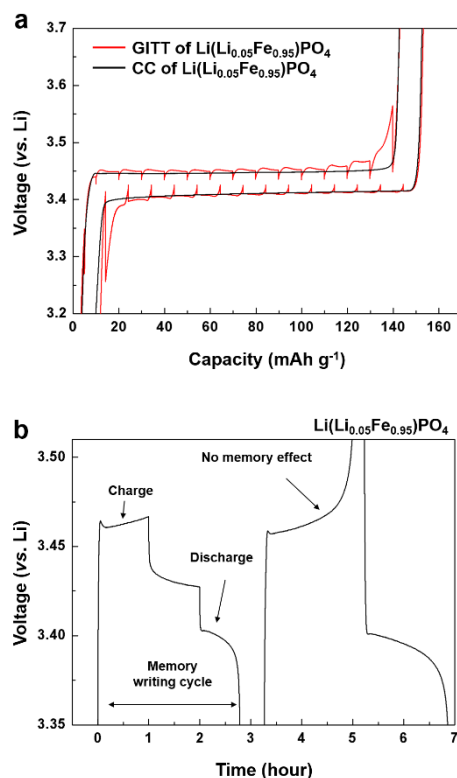


Figure4-7 Memory effect of lithium-excess LFP. Charge and discharge profile in CC (Constant current) and GITT (Galvanostatic intermittent titration technique) modes of (a) excess LFP at a current rate 10 mA g^{-1} . The rest time of GITT is about 20 minutes. (b) show the memory effect test LFPs. Memory writing cycles (first cycle) are conducted to SOC 50 % with one hour rest time between charge and discharge. Memory releasing cycles (second cycle) are conducted within 2.5 ~ 4.5 V (vs. Li) with a 80 mA g^{-1} current rate. The memory effect is not observed in lithium-excess LFP.

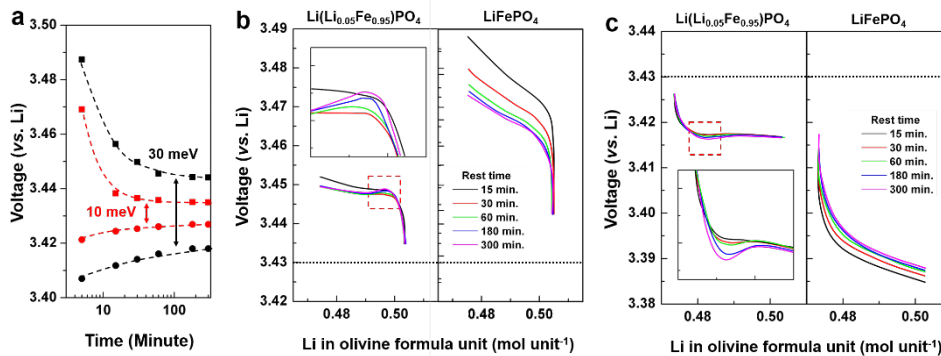


Figure4-8. OCV change of both electrodes. (a) OCV change of lithium-excess and normal LFPs as a function of the rest time. (black: normal LFP and red: lithium-excess LFP) The lithium-excess LFP relaxed faster than normal LFP with reaching 10 mV charge and discharge OCV gap. Partial GITT profile change depending on the rest times at each electrodes during (b) charge and (c) discharge. The each inset figures exhibits the magnified profiles marked by red squares. The black dot line indicates the equilibrium potential of LFP electrode vs. Li/Li^+ .

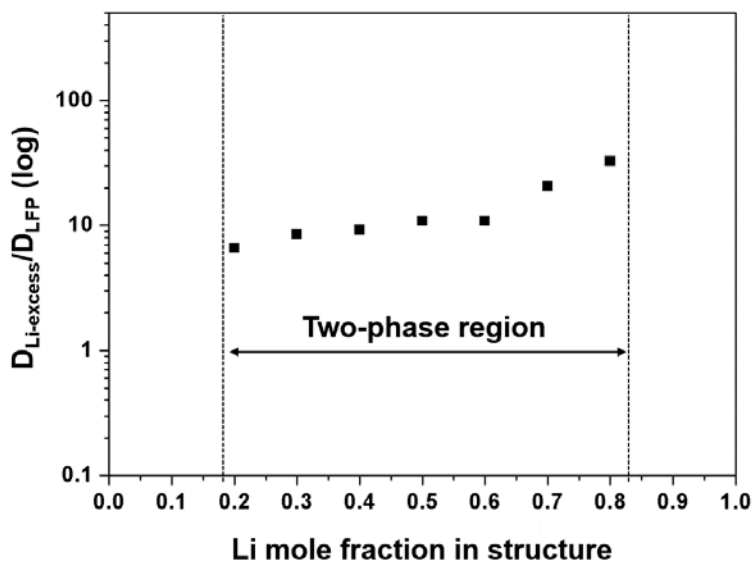
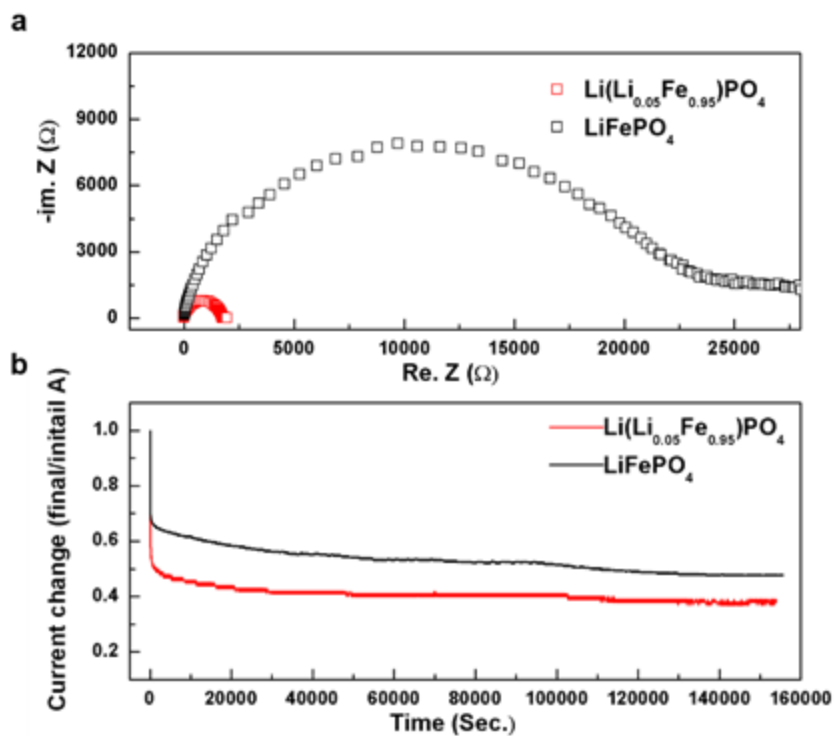


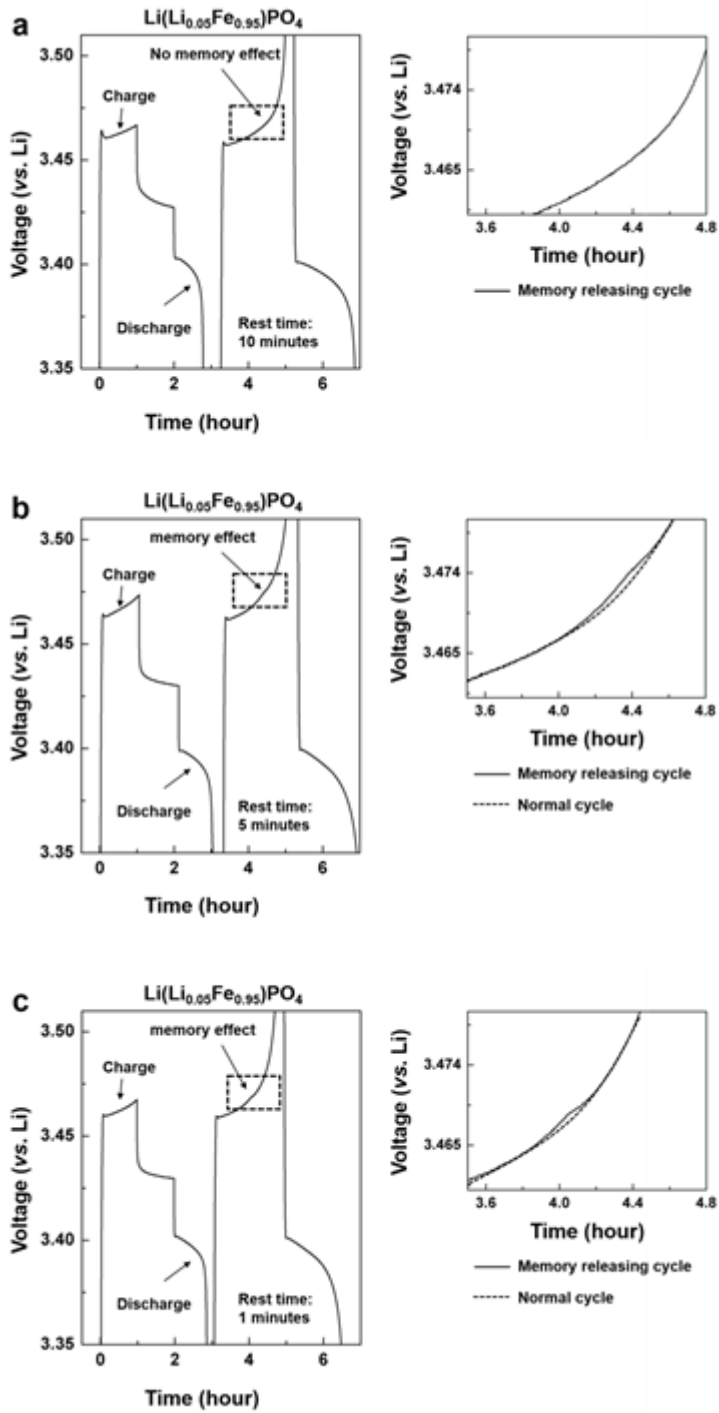
Figure4-9 . The effective diffusivity ratio ($D_{Li-excess}/D_{LFP}$) calculated from GITT results with in two-phase reaction region.⁵ The lithium-excess LFP shows statically 10 times higher diffusivity than normal LFP.



c

	σ (S cm ⁻¹)			Carbon (wt %)	Temp. (C°)	Ref.
	Total Con.	Ionic Con.	Elec. Con.			
Normal LFP	2.31×10^{-6}	1.27×10^{-6}	1.04×10^{-6}	2.5 (1)	20	-
Lithium-excess LFP	2.64×10^{-5}	1.63×10^{-5}	1.01×10^{-5}	2.9 (1)	20	-
Normal LFP	-	3.20×10^{-6}	2.00×10^{-10}	-	RT	6
Normal LFP	2.7×10^{-9}	$\sim 10^{-7-8}$	$\sim 10^{-9}$	-	25	7

Figure4-10 . Conductivity measurement (a) EIS measurement results of lithium-excess and normal LFPs. The powders are pelleted under 400 bar as disk shape with ~ 1 mm thickness and sintered at 500 °C for 5 hours in Ar atmosphere. The symmetric cells are assembled with Ag/sample/Ag configuration for measuring total conductivities. The EIS measurements are conducted with 3 MHz ~ 0.1 Hz at room temperature (20 °C). (b) Current change tendency under constant voltage applied (1 V). The currents are saturated over ~ 40 hours, and the electronic conductivity portions are confirmed by ~ 0.4 and 0.53 for lithium-excess and normal LFPs, respectively. The table (c) shows total, ionic, electronic conductivity at 20 °C and residual carbon ratio of normal, lithium-excess LFPs and previous reports. The ionic and electronic conductivities of lithium-excess LFP shows ~ 13 times and 10 times better than normal LFP respectively, and it is consistent with diffusivity measurement at S Fig. 19. The ionic conductivity of normal LFP powder is well matched with previous reports, the electronic conductivities of both powders show much higher ($\sim 10^{-5} \sim -6$) than previous reports ($\sim 10^{-9}$).^{6,7} As shown in Table (c), lithium-excess and normal LFPs contains 2 ~ 3 wt % residual carbon. We conjectured that these residual carbon are produced from carbon containing precursors, such as Li_2CO_3 and $\text{FeC}_2\text{O}_4 \cdot \text{H}_2\text{O}$, and higher electronic conductivities are came from residual carbon.



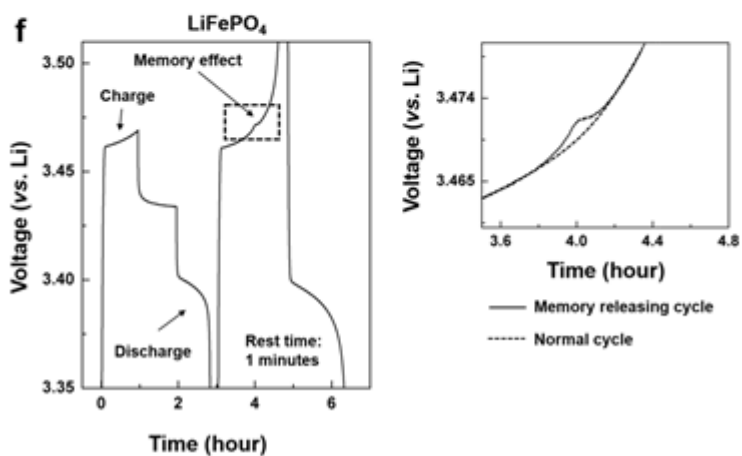
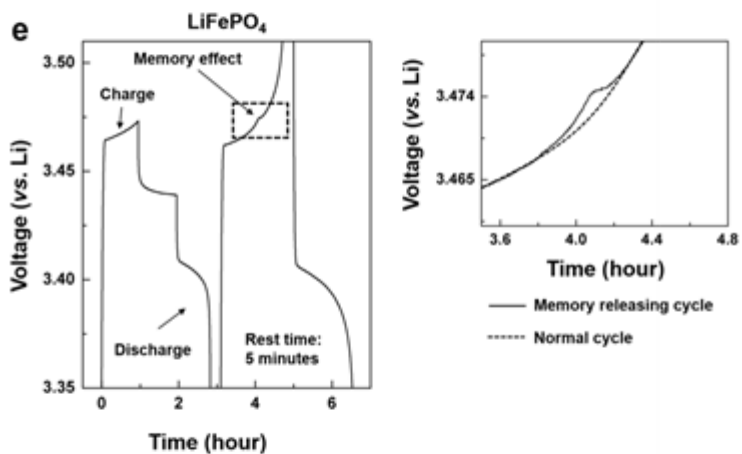
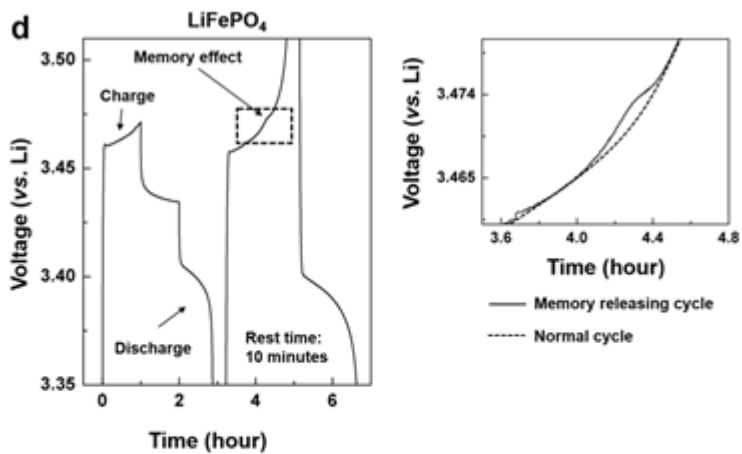


Figure4-11 . Confirmation on memory effect depending on rest time between memory writing (first half charge/discharge) cycle and memory releasing (second full charge/discharge) cycle. The all experiments are conducted with a 80 mA g^{-1} current density and $2.5 \sim 4.5 \text{ V (vs. Li)}$ voltage windows. (a)10 minutes rest time, (b) 5 minutes rest time and (c) 1minute rest time for lithium-excess LFP. (d)10 minutes rest time, (e) 5 minutes rest time and (f) 1minute rest time for normal LFP. The memory effect is reinforced with decreasing rest time between first cycle and second cycle at both LFPs. However, the degree of overshooting of lithium-excess LFP is remarkably lower than counterpart normal LFP electrode, and the overshooting (memory effect) has completely disappeared with more than 10 minutes rest time. We infer that the fast kinetic of lithium-excess configuration makes active particles fast reunion in the relaxation state (rest state), resulting in erasing memory effect as shown in (a). Also, the relatively low phase transition activation energy of lithium-excess LFP could affect on lowering degree of overshooting compared with normal LFP as show in (b) and (c).

4.2 Conclusion

In summary, we show that (i) lowers the spinodal decomposition point and (ii) significantly weakens the memory effect at lithium-excess LFP. We believe that unlocking the restrictive lithium ion diffusion in the olivine electrode is expected to affect other intrinsic thermodynamic and kinetic properties of olivine LFPs, such as the phase boundary configuration, intermediate phase, and relaxation behavior, which requires further investigation. Notably, all of these physical changes in olivine cathodes originate from only a small change in the Li/Fe compositions. Our results suggest that a simple excess ionic carrier concept in the electrode crystal not only enhances the power capability but also brings up unexpected properties for the pristine crystal and offers a novel interesting approach to tune solid-state ionic conductors.

4.3 References

1. Armand, M. and J.M. Tarascon, Building better batteries. *Nature*, 2008. **451**(7179): p. 652-657.
2. Vineyard, G.H. and G.J. Dienes, The Theory of Defect Concentration in Crystals. *Physical Review*, 1954. **93**(2): p. 265-268.
3. Islam, M.S., et al., Atomic-Scale Investigation of Defects, Dopants, and Lithium Transport in the LiFePO₄ Olivine-Type Battery Material. *Chemistry of Materials*, 2005. **17**(20): p. 5085-5092.
4. Wang, J., et al., Size-dependent surface phase change of lithium iron phosphate during carbon coating. *Nat Commun*, 2014. **5**.
5. Chen, J. and J. Graetz, Study of Antisite Defects in Hydrothermally Prepared LiFePO₄ by in Situ X-ray Diffraction. *ACS Applied Materials & Interfaces*, 2011. **3**(5): p. 1380-1384.
6. Delmas, C., et al., On the behavior of the Li_xNiO₂ system: an electrochemical and structural overview. *Journal of Power Sources*, 1997. **68**(1): p. 120-125.
7. Sasaki, T., Y. Ukyo, and P. Novák, Memory effect in a lithium-ion battery. *Nat Mater*, 2013. **12**(6): p. 569-575.
8. Li, Y., et al., Current-induced transition from particle-by-particle to concurrent intercalation in phase-separating battery electrodes. *Nat Mater*,

2014. **13**(12): p. 1149-1156.

9. Gibot, P., et al., Room-temperature single-phase Li insertion/extraction in nanoscale Li_xFePO_4 . *Nat Mater*, 2008. **7**(9): p. 741-747.

10. Delmas, C., et al., Lithium deintercalation in LiFePO_4 nanoparticles via a domino-cascade model. *Nat Mater*, 2008. **7**(8): p. 665-671.

11. Bai, P. and M.Z. Bazant, Charge transfer kinetics at the solid–solid interface in porous electrodes. *Nat Commun*, 2014. **5**.

12. Delacourt, C., et al., The existence of a temperature-driven solid solution in Li_xFePO_4 for $0 < x < 1$. *Nat Mater*, 2005. **4**(3): p. 254-260.

13. Padhi, A.K., K.S. Nanjundaswamy, and J.B. Goodenough, Phospho-olivines as Positive-Electrode Materials for Rechargeable Lithium Batteries. *Journal of The Electrochemical Society*, 1997. **144**(4): p. 1188-1194.

14. Nishijima, M., et al., Accelerated discovery of cathode materials with prolonged cycle life for lithium-ion battery. *Nat Commun*, 2014. **5**.

15. Yamada, A., S.C. Chung, and K. Hinokuma Optimized LiFePO_4 for Lithium Battery Cathodes. *Journal of The Electrochemical Society*, 2001. **148**(3): p. A224-A229.

16. Nishimura, S.-i., et al., Experimental visualization of lithium diffusion in Li_xFePO_4 . *Nat Mater*, 2008. **7**(9): p. 707-711.

17. Malik, R., et al., Particle Size Dependence of the Ionic Diffusivity.

Nano Letters, 2010. **10**(10): p. 4123-4127.

18. Tealdi, C., C. Spreatico, and P. Mustarelli, Lithium diffusion in $\text{Li}_{1-x}\text{FePO}_4$: the effect of cationic disorder. *Journal of Materials Chemistry*, 2012. **22**(47): p. 24870-24876.

19. Chung, S.-Y., et al., Atomic-Scale Visualization of Antisite Defects in LiFePO_4 . *Physical Review Letters*, 2008. **100**(12): p. 125502.

20. Chen, J., et al., The hydrothermal synthesis and characterization of olivines and related compounds for electrochemical applications. *Solid State Ionics*, 2008. **178**(31–32): p. 1676-1693.

21. Yang, S., P.Y. Zavalij, and M. Stanley Whittingham, Hydrothermal synthesis of lithium iron phosphate cathodes. *Electrochemistry Communications*, 2001. **3**(9): p. 505-508.

22. Chen, J. and M.S. Whittingham, Hydrothermal synthesis of lithium iron phosphate. *Electrochemistry Communications*, 2006. **8**(5): p. 855-858.

23. Park, K.-Y., et al., Anti-Site Reordering in LiFePO_4 : Defect Annihilation on Charge Carrier Injection. *Chemistry of Materials*, 2014. **26**(18): p. 5345-5351.

24. Radhamani, A.V., et al., Suppression of antisite defects in fluorine-doped LiFePO_4 . *Scripta Materialia*, 2013. **69**(1): p. 96-99.

25. Yuan, S. and K. Dai, Heat-rate-controlled hydrothermal synthesis of LiFePO_4 achieved by different heating sources. *Russian Journal of*

Electrochemistry, 2014. **50**(4): p. 385-389.

26. Hoang, K. and M. Johannes, Tailoring Native Defects in LiFePO₄: Insights from First-Principles Calculations. Chemistry of Materials, 2011. **23**(11): p. 3003-3013.

27. Amisse, R., et al., Nonstoichiometry in LiFe_{0.5}Mn_{0.5}PO₄: Structural and Electrochemical Properties. Journal of The Electrochemical Society, 2013. **160**(9): p. A1446-A1450.

28. Hamelet, S., et al., Existence of Superstructures Due to Large Amounts of Fe Vacancies in the LiFePO₄-Type Framework. Chemistry of Materials, 2011. **23**(1): p. 32-38.

29. Amisse, R., et al., Singular Structural and Electrochemical Properties in Highly Defective LiFePO₄ Powders. Chemistry of Materials, 2015. **27**(12): p. 4261-4273.

30. Chung, S.-Y., et al., Surface-Orientation-Dependent Distribution of Subsurface Cation-Exchange Defects in Olivine-Phosphate Nanocrystals. ACS Nano, 2015. **9**(1): p. 850-859.

31. Schuster, M.E., et al., Charging and Discharging Behavior of Solvothermal LiFePO₄ Cathode Material Investigated by Combined EELS/NEXAFS Study. Chemistry of Materials, 2013. **26**(2): p. 1040-1047.

32. Julien, C.M., A. Mauger, and K. Zaghib, Surface effects on electrochemical properties of nano-sized LiFePO₄. Journal of Materials

Chemistry, 2011. **21**(27): p. 9955-9968.

33. Armstrong, A.R., et al., The lithium intercalation process in the low-voltage lithium battery anode $\text{Li}_{1+x}\text{V}_{1-x}\text{O}_2$. *Nat Mater*, 2011. **10**(3): p. 223-229.

34. Lu, Z., D.D. MacNeil, and J.R. Dahn, Layered Cathode Materials $\text{Li}[\text{Ni}_x\text{Li}(1/3 - 2x/3)\text{Mn}(2/3 - x/3)]\text{O}_2$ for Lithium-Ion Batteries. *Electrochemical and Solid-State Letters*, 2001. **4**(11): p. A191-A194.

35. Yabuuchi, N., et al., Detailed Studies of a High-Capacity Electrode Material for Rechargeable Batteries, $\text{Li}_2\text{MnO}_3\text{-LiCo}_{1/3}\text{Ni}_{1/3}\text{Mn}_{1/3}\text{O}_2$. *Journal of the American Chemical Society*, 2011. **133**(12): p. 4404-4419.

36. Salager, E., et al., Solid-State NMR of the Family of Positive Electrode Materials $\text{Li}_2\text{Ru}_{1-y}\text{Sn}_y\text{O}_3$ for Lithium-Ion Batteries. *Chemistry of Materials*, 2014. **26**(24): p. 7009-7019.

37. Sathiya, M., et al., High Performance $\text{Li}_2\text{Ru}_{1-y}\text{Mn}_y\text{O}_3$ ($0.2 \leq y \leq 0.8$) Cathode Materials for Rechargeable Lithium-Ion Batteries: Their Understanding. *Chemistry of Materials*, 2013. **25**(7): p. 1121-1131.

38. Ma, J., et al., Feasibility of Using Li_2MoO_3 in Constructing Li-Rich High Energy Density Cathode Materials. *Chemistry of Materials*, 2014. **26**(10): p. 3256-3262.

39. Sathiya, M., et al., Origin of voltage decay in high-capacity layered oxide electrodes. *Nat Mater*, 2015. **14**(2): p. 230-238.

40. Sathiya, M., et al., Reversible anionic redox chemistry in high-capacity layered-oxide electrodes. *Nat Mater*, 2013. **12**(9): p. 827-835.
41. Lee, J., et al., Unlocking the Potential of Cation-Disordered Oxides for Rechargeable Lithium Batteries. *Science*, 2014. **343**(6170): p. 519-522.
42. Yoon, M.-S., et al., Synthesis of Li excess LiFePO₄/C using iron chloride extracted from steel scrap pickling. *Metals and Materials International*, 2014. **20**(4): p. 785-791.
43. Huang, W., Q. Cheng, and X. Qin, Effect of Li excess content and Ti dopants on electrochemical properties of LiFePO₄ prepared by thermal reduction method. *Russian Journal of Electrochemistry*, 2010. **46**(3): p. 359-362.
44. Kim, H., et al., Neutron and X-ray Diffraction Study of Pyrophosphate-Based Li_{2-x}MP₂O₇ (M = Fe, Co) for Lithium Rechargeable Battery Electrodes. *Chemistry of Materials*, 2011. **23**(17): p. 3930-3937.
45. Kang, B. and G. Ceder, Battery materials for ultrafast charging and discharging. *Nature*, 2009. **458**(7235): p. 190-193.
46. Zaghib, K., et al., Unsupported claims of ultrafast charging of LiFePO₄ Li-ion batteries. *Journal of Power Sources*, 2009. **194**(2): p. 1021-1023.
47. Ceder, G. and B. Kang, Response to “unsupported claims of ultrafast charging of Li-ion batteries”. *Journal of Power Sources*, 2009. **194**(2): p.

1024-1028.

48. Cabana, J., et al., MAS NMR Study of the Metastable Solid Solutions Found in the LiFePO₄/FePO₄ System. *Chemistry of Materials*, 2010. **22**(3): p. 1249-1262.

49. Tucker, M.C., et al., Hyperfine Fields at the Li Site in LiFePO₄-Type Olivine Materials for Lithium Rechargeable Batteries: A ⁷Li MAS NMR and SQUID Study. *Journal of the American Chemical Society*, 2002. **124**(15): p. 3832-3833.

50. Upreti, S., et al., Crystal Structure, Physical Properties, and Electrochemistry of Copper Substituted LiFePO₄ Single Crystals. *Chemistry of Materials*, 2011. **24**(1): p. 166-173.

51. Davis, L.J.M., I. Heinmaa, and G.R. Goward, Study of Lithium Dynamics in Monoclinic Li₃Fe₂(PO₄)₃ using ⁶Li VT and 2D Exchange MAS NMR Spectroscopy. *Chemistry of Materials*, 2010. **22**(3): p. 769-775.

52. Hamelet, S., et al., The effects of moderate thermal treatments under air on LiFePO₄-based nano powders. *Journal of Materials Chemistry*, 2009. **19**(23): p. 3979-3991.

53. Omenya, F., et al., Can Vanadium Be Substituted into LiFePO₄? *Chemistry of Materials*, 2011. **23**(21): p. 4733-4740.

54. Armstrong, A.R., et al., Demonstrating Oxygen Loss and Associated Structural Reorganization in the Lithium Battery Cathode

Li[Ni_{0.2}Li_{0.2}Mn_{0.6}]O₂. Journal of the American Chemical Society, 2006. **128**(26): p. 8694-8698.

55. Morgan, D., A. Van der Ven, and G. Ceder, Li Conductivity in Li_x MPO₄ (M = Mn , Fe , Co , Ni) Olivine Materials. Electrochemical and Solid-State Letters, 2004. **7**(2): p. A30-A32.

56. Kang, K. and G. Ceder, Factors that affect Li mobility in layered lithium transition metal oxides. Physical Review B, 2006. **74**(9): p. 094105.

57. Van der Ven, A. and G. Ceder, Lithium Diffusion in Layered Li_x CoO₂. Electrochemical and Solid-State Letters, 2000. **3**(7): p. 301-304.

58. Dathar, G.K.P., et al., Calculations of Li-Ion Diffusion in Olivine Phosphates. Chemistry of Materials, 2011. **23**(17): p. 4032-4037.

59. Tripathi, R., et al., Alkali-ion Conduction Paths in LiFeSO₄F and NaFeSO₄F Tavorite-Type Cathode Materials. Chemistry of Materials, 2011. **23**(8): p. 2278-2284.

60. Rissouli, K., et al., Electrical conductivity in lithium orthophosphates. Materials Science and Engineering: B, 2003. **98**(3): p. 185-189.

61. Choi, D. and P.N. Kumta, Surfactant based sol-gel approach to nanostructured LiFePO₄ for high rate Li-ion batteries. Journal of Power Sources, 2007. **163**(2): p. 1064-1069.

62. Zhu, C., et al., Electrospinning of Highly Electroactive Carbon-Coated Single-Crystalline LiFePO₄ Nanowires. Angewandte Chemie

International Edition, 2011. **50**(28): p. 6278-6282.

63. Oh, S.W., et al., Double Carbon Coating of LiFePO₄ as High Rate Electrode for Rechargeable Lithium Batteries. *Advanced Materials*, 2010. **22**(43): p. 4842-4845.

64. Lepage, D., et al., A Soft Chemistry Approach to Coating of LiFePO₄ with a Conducting Polymer. *Angewandte Chemie International Edition*, 2011. **50**(30): p. 6884-6887.

65. Malik, R., F. Zhou, and G. Ceder, Kinetics of non-equilibrium lithium incorporation in LiFePO₄. *Nat Mater*, 2011. **10**(8): p. 587-590.

66. Dreyer, W., et al., The thermodynamic origin of hysteresis in insertion batteries. *Nat Mater*, 2010. **9**(5): p. 448-453.

67. Bai, P., D.A. Cogswell, and M.Z. Bazant, Suppression of Phase Separation in LiFePO₄ Nanoparticles During Battery Discharge. *Nano Letters*, 2011. **11**(11): p. 4890-4896.

68. Perdew, J.P., K. Burke, and M. Ernzerhof, Generalized Gradient Approximation Made Simple. *Physical Review Letters*, 1996. **77**(18): p. 3865-3868.

69. Kresse, G. and J. Furthmüller, Efficiency of ab-initio total energy calculations for metals and semiconductors using a plane-wave basis set. *Computational Materials Science*, 1996. **6**(1): p. 15-50.

70. Anisimov, V.I., J. Zaanen, and O.K. Andersen, Band theory and Mott

insulators: Hubbard U instead of Stoner I. Physical Review B, 1991. **44**(3): p. 943-954.

Chapter 5. Summary

Lithium iron phosphate (LFP) has attracted tremendous attention as an electrode material for next-generation lithium rechargeable battery systems due to the use of low-cost iron, long cycle-life and its chemical/electrochemical stability. While the lithium diffusion in LFP, the essential property during battery operation, is relatively fast due to the one-dimensional tunnel present in the olivine crystal structure, the tunnel is inherently vulnerable to immobile anti-site defects which, if any, block the lithium diffusion and lead to the inferior performance. Herein, we demonstrate that the kinetic issue arising from the defects in LFP can be completely eliminated in lithium-excess olivine LFP, which we successfully synthesized for the first time. The presence of excess amount of lithium in the olivine structure reduces the concentration of defects in the tunnel by ~ 7 orders of magnitude. Moreover, it opens up a new lithium diffusion path along the [101] direction making the olivine LFP as a three-dimensional lithium diffuser. We also observe that the intrinsic energy barrier for phase transition is notably reduced in the lithium-excess olivine LFP. The fundamentally different nature of lithium-excess olivine LFP compared with normal LFP additionally induces a faster charging capability, reducing the thermal solid-solution temperature and resulting in a significantly less memory effect. The

excess ionic carrier concept in the electrode crystal brings up unexpected properties for the pristine crystal and offers a novel and interesting approach to enhance the diffusivity by opening up additional diffusion paths in solid-state ionic conductors.

Chapter 6. Abstract in Korean

현재 인류는 화석 연료의 고갈, 산업화에 따른 CO₂ 배출, 지구온난화와 같은 환경 문제에 직면하고 있다. 이 문제를 해결하고자, 기존의 화석 연료를 이용한 에너지 생산 및 이용에서 벗어난 친환경 에너지 생산 기술인 풍력, 수력, 태양열 발전 기술이 주목을 받고 있다. 그러나, 상위 친환경 에너지 발전 기술들은 공간적 혹은 시간적 제약이 존재하며, 간헐적인 발전을 하기 때문에 에너지 수요와 공급이 일치하지 못하는 문제를 가진다. 이 문제를 해결하고자 친환경 발전 기술을 보조할 수 있는 대형 에너지 저장 기술이 각광을 받고 있다. 다양한 에너지 저장 기술 중 리튬 이차전지 기술은 높은 에너지 밀도, 장수명성, 높은 효율성으로 친환경 발전 기술을 보조할 대형 에너지 저장 기술로 큰 주목을 받고 있다.

리튬 이차전지 기술에 사용되는 전극 물질은 대부분 intercalation 반응으로 충전과 방전 반응이 행해지며, 충전 중에는 구조 내에서 전자와 리튬 이온이 결정 구조 외로 탈리, 방전 중에는 결정 구조 내로 전자와 리튬 이온이 삽입이 되는 반응을 한다. 그렇기 때문에 전극 물질의 전기화학 특성은 결정 구조와 화학적 조성에

의해서 결정이 된다. 다양한 전극 물질 중 올리빈계 리튬 인산화 철 양극 물질은 높은 열적 안정성, 장 수명성, 낮은 가격으로 인하여 대형 에너지 저장 기술에 사용 적합한 물질로 주목을 받고 있다. 이론적으로 이 물질은 약 580 Wh Kg^{-1} (용량: 169 mAh g^{-1} , 전압: 3.42 V vs. Li)의 에너지 밀도를 가지고 있으며, 결정 구조에 기인하는 1차원 리튬 이온 확산 경로를 가지고 있다. 그러나, 이러한 결정학적 한계에 의해서 합성 시에 생성이 되는 양이온 자리 교환 결함에 굉장히 취약한 특징을 가진다. 충전과 방전과정에서 움직이지 않는다고 알려진 이 양이온 자리 교환 결함은 리튬 확산 경로에 존재하고 있으며, 통계적으로 약 1%의 자리 교환 결함은 1 마이크로 크기의 상위 전극 물질의 용량을 절반 가량 내놓지 못하게 하며, 리튬 이온의 전도도를 2~3승 이상 저하시키는 것으로 보고되었다.

본 연구는 리튬 이차전지용 양극 소재인 리튬 인산화 철 물질의 양이온 자리 결함의 문제를 해결하고자 진행이 되었으며, 2장에서는 전기화학반응을 이용한 양이온 자리 결함을 제거 하는 방법에 관하여 논한다. 공극이 더해진 결정 구조에서는 양이온 자리 결함이 원래의 자리를 되돌아 갈 수 있는 경로를 제공해

주게 되며, 전자를 삽입하는 과정에서 상위 물질의 양이온 자리 결함이 원래의 결정학적 자리를 찾아가게 되는 효과를 가진다.

3장에서는 상위 양극 물질을 리튬 과량으로 합성하여서 이 문제를 해결하는 방법을 소개한다. 리튬 과량으로 합성된 상위 물질은 결정 구조 내부의 철 이온 자리를 부분적으로 차지 하고 있음을 다양한 결정 분석 방법으로 확인을 하였으며, 전이 금속 산화수 변화로 인해 양이온 자리 교환 결함이 극적으로 사라지게 되는 것을 확인하였다. 뿐만 아니라, 과량 Li 이온은 새로운 확산 경로를 제공하게 되어서 더 이상 1차원 확산이 아닌 3차원 확산을 가능케 한다. 때문에, 기존 물질보다 2배 이상 높은 출력 특성을 보이며 장수명성 또한 뛰어난 것을 확인하였다. 또한, 최근 이슈가 되고 있는 LFP 양극 물질의 열역학적 Spinodal 분해 에너지가 기존보다 낮아지는 것을 확인 하였으며, 이 현상을 ‘*phase mixing seed*’라는 새로운 모델을 제시해 설명을 한다.